UNIVERSIDADE FEDERAL DO RIO GRANDE DO SUL

Instituto de Física

Busca e análise de sistemas estelares do halo externo da Galáxia

Elmer Fidel LUQUE CANAZA

Orientador: Dr. Basílio SANTIAGO

Porto Alegre

Brasil

Novembro de 2017

UNIVERSIDADE FEDERAL DO RIO GRANDE DO SUL

Instituto de Física

TESE DE DOUTORADO

Busca e análise de sistemas estelares do halo externo da Galáxia

---

Autor:
Elmer Fidel LUQUE CANAZA

Orientador:
Dr. Basílio SANTIAGO

Tese de doutorado realizada sob orientação do Dr. Basílio Xavier Santiago e apresentada ao Programa de Pós–Graduação em Física da UFRGS em preenchimento parcial dos requisitos para a obtenção do título de Doutor em Ciéncias na área de Astrofísica.

Porto Alegre

Brasil

Novembro de 2017

A Deus e meus pais.

Agradecimentos

Durante estes quatro anos, muitas são as pessoas que contribuiram diretamente ou indiretamente na realização deste trabalho. Espero que as seguintes linhas sirvam para expressar os meus mais profundos e sinceros agradecimentos a todas essas pessoas.

Em primeiro lugar, quero agradecer o apoio incondicional da minha família, meus pais, irmãos, sobrinhos e tios.

Meu profundo agradecimento ao meu orientador, professor Dr. Basílio Santiago, pela motivação, ensinamento, exemplo de ética e pelo apoio que recebi ao longo destes anos.

Agradeço ao meu amigo Leandro Kerber pelos conselhos, ensinamento e por confiar em mim desde que me iniciei na aventura da Astrofísica. Ao Adriano Pieres e à Anna Bárbara Queiroz, pelas contribuições dadas neste trabalho.

Agradeço a todos os meus amigos, tanto no Brasil quanto em Perú, que me apoiaram e acreditaram em mim.

Agradeço às instituições – DES-Brazil; LIneA – que tornaram possível a nossa participação no projeto DES.

À CAPES e ao CNPq, pelo tempo em que me concederam bolsa de doutorado.

Por fim, agradeço ao Programa de Pós–Graduação em Física da UFRGS e ao Departamento de Astronomia, pela oportunidade para a realização do doutorado.

"One thing I have learned in a long life: that all our science, measured against reality, is primitive and childlike — and yet it is the most precious thing we have."

– Albert Einstein

Universidade Federal do Rio Grande do Sul

Resumo

Instituto de Física

Busca e análise de sistemas estelares do halo externo da Galáxia

por Elmer Fidel LUQUE CANAZA

Uma previsão fundamental do cenário Λ *cold dark matter* (ΛCDM) na formação de estruturas é que os halos galácticos de DM do tamanho da Via Láctea (MW) crescem pela acreção de subsistemas menores. Neste contexto, simulações de N−corpos prevêem um número de sub-halos de matéria escura, cujo tamanho e massa são comparáveis às galáxias anãs, que é muito maior do que as galáxias satélites conhecidas. Este é o que se convencionu chamar de problema das satélites faltantes (MSP). A interpretação mais popular do MSP é que os sub-halos de matéria escura menores são extremamente ineficientes na formação de estrelas, o que torna mais difícil detectá-los. Com a chegada dos grandes levantamentos fotométricos, nos últimos anos, a descoberta de uma nova população de galáxias satélites que orbitam a MW fornece evidências empíricas para acreditar que realmente existem várias galáxias pouco luminosas não detectadas ou que simplesmente habitam regiões no céu que ainda não foram observadas.

Neste trabalho implementamos um algoritmo estatístico eficiente para detectar subestruturas ultra fracas da MW. O código, chamado SPARSEX, foi testado e otimizado usando um conjunto de objetos estelares previamente identificados nos dados do *Sloan Digital Sky Survey* (SDSS), conseguindo recuperar todos os objetos com sucesso. Além disso, a aplicação do algoritmo aos dados dos dois primeiro anos do *Dark Energy Survey* (DES) deu como resultado centenas de candidatos a sistemas estelares. Dezessete sistemas estelares detectados em comum com outras técnicas de busca por subestruturas, implementadas dentro do grupo de colaboração do DES, foram publicados em três artigos em 2015. Um dos candidatos publicados é o aglomerado estelar DES 1. DES1 foi detectado pelo código SPARSEX com uma alta significância estatística e aparece nas imagens do DES como uma concentração compacta de fontes pontuais azuis. O sistema estelar é consistente com uma população velha e pobre em metal. Assumindo dois diferentes perfis de densidade, os quais permitem estimar a probabilidade de que cada estrela realmente pertença ao sistema, determinamos uma distância heliocêntrica e uma magnitude absoluta total num intervalo de 77.6 — 87.1 kpc e $-3.00 \lesssim M_V \lesssim -2.21$, respectivamente. O raio à meia-luz desse objeto, $r_{\rm h} \sim 9.88$ pc, e a luminosidade são consistentes com um aglomerado estelar de baixa luminosidade do halo externo. DES1 também é

alongado ($\epsilon \sim 0.6$), o que faz supor que este objeto está em estágio avançado de dissolução. Mais tarde, através de uma cuidadosa reanálise de nossos resultados, dois novos candidatos foram detectados, DES J0111−1341 e DES J0225+0304. Os candidatos estão localizados a uma distância heliocêntrica de ~ 25 kpc e parecem também estar dominados por populações estelares velhas e pobres em metais. Suas distâncias ao plano orbital da galáxia anã de Sagitário, ~ 1.73 kpc (DES J0111−1341) e ~ 0.50 kpc (DES J0225+0304), indicam que eles estão possivelmente associados com a corrente da anã de Sagitário. O raio à meia-luz ($r_{\rm h} \simeq 4.55$ pc) e a luminosidade ($M_V \simeq +0.3$) de DES J0111−1341 são consistentes com um aglomerado estelar ultra fraco, enquanto o raio à meia-luz ($r_{\rm h} \simeq 18.55$ pc) e a luminosidade ($M_V \simeq -1.1$) de DES J0225+0304 colocam este objeto em uma região ambígua do plano tamanho-luminosidade entre aglomerados estelares e galáxias anãs. Determinações dos parâmetros característicos da corrente de Sagitário, tais como o espalhamento de metalicidade ($-2.18 \lesssim [{\rm Fe/H}] \lesssim -0.95$) e o gradiente de distância ($23\,{\rm kpc} \lesssim {\rm D}_\odot \lesssim 29\,{\rm kpc}$), dentro da área amostrada do DES no hemisfério sul, também indicam uma possível associação com estes sistemas. Se esses objetos forem confirmados através de *follow-up* espectroscópico como sistemas ligados gravitacionalmente e compartilharem uma trajetoria Galáctica com a corrente de Sagitário, DES J0111−1341 e DES J0225+0304 seriam os primeiros sistemas estelares ultra fracos associados com tal corrente.

Recentemente, nós reportamos a descoberta de um novo aglomerado estelar, DES 3. O novo sistema foi detectado como uma sobredensidade estelar nos dados do primeiro ano do DES e confirmado com *follow-up* fotométrico obtido com o *Southerm Astrophysical Research* (SOAR) *Telecope*. Nós determinamos que DES 3 está localizado a uma distância heliocêntrica de ~ 76 kpc e é dominado por uma população velha ($\simeq 9.8$ G anos) e pobre em metal ($[{\rm Fe/H}] \simeq -1.88$). Embora os valores de idade e metalicidade de DES 3 são semelhantes aos aglomerados globulares, o seu raio à meia-luz ($r_{\rm h} \sim 6.5$ pc) e a luminosidade ($M_V \sim -1.9$) são mais indicativos de um aglomerados estelar fraco. Com base no tamanho angular aparente, o DES 3, com um valor de $r_{\rm h} \sim 0\farcm3$, está entre os menores aglomerados estelares fracos conhecidos até à data.

Estas novas detecções indicam que o censo de satélites da MW é ainda incompleto. A identificação e estudo de novos satélites em futuros surveys, como por exemplo o *Large Synoptic Survey Telescope* (LSST) será crucial para a nossa compreensão das subestruturas existentes no halo Galáctico e a evolução da Galáxia como um todo.

Palavras-chave: galáxias anãs, aglomerados globulares, Grupo Local

Universidade Federal do Rio Grande do Sul

Abstract

Institute of Physics

Search and analysis of stellar systems of the outer halo of the Galaxy

by Elmer Fidel LUQUE CANAZA

A fundamental prediction of the Λ cold dark matter (ΛCDM) scenario of structure formation is that galactic DM haloes of the size of the Milky Way (MW) grow by the accretion of smaller sub-systems. In this context, N−body simulations predict a number of dark matter subhalos, with size and mass comparable to dwarf galaxies, but which is much larger than currently known satellite galaxies. This is what is conventionally called the missing satellites problem (MSP). The most popular interpretation of the MSP is that the smaller dark matter subhalos are extremely inefficient in star formation, making it more difficult to detect them. With the arrival of large photometric surveys, in recent years, the discovery of a new population of satellite galaxies orbiting the MW provides empirical evidence to believe that there are actually several low luminosity galaxies that were not yet detected or that simply inhabit regions in the sky that have not yet been observed.

In this work we present an efficient statistical algorithm to detect ultra-faint MW substructures. The code, called SPARSEX, was tested and optimized using a set of stellar objects previously identified in the Sloan Digital Sky Survey (SDSS) data. It has detected successfully all known objects. In addition, the algorithm was applied on the first two years of Dark Energy Survey (DES) data, resulting in hundreds of stellar system candidates. Seventeen stellar systems detected in common with other substructure search techniques implemented within the DES collaboration were published in three papers in 2015. In particular, one published candidate is a star cluster, DES 1. DES 1 was detected by the SPARSEX code with high statistical significance and appears in DES images as a compact concentration of blue point sources. The stellar system is consistent with being dominated by an old and metal-poor population. Assuming two different density profiles, based on which we may evaluate a membership probability for each star, we determined a heliocentric distance and total absolute magnitude in the ranges of 77.6 — 87.1 kpc and $-3.00 \lesssim M_V \lesssim -2.21$, respectively. The half-light radius of this object, $r_{\rm h} \sim 9.88$ pc, and luminosity are consistent with a low-mass halo star cluster. DES1 is also elongated ($\epsilon \sim 0.6$), which suggests that this object is in advanced stage of dissolution. Later, through a careful reanalysis of our results, two new candidates were detected, DES J0111−1341 e DES J0225+0304. The candidates are located at a heliocentric

distance of $\sim$ 25 kpc and appear to have old and metal-poor populations as well. Their distances to the Sagittarius dwarf orbital plane, $\sim$ 1.73 kpc (DES J0111−1341) and $\sim$ 0.50 kpc (DES J0225+0304), indicate that they are possibly associated with the Sagittarius dwarf stream. The half-light radius ($r_{\rm h} \simeq 4.55$ pc) and luminosity ($M_V \simeq +0.3$) of DES J0111−1341 are consistent with it being an ultra-faint star cluster, while the half-light radius ($r_{\rm h} \simeq 18.55$ pc) and luminosity ($M_V \simeq -1.1$) of DES J0225+0304 place it in an ambiguous region of size-luminosity space between star clusters and dwarf galaxies. Determinations of the characteristic parameters of the Sagittarius stream, such as its metallicity spread ($-2.18 \lesssim [{\rm Fe/H}] \lesssim -0.95$) and distance gradient (23 kpc $\lesssim {\rm D}_\odot \lesssim$ 29 kpc), within the DES footprint in the Southern hemisphere, also indicate a possible association with these systems. If theses objects are confirmed through spectroscopic follow-up to be gravitationally bound systems and to share a Galactic trajectory with the Sagittarius stream, DES J0111−1341 and DES J0225+0304 would be the first ultra-faint stellar systems associated with the Sagittarius stream.

Recently, we reported the discovery of a new star cluster, DES 3. The new system was detected as a stellar overdensity in first-year DES data, and confirmed with deeper photometry from the Southern Astrophysical Research (SOAR) telescope. We determine that DES 3 is located at a heliocentric distance of $\sim$ 76 kpc and it is dominated by an old ($\simeq$ 9.8 Gyr) and metal-poor ($[{\rm Fe/H}] \simeq -1.88$) population. While the age and metallicity values of DES 3 are similar to globular clusters, its half-light radius ($r_{\rm h} \sim 6.5$ pc) and luminosity ($M_V \sim -1.9$) are more indicative of faint star clusters. Based on the apparent angular size, DES 3, with a value of $r_{\rm h} \sim 0\farcm3$, is among the smallest faint star clusters known to date.

These new detections indicate that the MW satellites census is still incomplete. The identification and study of new satellites in future surveys, such as the Large Synoptic Survey Telescope (LSST), will be crucial to our understanding of substructures in the Galactic halo and the evolution of the Galaxy as a whole.

Keywords: dwarf galaxies, globular clusters, Local Group

Sumário

Lista de Figuras

Lista de Tabelas

Lista de Abreviaturas

APASS	**A**AVSO **P**hotometric **A**ll-**S**ky **S**urvey
APOGEE	**APO** **G**alactic **E**volution **E**xperiment
BOSS	**B**aryon **O**scillation **S**pectroscopic **S**urvey
BPG	**B**razilian **P**articipation **G**roup
CDM	**C**old **D**ark **M**atter
CMD	**C**olor–**M**agnitude **D**iagram
CTIO	**C**erro **T**ololo **I**nter-American **O**bservatory
DES	**D**ark **E**nergy **S**urvey
DESDM	**DES** **D**ata **M**anagement
DECam	**D**ark **E**nergy **Cam**era
DR	**D**ata **R**elease
GC	**G**lobular **C**luster
HB	**H**orizontal **B**ranch
IMF	**I**nitial **M**ass **F**unction
LIneA	**L**aboratório **In**ter-institucional de **e**–**A**stronomia
LSST	**L**arge **S**ynoptic **S**urvey **T**elescope
LMC	**L**arge **M**agellanic **C**loud
MARVELS	**M**ulti-object **A**PO **R**adial **V**elocity **E**xoplanet **L**arge-area **S**urvey
MF	**M**atched **F**ilter
MS	**M**ain **S**equence
MSP	**M**issing **S**atellite **P**roblem
MSTO	**M**ain **S**equence **T**urn-**O**ff
MW	**M**ilky **W**ay
OC	**O**pen **C**luster
Pan-STARRS	**Pan**oramic **S**urvey **T**elescope **A**nd **R**apid **R**esponse **S**ystem
PDF	**P**robability **D**istribution **F**unction
PS	**P**oisson **S**ignificance
PSF	**P**oint **S**pread **F**unction
RC	**R**ed **C**lump
RGB	**R**ed **G**iant **B**ranch
SDSS	**S**loan **D**igital **S**ky **S**urvey
SEGUE	**S**loan **E**xtension for **G**alactic **U**nderstanding and **E**xploration
SGB	**S**ub **G**iant **B**ranch
SMC	**S**mall **M**agellanic **C**loud
SOAR	**SO**uthern **A**strophysical **R**esearch

SPT	**S**outh **P**ole **T**elescope
SSP	**S**imple **S**tellar **P**opulation
SV	**S**cience **V**erification
S82	**S**tripe **82**
WAVG	**W**eighted–**AV**era**G**e
Y1P1	**Y**ear **1** **P**reliminary Release **1**
Y1A1	**Y**ear **1** **A**nnual Release **1**
Y2Q1	**Y**ear **2** **Q**uick Release **1**
2MASS	**Two**-**M**icron **A**ll-**S**ky **S**urvey

Capítulo 1

Introdução

Pelo paradigma mais aceito atualmente, as estruturas do Universo, desde escalas sub-galácticas até escalas de aglomerados de galáxias, formam-se pelo colapso gravitacional de não–homogeneidades primordiais inicialmente com contraste de densidade da ordem de $\delta\rho \simeq 10^{-4}$. Em modelos cosmológicos de matéria escura fria (CDM), as estruturas são formadas por um processo herárquico do tipo *bottom–up*, ou seja, estruturas menores colapsam primeiro e depois se agregam para formar as grandes estruturas (White & Rees 1978; Davis et al. 1985). Simulações de N–corpos com crescente resolução em escalas galácticas vêm revelando que uma galáxia como a nossa se formou pela fusão e acreção de fragmentos menores, também dominados por matéria escura, tendo este processo sido mais intenso nos primeiros bilhões de anos de sua formação (Klypin et al. 1999; Moore et al. 1999; Stewart et al. 2008). Essas simulações também mostraram que tal acreção de fragmentos é incompleta e que as subestruturas que sobreviveram orbitam as galáxias hospedeiras em forma de sub-halos de matéria escura. As simulações de N–corpos que descrevem este processo identificam que as escalas de tamanho e massa características de parte desses fragmentos são comparáveis às galáxias anãs. A possível identificação destas últimas como tijolos de formação de galáxias maiores é reforçada pelas evidências de que os exemplares remanescentes do sistema de satélites da Galáxia são ricos em matéria escura (Suntzeff et al. 1993; Walker et al. 2007; Battaglia et al. 2011). O censo de satélites de nossa Galáxia, contudo, corresponde a uma fração pequena do sistema que se esperaria existir ainda hoje de acordo com as simulações de N–corpos[1] (Moore et al. 1999; Tollerud et al. 2008). Este é o que se convencionou chamar de problema das satélites faltantes (MSP). Ainda não está claro se isso reflete a ausência de objetos de baixa massa preditos pelas simulações ou simplesmente o fato de que nenhuma estrela conseguiu se formar dentro de um grande número deles, devido, possivelmente, aos ventos de supernovas ou ao fundo ionizante intergaláctico (Klypin et al. 1999). Uma das alternativas para a discrepância numérica entre os halos subgalácticos ricos em matéria escura previstos pelas simulações e o censo de satélites da Galáxia é que este último esteja fortemente incompleto. Portanto, a detecção dos satélites da Via Láctea (MW) previstos pelas simulações numéricas vai

[1] Os modelos de CDM prevêem $\sim$ 500 — 1000 sub-halos para galáxias do tamanho da MW. No entanto, apenas algumas duzías ($\sim$ 57) de satélites de nossa Galáxia são conhecidos até à data.

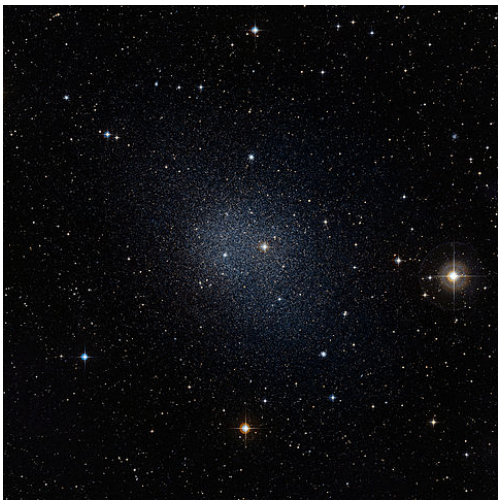

(A) Anã esferoidal Fornax. Crédito: ESO.

(B) Anã irregular SMC: Crédito: SDSS.

FIGURA 1.1: Dois satélites clássicos da MW.

permitir-nos estudar e entender melhor o limite de baixa luminosidade de formação de galáxias e associar melhor a componente bariônica das galáxias com os halos de matéria escura onde elas residem.

Baseado na morfologia, em geral, as galáxias anãs são classificadas em três tipos principais. Anãs elípticas: objetos que contêm pouco gás, população velha e não há evidências recentes de formação estelar. Ao contrário das galáxias elípticas normais, estes sistemas têm um brilho superficial significativamente menor e menos metalicidade. Eles são comumente encontrados em grupos e aglomerados de galáxias. Anãs esferoidais: sistemas mais esféricos do que elípticos, com muito pouco gás, de menor tamanho do que as anãs elípticas, pobres em metais e principalmente dominados por uma população estelar velha. Eles estão distribuidos no Grupo Local. Anãs irregulares: sistemas ricos em gás com evidência clara de formação estelar em curso, mas com baixo brilho superficial (como as anãs esferoidais). Na Figura 1.1 mostramos a galáxia anã esferoidal Fornax e a galáxia anã irregular Pequena Nuvem de Magalhães (SMC).

No contexto da teoría hierárquica de formação de galáxias, os aglomerados estelares são também excelentes traçadores deste processo. O aglomerado Palomar 5 é um exemplo interessante de um sistema físico que está passando agora pelo processo de ruptura de maré antes de ser absorvido pela MW (exemplo, Odenkirchen et al. 2002).

1.1 Aglomerados estelares

Um aglomerado estelar pode ser entendido como um sistema auto-gravitante de estrelas formada a partir da contração gravitacional de uma grande nuvem molecular. Desta forma, todas as estrelas componentes de um aglomerado teriam a mesma idade e composição química muito semelhantes. Dado que as distâncias relativas

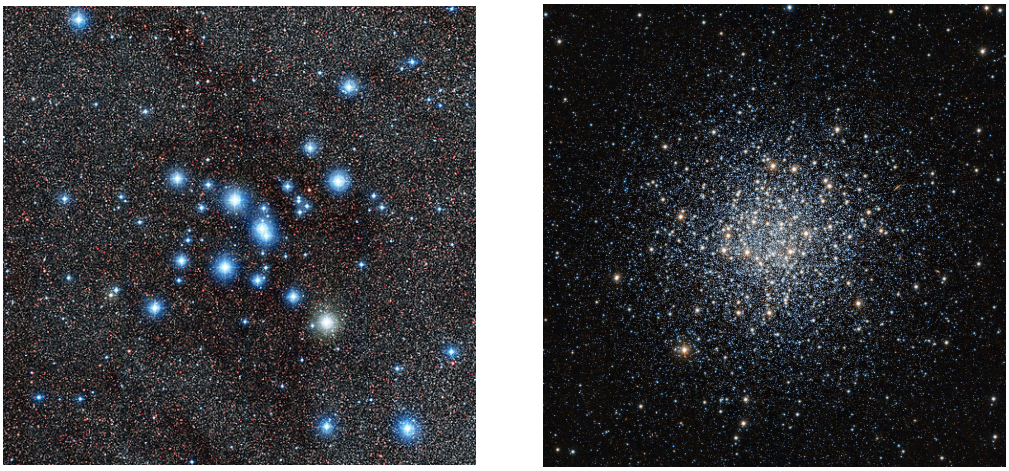

(A) Aglomerado aberto M 7. (B) Aglomerado globular M 55.

FIGURA 1.2: Exemplos típicos de aglomerados estelares da MW. Crédito: ESO.

entre as estrelas dentro de um aglomerado são muito pequenas em comparação com a distância que nos separa delas, podemos considerar que todas as estrelas pertencentes ao aglomerado estão à mesma distância de nós. Portanto, elas são distinguidas apenas pela massa, o qual definirá a evolução e o destino da estrela.

O estudo de diferentes aglomerados da Galáxia inicialmente permitiu classificar estes objetos em dois grupos: os aglomerados abertos (OCs), com baixa estatística estelar, em geral jovens (algumas centenas de milhões de anos), com metalicidade próxima da solar e localizados preferencialmente no plano do disco, e os aglomerados globulares (GCs), ricos em estrelas, velhos ($\sim$ 12 bilhões de anos), com metalicidades sub-solares e associados ao halo, ao bojo e, por vezes, encontrados próximos do centro da MW. Na Figura 1.2 mostramos exemplos destas duas categorias. Nos últimos anos esta dicotomia tem se revelado muito simplificada para atender a diversidade de sistemas. Por exemplo, os GCs incluem dois subsistemas: os globulares pobres em metais ([Fe/H]< -0.8), associados ao halo, e os globulares ricos em metais ([Fe/H] > -0.8), associados ao bojo e ao disco espesso da Galáxia (Zinn 1993), que teriam se formado após os primeiros. Além disso existem GCs em aparente dissolução que possuem densidade de estrelas semelhantes às dos aglomerados abertos, como é o caso do aglomerado Palomar 5 (Odenkirchen et al. 2001) e possivelmente os recentemente descobertos Koposov 1, Koposov 2, Balbinot 1 (Koposov et al. 2007; Balbinot et al. 2013), entre outros. Em relação aos OCs há também uma diversidade de objetos, tal como Berkeley 21, com baixa metalicidade ([Fe/H] $\simeq -0.97$, Friel & Janes 1993), Berkeley 17, com idade comparável a dos globulares (Bragaglia et al. 2006), e NGC 6791, como um dos mais massivos (Kaluzny & Udalski 1992).

Em particular, os GCs figuram entre as estruturas mais antigas do nosso universo e podem ser encontrados em quase todos os tipos de galáxia (por exemplo, Brodie & Strader 2006). Assim, esses sistemas constituem ferramentas importantes para traçar

as propriedades da nossa Galáxia no presente, bem como para reconstruir a história de formação da MW (ver Renaud, Agertz, & Gieles 2017, e referências nele contidas). Estes sistemas, por si mesmos, são interessantes, pois fornecem informações sobre os processos de formação estelar e do próprio aglomerado (exemplo, Downing & Sills 2007; D'Ercole et al. 2008). Além disso, são excelentes laboratórios para estudar sistemas auto-gravitantes (exemplo, Fall & Frenk 1985; Elson, Hut, & Inagaki 1987).

Como mencionado anteriormente, as galáxias maiores podem ter sido formadas a partir de substruturas menores, galáxias anãs (Searle & Zinn 1978). Quando uma galáxia anã é incorporada a uma galáxia do tamanho da MW, seus aglomerados estelares (globulares e abertos) são incorporados na população da Galáxia. A evidência direta desse cenário é a galáxia anã de Sagitário que está em processo de acreção à MW (Ibata, Gilmore, & Irwin 1994). Usando medidas de distâncias e velocidades de vários GCs, Law & Majewski (2010a) determinaram que vários desses objetos provavelmente estão associados com a anã de Sagitário (veja Seção 1.2). Zinn (1993) classificou os GCs da MW em dois grupos com base na metalicidade e morfologia do ramo horizontal (HB). Este autor descobriu que os GCs ricos em metal ($[\mathrm{Fe/H}] > -0.8$) são distribuídos no bojo e no disco da Galáxia, enquanto os aglomerados pobres em metal ($[\mathrm{Fe/H}] < -0.8$) estão geralmente localizado no halo Galáctico. A morfologia do HB dos GCs do halo da MW levou a Zinn (1993) a definir dois subsistemas, as chamadas populações de Halo jovem e do Halo velho[2]. Estes mesmos autores mostraram que ambas as populações possuem distribuições radiais e cinemáticas diferentes e indicam que possivelmente a população do Halo jovem se originou com as galáxias satélites, as quais foram canibalizadas pela MW. Mais tarde, este trabalho foi ampliado por Mackey & Gilmore (2004). Estes autores compararam a morfologia do HB dos subsistemas do Halo jovem, Halo velho e bojo/disco da Galáxia com GCs de quatro galáxias anãs: Fornax, Sagitário, a Grande e Pequena Nuvem de Magalhães. Eles descobriram que os GCs dos satélites da MW são semelhantes à população do Halo jovem em termos da morfologia do HB, mas aproximadamente 20—30% dos aglomerados dos satélites são semelhantes à população do Halo velho. Esses autores também compararam as distribuições do raio do core das populações do Halo jovem, Halo velho e a população de GCs dos satélites. Eles descobriram que as populações de Halo jovem e o Halo velho têm diferentes distribuições do raio de core, enquanto as distribuições do raio de core para as populações de Halo jovem e aquelas originárias de galáxias anãs são muito similares. Assim, eles concluíram que 30 dos aglomerados do Halo jovem e 10—12 aglomerados do Halo velho foram originadas em galáxias anãs e estimam que a MW se fundiu com cerca de sete galáxias anãs esferoidais.

Com base em observações, Willman & Strader (2012) fornecem uma distinção entre galáxias anãs e aglomerados estelares. As galáxias anãs distinguem-se dos aglomerados estelares por terem uma massa dinâmica, obtida via Teorema do Virial

[2]O grupo do Halo jovem é composto por aglomerados que são significativamente mais jovens (Δ idade > 1 G ano) que os aglomerados do Halo velho de $[\mathrm{Fe/H}]$ similar.

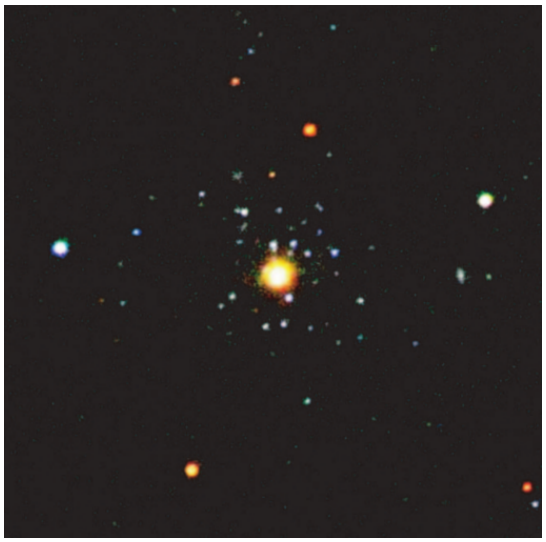

FIGURA 1.3: Figura extraida de Koposov et al. (2007). Aglomerado estelar fraco ($M_V \sim -2$) Koposov 1 localizado a uma distância heliocêntrica de ~ 50 kpc.

utilizando a determinação espectroscópica da dispersão de velocidades radiais, que é substancialmente maior do que a massa inferida a partir da população estelar luminosa e/ou um espalhamento significativo em metalicidade estelar, $\gtrsim 0.3$ dex, indicativo de múltiplas gerações de formação estelar e um potencial gravitacional suficiente para reter o material ejetado pela explosão de uma supernova.

O censo de satélites da MW tem crescido rapidamente nos últimos 15 anos. Além disso, vários objetos recém encontrados são sistemas estelares com baixas luminosidades ($-3 \lesssim M_V \lesssim 0$) e pequeno raio à meia-luz ($r_{\rm h} < 10$pc), sendo mais consistentes com aglomerados estelares (Koposov et al. 2007; Belokurov et al. 2010; Fadely et al. 2011; Muñoz et al. 2012; Balbinot et al. 2013). Na Figura 1.3 mostramos um exemplo desta nova classe de aglomerados estelares fracos. Acredita-se que estes aglomerados possam estar sofrendo perda de massa estelar através de processos dinâmicos, como perturbação de maré ou evaporação estelar (Koposov et al. 2007; Kim & Jerjen 2015a). O número de galáxias anãs em torno da Galáxia também aumentou significativamente, de 11 anãs clásicas conhecidas até o final da década de 1990, até um total de 27 que eram conhecidos no início de 2015 (McConnachie 2012), graças em grande parte ao *Sloan digital Sky Survey* (SDSS). Várias das anãs encontradas com o SDSS são sistemas de baixa luminosidade ($-18 \lesssim M_V \lesssim -8$) com uma alta razão massa–luminosidade, M/L, o que representa alguns dos objetos mais ricos em matéria escura (Simon & Geha 2007). As galáxias anãs precisam dessa matéria escura para explicar sua cinemática observada, enquanto a massa dos GCs pode ser explicada considerando apenas a matéria visível.

A classificação fotométrica provisória dos sistemas estelares como galáxias anãs se baseia em seu baixo brilho superficial, grande tamanho físico, grande elipticidade, e/ou grande distância heliocêntrica. No entanto, alguns desses objetos se encontram em uma região no plano tamanho-luminosidade onde a distinção entre galáxia

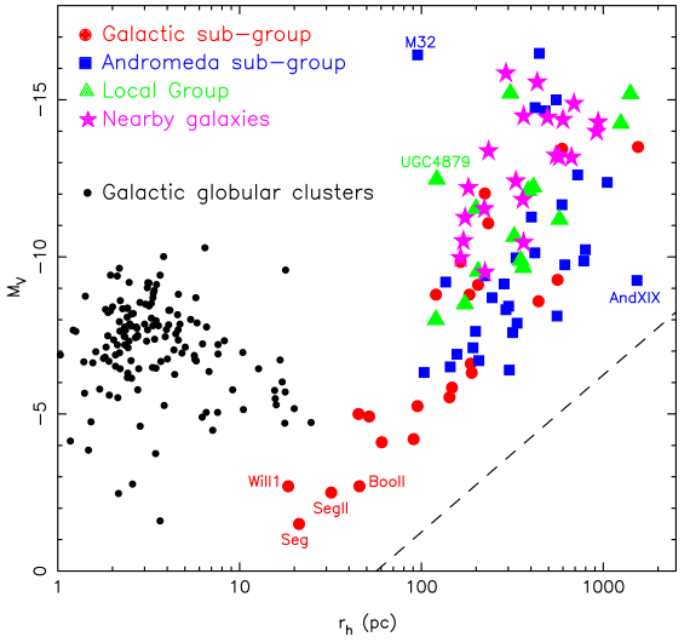

FIGURA 1.4: Figura extraida de McConnachie (2012). Magnitude absoluta vs raio à meia-luz para uma amostra de galáxias satélites da MW (círculos vermelhos), M31 (quadrados azuis), Grupo Local (triângulos verdes) e galáxias próximas (estrelas magentas). Os pontos pretos indicam os GCs da Galáxia (Harris 1996). A linha tracejada indica o contorno de brilho superficial constante em $\mu \simeq 31.5\,\mathrm{mag\,arcsec^{-2}}$. Uma versão atualizada deste gráfico será apresentada ao longo deste trabalho.

anã e aglomerado estelar é ambígua (Figura 1.4). Medidas espectroscópicas destes satélites podem esclarecer essa distinção (Willman & Strader 2012). Portanto, é importante obter um censo completo de sistemas estelares fracos que habitam no halo Galáctico e caracterizá-los em termos da estrutura, populações estelares e o conteúdo de matéria escura.

Um aumento considerável no número de satélites conhecidos da MW foi trazido pelo *Dark Energy Survey* (DES; The Dark Energy Survey Collaboration 2005). Usando a primeira liberação interna dos dados do DES (Y1A1), em março de 2015, Bechtol et al. (2015) relataram a descoberta de oito novos satélites da Galáxia em um ângulo sólido de $\sim 1800\,\mathrm{graus}^2$ no hemisfério sul equatorial. Seis destes sistemas têm tamanhos e luminosidades claramente consistentes com as anãs de baixa luminosidade detectadas anteriormente no SDSS. Para os outros dois objetos, sua classificação é menos clara. Em um esforço paralelo, Koposov et al. (2015a) relataram nove novos satélites da Galáxia usando os mesmos dados das imagens do DES, oito candidatos em comum com Bechtol et al. (2015) e um objeto adicional. Um dos objetos em comum entre os dois grupos, Kim 2, tinha de fato sido previamente encontrado por Kim et al. (2015), utilizando dados do *Stromlo Milky Way Satellite Survey*. Além disso, Kim & Jerjen (2015b) descobriram ainda outro objeto estelar em dados do primeiro ano do DES, Horologium II.

Posteriormente, usando as observações do segundo ano do DES, que cobre um

ângulo sólido de $\sim$ 5000 graus^2, e uma reanálise de nossos potenciais candidatos, Drlica-Wagner et al. (2015), Luque et al. (2016) e Luque et al. (2017b) anunciaram a descoberta de 11 novos satélites estelares da Galáxia adicionais aos reportados por Bechtol et al. (2015). Nove destes sistemas têm tamanho e luminosidade consistentes com as galáxias anãs fracas detectadas nos dados do DES Y1A1. Em particular, dois objetos são compactos e de baixa luminosidade, consistentes com um aglomerado estelar do halo da Galáxia. Ao longo dos últimos dois anos, muitos candidatos a satélites foram também encontrados nos seguintes surveys: *the Panoramic Survey Telescope and Rapid Response System 1* (Pan-STARRS; Laevens et al. 2014; Laevens et al. 2015a; Laevens et al. 2015b), *the Survey of the Magellanic Stellar History* (Martin et al. 2015), VST ATLAS (Torrealba et al. 2016a; Torrealba et al. 2016b), *the Hyper Suprime–Cam Subaru Strategic Program* (Homma et al. 2016; Homma et al. 2017), e *the Magellanic SatelLites Survey* (Drlica-Wagner et al. 2016). Em particular, dos 21 candidatos fracos que foram encontrados nos dados DES, até agora, medições espectroscópicas da velocidade radial e metalicidade confirmaram que Reticulum II (Koposov et al. 2015b; Simon et al. 2015; Walker et al. 2015), Horologium I (Koposov et al. 2015b), Tucana II (Walker et al. 2016), Grus I (Walker et al. 2016), Tucana III (Simon et al. 2017) e Eridanus II (Li et al. 2017) são de fato galáxias anãs. A possível associação dos candidatos a galáxias anãs recentemente descobertos nos dados do DES com a Grande e Pequena Nuvem de Magalhães tem sido discutida por vários autores (exemplo, Bechtol et al. 2015; Drlica-Wagner et al. 2015; Drlica-Wagner et al. 2016; Jethwa, Erkal, & Belokurov 2016; Koposov et al. 2015a; Dooley et al. 2017; Sales et al. 2017). Vários dos candidatos podem estar associados com a corrente de Sagitário (Luque et al. 2017b).

Além dos 21 novos satélites detectados nos dados do DES, também foi identificado uma nova corrente estelar associada à galáxia anã de Phoenix (Balbinot et al. 2016) e sobredensidades associados a Eridanus–Phoenix (Li et al. 2016). Recentemente, Pieres et al. (2017) detectaram uma densidade estelar alongada a 8° ao norte da SMC. Os autores indicam que tal sobredensidade provavelmente foi removido do disco da SMC através de efeitos de maré.

Tais subestruturas são evidências claras de que o processo hierárquico de acreção continua até tempos recentes, de forma que a população original de anãs da Galáxia era muito maior do que no presente.

1.2 A corrente de Sagitário e seu sistema de aglomerados estelares

A galáxia anã de Sagitário foi descoberta há relativamente pouco tempo devido à sua posição no outro lado da MW (Ibata, Gilmore, & Irwin 1994). Sua morfologia estendida em direção ao plano da MW sugeriu a existência de características adicionais de maré (Johnston, Spergel, & Hernquist 1995; Lynden-Bell & Lynden-Bell 1995; Mateo et al. 1996). O *Two-Micron All-Sky Survey* (2MASS) e o SDSS deixaram claro que esta

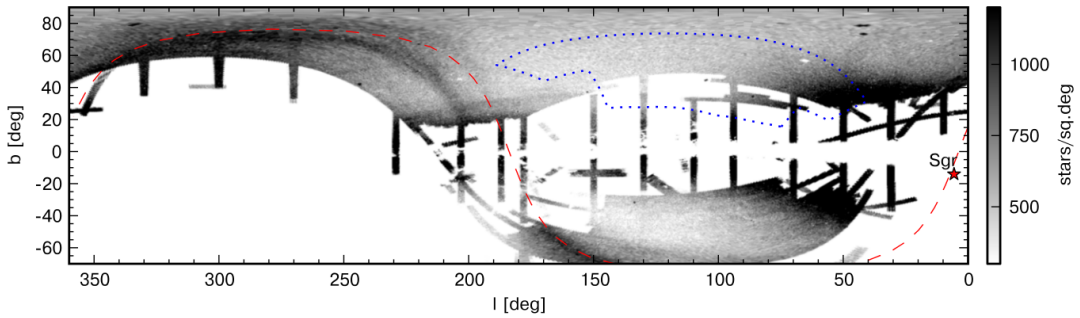

FIGURA 1.5: Figura extraida de Koposov et al. (2012). Mapa de densidade dos dados do SDSS *Data Release* 8, usando estrelas do *turn-off* da sequência principal, em coordenadas Galácticas. A corrente de Sagitário nos hemisférios norte e sul Galáctico é claramente visível. A localização atual da anã de Sagitário é marcado com uma estrela vermelha. A linha vermelha tracejada representa a trajetoria da anã.

galáxia anã é responsável pela subestrutura estelar de maré mais conspícua presente no halo Galáctico (Newberg et al. 2002; Majewski et al. 2003).

Os dados fotométricos mais profundos e também dados espectroscópicos, especificamente do SDSS, forneceram uma descrição mais detalhada da corrente de Sagitário, permitindo uma avaliação de suas propriedades morfológicas, estruturais e cinemáticas, e dissociar as estrelas de Sagitário de outras subestruturas da MW (Newberg et al. 2003; Newberg et al. 2007; Belokurov et al. 2006; Belokurov et al. 2014; Yanny et al. 2009). Esta grande quantidade de dados foi usada por Law & Majewski (2010c) para modelar o potencial gravitacional da MW e encontrar algumas evidências a favor da triaxialidade (ou seja, achatamento com relação a mais de um eixo ou plano de simetria).

Belokurov et al. (2006) demonstraram que a corrente de Sagitário no hemisfério norte Galáctico se bifurca em uma componente brilhante e uma mais fraca separados por $\sim 15^\circ$ no céu. Mais recentemente, Koposov et al. (2012) mostraram que uma bifurcação também aparece nas caudas de Sagitário no hemisfério sul Galáctico (ver Figura 1.5). O ramo mais fraco contém mais estrelas pobres em metal e apresenta uma mistura mais simples de populações estelares do que a estrutura principal. A bifurcação no sul, que se estende pelo menos 30° no céu, foi confirmada usando os dados do Pan-STARRS por Slater et al. (2013). Os autores encontraram evidências de que a subestrutura mais fraca está 5 kpc mais próxima do Sol do que a subestrutura mais brilhante, semelhante ao comportamento observado no hemisfério norte Galáctico. Eles também argumentam que a distância entre as correntes concorda com as previsões das simulações de N−corpos apresentadas por Law & Majewski (2010c). Com base em seu modelo, os mesmos autores também identificam sistemas estelares da MW, galáxias anãs e GCs, que podem estar fisicamente associados com esta galáxia anã. Em particular, observou-se que a anã de Sagitário contém pelo menos quatro GCs (NGC 6715, Arp 2, Terzan 7 e Terzan 8; ver Figura 1.6) dentro de seu corpo principal (Da Costa & Armandroff 1995; Bellazzini, Ferraro, & Ibata 2003).

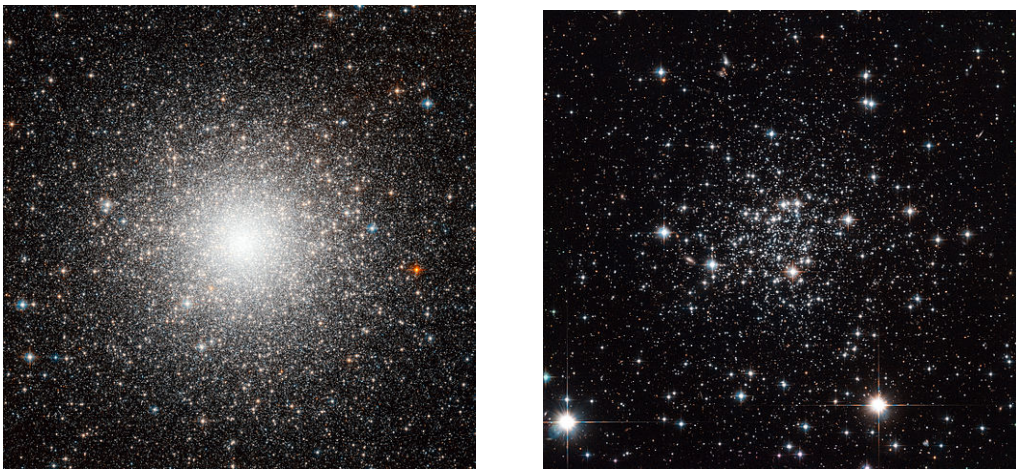

(A) NGC 6715. Crédito: ESA/Hubble & NASA.

(B) Terzan 7: Crédito: ESA/Hubble/NASA & Sarajedini.

FIGURA 1.6: Dois aglomerados estelares associados com o corpo principal da anã de Sagitário.

No entanto, diferentes estudos propuseram que vários GCs provavelmente estejam associados com a corrente de Sagitário (por exemplo, Bellazzini, Ferraro, & Ibata 2003; Dotter et al. 2010; Forbes & Bridges 2010; Dotter, Sarajedini, & Anderson 2011; Carballo-Bello et al. 2014; Sbordone et al. 2015). Até mesmo OCs foram sugeridos como membros da família Sagitário (por exemplo, Carraro et al. 2004; Carraro & Bensby 2009). É provável que os GCs e OCs adicionais possam ter sido removidos da anã de Sagitário durante a interação prolongada com a MW e agora estão espalhados por todo o halo Galáctico. Em uma análise recente baseada em novos modelos de ruptura de maré da anã de Sagitário, Law & Majewski (2010b) descobriram que vários dos candidatos propostos na literatura têm uma probabilidade não desprezível de pertencer à anã de Sagitário. No entanto, ao calcular a quantidade esperada de falsas associações na amostra, eles propuseram que apenas cinco GCs (Arp 2, NGC 6715, NGC 5634, Terzan 8 e Whiting 1) estão quase certamente associados com a anã de Sagitário; um adicional de quatro candidatos (Berkeley 29, NGC 5053, Pal 12 e Terzan 7) são moderadamente prováveis de serem associados.

Agora parece que as estrelas acretadas da anã de Sagitário envolvem completamente o centro Galáctico. Através da análise espectroscópica, Hyde et al. (2015) encontraram mais de 100 bons candidatos da corrente com metalicidades no intervalo de $-0.97 < [\mathrm{Fe/H}] < -0.59$ distribuídos sobre 142°. De Boer, Belokurov, & Koposov (2015) analisam a corrente de Sagitário na região do SDSS *Stripe* 82 (S82) com fotometria e espectroscopia, encontrando uma estreita relação idade−metalicidade. Eles também mostram que o ramo mais fraco da corrente de Sagitário é velho (> 9 G anos) e pobre em metais ($[\mathrm{Fe/H}] < -1.3$), enquanto o ramo dominante possui estrelas que cobrem grandes intervalos em idade e metalicidade.

1.3 Objetivos

As subestruturas (aglomerados estelares e galáxias anãs) da MW são excelentes laboratórios de estudo que podem nos ajudar a entender melhor vários aspectos de nossa Galáxia, tais como: a estrutura do halo estelar (exemplo, Helmi 2008), o histórico de acúmulo de massa de nossa Galáxia (exemplo, González-Samaniego et al. 2014), o potencial gravitacional no halo de matéria escura (exemplo, Law & Majewski 2010c), a natureza das partículas de matéria escura (exemplo, Bertone, Hooper, & Silk 2005; Feng 2010), entre outros. Portanto, a detecção e caracterização de estes sistemas são de grande importância no contexto astronômico.

Extrapolações dos resultados do SDSS em todo o céu e sobre a função luminosidade atualmente conhecida das galaxias anãs da MW indicam que este censo ainda está muito incompleto (veja Tollerud et al. 2008; Hargis, Willman, & Peter 2014). Tollerud et al. (2008) e Hargis, Willman, & Peter (2014) previram o número de galáxias anãs que seriam detectados na área amostrada do DES. Em particular, para uma luminosidade $L < 10^3 L_\odot$, cerca de 24 (99) galáxias com magnitude limite $r = 24\,\mathrm{mag}$ ($r = 25.8\,\mathrm{mag}$) seriam detectadas.

Motivados com estas previsões, e a fim de contribuir para a detecção dessas subestruturas, o que pode mitigar, em parte, o MSP, neste trabalho temos por objetivo desenvolver um código que seja capaz de detectar objetos fracos, tais como galáxias anãs e aglomerados estelares. Uma vez detectados, nos propomos caracterizá-los e, assim, confirmar a natureza destes sistemas.

Este trabalho está organizado da seguinte maneira: no Capítulo 2 descrevemos os dados do SDSS e DES utilizados neste trabalho. O método desenvolvido para a busca por subestruturas da MW e a avaliação do código é apresentado no Capítulo 3. Os resultados da aplicação do código nos dados do DES, a descoberta e a caracterização dos novos sistemas estelares são apresentados no Capítulo 4. As considerações finais são dadas no Capítulo 5. Por fim, no Capítulo 6 apresentamos um sumário e perspectivas de conclusão deste trabalho.

Capítulo 2

Dados

2.1 Sloan Digital Sky Survey

O SDSS (York et al. 2000) é um levantamento fotométrico e espectroscópico que cobre mais de 14000 graus^2 de área no céu. O SDSS utliliza um telescópio de 2.5 m localizado no Novo México nos EUA. Este está equipado com uma câmera que tem um grande campo de imageamento, 30 2048 $\times$ 2048 CCDs (Gunn et al. 1998). O tamanho do pixel é de 24 μm ($0\farcs396$ pixel^{-1}). A câmera foi preparada para imagear o céu em cinco bandas ópticas u, g, r, i, z, atingindo uma magnitude limite de $u \simeq 22.1$, $g \simeq 23.2$, $r \simeq 23.1$, $i \simeq 22.5$ e $z \simeq 20.8$ com uma razão sinal-ruido S/N $\simeq 5$.

O SDSS foi separado em quatro fases de observação; SDSS–I (2000–2005), SDSS–II (2005–2008), SDSS–III (2008–2014) e SDSS–IV (2014–2020). Em particular, o SDSS–III, que proviu o lote de dados fotométricos que usamos neste trabalho, é composto por quatro surveys, cada um focado a um diferente tema científico; *Baryon Oscillation Spectroscopic Survey* (BOSS), *Sloan Extension for Galactic Understanding and Exploration* (SEGUE-2), *APO Galactic Evolution Experiment* (APOGEE) e *Multi-object APO Radial Velocity Exoplanet Large-area Survey* (MARVELS). Atualmente na sua duodécima liberação pública, *Data Release* 12 (DR 12), o SDSS cobriu um área de $\sim$ 14555 graus^2 (Alam et al. 2015).

Para validar o nosso algoritmo de busca, nós usamos dados fotométricos do BOSS que faz parte do DR 8. Também usamos dados do SDSS em torno de cada um dos satélites alvos, aglomerados estelares e galáxias anãs, previamente identificados. As regiões utilizadas são apresentadas na Figura 2.1. Para a separação estrela/galáxia, nós usamos a classificação dada pelos catálogos reduzidos do SDSS. Ou seja, selecionamos todas as fontes classificadas como pontuais (`ObjType=6`). A fim de excluir estrelas brilhantes, fracas e aquelas estrelas de cores extremas, tais como estrelas vermelhas do disco Galáctico e possivelmente objetos espúrios, cortes em magnitude ($17 < g < 23$) e cor ($-0.5 < g - r < 1.2$) também são aplicados.

A nossa participação no SDSS-III ocorreu através do *Brazilian Participation Group* (BPG), coordenado pelo Laboratório Inter-institucional de e-Astronomia (LIneA), cujo grupo interno de populações estelares foi coordenado pelo Dr. Basílio Santiago.

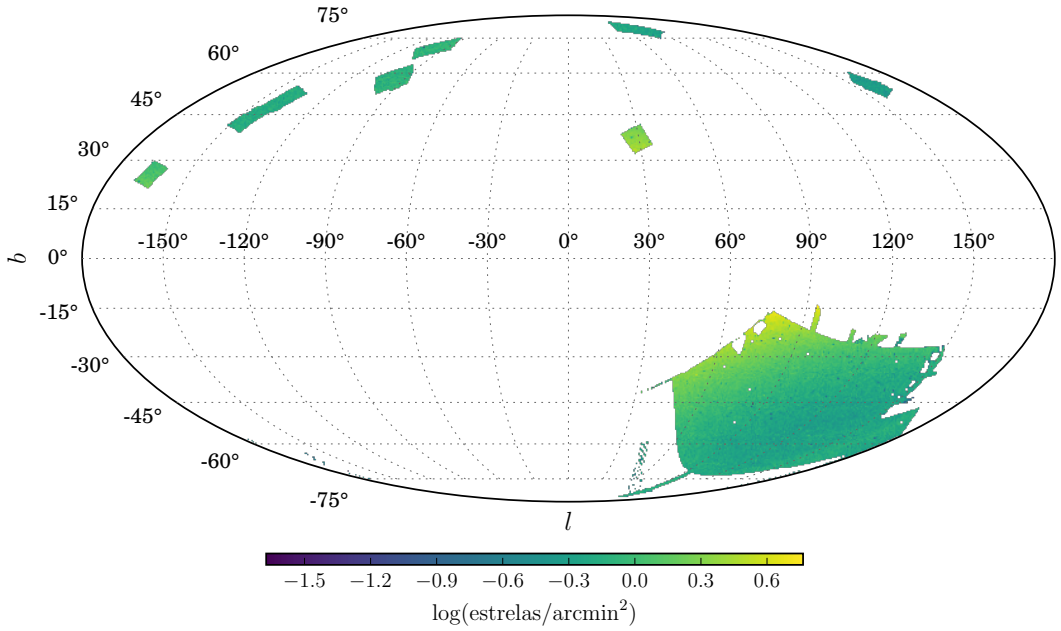

FIGURA 2.1: Projeção de Mollweide em coordenadas Galácticas. As regiões do BOSS e SDSS usadas em nossa validação são mostradas como um mapa de densidade construído utilizando estrelas com $17 < g < 23$ e $-0.5 < g - r < 1.2$.

2.2 Dark Energy Survey

O DES é um levantamento fotométrico que cobre cerca de 5000 graus^2 do hemisfério sul Galáctico. O principal objetivo do DES é determinar o parâmetro da equação de estado da energia escura, w (relação entre pressão e densidade de energía) e outros parâmetros cosmológicos com alta precisão ($\sim$ 5%), usando várias medidas distintas: contagens de aglomerados de galáxias, lenteamento gravitacional fraco e espectro de potência angular de galáxias. DES deve catalogar 300 milhões de galáxias com *redshifts* fotométricos. Além disso, milhares de supernovas de tipo Ia serão medidas através de monitoramento de regiões pré-estabelecidas.

O DES é um projeto iniciado em 2005 e que em agosto de 2013 iniciou um período de cinco anos (525 noites) de obtenção de imagens em cinco filtros que cobrem do azul ao infra-vermelho próximo, g, r, i, z, Y. Ao finalizar este período, espera-se atingir uma magnitude limite de $g \simeq 24.6$, $r \simeq 24.1$, $i \simeq 24.4$, $z \simeq 23.8$ e $Y \simeq 21.3$ para galáxias com uma razão sinal–ruido S/N $\simeq 10$.

O DES utiliza a *Dark Energy Camera* (DECam; Flaugher et al. 2015). A DECam, com um campo de visão de 2.°2 de diâmetro, está montada no foco principal do telescópio Blanco de 4 m situado no Observatório Interamericano de Cerro Tololo (CTIO). Os 570 megapixels do plano focal compreendem 62 CCDs para a geração de imagens e 12 CCDs para guiagem, foco e alinhamento. Os CCDs têm pixels de $15\mu m \times 15\mu m$ com uma escala de $0.''263$ pixels^{-1}. Na Figura 2.2 mostramos a imagem completa da DECam na direção do aglomerado de galáxias Fornax. As imagens da DECam são reduzidas pelo equipe *Data Management* (DESDM), que desenvolveu

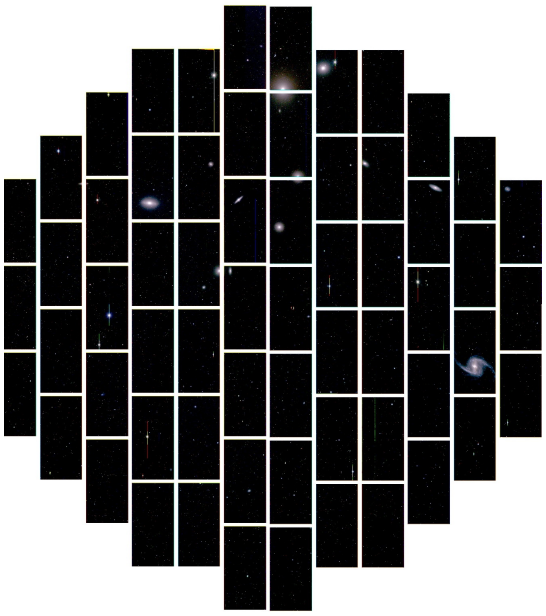

FIGURA 2.2: Imagem da DECam para o aglomerado de galáxias Fornax, que fica a cerca de 60 milhões de anos-luz da Terra.

e está constantemente aperfeiçoando um *pipeline* para processar os dados de uma única exposição e correções intrumentais até a calibração de imagens coadicionadas. Para mais detalhe sobre o DESDM, nós referimos a Sevilla et al. (2011) e Mohr et al. (2012).

Entre novembro de 2012 e março de 2013, a DECam passou por uma etapa de verificação científica (SV). Durante essa etapa, diversas características do instrumento foram colocadas a prova, além de ser testada a capacidade de processamento de dados do DESDM (astrometria, qualidade da imagem, calibração e fotometria). Durante o periodo de SV a DECam gerou imagens com profundidade fotométrica, $\sim$ 24.5 para as bandas g, r e i, aproximadas aos limites esperados com o DES. A região contígua (200 graus^2) que cobre a periferia norte da Grande Nuvem de Magalhães (LMC) é chamada de SPT-E devido a que cobre uma região em comum com o *South Pole Telescope* (SPT). Devido à profundidade alcançada, essas imagens deram a possibilidade de estudar algumas propriedades da LMC (Balbinot et al. 2015; Pieres et al. 2016).

Embora seja verdade que o DES tem como objetivo principal o estudo da cosmologia, as imagens da DECam estão revelando muito sobre outras áreas da Astronomia. Em particular, dá-nos a oportunidade de buscar/detectar novos satélites fracos da MW e, assim, aumentar o censo de satélites da Galáxia conhecidos até a presente data, que é o principal objetivo deste trabalho. Para a busca deste tipo de sistemas estelares, nós utilizamos dados coadicionados do primeiro ano (DES Y1A1; Agosto de 2013 a Fevereiro de 2014, Bechtol et al. 2015) e dados do segundo ano que foram gerados com imagens de uma única época (DES Y2Q1; Agosto de 2014 a Fevereiro de 2015, Drlica-Wagner et al. 2015). Ao incorporar o segundo ano de observações do DES, a cobertura do ângulo sólido no hemisfério sul Galáctico se

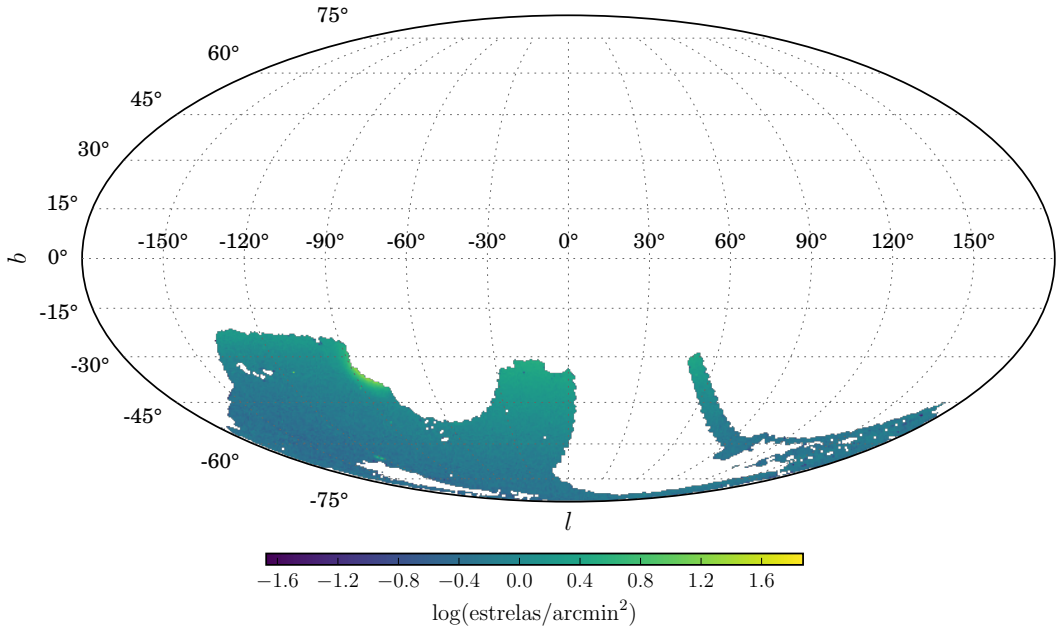

FIGURA 2.3: Projeção de Mollweide em coordenadas Galácticas. A cobertura do DES para os dois primeiro anos de observação ($\sim$ 5000 graus^2) é mostrada como um mapa de densidade construído utilizando estrelas com $17 < g < 23$ e $-0.5 < g - r < 1.2$.

expande de $\sim$ 1800 graus^2 a $\sim$ 5000 graus^2. A área amostrada do DES para os dois primeiros anos é mostrado na Figura 2.3 como um mapa de densidade estelar.

A amostra estelar usada neste trabalho foi estabelecida usando os parâmetros do SEXTRACTOR/PSFEX[1] `FLAGS`, `SPREAD_MODEL` e magnitudes *point spread function* (`PSF`) (Bertin & Arnouts 1996; Bertin 2011; Desai et al. 2012; Bouy et al. 2013). Os critérios que usamos para garantir a qualidade das fontes foram `FLAGS` < 4 sobre as bandas g, r e i (g e r) para Y1A1 (Y2Q1). Esses critérios de qualidade são usados para evitar objetos misturados e fontes perto de objetos brilhantes que podem influenciar significativamente a fotometría ou outros pixels. Para evitar problemas relacionados no ajuste de `PSF` através da profundidade variável nas imagens coadicionadas, nós utilizamos a média ponderada (`WAVG`) das medições do `SPREAD_MODEL` a partir das exposições de uma única época (Bechtol et al. 2015).

Para selecionarmos uma amostra estelar usamos o `WAVG_SPREAD_MODEL` na banda i (r) para Y1A1 (Y2Q1). Especificamente, nossa amostra estelar consiste de objetos

[1]SEXTRACTOR é um software que cria um catálogo de objetos a partir de uma imagem astronômica. Um pacote do software identifica e seleciona as fontes acima de um limite baseado no fundo da imagem. O parâmetro `DEBLENDING` determina se um grupo de pixels vizinhos deve ser classificado como uma única fonte ou vários objetos. PSFEX extrai modelos `PSF` a partir de imagens processadas com SEXTRACTOR e mede a qualidade das imagens. Os modelos de `PSF` gerados podem ser usados para fotometria ajustada pelo modelo ou análise morfológica. Portanto, o catálogo final poduz várias medições de magnitude (`MAG_AUTO`, `MAG_PSF`, entre outras), `FLAGS` e `SPREAD_MODEL` como o principal separador estrela/galáxia. Isto é baseado na diferença entre o melhor ajuste local do modelo da `PSF` e um modelo ligeiramente mais estendido feito da mesma `PSF` convoluída com um modelo de disco exponencial circular com comprimento de escala igual a `FWHM`/16, onde `FWHM` representa a largura à meia altura do modelo de `PSF` (para mais detalhes, veja Bertin & Arnouts 1996 e Bertin 2011).

com $|\texttt{WAVG\_SPREAD\_MODEL}| < 0.003 + \texttt{WAVG\_SPREADERR\_MODEL}$. Para alcançar magnitudes fracas, fizemos cortes em magnitude de $17 < g < 24$. Além disso, cortes em cor de $-0.5 < g - r < 1.2$ foram realizados.

A nossa participação no DES ocorreu através do consórcio de pesquisadores chamado DES–Brazil, coordenado pelo LIneA. Compusemos o grupo de trabalho de *Milky Way* da colaboração, que foi coordenado pelo Dr. Basílio Santiago.

Capítulo 3

Método de detecção de subestruturas

3.1 Matched Filter

A técnica de *Matched Filter* (MF) tem muitas aplicações em processamento de sinais. No contexto da Astronomia, tem sido utilizada para detectar populações estelares de baixa densidade em dados de imageamento (Szabo et al. 2011; Rockosi et al. 2002). Neste trabalho usamos esta técnica para procurar novos sistemas estelares (aglomerados estelares e galáxias anãs) seguindo o trabalho de Balbinot et al. (2011).

O número de estrelas em função da posição no céu (α,δ), da cor (c), e magnitude (m) pode ser descrito como

$$n(\alpha, \delta, c, m) = n_{\rm cl}(\alpha, \delta, c, m) + n_{\rm bg}(\alpha, \delta, c, m). \tag{3.1}$$

O primeiro termo da direita corresponde à contribuição do sistema estelar (cl) que queremos descobrir, enquanto que o segundo termo representa o campo (bg), que inclui estrelas *foreground* do halo e as galáxias de fundo não resolvidas. Ambos os termos podem ser separados em um termo de normalização e uma função de distribuição de probabilidade (PDF):

$$n_{\rm cl}(\alpha, \delta, c, m) = \zeta_{\rm cl}(\alpha, \delta) f_{\rm cl}(c, m), \tag{3.2}$$

onde $\zeta_{\rm cl}$ e $f_{\rm cl}$ são respectivamente, a normalização do número de estrelas e sua PDF no plano do CMD, para a população estelar a ser encontrada. A população estelar pode ser estendida no espaço (como uma corrente estelar), mas iremos assumir que seu CMD é o mesmo em todo lugar. Para as estrelas de campo, os modelos da estrutura da Galáxia mostram que tanto o número de estrelas quanto o CMD variam em função da posição no céu (Jurić et al. 2008). Dessa forma, escrevemos

$$n_{\rm bg}(\alpha, \delta, c, m) = \zeta_{\rm bg}(\alpha, \delta) f_{\rm bg}(\alpha, \delta, c, m). \tag{3.3}$$

Com as definições anteriores, a equação 3.1 passa a ser

$$n(\alpha, \delta, c, m) = \zeta_{\rm cl}(\alpha, \delta) f_{\rm cl}(c, m) + \zeta_{\rm bg}(\alpha, \delta) f_{\rm bg}(\alpha, \delta, c, m). \tag{3.4}$$

Nós dividimos o céu em bins de $1' \times 1'$, usando o índice i, e o CMD em bins de $0.01\,\mathrm{mag} \times 0.05\,\mathrm{mag}$, indexado por j. Os detalhes sobre a construção da PDF $f_{\rm cl}$ and $f_{\rm bg}$ são apresentados nas Seções 3.2 e 3.3, respectivamente. Com esta notação

$$n(i, j) = \zeta_{\rm cl}(i) f_{\rm cl}(j) + \zeta_{\rm bg}(i) f_{\rm bg}(i, j). \tag{3.5}$$

O lado esquerdo representa o número previsto de estrelas em uma dada posição do céu e do CMD. Se o número de estrelas observadas no catálogo é $N(i, j)$, a variança entre os dados e o modelo é

$$s^2(i) = \sum_j \frac{[N(i, j) - \zeta_{\rm cl}(i) f_{\rm cl}(j) - \zeta_{bg}(i) f_{\rm bg}(i, j)]^2}{\zeta_{\rm bg}(i) f_{bg}(i, j)}. \tag{3.6}$$

O termo no denominador representa a flutuação de Poisson esperada na contagem de estrelas, que, por simplicidade, nós assumimos ser dominada pelas estrelas do campo. Minimizando a variança e resolvendo para $\zeta_{\rm cl}(i)$, temos o número de estrelas observadas que, de acordo com o modelo dado pela equação 3.4, são consistentes com o modelo da população estelar.

$$\zeta_{\rm cl}(i) = \frac{\sum_j N(i, j) f_{\rm cl}(j) / f_{\rm bg}(i, j)}{\sum_j f_{\rm cl}^2(j) / f_{\rm bg}(i, j)} - \frac{\zeta_{\rm bg}(i)}{\sum_j f_{\rm cl}^2(j) / f_{\rm bg}(i, j)}. \tag{3.7}$$

A saída do MF é um mapa de densidade de estrelas que são prováveis membros do objeto estelar, ou seja, $\zeta_{\rm cl}(i)$. Na prática, $f_{\rm bg}(i, j)$ é gerado diretamente de nosso catálogo de estrelas. Nós fazemos isso sob a suposição de que os objetos a ser detectados (aglomerados estelares, galáxias anãs e correntes estelares) não mudam a PDF do campo. A PDF do objeto faz uso de amostras simuladas e será descrita na seguinte seção.

3.2 Grade de Modelos

Desde que não sabemos a priori as populações estelares que vamos encontrar, nós geramos uma grade de populações estelares simples (SSP) com o código GENCMD[1]. O GENCMD usa isócronas de PARSEC (Bressan et al. 2012) para diferentes distâncias e seleciona aleatoriamente massas estelares seguindo uma função de massa inicial (IMF). Atualmente, estamos usando uma IMF[2] tipo Kroupa (2001) neste código. Para cada massa estelar, interpolamos as isócronas para obter as magnitudes absolutas para os filtros desejados. As magnitudes absolutas são convertidas em magnitudes

[1] https://github.com/balbinot/gencmd

[2] Como pretendemos detectar objetos estelares com massas mínimas de $\sim 0.45 M_\odot$, não esperamos resultados diferentes se usarmos outra IMF, por exemplo, uma IMF de Salpeter (1955). Isso porque as diferentes IMF diferem mais no regime de bem baixas massas estelares.

aparentes usando o módulo de distância, assumindo as incertezas das magnitudes tomadas do SDSS ou DES, e o mapa do avermelhamento do Schlegel, Finkbeiner, & Davis (1998). Nós simulamos várias SSP em diferentes idades (τ), metalicidades (Z) e distâncias que cobrem uma ampla gama de isócronas, incluindo populações estelares jovens e de alta metalicidade. A grade de parâmetros destas simulações é apresentada na Tabela 3.1.

TABELA 3.1: Grade de parâmetros usada nas simulações de SSPs para a busca de sistemas estelares no SDSS e DES. Um total de 300 modelos de SSPs são gerados.

Parâmetros	Limite inferior	Limite superior	Passos
$\log(\tau)$	9.0	10.2	0.3
Distância (kpc)	10	200	10
Metalicidade, Z		0.0002, 0.001 e 0.007	

3.3 Detecção de candidatos

Ao aplicar o método MF em um catálogo estelar conforme descrito na Seção 3.1, usando a grade de modelos de SSP descrita na Seção 3.2, este processo gera um mapa de densidade para cada modelo da grade simulada.

Como não é prático inspecionar visualmente todos os mapas de densidades resultantes destes modelos, nós usamos a rotina SEXTRACTOR (Bertin & Arnouts 1996) para procurar automaticamente picos de densidade nos diferentes mapas. Como queremos destacar subestruturas em escalas típicas de aglomerados estelares e galáxias anãs, nós geramos de uma forma independente *kernels* gaussianos de convolução de diferentes tamanhos $\{\sigma = 0'$ (sem convolução) até $\sigma = 9'\}$. Estes *kernels* complementam aqueles adotados no SEXTRACTOR. De fato, os *kernels* de convolução são aplicados dentro do próprio SEXTRACTOR aos mapas de densidade de cada modelo de SSP. Qualquer objeto detectado pelo SEXTRACTOR é salvo para posterior análise.

Neste trabalho, os candidatos a objetos estelares são selecionados baseados em dois critérios: (1) De acordo com o número de vezes que são detectados pelo SEXTRACTOR. Neste caso, os dez primeiros candidatos do *ranking* para cada *kernel* de convolução são analizados visualmente (este critério será amplamente discutido na Seção 3.4.1). (2) De acordo com a significância estatística[3] do excesso de estrelas em relação ao campo (veja detalhes na Seção 3.4.1). Neste critério, aplicamos um simples corte em significância. Todos os candidatos com significância $> 5\sigma$ são analizados visualmente para descartar objetos artificiais (flutuações na contagem de estrelas de campo), assim como contaminação por galáxias fracas.

Finalmente, a lista final de SEXTRACTOR que contém as coordenadas equatoriais (α, δ) para cada candidato encontrado nos mapas de densidade é comparada com

[3]Este critério de seleção foi recentemente implementado para os dados do segundo ano do DES.

catálogos de objetos conhecidos (Harris 2010; Abell 1958; McConnachie 2012, entre outros) estabelecendo uma correspondência posicional entre nossos candidatos com aqueles dos catálogos. Neste processo eliminamos objetos conhecidos, tais como, aglomerados estelares, galáxias anãs e aglomerados de galáxias.

3.4 Validação do Método

Para validar e otimizar nosso código de busca por subestruturas, o qual chamamos de SPARSEX, nós usamos satélites estelares previamente identificados nos dados do SDSS. Em particular, selecionamos 17 objetos estelares (11 galáxias anãs e seis aglomerados estelares) que são caracterizados como objetos distantes e fracos. Estes objetos são apresentados na Tabela 3.2.

Para detectar toda a amostra selecionada nos primeiros lugares do *ranking* é necessário estabelecer um conjunto adequado de parâmetros de detecção do SEXTRACTOR, principalmente `DETECT_THRESH` e `DETECT_MINAREA`, para cada *kernel* de convolução. O parâmetro `DETECT_THRESH` define o valor limite. Como nós usamos um único valor, este é interpretado como limite em unidades do desvio padrão do fundo. O parâmetro `DETECT_MINAREA` estabelece o número mínimo de pixels adjacentes uns aos outros que deve ter para iniciar a detecção. Para estabelecer estes parâmetros, nós aplicamos o código SPARSEX em regiões de $\sim 9^\circ \times 9^\circ$ em torno de cada um de nossos objetos selecionados (veja Figura 2.1). Uma vez estabelecido os parâmetros de detecção do SEXTRACTOR, todos os objetos de nossa amostra foram detectados por SPARSEX entre os primeiros lugares do *ranking*. Na Tabela 3.2 mostramos os sistemas recuperados e seus parâmetros resultantes da aplicação do SPARSEX.

Os parâmetros de saída do SExtractor α_0 e δ_0 (posição central[4] do candidato em coordenadas equatoriais), e tamanho (semi-eixo maior) são inicialmente utilizados para construir nossos gráficos de análise, CMDs e perfis de densidade. Uma análise visual dos mapas de densidade (saída do MF) revelou que em alguns objetos (especialmente objetos pequenos) os parâmetros de posição obtidos do SEXTRACTOR diferem daqueles observados nos mapas de densidade. Na Figura 3.1 mostramos os mapas de densidade obtidos do MF em torno de Koposov 2 e Leo IV. Note que a posição central dada por SEXTRACTOR para Koposov 2 (centro do círculo verde) está claramente deslocada da sobredensidade, enquanto que para Leo IV não é tão claro este deslocamento.

Já que a nossa intenção é também detectar objetos compactos, como aglomerados estelares, precisamos que a posição do objeto coincida com a posição da sobredensidade. Para solucionar o problema indicado anteriormente, nós desenvolvemos um código simples que faz a recentragem de uma maneira automática. Basicamente este código procura sobredensidades de pontos em pequenas regiões do céu. Estimamos o centro como segue. Primeiro pegamos do catálogo estelar uma região de $3' \times 3'$ ao

[4]Estes parâmetros de posição não são apresentados na Tabela 3.2.

TABELA 3.2: Coluna 1: nome do objeto. Colunas 2 e 3: coordenada central do objeto. Coluna 4: número de modelos de SSP detectados pelo SExtractor. Coluna 5: posição do candidato no *ranking*. Coluna 6: número total de objetos detectados. Coluna 7: *kernel* de convolução Gaussiano usado para suavizar o mapa de densidade.

Objetos	α_0	δ_0	Nro Modelos	*Ranking*	Nro Objetos	Conv. Gauss
	graus†					pixels
Canes Venatici I	202.01	33.56	106	1	50	5.0
Canes Venatici II	194.29	34.32	16	1	363	1.5
Coma	186.74	23.92	28	1	33	5.0
Hercules	247.77	12.79	10	1	1351	2.5
Leo IV	173.24	−0.53	30	3	3867	3.0
Leo V	172.79	2.22	11	3	1464	4.0
Leo T	143.72	17.05	84	1	668	2.5
Segue 1	151.77	16.08	16	3	344	4.0
Segue 2	34.82	20.18	10	2	510	4.0
Ursa Maior I	158.70	51.94	17	3	1889	3.0
Willman 1	162.34	51.05	81	1	306	5.0
Balbinot 1	332.68	14.95	510	1	1108	sem conv
Koposov 1	179.83	12.26	62	1	4438	sem conv
Koposov 2	119.57	26.26	13	1	272	1.5
Palomar 13	346, 69	12.77	1192	1	110	sem conv
Segue 3	320.38	19.12	1075	1	5242	sem conv
Whiting 1	30.74	−3.27	1154	1	1477	sem conv

Nota. †Centros obtidos a partir de nosso código de recentragem (ver Seção 3.4).

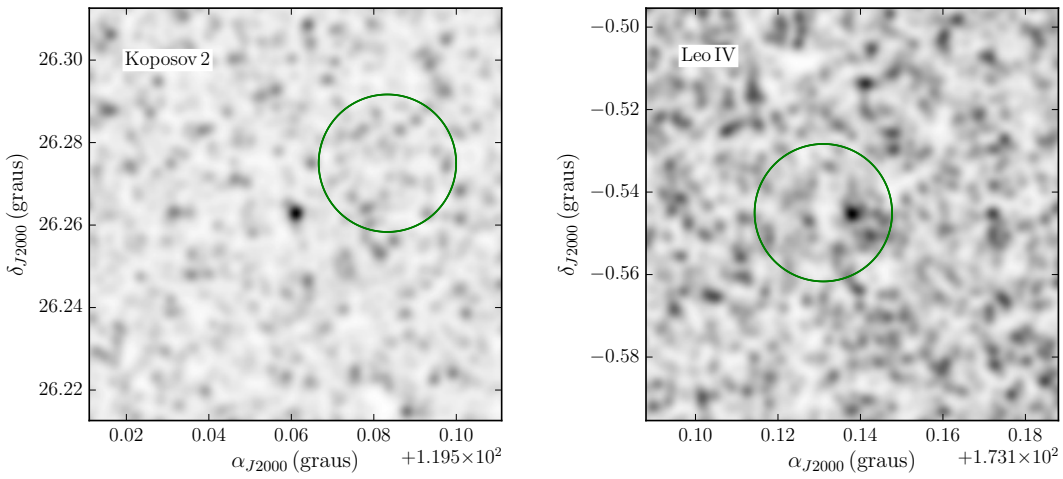

FIGURA 3.1: Deteção do aglomerado estelar Koposov 2 e a galáxia anã Leo IV. No painel esquerdo é mostrado o mapa de densidade centrado em Koposov 2, resultante da aplicação do MF com um modelo de SSP com parâmetros de: $\log(\tau) = 9.30$, $Z = 0.0002$ e $D_{\odot} = 170\,\mathrm{kpc}$. O painel direito mostra a mesma informação do painel anterior, mas para o Leo IV. Este mapa de densidade foi gerado por um modelo cujos parâmetros são: $\log(\tau) = 9.90$, $Z = 0.0002$ e $D_{\odot} = 150\,\mathrm{kpc}$. Os mapas de densidade foram suavizados com um *kernel* gaussiano com desvio padrão $\simeq 0.^{\circ}03$. Em ambos painéis, o centro do círculo verde representa a posição do objeto dada pela rotina SExtractor.

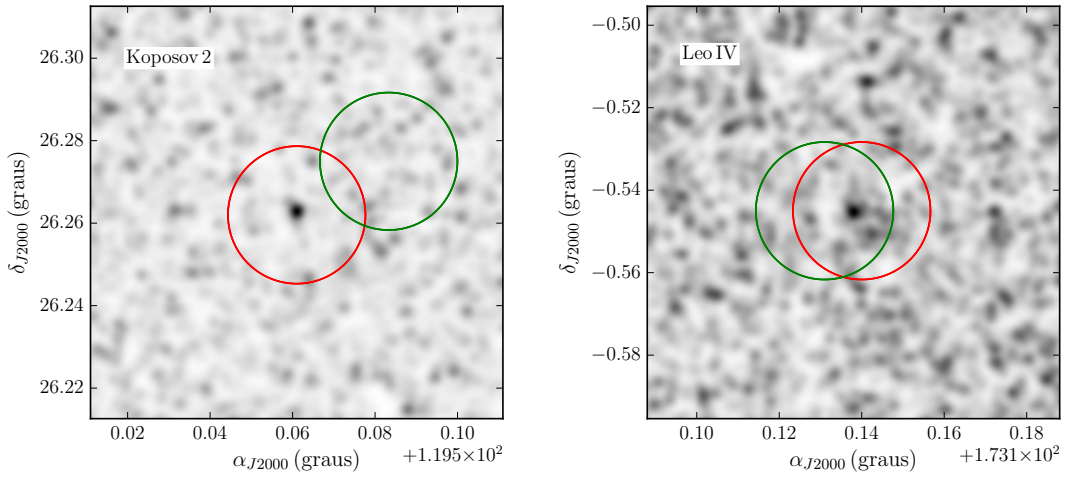

FIGURA 3.2: Mapas de densidade de Koposov 2 e Leo IV como mostrado na Figura 3.1. Em ambos painéis, o centro do círculo verde representa a posição do objeto dada pela rotina SEXTRACTOR, enquanto que o centro do círculo vermelho representa a posição do objeto obtido a partir de nosso código de recentragem.

redor do centro fornecido pelo SEXTRACTOR. Dividimos esta região em subregiões de $\sim 0\farcm5 \times 0\farcm5$ e fazemos a contagem de pontos em cada uma dessas subregiões. O centro da subregião que contenha a maior densidade de pontos será considerado o novo centro do objeto. Este processo é iterado 20 vezes até encontrar a maior sobredensidade. Na Figura 3.2 mostramos o centro para Koposov 2 e Leo IV determinados com o código descrito acima (centro do círculo vermelho).

Os parâmetros de detecção do SEXTRACTOR determinados a partir dos dados do SDSS também foram testados nos dados DES. Para estes testes foram utilizados os dados preliminares do primeiro ano do DES (Y1P1) e objetos simulados[5] com características similares a Willman 1, Hercules, Canes Venatici I e Balbinot 1. Estes objetos simulados foram posteriormente adicionados em diferentes regiões da área amostrada do DES. Mais uma vez, o código detectou com sucesso os quatro objetos simulados nos primeiros lugares do *ranking*. Em geral, nós decidimos sempre adicionar objetos simulados em qualquer catálogo fotométrico de forma a testar a eficiência do método e, se necessário, redefinir os parâmetros de detecção do SEXTRACTOR.

Como a área amostrada do DES cobre $\sim 5000\,\text{graus}^2$ no céu, foi necessario automatizar o código SPARSEX para cobrir toda a área requerida, buscando toda a informação possível sobre os candidatos a objetos estelares. Para esse objetivo, implementamos algumas ferramentas de análise que facilitam a identificação de novos sistemas físicos. Na seguinte seção citamos essas ferramentas.

[5]Nós usamos o código GENCMD para simular os sistemas estelares. As posições das estrelas no céu foram simuladas usando dois modelos de perfil de densidade: Hubble modificado (Binney & Tremaine 2008, página 68) e *empirical* King (King 1962).

3.4.1 Ferramentas adicionais

Nesta seção, descrevemos brevemente os gráficos de análise que são gerados pelo código SPARSEX.

Representação espacial: Este gráfico mostra uma região do céu (em α e δ) de $\sim 0.^{\circ}5 \times 0.^{\circ}5$ centrada no candidato. O centro do candidato foi determinado usando o código de recentragem descrito acima.

Mapa de densidade: Este gráfico mostra o mapa de densidade no céu, construído com fontes estelares e posteriormente convoluído com um *kernel* gaussiano com desvio padrão de $\sim 0.^{\circ}03$. Este gráfico é primordial para a deteção de candidatos ultra fracos, como aqueles sistemas estelares (aglomerados estelares e galáxias anãs) reportados nos dados do SDSS.

Perfil de significância de Poisson (PS): Este perfil é construído tomando a razão entre o número de estrelas dentro de cada raio r e em excesso do campo ($N_{\rm bgd}$), $N_{\rm obj}$, à flutuação esperada no mesmo campo, ou seja, $N_{\rm obj}/\sqrt{N_{\rm bgd}}$. Definindo $N_{\rm obs}$ como o número de estrelas observadas, então $N_{\rm obj} = N_{\rm obs} - N_{\rm bgd}$. Para evitar uma baixa estatística estelar, construímos o perfil de significância usando raios cumulativos de $1'$ centrado no candidato. $N_{\rm bgd}$ é calculado dentro de um anel circular ($30' < r < 34'$) a partir do centro do candidato.

CMDs: O CMD do candidato é construído com estrelas dentro de uma região circular com $r = 3'$, enquando que o CMD do campo é construído com estrelas dentro de um anel da mesma área que do candidato, cujo raio interno é igual a $30'$ centrado no candidato.

Diagrama de Hess: Na prática, este diagrama é basicamente usado para subtrair o número esperado de estrelas de campo coincidindo com o candidato.

Para uma melhor compreensão do processo que compõe o método SPARSEX, uma representação esquemática é apresentada na Figura 3.3. O resultado final do código SPARSEX é mostrado na Figura 3.4. A análise dos seis gráficos gerados pelo código é de grande importância em nossa tarefa de detectar novas subestruturas estelares da Galáxia.

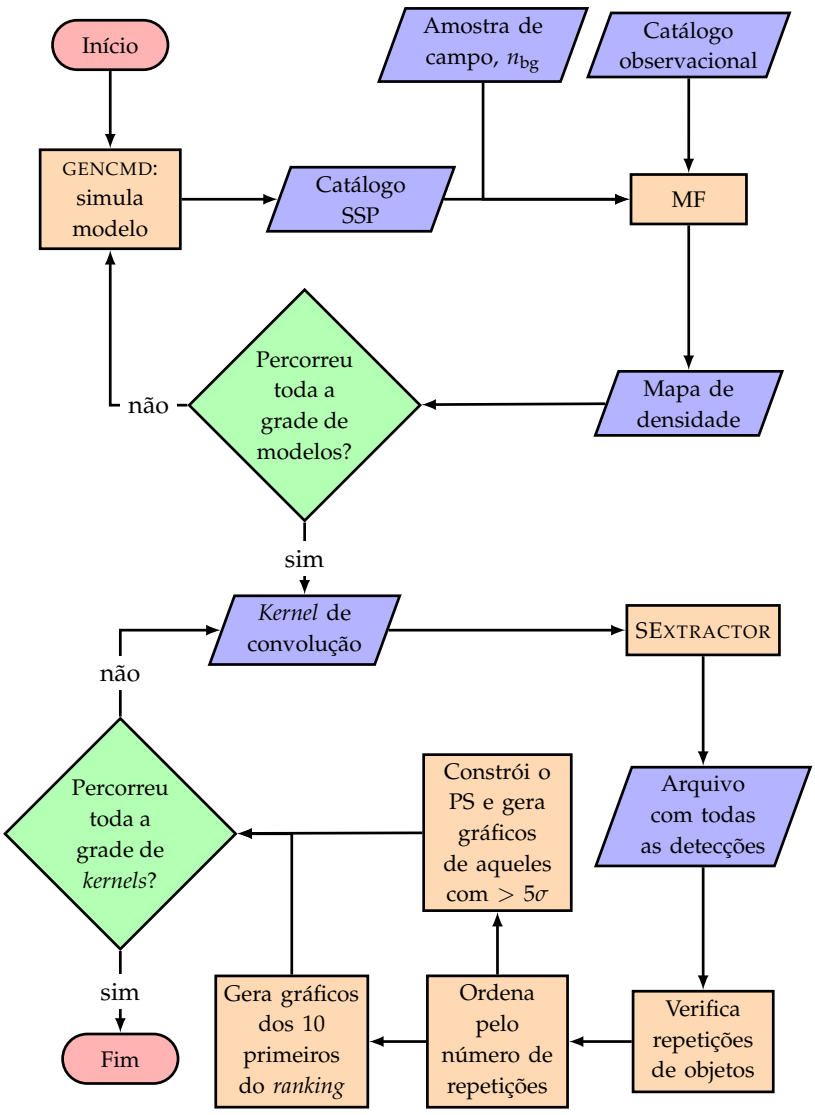

FIGURA 3.3: Fluxograma mostrando o processo de detecção de sistemas estelares. Primeiro simulamos um modelo de SSP como entrada para o MF, juntamente com o catálogo observacional e uma amostra do campo. O MF gera um mapa de densidade com as estrelas consistentes com a SSP. Cada mapa de densidade resultante do MF é convoluído com diferentes tamanhos de *kernels* gaussianos. O SExtractor faz a busca por picos de densidade nos mapas de densidade, provendo uma lista de candidatos. Faz-se a verificação de repetições na lista, para depois serem os candidatos ordenados segundo o número de repetições. Na sequência, geram-se gráficos dos 10 primeiros candidatos com maior número de repetições. Além disso, o PS dos candidatos ordenados é construido e, em seguida, geram-se gráficos de aqueles candidatos com pico de significância $> 5\sigma$. Após a grade de *kernels* ser completada, o SParSEx finaliza.

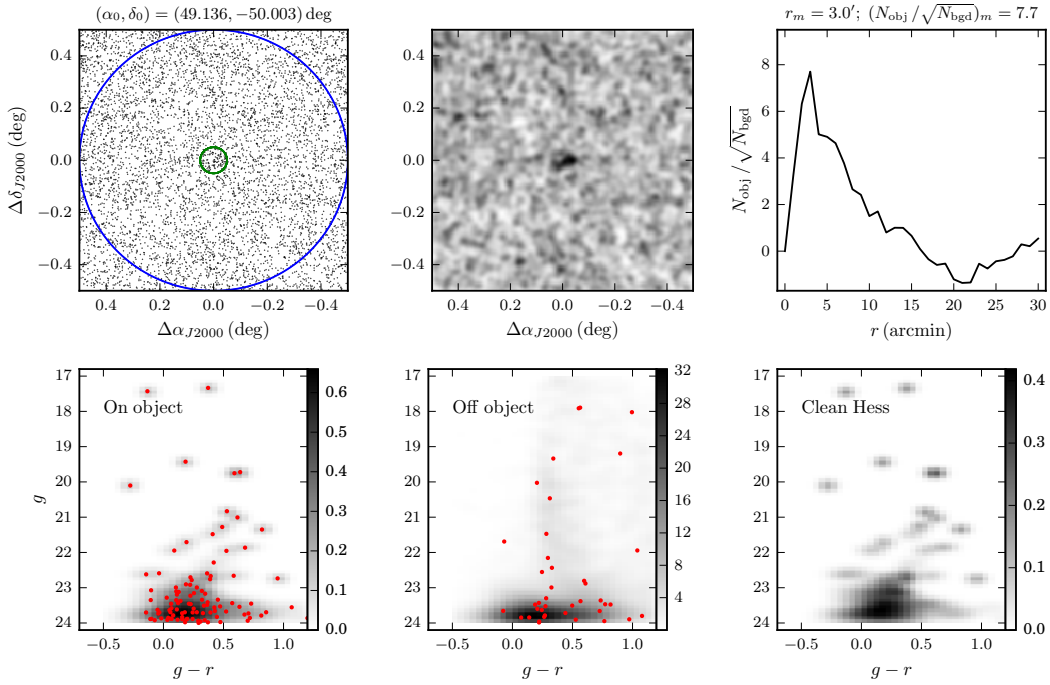

FIGURA 3.4: Painel superior esquerdo: representação espacial em torno do candidato a galáxia anã Horologium II. Do centro para a periferia, os círculos concêntricos limitam a região do objeto (cor verde) e a região onde começa o campo (cor azul). A posição de Horologium II é mostrado no topo do painel. Painel superior central: mapa de densidade de fontes estelares ao redor do objeto, com aplicação de uma suavização Gaussiana. Painel superior direito: perfil de significância em função do raio a partir do centro de Horologium II. Nós adotamos um valor de significância igual a zero em $r = 0'$. O valor máximo da significância e o raio onde ele é atingido são mostrados no topo deste painel. Painel inferior esquerdo: diagrama de Hess construído com estrelas dentro de um círculo de raio $r = 3'$ centrado no objeto (círculo verde no painel esquerdo superior). O conjunto de estrelas também é mostrado neste painel como pontos vermelhos. Painel inferior central: diagrama de Hess para a região do campo, construido com estrelas dentro de um anel circular com $30' < r < 45'$ centrado no objeto. No mesmo painel, as estrelas dentro de um anel circular, com raio interno $r = 30'$ (círculo azul no painel esquerdo superior), de igual área que o painel anterior são mostradas como pontos vermelhos. Painel inferior direito: diagrama de Hess descontaminado calculado como a diferença entre os diagramas de Hess dos paineis anteriores ponderadas por suas respectivas áreas.

Capítulo 4

Resultados

Nos últimos quatro anos, nós trabalhamos junto com o grupo de *Milky Way* do DES na detecção de subestruturas da MW. Para este propósito, o grupo de colaboração tem implementados três diferentes estratégias de busca por sobredensidades de estrelas resolvidas: *Stellar Density Maps*, *Likelihood-based Search*[1] e SPARSEX. Como neste trabalho não faremos uma descrição dos dois primeiros métodos, referimo-nos a Bechtol et al. (2015) e Drlica-Wagner et al. (2015) para uma descrição detalhada. A descrição do método SPARSEX foi dada no Capítulo 3. Depois de completar a validação do código SPARSEX com objetos conhecidos do SDSS e objetos simulados, o código foi aplicado na área amostrada do DES. Na seguinte seção nós apresentamos os resultados da aplicação do código neste conjunto de dados.

4.1 Companheiros da MW reportados nos dados do DES

Em 2015 a colaboração DES anunciou a descoberta de 17 novos sistemas estelares, oito objetos no mês de março e nove no mês de agosto, usando os dados dos dois primeiros anos de observação (Y1A1 e Y2Q1). Todos os sistemas físicos anunciados foram detectados simultaneamente pelas três estratégias de busca.

Os sistemas estelares anunciados por Bechtol et al. (2015) and Drlica-Wagner et al. (2015) são de baixa luminosidade ($M_V \gtrsim -7.4$), semelhantes às galáxias anãs fracas conhecidas da MW. E a maioria possui tamanhos físicos que são suficientemente grandes ($\gtrsim 11$ pc) como para serem classificadas como galáxias anãs, à exceção do Kim 2, que foi confirmado como um aglomerado estelar fraco (Kim & Jerjen 2015a).

Como mencionado ao longo deste trabalho, o SPARSEX foi desenvolvido para ser aplicado nos dados do DES. Como no caso dos objetos estelares do SDSS e objetos simulados, o SPARSEX conseguiu detectar com sucesso todos os objetos que foram encontrados nos dados do DES (Bechtol et al. 2015; Koposov et al. 2015a; Kim et al. 2015; Drlica-Wagner et al. 2015; Kim & Jerjen 2015b). Adicionalmente, o código SPARSEX levou à descoberta de quatro sistemas estelares: DES 1, DES J0111-1341, DES J0225+0304 e DES 3 (Luque et al. 2016; Luque et al. 2017a; Luque et al. 2017b). A Tabela 4.1 mostra os objetos detectados e os parâmetros resultantes da aplicação do SPARSEX nos dois primeiros anos do DES. Como pode ser visto na Tabela 4.1,

[1] https://github.com/DarkEnergySurvey/ugali

todos os objetos reportados pela colaboração DES foram detectados nos primeiros lugares do *ranking*[2], incluindo os objectos adicionais. Alguns dos novos candidatos ofereciam evidências suficientes para confirmar sua existência, enquanto outros precisaram de imagens fotométricas mais profundas para serem confirmados sistemas físicos. Estes casos serão discutidos ao longo deste capítulo.

TABELA 4.1: Coluna 1: nome do objeto. Colunas 2 e 3: coordenada central do candidato. Coluna 4: número de modelos de SSP detectados pelo SExTRACTOR. Coluna 5: posição do candidato no *ranking*. Coluna 6: número total de objetos detectados. Coluna 7: *kernel* de convolução Gaussiano usado para suavizar o mapa de densidade.

Objetos	α_0	δ_0	Nro Modelos	*Ranking*	Nro Objetos	Conv. Gauss
	graus					pixels
Reticulum II	53.97	−54.05	60	1	165	7.0
Eridanus II	56.09	−43.53	130	1	146	7.0
Horologium I	43.89	−54.11	47	1	144	7.0
Tucana II	342.96	−58.55	17	1	973	7.0
Pictoris I	70.94	−50.29	26	1	1094	3.0
Eridanus III	35.69	−52.28	5	5	294	5.0
Kim 2	317.21	−51.16	61	1	1933	3.0
Phoenix II	354.99	−54.40	16	1	263	3.0
Horologium II	49.14	−50.00	5	2	205	5.0
DES 1	8.49	−49.04	5	4	139	1.5
DES 3	325.06	−52.54	60	2	10123	1.5
Columba I	82.85	−28.03	69	1	5642	7.0
Tucana IV	0.71	−60.84	24	1	377	7.0
Grus II	331.02	−46.44	37	1	3660	7.0
Tucana III	359.19	−59.62	13	2	605	5.0
Tucana V	354.32	−63.28	40	1	605	5.0
Cetus II	19.47	−17.40	21	1	2021	5.0
Reticulum III	56.36	−60.46	11	1	214	7.0
Grus I	344.18	−50.16	20	1	1240	5.0
Indus I	309.72	−46.16	53	10	6908	5.0
DES J0111−1341	17.79	−13.68	10	3	2221	não conv
DES J0225+0304[†]	36.43	3.07	−−	−−	−−	−−

Nota. Em nossos artigos publicados, nós re-determinamos o centro (α_0, δ_0) de cada sistema estelar utilizando o método descrito na Seção 4.2.2.

[†] Objeto detectado com nosso segundo critério de seleção (ver Seção 3.3).

Para caracterizar os novos objetos estelares, temos desenvolvido um conjunto de ferramentas que descrevemos na seção seguinte.

[2]O candidato J0225+0304 foi detectado com base no nosso segundo critério de seleção (veja Seção 3.3).

4.2 Método de caracterização

Para caracterizar nossos sistemas físicos, ou seja, estimar os parâmetros estruturais e propriedades da população estelar, utilizamos três modelos de perfil de densidade radial: exponencial, Plummer (Plummer 1911) e King (King 1962). Estes modelos são amplamente utilizados na literatura (por exemplo, Martin, de Jong, & Rix 2008, Muñoz, Geha, & Willman 2010 e Pieres et al. 2016). Como os objetos descobertos nos últimos anos contêm uma baixa estatística estelar, isto nos impede de usar métodos tradicionais de caracterização, tais como ajuste visual de um modelo de isócrona no CMD e ajuste de perfil de densidade com base na contagem de estrelas. Em vez disso, aqui usamos um método estatístico baseado na máxima verossimilhança para estimar as propriedades de nossos novos candidatos.

4.2.1 Máxima verossimilhança

A máxima verossimilhança é um método estatístico que estima um conjunto de parâmetros desconhecidos de um dado modelo de distribuição através da maximização da função de verossimilhança. Se assumirmos que uma amostra observacional vem de um modelo de distribuição que é descrita por j parâmetros, $p_1, p_2, p_3, \ldots, p_j$, a função de verossimilhança pode ser definido como

$$\mathcal{L}(p_1, p_2, \ldots, p_j) = \prod_i \ell_i(p_1, p_2, \ldots, p_j), \tag{4.1}$$

onde $\ell_i(p_1, p_2, \ldots, p_j)$ é a probabilidade de encontrar o dado observado i dado o conjunto de parâmetros $p_1, p_2, p_3, \ldots, p_j$. Na prática, usamos o logaritmo natural da função de verossimilhança para encontrar o conjunto de parâmetros para os quais as observações são mais prováveis

$$\ln \mathcal{L}(p_1, p_2, \ldots, p_j) = \sum_i \ln \ell_i(p_1, p_2, \ldots, p_j). \tag{4.2}$$

4.2.2 Determinando os parâmetros estruturais

Embora seja verdade que a determinação dos parâmetros estruturais para sistemas estelares diretamente de um catálogo de estrelas, através do método de máxima verosimilhança, foi já estabelecido (Kleyna et al. 1998; Westfall et al. 2006), este não foi amplamente utilizado. Martin, de Jong, & Rix (2008) implementaram um modelo de perfil exponencial elíptico, usando o método de máxima verossimilhança, para determinar os parâmetros estruturais de várias galáxias anãs da MW encontradas nos dados do SDSS. Estes autores assumiram que as posições das estrelas deste conjunto de dados seguem a distribuição do modelo exponencial, o qual é descrito pelos seguintes parâmetros: coordenadas centrais α_0 and δ_0, posição angular θ, elipticidade ϵ, raio de escala exponencial r_e e densidade do campo $\Sigma_{\rm bgd}$.

Neste trabalho, usamos uma metodologia similar à descrita por Martin, de Jong, & Rix (2008) para tratar 3 diferentes modelos de perfil de densidade, exponencial, Plummer e King:

$$\begin{aligned}
\Sigma_{\rm exp}(r) &= \Sigma_{0,e} \exp\left(-\frac{r}{r_e}\right), \\
\Sigma_{\rm Plummer}(r) &= \Sigma_{0,P}\left(1+\frac{r^2}{r_P^2}\right)^{-2}, \\
\Sigma_{\rm King}(r) &= k\left(\frac{1}{\sqrt{1+(r/r_c)^2)}} - \frac{1}{\sqrt{1+(r_t/r_c)^2)}}\right)^2,
\end{aligned} \tag{4.3}$$

onde r_P é o raio de escala de Plummer, enquanto r_c e r_t correspondem ao raio de core e raio da maré, respectivamente. Uma análise do modelo exponencial, que inclui a densidade central ($\Sigma_{0,e}$), é realizada por Martin, de Jong, & Rix (2008).

Uma vez que o modelo de King não tem uma expressão analítica para a densidade central, por simplicidade, neste trabalho, apresentamos a análise do modelo de Plummer a fim de se obter a $\Sigma_{0,P}$ em função dos outros parâmetros, e a relação entre o raio à meia-luz ($r_{\rm h}$) e r_P. Para isso, começamos definindo ℓ_i como

$$\ell_i(\alpha_0, \beta_0, \theta, \epsilon, \Sigma_{\rm bgd}) = \Sigma_{0,P}\left(1+\frac{r_i^2}{r_P^2}\right)^{-2} + \Sigma_{\rm bgd}, \tag{4.4}$$

onde r_i é o raio elíptico (ou semi-eixo maior da elipse) do dado i. A estrela i da amostra, com uma coordenada no céu (α_i, δ_i), tem uma posição espacial (X_i, Y_i) que está relacionado com o centróide (X_0, Y_0) por

$$\begin{aligned}
X_i - X_0 &= (\alpha_i - \alpha_0)\cos\delta_0, \\
Y_i - Y_0 &= \delta_i - \delta_0.
\end{aligned} \tag{4.5}$$

Enquanto o raio elíptico está relacionado com a posição espacial por

$$r_i = \left\{\left[\frac{1}{1-\epsilon}(X_i\cos\theta - Y_i{\rm sen}\,\theta)\right]^2 + (X_i{\rm sen}\,\theta + Y_i\cos\theta)^2\right\}^{1/2} \tag{4.6}$$

Nesta expressão, o ângulo de posição é definido do norte ao leste, e o semi-eixo maior do sistema indica o ângulo de posição.

A densidade central é restringida pelo número de estrelas do objeto, $N_{\rm obj}$. Se definirmos $N_{\rm obs}$ ($N_{\rm bgd}$) como o número de estrelas observadas (campo), então, $N_{\rm obs} = N_{\rm obj} + N_{\rm bgd}$. $N_{\rm obs}$ é obtido através da integração da densidade superficial do objeto e a densidade do campo centrado no objeto, ou seja,

$$N_{\rm obs} = \oiint_S \Sigma_{0,P}\left(1+\frac{r^2}{r_P^2}\right)^{-2} {\rm d}S + \oiint_S \Sigma_{\rm bgd}\,{\rm d}S. \tag{4.7}$$

Por exemplo, se a integração se realiza sobre um círculo de raio $r' = 1^\circ$, temos

$$N_{\rm obs} = \Sigma_{0,P} \int_0^{60'} \int_0^{2\pi} \left(1 + \frac{r'^2}{r_P^2}\right)^{-2} r' \, {\rm d}\theta {\rm d}r' + 3600\pi\Sigma_{\rm bgd}, \tag{4.8}$$

onde $\Sigma_{0,P}$ e $\Sigma_{\rm bgd}$ são expressos em unidades de estrelas/arcmin^2. É razoável supor que quando $r' \to 60'$ o integrando da equação 4.8, $r_P^4(r_P^2/\sqrt{r'} + r'^{3/2})^{-2}$, é desprezível. Usando este critério, podemos integrar o termo da direita da equação 4.8 até $r' = +\infty$. Antes disso, é necessário mudar a simetria circular da integral para uma simetria elíptica. Para isso, podemos usar as seguintes transformações: $x = ar_1 \cos\theta$ e $y = br_1 {\rm sen}\,\theta$ (com $r_1 < 1$), onde a (b) representa o semi-eixo maior (menor) de uma elipse. Portanto, o novo Jacobiano $J = abr_1$ leva a

$$N_{\rm obj} = 2\pi\Sigma_{0,P} \int \left(1 + \frac{r^2}{r_P^2}\right)^{-2} abr_1 \, {\rm d}r_1. \tag{4.9}$$

Uma vez que o raio elíptico r (equação 4.6) coincide com o semi-eixo maior da elipse, é fácil verificar que $r = ar_1$ e ${\rm d}r = {\rm d}(ar_1)$. Com isso, finalmente obtemos

$$N_{\rm obj} = 2\pi(1-\epsilon)\Sigma_{0,P} \int_0^{\infty} \left(1 + \frac{r^2}{r_P^2}\right)^{-2} r \, {\rm d}r, \tag{4.10}$$

onde $b/a = (1-\epsilon)$. Depois de integrar tem-se

$$N_{\rm obj} = \pi r_P^2 (1-\epsilon)\Sigma_{0,P}, \tag{4.11}$$

e consequentemente

$$\Sigma_{0,P} = \frac{N_{\rm obj}}{\pi r_P^2 (1-\epsilon)}. \tag{4.12}$$

Por último, a relação entre $r_{\rm h}$ e r_P é obtida a partir da equação 4.10. A ideia é resolver

$$\int_0^{r_{\rm h}} \left(1 + \frac{r^2}{r_P^2}\right)^{-2} r \, {\rm d}r = \frac{1}{2} \int_0^{\infty} \left(1 + \frac{r^2}{r_P^2}\right)^{-2} r \, {\rm d}r. \tag{4.13}$$

A resolução da equação 4.13 leva a $r_P = r_{\rm h}$.

Uma vez que todos os parâmetros do perfil do Plummer estão bem estabelecidos, nós podemos usar o método de Martin, de Jong, & Rix (2008), mas agora para um perfil de Plummer.

4.2.3 Determinando os parâmetros do CMD

Para determinar os parâmetros do CMD dos nossos candidatos, como a idade τ, a metalicidade[3] Z, o módulo de distância $(m-M)_0$ e o avermelhamento $E(B-V)$,

[3] Adotamos $Z_\odot = 0.0152$ (Bressan et al. 2012) para converter de Z para [Fe/H], assumindo $[{\rm Fe/H}] = \log(Z/Z_\odot)$

nós seguimos uma metodologia muito similar à apresentada por Pieres et al. (2016). Este método, primeiro, pesa cada estrela pela probabilidade de associação p obtida a partir do melhor ajuste do perfil de densidade. A probabilidade p para uma estrela i é definida como

$$p_i = \frac{\Sigma(r_i)}{\Sigma_{\rm bgd} + \Sigma(r_i)}. \tag{4.14}$$

Em seguida, todas as estrelas com $p > 0.01$ são selecionadas para ajustar um modelo de isócrona. A razão básica desse limite de probabilidade é o baixo número de estrelas observadas em nossos candidatos. Assumindo que as distâncias (d) de um conjunto de estrelas a um modelo de isócrona, no plano de magnitudes g e r, são descritas por um distribuição Gaussiana, a probabilidade de que uma estrela i seja descrita por um modelo de isócrona j é dada por

$$\ell_{ij} = \frac{1}{(2\pi\sigma_i)^{1/2}} \exp\left(-\frac{d_{ij}^2}{2\sigma_i^2}\right), \tag{4.15}$$

onde σ_i representa a incerteza da i-ésima estrela no plano de magnitudes. Portanto, o logaritmo natural da função de verossimilhança para o conjunto de estrelas com $p > 0.01$ que são descritas por um modelo de isócrona pode ser escrito como

$$\ln \mathcal{L}_j = \ln \prod_{i=1}^{N} (\ell_{ij} p_i). \tag{4.16}$$

Nas próximas seções deste capítulo, nós damos uma breve descrição das propriedades obtidas para os quatro objetos adicionais detectados pelo código SPARSEX, DES 1, DES J0111−1341, DES J0225+0304 e DES 3. Uma descrição mais detalhada é dada nos artigos publicados, os quais estão anexados a este trabalho.

4.3 Aglomerado estelar DES 1

DES 1 é detectado nos dados de Y1A1 com uma alta significância ($\sim 14\sigma$), e se destaca com o candidato mais conspícuo de nossa busca. Este sistema físico é visto diretamente como uma sobredensidade de estrelas azuis fracas nas imagens coadicionadas (veja Figura 4.1). O fato de que eles são fontes azuis indica que esta sobredensidade não é um aglomerado de galáxias.

Usamos a técnica de máxima verossimilhança para inferir os parâmetros do DES 1 (ver a Seção 4.2). Para estimar os parâmetros estruturais, usamos dois modelos de perfil de densidade: exponencial e King (equação 4.3). O perfil exponencial tem cinco parâmetros livres: α_0, δ_0, θ, ϵ e $r_{\rm e}$, enquanto o perfil de King tem seis parâmetros livres: α_0, δ_0, θ, ϵ, $r_{\rm c}$, e r_t. Em ambos os casos, a densidade do campo, $\Sigma_{\rm bgd}$, é determinada usando uma região externa em torno de DES 1, a qual resulta em $2.02\ \frac{\text{estrelas}}{\text{arcmin}^2}$, e é mantida constante nos ajustes. Dado que o raio de escala exponencial está relacionado ao raio à meia luz pela relação $r_{\rm h} = 1.68 r_{\rm e}$ (Martin, de Jong, &

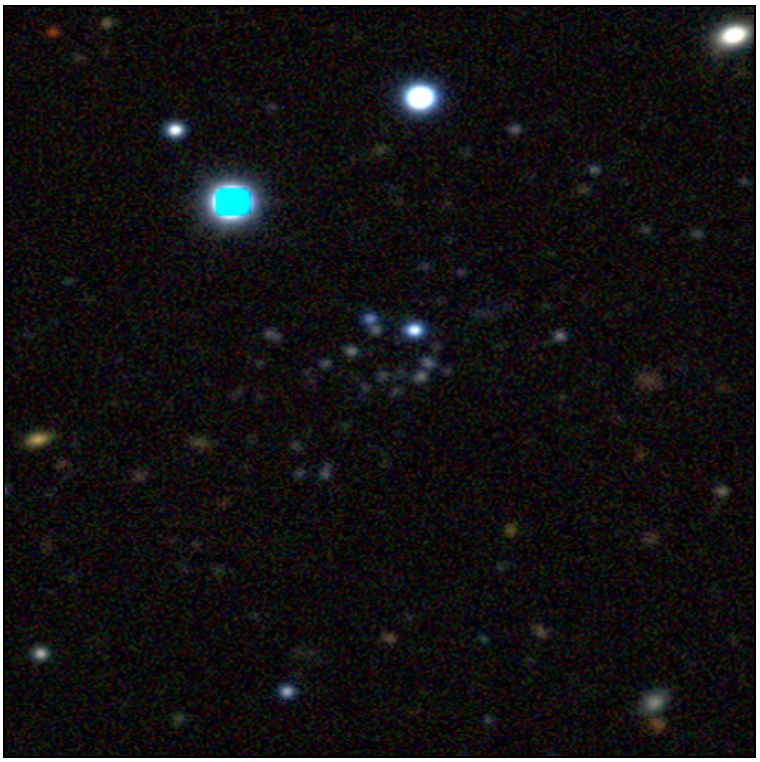

FIGURA 4.1: Imagen coadicionada de DES 1 obtida do portal científico do DES, mantido pelo LIneA. A imagem tem dimensões de $1\farcm78 \times 1\farcm78$ e está centrada em DES 1. Os canais R,G,B correspondem às bandas i, r, g.

Rix 2008), nós obtemos o raio à meia-luz para o perfil de King como segue. Primeiro, temos subtraído o número esperado de estrelas de campo coincidindo com DES 1, para obter $N_{\rm DES1}$, onde $N_{\rm DES1}$ é o número de estrelas que pertecem a DES 1. Em seguida, calculamos $r_{\rm h}$ como sendo o semi-eixo maior da elipse que contém $N_{\rm DES1}/2$ estrelas (Balbinot et al. 2013). A partir de ambos os modelos, nós achamos que DES 1 é compacto ($r_{\rm h} \sim 10\,{\rm pc}$) e muito alongado ($\epsilon \sim 0.6$). Nossos resultados são resumidos na Tabela 4.2.

Utilizando o método descrito na Seção 4.2.3, nós achamos que DES 1 é bem descrito por um modelo de isócrona de PARSEC (Bressan et al. 2012) com idade $10.0 \pm 2.1\,{\rm G\,anos}$, $[{\rm Fe/H}] = -1.88 \pm 0.25$ e $(m-M)_0 = 19.70 \pm 0.36$ para um perfil exponencial e $10.0 \pm 1.4\,{\rm G\,anos}$, $[{\rm Fe/H}] = -1.88 \pm 0.05$ e $(m-M)_0 = 19.45 \pm 0.11$ para um modelo de King. Portanto, DES 1 é dominado por uma população estelar velha e pobre em metal.

A sobredensidade de estrelas na posição de DES 1 também é evidente a partir do mapa de densidade mostrado no painel esquerdo da Figura 4.2. Para efeito de comparação, no painel central da Figura 4.2 mostramos o mapa de densidade de fontes classificadas como galáxias. Note-se que as galáxias fracas não contribuem com a sobredensidade observada na posição do DES 1. Ambos os mapas de densidade são construídos usando fontes próximas do melhor ajuste de isócrona (veja a discussão abaixo no texto).

TABELA 4.2: Propriedades de DES 1.

Parâmetros	Perfil Exponencial	Perfil de King
α_0 ($J2000$)	$00^h33^m59.7^s \pm 9.4^s$	$00^h33^m59.6^s \pm 1.4^s$
δ_0 ($J2000$)	$-49\,\mathrm{deg}\,02'20.0'' \pm 3.6''$	$-49\,\mathrm{deg}\,02'19.8'' \pm 2.1''$
$D_\odot$ (kpc)	~ 87.1	~ 77.6
r_e	$0'.23 \pm 0'.17$	–
θ (deg)	-57.9 ± 26.0	-52.5 ± 22.8
ϵ	0.69 ± 0.24	0.53 ± 0.22
Σ_c	204.98 ± 35.81	522.38 ± 88.30
Σ_{bgd}	2.02 ± 0.01	2.02 ± 0.01
r_h (arcmin)	0.39 ± 0.28^a	$0.39^{+0.13}_{-0.02}$
r_h (pc)	9.88 ± 7.09^b	$9.88^{+2.93}_{-0.45}{}^c$
M_V	$-3.00^{+0.66}_{-0.41}$	$-2.21^{+0.71}_{-0.48}$
PS	13.7 ± 4.1	11.6 ± 3.9
r_c	–	$0'.08 \pm 0'.04$
r_t	–	$10'.75 \pm 5'.6$
$[Fe/H]^d$	-1.88 ± 0.25	-1.88 ± 0.05
$\log(\tau)$	10.00 ± 0.09	10.00 ± 0.06
A_V	0.0 ± 0.04	0.10 ± 0.07
$(m-M)_0$	19.70 ± 0.36	19.45 ± 0.11

[a] Usando a relação, $r_h = 1.68 r_e$ (Martin, de Jong, & Rix 2008).
[b] Adotando a distância de 87.1 kpc.
[c] Adotando a distância de 77.6 kpc.
[d] Adotando $Z_\odot = 0.0152$ (Bressan et al. 2012).
Nota. Σ_c e Σ_{bgd} têm unidades estrelas/arcmin^2.

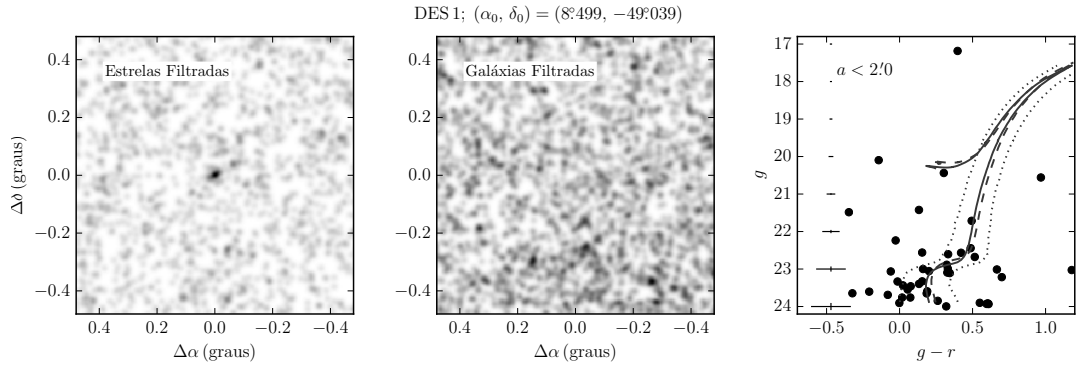

FIGURA 4.2: Painel esquerdo: mapa de densidade de fontes estelares próximas do melhor ajuste de isócronas em torno de DES 1. Painel central: o mesmo que o painel anterior, mas agora para galáxias. Os mapas de densidade foram suavizados com um *kernel* Gaussiano de $0.^\circ03$. Painel direito: CMD de estrelas dentro de uma elipse com semi-eixo maior $a = 2'$ centrado em DES 1. Os melhores ajustes de isócronas de PARSEC (Bressan et al. 2012) usando as estrelas selecionadas a partir do modelo de perfil exponencial (linha sólida) e perfil de King (linha tracejada) são mostrados. O filtro de isócrona (linhas pontilhadas) baseado nas incertezas fotométricas contém os membros mais prováveis. Os erros fotométricos médios na cor e na magnitude são mostrados no extremo esquerdo deste painel.

O CMD de DES 1 é mostrado no painel direito da Figura 4.2. Apenas as estrelas dentro de uma elipse com semi-eixo maior $a = 2'$ centrada em DES 1 são graficadas. Este CMD mostra claramente estrelas do *turn-off* da sequência principal (MSTO), ramo de subgigantes (SGB), ramo de gigantes vermelhas (RGB), e do ramo horizontal (HB). Os melhores ajustes de isócronas derivados a partir dos membros mais prováveis baseados no perfil exponencial e perfil de King são também graficados nesta figura, junto com um filtro de isócrona que contém os membros mais prováveis. O filtro de isócrona é construído usando as incertezas fotométricas tanto em magnitude como na cor. Estas curvas delimitam o melhor ajuste de isócrona a uma distância de $\sqrt{0.1^2 + \texttt{MAG\_ERR}^2 + \texttt{COL\_ERR}^2}$ no plano do CMD, onde `MAG_ERR` e `COL_ERR` são as incertezas fotométricas médias ao longo dos eixos do CMD. O valor 0.1 dentro da raiz quadrada se destina a evitar filtros de isócronas muito estreitos nas magnitudes brilhantes, onde as incertezas são pequenas.

A magnitude absoluta (M_V) foi determinada usando uma abordagem semelhante à de Koposov et al. (2015a). Nós integramos todas as massas ao longo do modelo de melhor ajuste de isócrona assumindo uma IMF de Kroupa (2001), e normalizamos o número de objetos por aqueles observados no CMD com $r < 23$ mag e que caem no filtro de isócrona. Para este propósito, selecionamos todas as estrelas com $p > 0.01$ obtidas dos perfis de densidade. Nós corrigimos as estrelas para a completeza da amostra, pesando cada estrela por $w_i = 1/c_i$, onde c_i é a completeza da estrela interpolada em um intervalo de magnitude. Devido ao baixo número de estrelas observadas neste tipo de objeto, a determinação da magnitude absoluta tem grande incerteza. Então, calculamos a incerteza estimando os limites superior e inferior para a magnitude V integrada, levando em conta as flutuações esperadas no processo de normalização. Convertemos as magnitudes $g_{\rm DES}$ e $r_{\rm DES}$ para a magnitude V usando uma amostra de calibração estelar do SDSS (Bechtol et al. 2015) e a equação de Jester et al. (2005),

$$\begin{aligned} g_{\rm SDSS} &= g_{\rm DES} + 0.104(g_{\rm DES} - r_{\rm DES}) - 0.01 \\ r_{\rm SDSS} &= r_{\rm DES} + 0.102(g_{\rm DES} - r_{\rm DES}) - 0.02 \\ V &= g_{\rm SDSS} - 0.59(g_{\rm SDSS} - r_{\rm SDSS}) - 0.01. \end{aligned} \tag{4.17}$$

Este procedimento gera uma magnitude absoluta de $M_V = -3.00^{+0.66}_{-0.41}$ para o modelo exponencial e $M_V = -2.21^{+0.71}_{-0.48}$ para o modelo de King. Portanto, no plano tamanho-luminosidade, DES 1 encontra-se localizado na região ocupada por aglomerados estelares fracos (veja a Figura 4.3). Além disso, sua distância heliocêntrica ($D_\odot \sim 83$ kpc) coloca DES 1 entre os aglomerados estelares mais distantes conhecidos até a presente data. Por último, a grande elipticidade ($\epsilon \sim 0.6$) inferida sugere que DES 1 está em processo dinâmico de ruptura de maré, apesar de sua grande distância, e o torna um objeto muito interessante para imageamento mais profundo e *follow-up* espectroscópico.

Junto com DES 1, confirmamos a existência da galáxia anã Horologium II previamente identificada por Kim & Jerjen (2015b). A análise das propriedades deste

objeto é apresentada na Seção 5 de nosso artigo publicado e anexado neste trabalho.

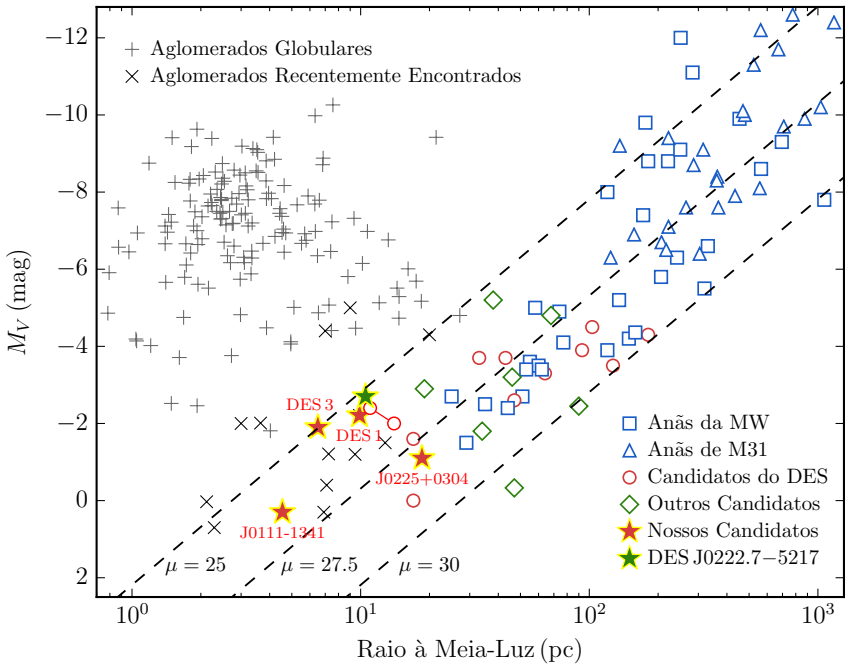

FIGURA 4.3: Magnitude absoluta em função do raio à meia-luz. Os aglomerados globulares da MW (símbolos '+'; Harris 2010), aglomerados estelares recentemente encontrados ('×'; Koposov et al. 2007; Belokurov et al. 2010; Muñoz et al. 2012; Balbinot et al. 2013; Laevens et al. 2014; Laevens et al. 2015b; Kim & Jerjen 2015a; Kim et al. 2015; Kim et al. 2016a; Koposov, Belokurov, & Torrealba 2017), galáxias anãs da MW (quadrados azuis; McConnachie 2012; Bechtol et al. 2015, Drlica-Wagner et al. 2015; Koposov et al. 2015a; Kim et al. 2016b; Torrealba et al. 2016a; Torrealba et al. 2016b), galáxias anãs de M31 (triângulos azuis; McConnachie 2012), candidatos a galáxias anãs previamente identificados na área amostrada do DES (círculos vermelhos; Bechtol et al. 2015; Drlica-Wagner et al. 2015; Koposov et al. 2015a; Kim & Jerjen 2015b), outros candidatos a galáxias anãs recentemente reportados (diamantes verdes; Martin et al. 2015; Laevens et al. 2015a; Laevens et al. 2015b; Drlica-Wagner et al. 2016; Homma et al. 2016; Homma et al. 2017), os nossos candidatos (estrelas vermelhas), e DES J0222.7−5217 (estrela verde) são mostrados. Os círculos vermelhos conectados com uma linha representam as duas estimativas anteriores de DES J0222.7−5217. Note que DES 1, DES J0111−1341, DES J0222.7−5217, e DES 3 residem dentro da região habitada pelos aglomerados estelares fracos, enquanto DES J0225+0304 está localizado em uma região ambígua entre aglomerados estelares e galáxias anãs. As linhas tracejadas indicam os contornos do brilho superficial constante em $\mu = \{25, 27.5, 30\}$ mag arcsec^{-2}.

4.4 Dois candidatos possivelmente associados com a corrente da anã de Sagitário

Usando dados dos dois primeiros anos do DES, nós conseguimos detectar dois candidatos a sistemas estelares, DES J0111−1341 e DES J0225+0304, que podem estar associados com a corrente da galáxia anã de Sagitário no hemisfério sul Galáctico.

Na Figura 4.4, mostramos um mapa de densidade de estrelas, com $17 < g < 23$ e $-0.5 < g - r < 1.2$, localizadas na área amostrada do catálogo DES Y2Q1, em dois sistemas de coordenadas diferentes. O painel esquerdo está no sistema de coordenadas alinhado com a corrente de Sagitário (Λ, B) (Majewski et al. 2003; Belokurov et al. 2014), enquanto o painel da direita está em coordenadas Galácticas (l, b). Várias sobredensidades são visíveis, como alguns GCs (Harris 2010) e galáxias anãs (McConnachie 2012; Bechtol et al. 2015; Koposov et al. 2015a). A corrente de Sagitário no hemisfério sul também é visível entre $90^\circ < \Lambda < 120^\circ$ e $-15^\circ < B < 12^\circ$ em coordenadas de Sagitário e entre $120^\circ < l < 190^\circ$ e $-80^\circ < b < -45^\circ$ em coordenadas Galácticas (ver os mapas ampliados no canto superior esquerdo de cada painel). Na mesma figura, mostramos com círculos vermelhos os dois candidatos a sistemas estelares, DES J0111−1341 e DES J0225+0304. Dadas as suas localizações físicas, esses novos candidatos estão possivelmente associados com a corrente de Sagitário. Nesta figura, também mostramos as regiões On e Off. A região On (linhas sólidas), definida por $95^\circ < \Lambda < 115^\circ$ e $-5^\circ < B < 5^\circ$, representa a região melhor amostrada da corrente de Sagitário, enquanto a região Off (linhas tracejadas) representa a amostra de estrelas de campo localizadas na mesma latitude Galáctica que a região On. A linha sólida amarela representa a posição de um possível ramo secundário da corrente estelar da anã de Sagitário[4] previamente identificado por (Koposov et al. 2012).

O fato de que esses dois objetos estão localizados muito perto da corrente de Sagitário, nos leva à seguinte pergunta: Estes candidatos têm propriedades semelhantes à corrente de Sagitário? Para responder esta questão, nós vamos determinar as propriedades básicas da corrente de Sagitário, tais como intervalos de idade, metalicidade e distância, e, então, comparamos estas propriedades com aquelas inferidas para os novos candidatos. A compatibilidade entre as estrelas da corrente e estes sistemas recentemente encontrados ajuda a elucidar sua possível associação física. Nas seguintes duas seções, nós usamos as regiões On e Off para estimar as propriedades da corrente de Sagitário.

[4]Nós temos analisado a corrente de Sagitário, usando os dados DES, para tentar detectar qualquer ramo secundário. A análise pode ser encontrada na Seção 3.1 de nosso artigo publicado e anexado neste trabalho.

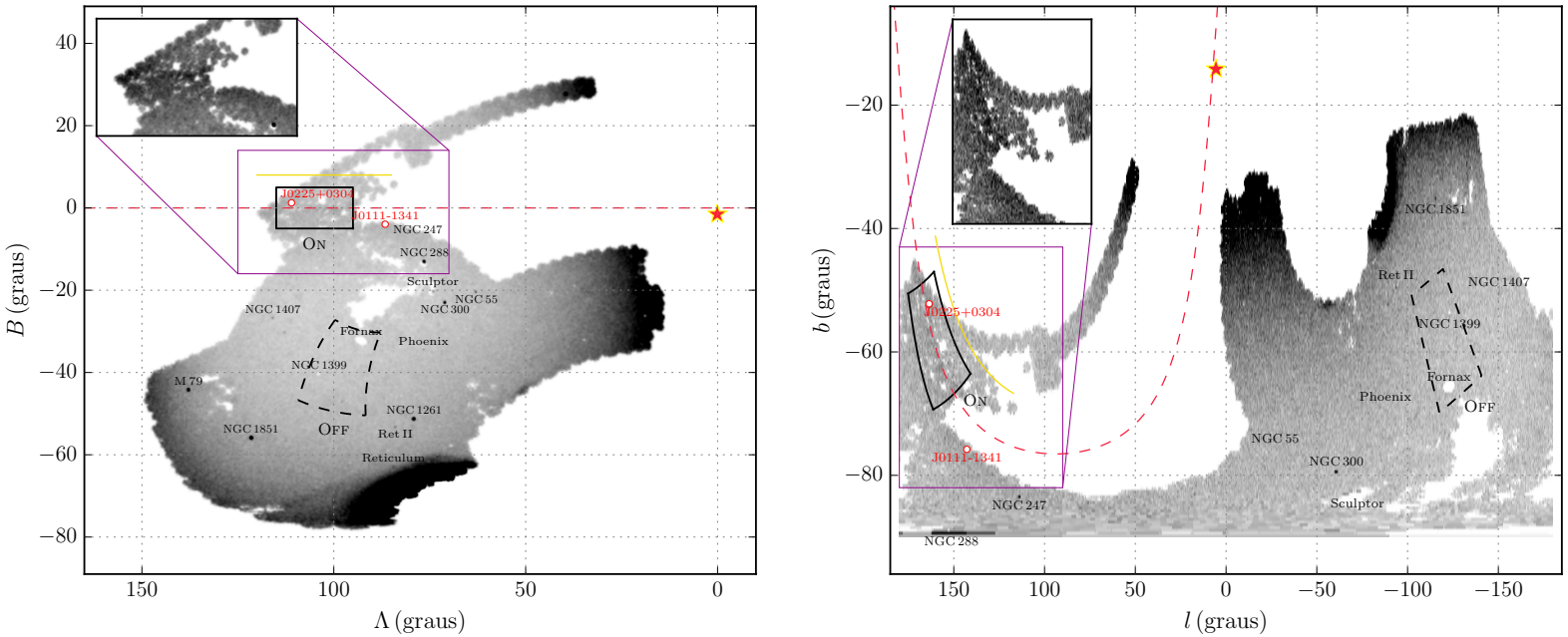

FIGURA 4.4: Mapa de densidade de estrelas com $17 < g < 23$ e $-0.5 < g - r < 1.2$ para a área amostrada do DES Y2Q1 em dois diferentes sistemas de coordenadas. O painel esquerdo é mostrado em um sistema de coordenadas definida pela órbita da anã de Sagitário (Majewski et al. 2003; Belokurov et al. 2014), enquanto o painel da direita está em coordenadas Galácticas (l, b). A localização atual da galáxia anã de Sagitário é indicada por uma estrela vermelha. A linha tracejada vermelha traça a cauda de maré de Sagitário (Majewski et al. 2003). No canto superior esquerdo de cada painel, mostramos uma inserção do mapa de densidade onde a corrente é mais visível. As sobredensidades de alguns GCs (Harris 2010) e galáxias anãs (McConnachie 2012; Bechtol et al. 2015) são também indicadas. Os novos candidatos a sistemas estelares descobertos, DES J0111−1341 e DES J0225+0304, são marcados com círculos vermelhos. A região ON (linhas sólidas) definida por $95° < \Lambda < 115°$ e $-5° < B < 5°$ representa a região melhor amostrada da corrente de Sagitário, enquanto que a região OFF (linhas tracejadas) representa a região das estrelas usadas para o campo com a mesma latitude Galáctica que a região ON. A galáxia anã de Fornax e NGC 1399 foram mascaradas para evitar superestimar a densidade de nossa amostra estelar do campo (região OFF). Essas regiões são usadas para construir os diagramas de Hess nas Figuras 4.5 e 4.6. A linha sólida amarela indica a posição do possível ramo fraco da corrente de Sagitário na área amostrada do DES.

4.4.1 Espalhamento de metalicidade

A corrente de Sagitário no hemisferio norte Galáctico e o equador celeste, S82, é conhecida por ter um intervalo de metalicidade (por exemplo, Koposov et al. 2012; De Boer, Belokurov, & Koposov 2015; Hyde et al. 2015). Em particular, usando dados fotométricos e espectroscópicos dentro da região do S82 do SDSS (região em comum com a área amostrada do DES), Koposov et al. (2012) determinaram que as estrelas pertencentes aos ramos brilhante e fraco cobrem um intervalo de metalicidade de $-2 \lesssim [\mathrm{Fe/H}] \lesssim 0$, enquanto De Boer, Belokurov, & Koposov (2015) determinaram um intervalo de metalicidade de $-2.5 \lesssim [\mathrm{Fe/H}] \lesssim -0.3$. No entanto, o ramo mais brilhante contém um número significativo de estrelas ricas em metal em comparação com o ramo mais fraco (Koposov et al. 2012).

Nós realizamos uma análise global das populações estelares que contribuem à corrente de Sagitário. Nós primeiro utilizamos as estrelas do RGB para determinar um espalhamento de metalicidade da seguinte forma. Primeiro, selecionamos as estrelas dentro da região definida por $95^\circ < \Lambda < 115^\circ$ e $-5^\circ < B < 5^\circ$ (região On, painel esquerdo da Figura 4.4). O intervalo em B se destina a reduzir os efeitos da cobertura do céu e a evitar qualquer possível contaminação pelo ramo fraco. Usando essas estrelas, nós construímos e descontaminamos um diagrama de Hess representativo da corrente de Sagitário. Os painéis esquerdo e central da Figura 4.5 mostram os diagramas Hess para as regiões On e Off, respectivamente. Essas regiões têm aproximadamente a mesma latitude Galáctica (veja o painel direito da Figura 4.4). O diagrama de Hess descontaminado mostrado no painel direito da Figura 4.5 foi calculado como a diferença entre os diagramas de Hess das regiões On e Off pesadas por suas respectivas áreas[5]. Nós utilizamos o *software* HEALPIX[6] para determinar a área efetiva de cada região. No diagrama de Hess descontaminado, podemos identificar estrelas da MS, RGB e algumas estrelas da população mais joven.

Nós selecionamos as estrelas dentro da região do CMD descontaminado definida por $0.4 < g - r < 0.8$ e $19.3 < g < 20.5$. Para cada intervalo de ~ 0.4 mag ao longo do CMD, contamos as estrelas como uma função da cor e usamos o pacote PYTHON `scipy.optimize`[7] para ajustar uma distribuição gaussiana e assim determinar o valor da cor média e o desvio padrão associado. A média e os desvios padrões ($\pm 1\sigma$) obtidos dos ajustes são mostrados como pontos pretos e vermelhos no painel direito da Figura 4.5. Em seguida, escolhemos um conjunto de modelos de isócronas de PARSEC para ajustar visualmente as cores médias do RGB e os desvios padrões $\pm 1\sigma$ resultantes dos ajustes Gaussianos, assim como o MSTO e MS. Isto é feito impondo as seguintes restrições aos modelos de isócronas: (1) a idade e metalicidade do modelo devem respeitar a relação idade-metalicidade de De Boer, Belokurov, & Koposov (2015) e (2) uma única distância deve ser usada para os três conjuntos de pontos ao longo da MS, MSTO e RGB.

[5] Nós substituimos os valores negativos no diagrama de Hess descontaminado por zero.
[6] http://healpix.sourceforge.net/
[7] http://docs.scipy.org/doc/scipy-0.17.0/reference/optimize.html

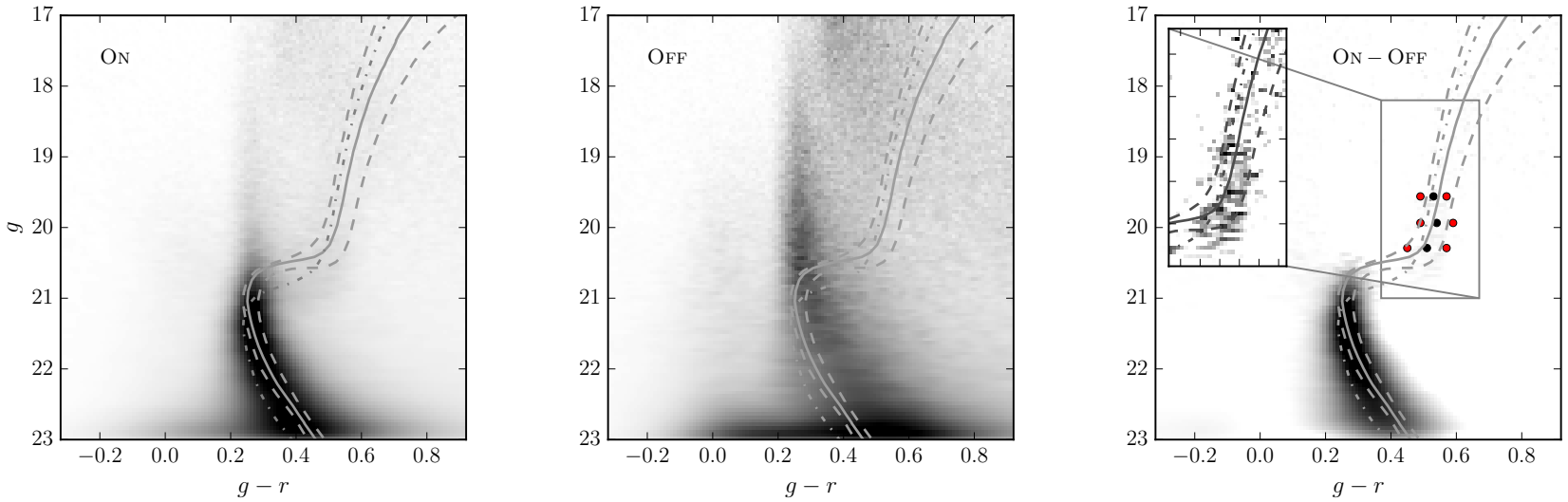

FIGURA 4.5: Painel esquerdo: diagrama de Hess construído com estrelas dentro de uma região da corrente de Sagitário definida por $95^\circ < \Lambda < 115^\circ$ e $-5^\circ < B < 5^\circ$ (região On; Figura 4.4). Painel central: diagrama de Hess do campo construído com estrelas dentro da região Off (Figura 4.4). Painel direito: diagrama de Hess da diferença entre as regiões On e Off. Os círculos sólidos pretos (vermelhos) representam os valores das cores médias (desvio padrão) das estrelas do RGB como uma função da cor $(g-r)$ para diferentes intervalos de magnitude. O valor da cor média (μ) e o desvio padrão (σ) obtidos a partir do ajuste Gaussiano são: $\mu = 0.527 \pm 0.002$ e $\sigma = 0.043 \pm 0.002$ (círculos superiores), $\mu = 0.544 \pm 0.003$ e $\sigma = 0.051 \pm 0.005$ (círculos do meio), $\mu = 0.509 \pm 0.004$ e $\sigma = 0.061 \pm 0.006$ (círculos inferiores). A linha sólida, em cada painel, representa o melhor ajuste de isócrona (Bressan et al. 2012) determinada a partir dos valores das cores médias. A linha tracejada inferior (superior) representa 1σ (-1σ) da isócrona. De baixo para cima, os parâmetros das isócronas são: $\log(\tau) = 9.98$, $D_\odot = 24.5$ kpc e $[Fe/H] = -0.95$ (linha tracejada inferior), $\log(\tau) = 10.02$, $D_\odot = 24.5$ kpc e $[Fe/H] = -1.34$ (linha contínua), $\log(\tau) = 10.12$, $D_\odot = 24.5$ kpc e $[Fe/H] = -2.18$ (linha tracejada superior). Além disso, um modelo de isócrona com parâmetros $[Fe/H] = -2.18$, $\log(\tau) = 10.12$ e $(m-M)_0 = 17.31$ também é graficado em cada painel (linha pontilhada-tracejada).

Os melhores ajustes de isócronas para os valores médios e os desvios padrões (conforme descrito acima) são mostrados na Figura 4.5. Nossos resultados mostram que a população da corrente é velha mas exibe um espalhamento significativo em metalicidade. Enquanto os valores médios do RGB são consistentes com $[\mathrm{Fe/H}] = -1.34$, seus extremos mais vermelhos e mais azuis são mais ricas em metal ($[\mathrm{Fe/H}] = -0.95$) e pobres em metal ($[\mathrm{Fe/H}] = -2.18$), respectivamente. O espalhamento em metalicidade encontrado nesta análise também é muito maior do que os erros fotométricos ($\sigma_{g-r} \simeq 0.01$ para estrelas do RGB em $g \sim 20$) e incerteza na calibração[8] [$\Delta(g-r) = 0.013$ para a região ON] o que atesta a sua realidade. No entanto, as determinações de metalicidade na literatura (Koposov et al. 2012; De Boer, Belokurov, & Koposov 2015) sugerem que a corrente de Sagitário na região do S82 contém estrelas ainda mais ricas em metal do que nossas determinações.

4.4.2 Gradiente de distância

As determinações de distância para diferentes regiões da corrente de Sagitário no hemisfério norte Galáctico foram realizadas por diferentes autores (por exemplo, Belokurov et al. 2006; Correnti et al. 2010). Estudos recentes da corrente de Sagitário no hemisfério sul Galáctico foram realizados por (Koposov et al. 2012) e Slater et al. (2013). Usando dados do SDSS DR 8, Koposov et al. (2012) determinaram um gradiente de distância de 22.08 ($\Lambda \simeq 97.^{\circ}5$) a 27.2 kpc ($\Lambda \simeq 112.^{\circ}5$), enquanto Slater et al. (2013), usando dados Pan-STARRS, determinaram um gradiente de distância de 29.5 ($\Lambda \simeq 102^{\circ}$) a 33.1 kpc ($\Lambda \simeq 110^{\circ}$). Observamos uma discrepância na determinação do gradiente de distância entre os dois grupos. Embora seja verdade que ambos os grupos usam estrelas do red clump (RC) para determinar o gradiente de distância ao longo da corrente de Sagitário, a diferença está no valor da magnitude absoluta assumida nestas determinações. Para comparar nossos resultados com a literatura, nós mostramos apenas resultados em nossa região de análise, $95^{\circ} < \Lambda < 115^{\circ}$. Aqui, realizamos uma estimativa independente do gradiente de distância ao longo da corrente Sagitário no hemisfério sul Galáctico, de modo a compará-los com os estudos anteriores.

Para cada intervalo de $2.^{\circ}5$ em Λ, construímos um diagrama de Hess ao longo da corrente de Sagitário (região ON, painel esquerdo da Figura 4.4), oito no total. Para descontaminar cada um dos diagramas de Hess, primeiro dividimos a região OFF em sub-regiões aproximadamente iguais àquelas utilizadas na região ON, mantendo a mesma latitude Galáctica. Então, seguimos o mesmo procedimento descrito na Seção 4.4.1. Os resultados são mostrados na Figura 4.6.

[8] A incerteza na calibração foi determinada comparando a calibração do *stellar locus regression* para Y2Q1 contra catálogos externos (2MASS e AAVSO *Photometric All-Sky Survey*, APASS-DR9). Estes últimos transformados aos filtros do DES.

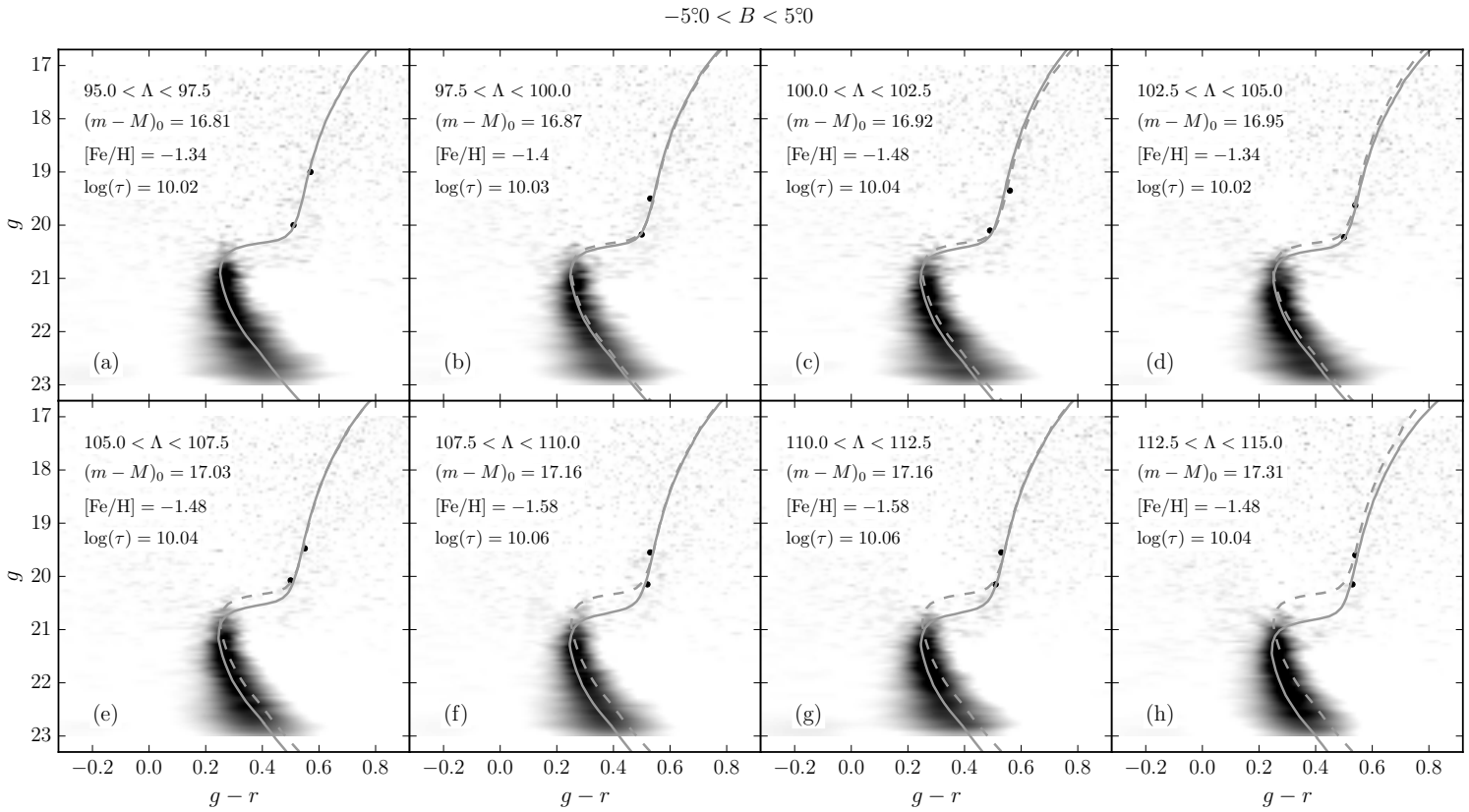

FIGURA 4.6: Diagramas de Hess, após da descontaminação das estrelas do campo, construídos ao longo da corrente de Sagitário (região ON) de $95^{\circ} < \Lambda < 97.^{\circ}5$ a $112.^{\circ}5 < \Lambda < 115^{\circ}$ como indicado em cada painel. Os pontos pretos sólidos representam os valores médios em cor obtidos a partir ajuste Gaussiano usando as estrelas do RGB. Um modelo de isócrona de PARSEC (Bressan et al. 2012) é graficado em cada painel com uma linha sólida. Os parâmetros da isócrona também são indicados em cada painel. Para fins de comparação, nos painéis (b) a (h) é graficado também (com uma linha tracejada) o modelo de isócrona mais próximo [painel (a)].

Nós estimamos o gradiente de distância ao longo da corrente como segue. Para cada intervalo em Λ, selecionamos as estrelas do CMD com $0.4 < g - r < 0.8$. Para dois intervalos de magnitude, contamos as estrelas como uma função da cor e ajustamos uma Gaussiana para determinar o valor da cor média (μ). A escolha de apenas dois intervalos de magnitude deve-se à baixa estatística de estrelas do RGB presentes em todos os CMDs. Ao aplicar esta restrição, obtemos ~ 150 estrelas em cada intervalo de magnitude. Os valores médios são mostrados como pontos sólidos pretos na Figura 4.6. Usamos, então, um conjunto de modelos de isócronas de PARSEC para ajustar visualmente os valores médios do RGB resultantes dos ajustes Gaussianos, assim como a MS e MSTO. Isto é realizado novamente impondo que a idade e metalicidade do modelo respeite a relação idade-metalicidade de De Boer, Belokurov, & Koposov (2015). Os melhores ajustes de isócronas usando o método descrito acima são graficados nos diagramas de Hess descontaminados (Figura 4.6). Nossos melhores ajustes de isócronas mostram um gradiente de distância ao longo da corrente de Sagitário de ~ 23 kpc para $95^\circ < \Lambda < 97.^\circ5$ e ~ 29 kpc para $112.^\circ5 < \Lambda < 115^\circ$. Nós estimamos a incerteza da distância em cada intervalo Λ variando a idade e metalicidade das isócronas de PARSEC em torno do melhor ajuste (mas ainda vinculado à mesma relação idade-metalicidade) e refazendo o ajuste visual de isócrona. Nós estimamos uma incerteza média para a distância de ± 0.3 kpc. Portanto, nossos resultados estão de acordo com os obtidos por Koposov et al. (2012).

Para quantificar o efeito do gradiente de distância ao longo da corrente sobre o espalhamento de metalicidade (ver Seção 4.4.1), nós graficamos na Figura 4.5 o modelo de isócrona que melhor ajusta em -1σ da Gaussiana ($[\mathrm{Fe/H}] = -2.18$, $\log(\tau) = 10.12$; pontos mostrados no lado azul do locus do RGB), mas agora deslocados para um valor de $(m - M)_0 = 17.31 \simeq 29$ kpc (linha pontilhada-tracejada). Esta distância corresponde ao valor máximo determinado na análise do gradiente de distância. Nós concluímos que uma variação na distância tão grande como a inferida nesta seção ainda assim não explica o espalhamento da cor observada no RGB (Figura 4.5).

4.4.3 DES J0111−1341 e DES J0225+0304

DES J0111−1341 e DES J0225+0304 foram detectados muito perto da corrente de Sagitário com um significância estatística relativamente alta, 8.2σ e 7.5σ, respectivamente. Nesta seção vamos estimar as propriedades físicas desses candidatos.

Para determinar as propriedades estruturais de DES J0111−1341 e DES J0225+0304, usamos o método descrito na Seção 4.2, assumindo que ambos os objetos são bem descritos por um modelo exponencial. Para estes ajustes usamos seis parâmetros livres: α_0, δ_0, ϵ, θ, r_e, e Σ_bgd. Nossos resultados indicam que DES J0111−1341 é compacto ($r_\mathrm{h} = 4.55^{+1.33}_{-0.95}$ pc) e ligeiramente alongado ($\epsilon = 0.27^{+0.20}_{-0.17}$), enquanto que DES J0225+0304 é de maior tamanho ($r_\mathrm{h} = 18.55^{+9.22}_{-4.86}$ pc) e mais alongado ($\epsilon = 0.61^{+0.14}_{-0.23}$) do que DES J0111−1341. As propriedades destes candidatos são resumidas na Tabela 4.3.

TABELA 4.3: Propriedades de DES J0111−1341 e DES J0225+0304

Parâmetros	DES J0111−1341	DES J0225+0304	Unidade
$\alpha_0\,(J2000)$	$01:11:10.3^{+0.40}_{-0.48}$	$02:25:42.4^{+1.52}_{-1.60}$	h:m:s
$\delta_0\,(J2000)$	$-13:41:05.4^{+5.4}_{-6.6}$	$03:04:10.1^{+45.6}_{-39.6}$	$\circ:\prime:\prime\prime$
l	142.83	163.58	graus
b	−75.79	−52.20	graus
Λ	86.61	111.02	graus
B	−3.97	1.24	graus
θ	$-53.24^{+31.70}_{-23.24}$	$31.25^{+11.48}_{-13.39}$	graus
ϵ	$0.27^{+0.20}_{-0.17}$	$0.61^{+0.14}_{-0.23}$	
$\Sigma_{\rm bgd}$	$1.040^{+0.001}_{-0.001}$	$1.679^{+0.002}_{-0.002}$	$\frac{\text{estrelas}}{\text{arcmin}^2}$
$D_\odot$	$26.5^{+1.3}_{-1.3}$	$23.8^{+0.7}_{-0.5}$	kpc
$r_{\rm h}{}^a$	$0.59^{+0.17}_{-0.12}$	$2.68^{+1.33}_{-0.70}$	arcmin
$r_{\rm h}$	$4.55^{+1.33}_{-0.95}{}^b$	$18.55^{+9.22}_{-4.86}{}^c$	pc
M_V	$+0.3^{+0.9}_{-0.6}$	$-1.1^{+0.5}_{-0.3}$	mag
$D_{\rm orb}$	~ 1.73	~ 0.50	kpc
$[{\rm Fe/H}]^d$	$-1.38^{+0.07}_{-0.05}$	$-1.26^{+0.03}_{-0.03}$	
$\log(\tau)$	$10.06^{+0.02}_{-0.02}$	$10.07^{+0.01}_{-0.01}$	
$(m-M)_0$	$17.12^{+0.11}_{-0.11}$	$16.88^{+0.06}_{-0.05}$	

[a] Usando a relação, $r_{\rm h} = 1.68 r_{\rm e}$ (Martin, de Jong, & Rix 2008).
[b] Adotando a distância de 26.5 kpc.
[c] Adotando a distância de 23.8 kpc.
[d] Adotando $Z_\odot = 0.0152$ (Bressan et al. 2012).

No painel esquerdo da Figura 4.7, mostramos o mapa de densidade construído usando estrelas dentro do filtro de isócrona. Para comparação, mostramos no painel central o mapa de densidade de objetos classificados como galáxias. Observe a sobredensidade estelar proeminente centrada em DES J0111−1341. Na mesma figura, o CMD para DES J0111−1341 é mostrado no painel direito. Somente são mostradas estrelas dentro de uma elipse com semi-eixo maior $a \sim 2r_{\rm h}$. O CMD mostra predominantemente as estrelas da MS. A Figura 4.8 mostra a informação análoga à Figura 4.7 para DES J0225+0304. O CMD deste candidato mostra estrelas da MS, RGB e uma possível estrela pertencente ao RC.

Usando o método de máxima verossimilhança para ajustar o CMD, nós achamos que a população estelar de DES J0111−1341 (DES J0225+0304) é bem descrita por um modelo de isócrona com idade $11.5^{+0.5}_{-0.5}$ G anos ($11.7^{+0.3}_{-0.3}$ G anos), $[{\rm Fe/H}] = -1.38^{+0.07}_{-0.05}$ ($[{\rm Fe/H}] = -1.26^{+0.03}_{-0.03}$), e $D_\odot = 26.5^{+1.3}_{-1.3}$ kpc ($D_\odot = 23.8^{+0.7}_{-0.5}$ kpc). O melhor modelo de isócrona para DES J0111−1341 (DES J0225+0304) é graficado no painel direito da Figura 4.7 (4.8) como uma linha sólida.

Para estimar a magnitude absoluta de DES J0111−1341 e DES J0225+0304, nós seguimos a mesma descrição apresentada na Seção 4.3. Este procedimento estima que ambos os objetos são ultra fracos, com $M_V = +0.3^{+0.9}_{-0.6}$ para DES J0111−1341 e $M_V = -1.1^{+0.5}_{-0.3}$ para DES J0225+0304. Portanto, no plano tamanho-luminosidade,

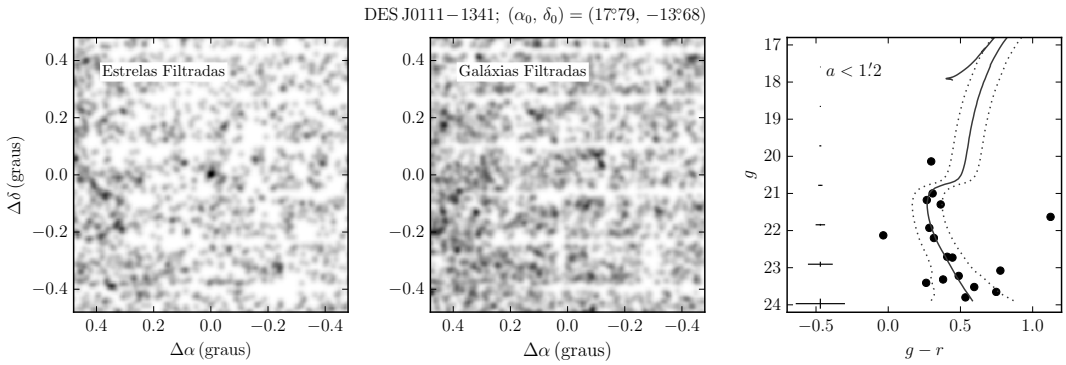

FIGURA 4.7: Painel esquerdo: mapa de densidade de fontes estelares próximas do melhor ajuste de isócronas em torno de DES J0111−1341. Painel central: o mesmo que o painel anterior, mas agora para galáxias. Os mapas de densidade foram suaviazdos com um *kernel* Gaussiano de $0.^\circ03$. Painel direito: CMD de estrelas dentro de uma elipse com semi-eixo maior $a \sim 2r_h$ centrado no DES J0111−1341. O melhor ajuste de isócrona de PARSEC (Bressan et al. 2012) usando as estrelas selecionadas a partir do modelo de perfil exponencial é mostrado. O filtro de isócrona (linhas pontilhadas) baseado nas incertezas fotométricas contém os membros mais prováveis. Os erros fotométricos médios na cor e na magnitude são mostrados no extremo esquerdo deste painel.

DES J0111−1341 está localizado entre outros objetos estelares classificados como aglomerados estelares da Galáxia, enquanto DES J0225+0304 está em uma região ambígua entre aglomerados estelares e galáxias anãs (veja Figura 4.3).

4.4.4 Associação com a corrente de Sagitário

Conforme mencionado anteriormente, DES J0111−1341 e DES J0225+0304 provavelmente estão associados com a corrente da anã de Sagitário. Seus parâmetros $\log(\tau)$, [Fe/H] e $D_\odot$ (ver Tabela 4.3) estão bem colocados nos intervalos de idade, metalicidade e distância determinados nas Seções 4.4.1 e 4.4.2 para a corrente. De fato, as idades e metalicidades de ambos candidatos são semelhantes, e concordam muito bem com o ajuste de isochrone obtida a partir das cores médias do RGB da corrente, $\log(\tau) = 10.02$, $[\mathrm{Fe/H}] = -1.34$ e $D_\odot = 24.5$ kpc.

Para explorar melhor essa associação, estimamos a distância dos dois novos candidatos ao plano orbital de Sagitário (D_{orb}). Para este propósito, usamos o melhor ajuste do plano orbital de Sagitário determinado por Majewski et al. (2003). Nós então obtemos uma distância de ~ 1.73 kpc e ~ 0.50 kpc para DES J0111−1341 e DES J0225+0304, respectivamente. Quando comparamos a D_{orb} dos novos candidatos com a D_{orb} determinado para o conjunto de aglomerados estelares associados com a anã de Sagitário (Bellazzini, Ferraro, & Ibata 2003, e referências nele contidas), notamos que DES J0111−1341 possui um D_{orb} semelhante ao de Terzan 7 ($\sim$ 1.89 kpc), enquanto a D_{orb} de DES J0225+0304 é comparável à de NGC 6715 (~ 0.45 kpc). Esses resultados indicam que DES J0111−1341 e DES J0225+0304 estão muito próximos do plano de Sagitário, algo que aumenta fortemente a probabilidade

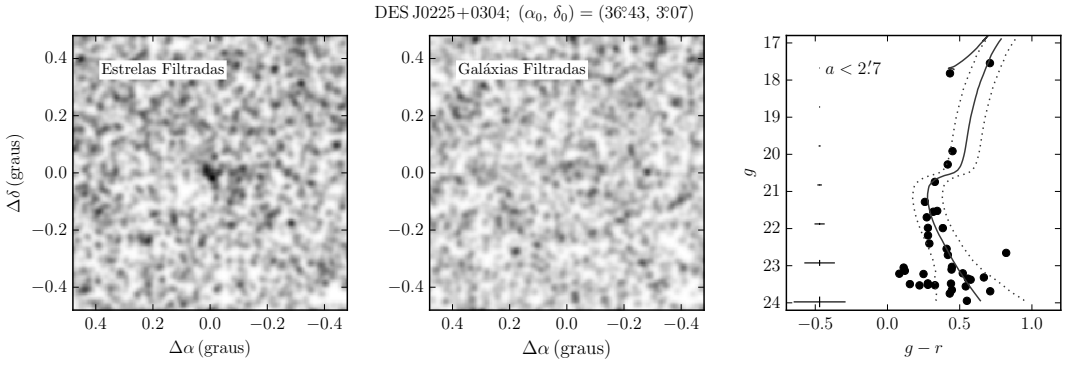

FIGURA 4.8: Painel esquerdo: mapa de densidade de fontes estelares próximas do melhor ajuste de isócronas em torno de DES J0225+0304. Painel central: o mesmo que o painel anterior, mas agora para galáxias. Os mapas de densidade foram suaviazdos com um *kernel* Gaussiano de $0.^\circ03$. Painel direito: CMD de estrelas dentro de uma elipse com semi-eixo maior $a \sim 1r_h$ centrado no DES J0225+0304. O melhor ajuste de isócrona de PARSEC (Bressan et al. 2012) usando as estrelas selecionadas a partir do modelo de perfil exponencial é mostrado. O filtro de isócrona (linhas pontilhadas) baseado nas incertezas fotométricas contém os membros mais prováveis. Os erros fotométricos médios na cor e na magnitude são mostrados no extremo esquerdo deste painel.

de associação destes candidatos com a corrente de Sagitário. No entanto, existem GCs espacialmente compatíveis com a órbita de Sagitário (por exemplo, NGC 4147 e NGC 288) mas não associados com Sagitário quando suas velocidades radiais e movimentos próprios são considerados (Law & Majewski 2010b). Isso sugere que a determinação espectroscópica da velocidade radial e o movimento próprio destes sistemas são cruciais para confirmar esta associação.

Por último, usamos uma técnica de amostragem aleatória para dar um argumento estatístico para essa possível associação. Para este propósito, utilizamos a amostra de aglomerados de estrelas e galáxias anãs de várias fontes conhecidas (Harris 2010; McConnachie 2012; Balbinot et al. 2013; Laevens et al. 2014; Laevens et al. 2015b; Laevens et al. 2015a; Bechtol et al. 2015; Drlica-Wagner et al. 2015; Koposov et al. 2015a; Kim & Jerjen 2015a; Kim et al. 2015; Kim et al. 2016a; Martin et al. 2015; Luque et al. 2016). A hipótese nula pressupõe que os sistemas estelares da nossa amostra não estão associados à galáxia anã de Sagitário; Assim, removemos os quatro GCs confirmados para serem associados com a anã de Sagitário (NGC 6715, Arp 2, Terzan 7 e Terzan 8). Primeiro, calculamos a $D_{\rm orb}$ para cada sistema estelar. Em seguida, selecionamos aleatoriamente dois sistemas da amostra, atribuindo uma probabilidade de seleção igual para cada sistema. Após realizar 10^6 seleções, estimamos uma probabilidade de 0.08 de encontrar dois sistemas estelares com $D_{\rm orb} \leqslant 1.73$ kpc. Embora seja verdade que esse valor de probabilidade não é desprezível, esses pares de objetos extraídos aleatoriamente não estão necessariamente tão próximos da órbita de Sagitário como nossos candidatos.

4.5 Novo aglomerado estelar DES 3

Recentemente detectamos um novo aglomerado de estrelas, DES 3, na constelação de Indus. O novo sistema foi detectado como uma sobredensidade estelar nos dados do primeiro ano do DES e confirmado com fotometria mais profunda obtida com o *Southern Astrophysical Research* (SOAR) *telescope*. DES 3 foi detectado com uma significância relativamente alta e aparece nas imagens DES como uma concentração compacta de fontes azuis fracas. Nós determinamos que DES 3 está localizado a uma distância heliocêntrica de ~ 76 kpc e está dominado por uma população velha ($\simeq 9.8$ G anos) e pobre em metal ($[\mathrm{Fe/H}] \simeq -1.88$). Enquanto os valores de idade e metalicidade de DES 3 são semelhantes aos aglomerados globulares da Galáxia, o seu raio à meia-luz ($r_\mathrm{h} \sim 6.5$ pc) e luminosidade ($M_V \sim -1.9$) são mais indicativos de um aglomerado de estrelas fraco. Com base no tamanho angular aparente, DES 3, com um valor de $r_\mathrm{h} \sim 0\farcm3$, está entre os aglomerados estelares fracos mais pequenos conhecidos até o presente. Além disso, obtivemos imagens mais profundas de DES J0222.7−5217 (Eridanus III) com o telescópio SOAR para atualizar os seus parâmetros estruturais. Nossa análise levou à primeira estimativa de idade ($\simeq 12.6$ G anos) e metalicidade ($[\mathrm{Fe/H}] \sim -2.01$) para este objeto. O raio à meia-luz ($r_\mathrm{h} \sim 10.5$ pc) e luminosidade ($M_V \sim -2.7$) de DES J0222.7−5217 sugerem que este objeto possivelmente seja um aglomerado estelar fraco. A análise desses dois sistemas estelares é apresentada no artigo anexado nesta seção.

Este artigo foi enviado à revista *Monthly Notices of the Royal Astronomical Society* (MNRAS). Recentemente, nós recebemos alguns comentários menores do *referee*, os quais estão sendo executados pelos principais autores e a revisão interna do DES.

DES 2017-0238
Fermilab PUB-17-349-AE

MNRAS **000**, 1–11 (2015) Preprint 19 September 2017 Compiled using MNRAS LATEX style file v3.0

Deep SOAR follow-up photometry of two Milky Way outer-halo companions discovered with Dark Energy Survey

E. Luque,[1,2⋆] B. Santiago,[1,2] A. Pieres,[1,2] J. L. Marshall,[3] A. B. Pace,[3]
R. Kron,[4,5] A. Drlica-Wagner,[4] A. Queiroz,[1,2] E. Balbinot,[6] M. dal Ponte,[1,2]
A. Fausti Neto,[2] L. N. da Costa,[2,7] M. A. G. Maia,[2,7] A. R. Walker,[8]
F. B. Abdalla,[9,10] S. Allam,[4] J. Annis,[4] K. Bechtol,[11] A. Benoit-Lévy,[9,12,13]
E. Bertin,[12,13] D. Brooks,[9] A. Carnero Rosell,[2,7] M. Carrasco Kind,[14,15]
J. Carretero,[16] M. Crocce,[17] C. Davis,[18] P. Doel,[9] T. F. Eifler,[19,20]
B. Flaugher,[4] J. García-Bellido,[21] D. W. Gerdes,[22,23] D. Gruen,[18,24]
R. A. Gruendl,[14,15] G. Gutierrez,[4] K. Honscheid,[25,26] D. J. James,[27]
K. Kuehn,[28] N. Kuropatkin,[4] R. Miquel,[16,29] R. C. Nichol,[30] A. A. Plazas,[20]
E. Sanchez,[31] V. Scarpine,[4] R. Schindler,[24] I. Sevilla-Noarbe,[31] M. Smith,[32]
M. Soares-Santos,[4] F. Sobreira,[2,33] E. Suchyta,[34] G. Tarle[23] and D. Thomas[30]

Affiliations are listed at the end of the paper

Released 19 September 2017

ABSTRACT

We report the discovery of a new star cluster, DES 3, in the constellation of Indus, and deeper observations of the previously identified satellite DES J0222.7−5217 (Eridanus III). DES 3 was detected as a stellar overdensity in first-year Dark Energy Survey data, and confirmed with deeper photometry from the 4.1 metre Southern Astrophysical Research (SOAR) telescope. The new system was detected with a relatively high significance and appears in the DES images as a compact concentration of faint blue point sources. We determine that DES 3 is located at a heliocentric distance of ~ 76 kpc and it is dominated by an old ($\simeq 9.8$ Gyr) and metal-poor ([Fe/H] $\simeq -1.88$) population. While the age and metallicity values of DES 3 are similar to globular clusters, its half-light radius ($r_{\rm h} \sim 6.5$ pc) and luminosity ($M_V \sim -1.9$) are more indicative of faint star clusters. Based on the apparent angular size, DES 3, with a value of $r_{\rm h} \sim 0\farcm3$, is among the smallest faint star clusters known to date. Furthermore, using deeper imaging of DES J0222.7−5217 taken with the SOAR telescope, we update structural parameters and perform the first isochrone modeling. Our analysis yields the first age ($\simeq 12.6$ Gyr) and metallicity ([Fe/H] $\simeq -2.01$) estimates for this object. The half-light radius ($r_{\rm h} \sim 10.5$ pc) and luminosity ($M_V \sim -2.7$) of DES J0222.7−5217 suggest that it is likely a faint star cluster. The discovery of DES 3 indicates that the census of stellar systems in the Milky Way is still far from complete, and demonstrates the power of modern wide-field imaging surveys to improve our knowledge of the Galaxy's satellite population.

Key words: Galaxy: halo – globular clusters: general.

1 INTRODUCTION

A fundamental prediction of the Lambda cold dark matter (ΛCDM) theory of structure formation is that galactic

⋆ **E-mail**: elmer.luque@ufrgs.br

DM haloes of the size of the Milky Way (MW) grow by the accretion of smaller sub-systems (e.g. White & Rees 1978; Davis et al. 1985; Font et al. 2011). The Sagittarius dwarf galaxy and the globular cluster Palomar 5 are interesting examples of physical systems that are even now going through the process of tidal disruption before being absorbed by the MW (see e.g. Ibata et al. 1994; Odenkirchen et al. 2002). Spectroscopic observations have shown that the dwarf galaxies are DM dominated systems, while there is virtually no evidence of DM halos surrounding the globular clusters (e.g. Willman & Strader 2012; Ibata et al. 2013).

Based on the horizontal branch (HB) morphology, metallicity, structure and kinematics, the globular clusters of the MW halo have been classified into two groups: the Young and Old Halo globular clusters (Zinn 1985, 1993; Mackey & Gilmore 2004; Mackey & van den Bergh 2005; Milone et al. 2014; Marino et al. 2014, 2015). It is established observationally that the accretion of dwarf galaxies leads to the accretion of globular clusters, the so-called Young Halo clusters, and possibly open clusters (e.g. Mackey & Gilmore 2004; Mackey & van den Bergh 2005; Carraro & Bensby 2009; Law & Majewski 2010, and references therein). Therefore, searching for star clusters can help us understand the assembly history of our Galaxy and the associated globular cluster system.

With the advent of the Sloan Digital Sky Survey (SDSS; York et al. 2000), a new class of star clusters was discovered (e.g. Koposov et al. 2007; Belokurov et al. 2010; Fadely et al. 2011; Muñoz et al. 2012; Kim & Jerjen 2015a). These star clusters have very low luminosities ($-3.0 \lesssim M_V \lesssim 0$), small half-light radii ($r_{\rm h} < 10\,{\rm pc}$), and are thought to suffer mass-loss via dynamical processes such as tidal disruption or evaporation (see e.g. Koposov et al. 2007; Kim & Jerjen 2015a). The census of MW satellite galaxies has also increased considerably, from 11 classical dwarfs known in 1990, up to a total of 27 that were known by early 2015 (McConnachie 2012). Over the past two years many satellite candidates have been found in the following surveys: the Dark Energy Survey (DES; The Dark Energy Survey Collaboration 2005), the Panoramic Survey Telescope and Rapid Response System 1 (Laevens et al. 2014, 2015a,b), the Survey of the Magellanic Stellar History (Martin et al. 2015), VST ATLAS (Torrealba et al. 2016a,b), the Hyper Suprime-Cam Subaru Strategic Program (Homma et al. 2016, 2017), and the Magellanic SatelLites Survey (Drlica-Wagner et al. 2016). In particular, 21 stellar system candidates with $M_V \gtrsim -8$ have been found in DES (Bechtol et al. 2015; Drlica-Wagner et al. 2015; Koposov et al. 2015a; Kim & Jerjen 2015b; Luque et al. 2016, 2017). Thus far, spectroscopic measurements of radial velocity and metallicity have confirmed that Reticulum II (Koposov et al. 2015b; Simon et al. 2015; Walker et al. 2015), Horologium I (Koposov et al. 2015b), Tucana II (Walker et al. 2016), Grus I (Walker et al. 2016), Tucana III (Simon et al. 2017), and Eridanus II (Li et al. 2017) are indeed dwarf galaxies. The possible association of the recently discovered DES dwarf galaxy candidates with Large and Small Magellanic Clouds (LMC and SMC) has been discussed by several authors (e.g. Bechtol et al. 2015; Drlica-Wagner et al. 2015, 2016; Koposov et al. 2015a; Jethwa et al. 2016; Dooley et al. 2017; Sales et al. 2017). Several of the candidates may be associated with the Sagittarius stream (Luque et al. 2017).

Here, we announce the discovery of a new MW star cluster, which we call DES 3, in the constellation of Indus. The object was detected as a stellar overdensity in the first internal release of the DES co-add data (Y1A1), which covers a solid angle of $\sim 1800\,{\rm deg}^2$ in the southern equatorial hemisphere, and later confirmed with deep SOAR imaging. We additionally present deeper imaging of DES J0222.7−5217 (Eridanus III) taken with the SOAR telescope in order to determine its properties, several of which have not been reported in the literature (Bechtol et al. 2015; Koposov et al. 2015a). We use these deeper data to better investigate the nature of this object, whether it be a star cluster or a very small faint dwarf. If DES J0222.7−5217 is confirmed to be a star cluster, it will be named DES 4. This paper is organized as follows. Section 2 describes the method used to search for star clusters and other stellar systems. In Section 3, we describe the first-year DES data and discovery of DES 3. The photometric follow-up observations and data reduction are presented in Section 4. In Section 5, we quantify the physical properties of the new stellar object. In Section 6, we present the updated properties of DES J0222.7−5217 with deeper imaging. Our final remarks are given in Section 7.

2 SUBSTRUCTURE SEARCH METHOD

Here we briefly review our overdensity search technique (SPARSEX; Luque et al. 2016). The SPARSEX code is based on the matched-filter (MF) method (Rockosi et al. 2002; Szabo et al. 2011). It minimizes the variance between star counts from a data catalogue and a model containing a simple stellar population (SSP) and a MW field star contamination. This minimization is carried out over colour and magnitude bins for each individual and small spatial cell. A grid of SSPs covering a wide range of ages, metallicities, and distances, is created using the code GENCMD[1]. The model of field stars is created from the catalogue data over $10^\circ \times 10^\circ$ regions, to account for possible variations in the field population mix. The variance minimization yields the SSP model normalization as a function of position, i.e., a map with the number density of stars consistent with that particular SSP. We then convolve each SSP map with different spatial kernels to highlight substructures of different sizes. For each of these maps, we apply SExtractor (Bertin & Arnouts 1996) to identify the most significant and/or frequently detected overdensities. Then we perform visual inspection on the images, colour-magnitude diagram (CMD) and significance profile of each candidate. The significance profile is defined as the ratio of the number of stars $N_{\rm obj}$ inside a given radius in excess of the number $N_{\rm bgd}$, relative to the expected fluctuation in the same field background, i.e, $N_{\rm obj}/\sqrt{N_{\rm bgd}}$. Defining $N_{\rm obs}$ to be the total number of observed stars, then $N_{\rm obj} = (N_{\rm obs} - N_{\rm bgd})$. To avoid a low stellar statistic, we built the significance profile using a cumulative radius of $1'$ centred on the candidate. $N_{\rm bgd}$ is computed within a circular annulus at $30' < r < 36'$ from each candidate. We refer

[1] https://github.com/balbinot/gencmd

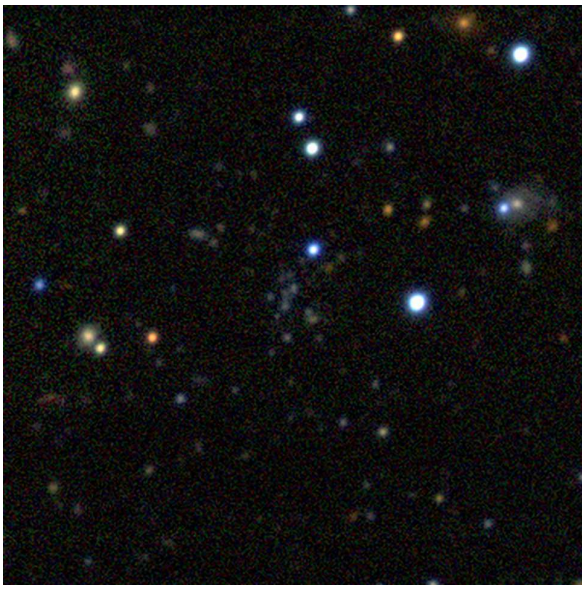

Figure 1. DES co-add image cutout of DES 3 taken from the DES Science portal. The 1.58 arcmin × 1.58 arcmin image is centred on DES 3. The R,G,B channels correspond to the i, r, g bands.

to Luque et al. (2016, 2017) and to Sections 3 and 5 below for more details.

3 DES DATA AND DISCOVERY

DES is a wide-field optical survey that uses the Dark Energy Camera (DECam; Flaugher et al. 2015) to image 5000 deg^2 in the southern equatorial hemisphere. DECam is an array of 62 2k × 4k CCDs, with pixel scale of 0.″263, that images a 2.°2 diameter field of view. It is installed at the prime focus of the 4-metre Blanco telescope at Cerro Tololo Inter-American Observatory. DECam images are reduced by the DES Data Management (DESDM) system. The pipeline consists of image detrending, astrometric calibration, nightly photometric calibration, global calibration, image coaddition, and object catalogue creation (see Sevilla et al. 2011; Desai et al. 2012; Mohr et al. 2012; Balbinot et al. 2015; Drlica-Wagner et al. 2017, for a more detailed description). The SExtractor toolkit is used to create catalogues from the processed and co-added images (Bertin & Arnouts 1996; Bertin 2011).

To search for stellar substructures in the DES Y1A1 catalogue, we applied cuts based on the SExtractor parameters `SPREAD_MODEL`, `FLAGS` and point spread function (`PSF`) magnitudes. The `FLAGS` parameter denotes if an object is saturated or has been truncated at the edge of the image and a cut of `FLAGS` < 4 is sufficient for our purposes. We apply this restriction in all our subsequent analyses. The `SPREAD_MODEL` parameter is the main star/galaxy separator. To avoid issues arising from fitting the `PSF` across variable-depth co-added images, we utilized the weighted-average (`WAVG`) of the `SPREAD_MODEL` measurements from the single-epoch exposures (see Bechtol et al. 2015). Therefore, our stellar sample consists of sources in the i band with |`WAVG_SPREAD_MODEL`| $<$ 0.003 + `SPREADERR_MODEL` as described in Drlica-Wagner et al. (2015) and Luque et al. (2016). In addition, magnitude[2] ($17 < g_{\rm DES} < 24$) and colour ($-0.5 < g_{\rm DES} - r_{\rm DES} < 1.2$) cuts were also applied. The colour cut was performed to exclude stars from the Galactic disc and possibly spurious objects that can contaminate our sample. Each star was extinction corrected from the reddening map of Schlegel et al. (1998).

Applying the method described in Section 2 on DES Y1A1 data, we have successfully recovered all ten stellar objects that have been reported in first-year DES data[3] (Bechtol et al. 2015; Koposov et al. 2015a; Kim & Jerjen 2015b; Luque et al. 2016). These detections include the faint satellite DES J0222.7−5217, which we detect with significance of 16.1σ. Bechtol et al. (2015) reported DES J0222.7−5217 with a heliocentric distance of 95 kpc, an absolute magnitude of -2.4 ± 0.6, and a half-light radius of 11^{+8}_{-5} pc. In contrast, Koposov et al. (2015a) found DES J0222.7−5217 to be slightly less distant, 87 kpc, with an absolute magnitude of -2.0 ± 0.3, and a half-light radius of $14.0^{+12.5}_{-2.6}$ pc. Deeper imaging is necessary to conclusively determine the characteristics of this faint satellite.

In addition, to the previously detected satellites, we detected one new star cluster, DES 3, with a statistical significance of 8.3σ. DES 3 is readily visible as a cluster of faint blue stars in the DES co-add images[4] (see Fig. 1). The fact that they are blue sources indicates that this overdensity is not a galaxy cluster. The overdensity is also clear from the DES stellar map shown in panel (a) of Fig. 2. For comparison, in panel (b), we show the density map of sources classified as galaxies. Note that faint galaxies do not contribute to the observed overdensity of DES 3. In panel (c) of Fig. 2, the circular significance profile is shown. Note that the significance profile shows the higher peak at $r = 1'$ from the centre of DES 3, where $N_{\rm obj} = 22$ and $N_{\rm bgd} = 7$ stars. To take into account the missing coverage[5] observed in panels (a) and (b) of Fig. 2, in this analysis, we estimated the effective area ($A_{\rm eff}$) for each circular region as follows. After inserting a certain number of uniformly distributed random points (N) inside a circle with radius r centred on DES 3, we computed the ratio between the number of points that fall inside the region of the sky that is covered by the DES data ($N_{\rm in}$) and N. Therefore, for each region $A_{\rm eff} = A\frac{N_{\rm in}}{N}$, where A is the area of the circle.

In panel (d) of Fig. 2, we show the CMD of DES 3 constructed with stars within a circle of radius $r = 0.'6$. We also have plotted a PARSEC (CMD v3.0;[6] Bressan et al. 2012) isochrone model (solid line) corresponding to the best-fitting parameters (this will be discussed fully in Section 5). There are stars with $g_{\rm DES} \gtrsim 22.5$ mag scattered in the CMD, some

[2] We refer the `WAVG_MAG_PSF` measurements in the DES gri filters as $g_{\rm DES}$, $r_{\rm DES}$ and $i_{\rm DES}$, respectively.
[3] The eleventh object, Grus 1, reported by Koposov et al. (2015a) is in a region of Y1 data that is not included in the Y1A1 coadd due to limited coverage in some of the DES filters.
[4] The images were taken from the DES Science portal. The latter is a web-based system being developed by DES-Brazil and Laboratório Interinstitucional de e-Astronomia (LIneA, http://www.linea.gov.br) for the DES collaboration.
[5] We masked the regions on the sky where there is absence of sources.
[6] We are using PARSEC isochrones revised to include instrumental and atmosphere response.

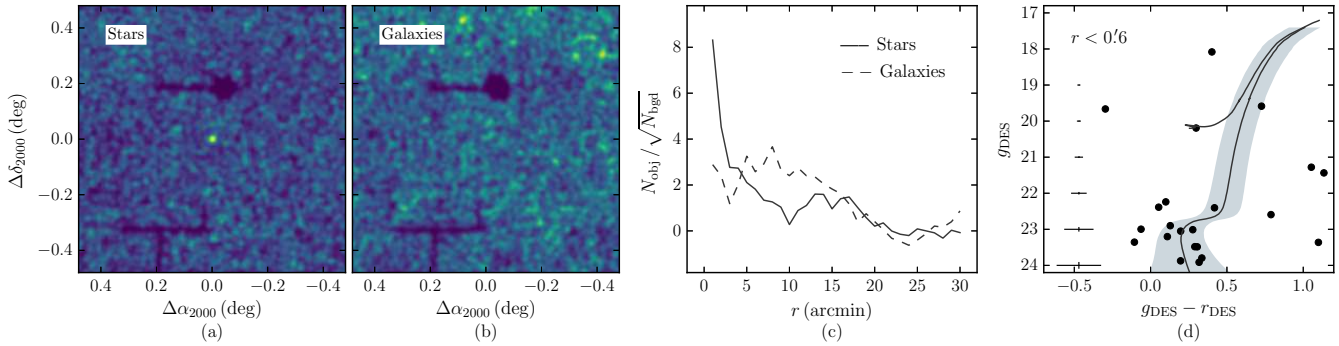

Figure 2. Detection of DES 3 from the DES data. Panel (a): stellar density map around DES 3. Panel (b): similar to previous panel, but now for galaxies. Panel (c): significance profile as a function of radius r from the centre of DES 3. The solid line corresponds to stars, while the dashed line corresponds to galaxies. Panel (d): CMD of stars within a circle with radius $r = 0.'6$ from the centre of DES 3. A PARSEC (solid line) isochrone model with age 9.8 Gyr and [Fe/H] $= -1.88$ is overplotted at a distance of 76.2 kpc (see Section 5 for details of the best-fitting isochrone). The isochrone filter (gray shaded area) based on photometric uncertainties contains the most likely members. The mean photometric errors in both colour and magnitude are shown in the extreme left of this panel.

of which fall inside the isochrone filter[7] (gray shaded area). We are tempted to say that these stars belong to the main sequence turn-off (MSTO) and sub-giant branch (SGB) of DES 3. Note that the CMD also shows one star that may belong to the HB. However, based on the limited information given by this CMD, we are not able to confirm the nature and infer reliable parameters for DES 3. In order to reach the main sequence (MS; $g_{\rm DES} \sim 25.5$ mag) in the CMD, deeper follow-up observations are required.

4 SOAR FOLLOW-UP DATA

Follow-up imaging of DES 3 and DES J0222.7−5217 was carried out on 2016 July 29 and October 20 respectively, using the SOAR Optical Imager (SOI) on the 4.1-metre Southern Astrophysical Research (SOAR) telescope. SOI consists of two 2048×4096 CCDs and covers a $5.'2 \times 5.'2$ field. The SOI CCDs have a scale of $0.''077$/pixel. As the images were binned 2×2, the final image scale is $0.''154$/pixel. We observed each object for a total of 45 min in each SDSS filter (g and r; hereafter g' and r'). The integrations were split into nine exposures of 300 s to avoid overexposing. The observations were carried out with an airmass below 1.20.

Raw exposures were trimmed, corrected for bias, and flat fielded by the SOAR Brazilian Resident Astronomers, David Sanmartin and Luciano Fraga, using SOAR/IRAF packages. Individual exposures for each filter, g' and r', were co-added. In particular, Fig. 3 shows the SOAR/SOI (g' band only) coadded images of DES 3. The figure attests to the increase in spatial resolution[8] and in photometric depth when the latter is compared with the DES images (see Fig. 1). The

Figure 3. SOAR g band co-add image cutout of DES 3. The 1.58 arcmin × 1.58 arcmin image is centred on DES 3.

scattered light observed in Fig. 3 is discussed in the text below. To create a source catalogue in the direction of DES 3 and DES J0222.7−5217, we use a combination of the SExtractor/PSFEx routines (Bertin & Arnouts 1996; Bertin 2011). A first pass of SExtractor is run to create an input catalogue for PSFEx. The PSFEx routine creates a `PSF` image for a second pass of SExtractor that determines the `PSF` magnitude and the `SPREAD_MODEL` parameter.

We transformed the instrumental magnitudes, $g_{\rm inst}$ and $r_{\rm inst}$, to apparent magnitudes[9], g and r, by using a set of DES stars in the direction of each object. This process was performed as follows: first we built a SOAR catalogue by merging the g' and r' full photometric lists, using a match-

[7] The isochrone filter is built by using the photometric uncertainties in both colour and magnitude. We added a value of 0.1 mag in the colour-magnitude space to avoid too narrow isochrone filters at the bright magnitudes, where the uncertainties are small (for details, see Luque et al. 2016).

[8] By using several bright and isolated stars in the direction of DES 3, we determined that the DES co-added images have an average `PSF` FWHM of $\simeq 1.''19$ and $0.''94$ in the g and r bands, respectively, while the SOAR co-added images have a value of $\simeq 0.''8$ in both g' and r' bands.

[9] The $g_{\rm inst}$ and $r_{\rm inst}$ magnitudes are given by $-2.5 \times \log(\text{counts})$, while the g and r magnitudes correspond to $g_{\rm DES}$ and $r_{\rm DES}$, respectively.

Table 1. Calibration coefficients obtained from the fit of the set of equations presented in equation 1.

Coefficient	DES 3	DES J0222.7−5217
β (mag)	31.71 ± 0.02	31.43 ± 0.08
γ	-0.10 ± 0.02	-0.16 ± 0.09
ζ (mag)	31.70 ± 0.02	31.51 ± 0.03
η	-0.15 ± 0.03	-0.12 ± 0.02

ing radius of 0.′5. We also selected DES stellar sources with |WAVG_SPREAD_MODEL| < 0.003 and WAVG_MAGERR_PSF < 0.03 to obtain a sufficiently pure stellar sample. Next, we matched the SOAR sources with DES brightest (from 17 to 22 mag) stars, on g' and r' filters, using a radial tolerance of 0.′5. Then, we use these brightest stars to fit the following calibration curves:

$$\begin{aligned} g &= g_{\rm inst} + \beta + \gamma(g_{\rm DES} - r_{\rm DES}), \\ r &= r_{\rm inst} + \zeta + \eta(g_{\rm DES} - r_{\rm DES}), \end{aligned} \quad (1)$$

where the β and ζ coefficients represent the zero points of the two bands, while γ and η are the colour term coefficients. Airmass correction, in both filters, was assumed to be constant and, therefore, it is absorbed by the zero point coefficient. The results of our fits are presented in Table 1. Estimates for the two objects are identical within uncertainties. The calibration was then applied to all instrumental magnitudes in the photometric list. Finally, all magnitudes of the calibrated sources were corrected for Galactic reddening using the Schlegel et al. (1998) dust maps.

For our further analysis, we modify the cuts to reach faint magnitudes. Our stellar sample consists of sources with |SPREAD_MODEL| < 0.003 + SPREADERR_MODEL. Moreover, we applied colour ($-0.5 < g_{\rm DES} - r_{\rm DES} < 1.2$) and magnitude ($g_{\rm DES} > 17$) cuts. The faint $g_{\rm DES}$ magnitude, for each catalogue, is established based on the magnitude error (σ_g), where σ_g has a value of ≈ 0.07 mag. Therefore, this limiting magnitude corresponds to $g_{\rm DES} < 25$ ($g_{\rm DES} < 24.5$) for the star catalogue in the direction of DES 3 (DES J0222.7−5217).

We have verified that the scattered light observed only in the DES 3 images (see Fig. 3) does not affect the completeness of sources (stars and galaxies) down to a magnitude depth $g_{\rm DES} \sim 25$ mag. To check we count sources as a function of magnitude both inside and outside scattered light affected regions. These regions have equal areas, which contain 159 and 154 sources, respectively. Thus, we find that both counts of sources in function of the magnitude are similar.

The completeness of our photometry has been evaluated performing artificial star tests on the SOAR images. The completeness curves are constructed with reference to the centre of each object up to an external radius $r = 1'$, taking regular intervals of $\Delta r = 0.'1$. Artificial stars from 20th to 27th magnitudes in steps of 0.5 mag were added to the same image with the IRAF/ADDSTAR routine using a PSF model derived from several bright and isolated stars. In order to avoid the crowding in the images, only 15 per cent of the original number of sources (stars and galaxies) detected in each region were added per run[10]. After inserting the artificial stars, these artificial images were reduced with the same SExtractor/PSFex routines as the SOAR images. SExtractor/PSFex assigns each detected object a SPREAD_MODEL value. We consider point source candidates those sources with |SPREAD_MODEL| < 0.003 + SPREADERR_MODEL (see text above for details). At last, the artificial stars are considered to be recovered if the input and output positions are closer than 0.′5, and magnitude differences are less than 0.5 mag. The completeness curves as a function of magnitude and distance from the centre of DES 3 are shown in Fig. 4.

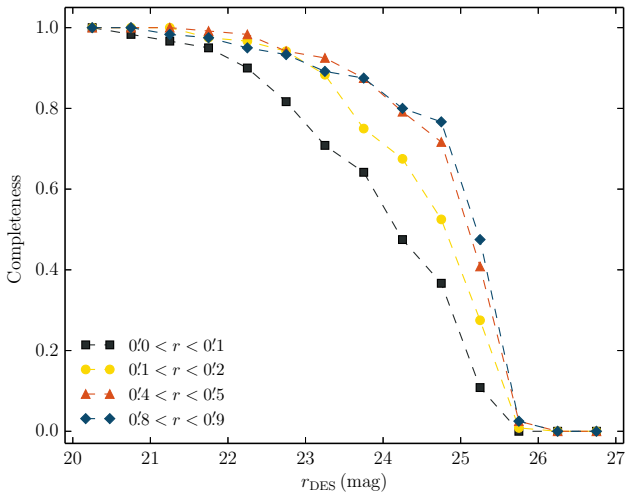

Figure 4. Completeness curves as function of magnitude and radius from the SOAR data. The solid squares represent the completeness at a radius of 0.′1 from the centre of DES 3, the solid dots represent the completeness within an annulus with radius $0.'1 < r < 0.'2$, the solid triangles represent the completeness within an annulus with radius $0.'4 < r < 0.'5$, and the solid diamonds represent the completeness within an annulus with radius $0.'8 < r < 0.'9$.

5 PROPERTIES OF DES 3

In order to better constrain the properties and the nature of DES 3, we use SOAR data, which is ∼ 1 mag deeper than the DES data in the region of this stellar object (see Fig. 3).

We use the maximum likelihood method to determine the structural and CMD parameters for DES 3. We used the EMCEE[11] Python package (Foreman-Mackey et al. 2013), which implements an affine invariant Markov Chain Monte Carlo (MCMC) ensemble sampler, to sample the ln–likelihood function over the parameter space. We have assumed flat priors for all parameters. We take the median of each marginalized posterior distribution function (PDF) to be the best-fitting solution, with uncertainties given by the 16th and 84th percentiles, equivalent to $\pm 1\sigma$ assuming the PDFs are normal distributions.

[10] After multiple runs, we obtained a total of 120 artificial stars in each bin of magnitude.
[11] http://dan.iel.fm/emcee/current/

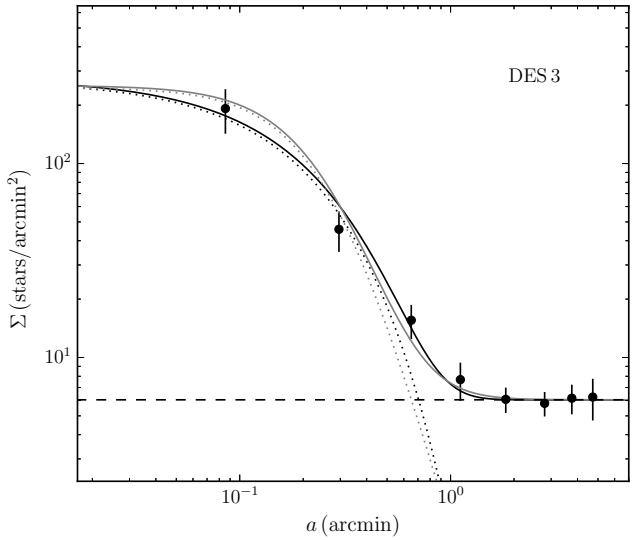

Figure 5. Filled points show a binned version of the density profile of DES 3, constructed in elliptical annuli using the derived structural parameters from the best-fitting exponential profile (see Table 2). The error bars are 1σ Poisson uncertainties. The gray (black) dotted line represent the best-fitting of Plummer (exponential) profile. The horizontal dashed line shows the field background level. The gray (black) solid line is the combination of the background level with the Plummer (exponential) profile.

To estimate the structural parameters, we follow a convention similar to that of Martin et al. (2008). We adopt two different density profile models: exponential and Plummer (Plummer 1911). Due to the small field covered by the SOAR/SOI images, we parameterize both models with just five free parameters. For the exponential profile, the free parameters are: central coordinates α_0 and δ_0, position angle θ, ellipticity ϵ and exponential scale radius r_e. For the Plummer profile, the parameters are: α_0, δ_0, θ, ϵ and Plummer scale radius r_p. The exponential scale radius is related to the half-light radius by the relation $r_h = 1.68 r_e$, whereas the Plummer scale radius, r_p, is equivalent to r_h. The background density, Σ_{bgd}, is determined by using a region outside $r > 1'.5$ around DES 3, which results in 6.1 $\frac{\text{stars}}{\text{arcmin}^2}$, and it is kept constant in the fits.

Fig. 5 shows the binned elliptical density profile of DES 3. To determine the effective area of each elliptical annulus, correcting for the gap and borders of the field covered by the SOI CCDs, we follow the same technique used in Section 3. The best-fitting exponential and Plummer models are also overplotted in this figure. As it can be seen, both the exponential and Plummer profiles adequately describe the observed data. From both models, we find that DES 3 is only slightly elongated ($\epsilon \sim 0.15$) and compact, with a half-light radius of $r_h \sim 0'.3$. Its ellipticity is very similar to Kim 2 ($\epsilon \simeq 0.12$; Kim et al. 2015) and Kim 3 ($\epsilon \simeq 0.17$; Kim et al. 2016a). Only Koposov 1 and Koposov 2, with $r_h \sim 0'.21$ and $r_h \sim 0'.26$, respectively (Koposov et al. 2007), have slightly smaller apparent angular sizes than DES 3. The set of structural parameters for DES 3 is presented in Table 2.

For CMD fits, we first weight each star by the membership probability p taken from the best profile fits. We

Table 2. Properties of DES 3.

Parameters	Exponential profile	Plummer profile	Unit
α_0 ($J2000$)	$21\ 40\ 13.27^{+0.09}_{-0.09}$	$21\ 40\ 13.20^{+0.11}_{-0.11}$	h m s
δ_0 ($J2000$)	$-52\ 32\ 31.20^{+1.50}_{-1.50}$	$-52\ 32\ 30.48^{+1.62}_{-1.68}$	$^\circ\ '\ ''$
l	343.83	343.83	deg
b	-46.51	-46.51	deg
$D_\odot$	$76.2^{+2.8}_{-4.9}$	$76.2^{+3.2}_{-5.3}$	kpc
r_h	$0.31^{+0.04}_{-0.03}$	$0.28^{+0.04}_{-0.03}$	arcmin
r_h	$6.87^{+0.92\,a}_{-0.80}$	$6.21^{+0.92\,a}_{-0.79}$	pc
θ	$-47.0^{+31.1}_{-32.8}$	$-34.9^{+28.8}_{-25.7}$	deg
ϵ	$0.13^{+0.12}_{-0.09}$	$0.17^{+0.13}_{-0.11}$	
Σ_{bgd}	6.1 ± 0.5	6.1 ± 0.5	$\frac{\text{stars}}{\text{arcmin}^2}$
M_V	$-1.8^{+0.4}_{-0.3}$	$-2.0^{+0.4}_{-0.3}$	mag
[Fe/H]	$-1.88^{+0.17}_{-0.13}$	$-1.88^{+0.22}_{-0.15}$	dex
Age	$9.8^{+1.4}_{-1.1}$	$9.8^{+1.4}_{-1.1}$	Gyr
$(m-M)_0$	$19.41^{+0.08}_{-0.14}$	$19.41^{+0.09}_{-0.15}$	mag

Note. [a]Adopting a distance of 76.2 kpc.

then selected all the stars with a threshold of $p \geqslant 0.01$ to fit an isochrone model. The free parameters age, $(m-M)_0$ and metallicity[12], Z, are simultaneously determined by this fitting method (Luque et al. 2016, 2017; Pieres et al. 2016). To investigate a possible range in the CMD parameters, in this analysis we use the selected stars from both exponential and Plummer models.

In the left panel of Fig. 6, we show the CMD of DES 3 from the SOAR data. We show only stars within an ellipse with semimajor axis $a \sim 2r_h$ according to the best-fitting exponential profile (see Table 2). This CMD clearly shows the presence of MS and SGB stars down to $g_{DES} \simeq 25.5$. We can also identify one star that may belong to the HB. In the middle panel of Fig. 6, we show the CMD of background stars contained in an elliptical annulus, centred on DES 3, of equal area as the previous panel, whose inner semimajor axis is equal to $a = 2'$. We used the technique described in Section 3 to determine the effective area of this region. The excess of stars within the isochrone filter seen in the left panel relative to the background is remarkable, attesting not only the physical reality of DES 3, but also allowing a detailed CMD analysis. For comparison, in the right panel of this figure, we show the CMD of DES 3 from the DES data (see right panel of Fig. 2). As expected, the SOAR-based CMD is substantially more informative.

By using the maximum-likelihood method to fit the CMD distribution, we find that DES 3 population is well described by a PARSEC (Bressan et al. 2012) isochrone model with age 9.8 Gyr, $(m-M)_0 \simeq 19.41$, and [Fe/H] $\simeq -1.88$. These parameters agree for both density profile models (exponential and Plummer). This is not surprising given that these models adequately describe the observed density profile of DES 3 (see Fig. 5). The best-fitting isochrone is overplotted in each panel of Fig. 6 as the solid line. In the same figure, an isochrone filter (gray shaded area) is also shown in each panel.

The absolute magnitude (M_V) has been determined using a similar approach as Koposov et al. (2015a). We integrate over all masses along the best-fitting model isochrone

[12] We adopted $Z_\odot = 0.0152$ (Bressan et al. 2012) in order to convert from Z to [Fe/H], assuming [Fe/H] $= \log(Z/Z_\odot)$.

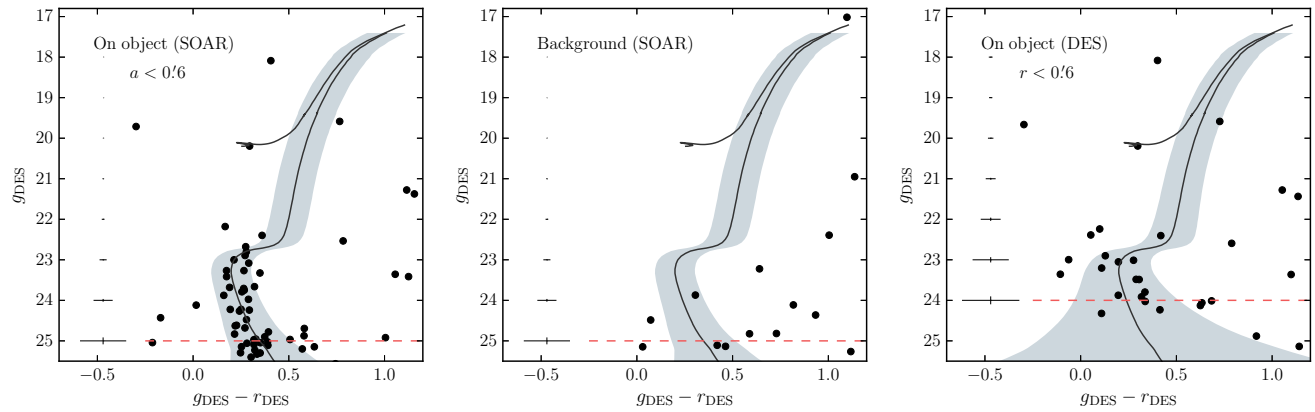

Figure 6. Left panel: CMD of DES 3 from the SOAR data. Only stars inside an ellipse with semi-major axis $a \sim 2r_{\rm h}$ from the centre of DES 3 are shown. In this and the other two panels, the best-fitting PARSEC (Bressan et al. 2012) isochrone derived from the SOAR data is shown. The isochrone filter (gray shaded area) based on photometric uncertainties contains the most likely members. Middle panel: CMD of field stars in an elliptical annulus of equal area on the sky as the previous panel. Right panel: CMD of DES stars within a radius $r = 0.'6$ centred on DES 3. The horizontal dashed line in each panel indicates the faint magnitude limit used. The mean photometric errors in both colour and magnitude are shown in the extreme left of each panel.

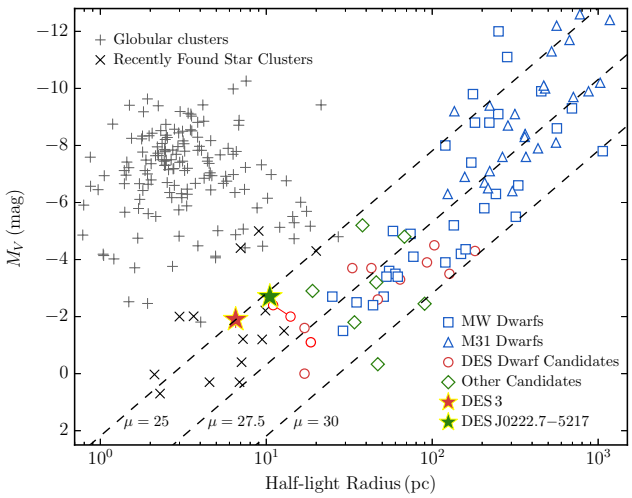

Figure 7. Absolute magnitude as a function of half-light radius. MW globular clusters ('+' symbols; Harris 2010), recently found MW star clusters ('×' symbols; Koposov et al. 2007; Belokurov et al. 2010; Muñoz et al. 2012; Balbinot et al. 2013; Laevens et al. 2014, 2015b; Kim & Jerjen 2015a; Kim et al. 2015, 2016a; Luque et al. 2016, 2017; Koposov et al. 2017), MW dwarf galaxies (blue squares; McConnachie 2012; Bechtol et al. 2015, Drlica-Wagner et al. 2015; Koposov et al. 2015a; Kim et al. 2016b; Torrealba et al. 2016a,b), M 31 dwarf galaxies (blue triangles; McConnachie 2012), previously reported dwarf galaxy candidates in the DES footprint (red circles; Bechtol et al. 2015; Drlica-Wagner et al. 2015; Koposov et al. 2015a; Kim & Jerjen 2015b; Luque et al. 2017), other recently reported dwarf galaxy candidates (green diamonds; Laevens et al. 2015a,b; Martin et al. 2015; Drlica-Wagner et al. 2016; Homma et al. 2016, 2017), DES 3 (red star), and DES J0222.7−5217 (green star) are shown. The red circles connected with a line represent the two previous DES J0222.7−5217 estimates. Note that DES 3 and DES J0222.7−5217 lie inside the region inhabited by faint star clusters. The uncertainties of both objects are comparable to the symbol size. The dashed lines indicate contours of constant surface brightness at $\mu = \{25, 27.5, 30\}$ mag arcsec^{-2}.

assuming a Kroupa (2001) initial mass function, and normalize the number of objects by those observed in the CMD with $r_{\rm DES} < 24.5$ mag and which fall in the isochrone filter. For this estimate, we selected all stars with a membership threshold of $p \geqslant 0.01$ taken from the best profile fits. We corrected the star counts for completeness by weighting each star by $w_i = 1/c_i$, where c_i is the completeness of the star interpolated in magnitude for an interval of radius (see Fig. 4). Due to the low number of stars observed in this type of objects, the estimate of the absolute magnitude has large uncertainty. We then calculate the uncertainty by estimating the upper and lower limits for the integrated V magnitude. We convert the $g_{\rm DES}$ and $r_{\rm DES}$ magnitudes to V magnitude using a SDSS stellar calibration sample[13] and the equation from Jester et al. (2005),

$$\begin{aligned} g_{\rm DES} &= g_{\rm SDSS} - 0.075(g_{\rm SDSS} - r_{\rm SDSS}) + 0.001 \\ r_{\rm DES} &= r_{\rm SDSS} - 0.069(g_{\rm SDSS} - r_{\rm SDSS}) - 0.009 \\ V &= g_{\rm SDSS} - 0.59(g_{\rm SDSS} - r_{\rm SDSS}) - 0.01. \end{aligned} \quad (2)$$

This procedure yields an absolute magnitude of $M_V = -1.8^{+0.4}_{-0.3}$ for the exponencial model and $M_V = -2.0^{+0.4}_{-0.3}$ for the Plummer model. Therefore, in the size-luminosity plane DES 3 lies in the faint star cluster region (see Fig. 7). The luminosity of DES 3 is comparable to Koposov 1 ($M_V \sim -2$; Koposov et al. 2007), DES 1 ($M_V \sim -2.21$; Luque et al. 2016), and Gaia 2 ($M_V \simeq -2$; Koposov et al. 2017). However, the small size ($r_{\rm h} \sim 6.5$ pc) of DES 3 is comparable to Balbinot 1 ($r_{\rm h} \simeq 7.24$ pc; Balbinot et al. 2013), Kim 1 ($r_{\rm h} \simeq 6.9$ pc; Kim & Jerjen 2015a) and Laevens 3 ($r_{\rm h} \simeq 7$ pc; Laevens et al. 2015b).

[13] This new version of transformation equations are based on SDSS Data Release 13 (DR13) and DES Year 3 Annual Release (Y3A1) single-epoch data.

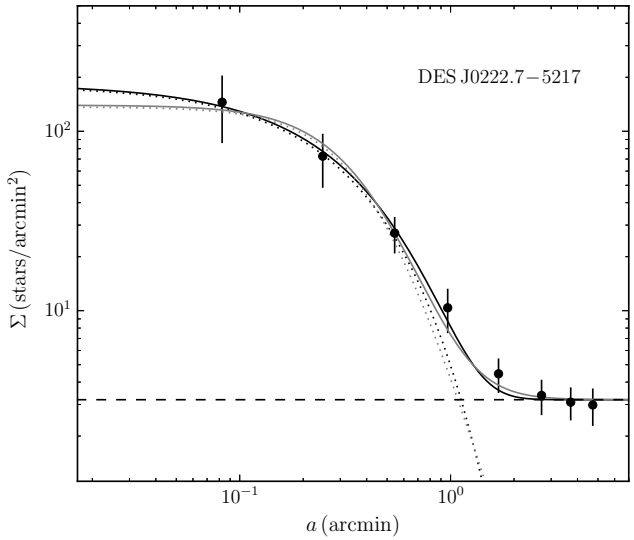

Figure 8. Elliptical surface density profile of DES J0222.7−5217. The filled points represent the observed values with 1σ error bars. The gray (black) dotted line represents the best-fitting of Plummer (exponential) profile. The horizontal dashed line represents the background density. The gray (black) solid line is the combination of the background level with the Plummer (exponential) profile.

Table 3. Properties of DES J0222.7−5217.

Parameters	Exponential profile	Plummer profile	Unit
α_0 ($J2000$)	02 22 45.46$^{+0.16}_{-0.19}$	02 22 45.56$^{+0.20}_{-0.20}$	h m s
δ_0 ($J2000$)	−52 17 06.00$^{+1.44}_{-1.44}$	−52 17 06.06$^{+1.38}_{-1.38}$	° ′ ″
l	274.96	274.96	deg
b	−59.60	−59.60	deg
$D_\odot$	$77.6^{+2.1}_{-3.2}$	$77.6^{+2.1}_{-2.9}$	kpc
r_h	$0.47^{+0.06}_{-0.05}$	$0.46^{+0.06}_{-0.05}$	arcmin
r_h	$10.61^{+1.38}_{-1.21}$ [a]	$10.38^{+1.38}_{-1.19}$ [a]	pc
θ	$-83.2^{+6.7}_{-6.2}$	$-84.6^{+6.1}_{-5.6}$	deg
ϵ	$0.52^{+0.07}_{-0.09}$	$0.53^{+0.07}_{-0.09}$	
Σ_{bgd}	3.2 ± 0.4	3.2 ± 0.4	$\frac{\text{stars}}{\text{arcmin}^2}$
M_V	$-2.6^{+0.5}_{-0.3}$	$-2.8^{+0.4}_{-0.3}$	mag
[Fe/H]	$-2.01^{+0.38}_{-0.12}$	$-2.01^{+0.23}_{-0.12}$	dex
Age	$12.6^{+0.6}_{-0.6}$	$12.6^{+0.3}_{-0.6}$	Gyr
$(m-M)_0$	$19.45^{+0.06}_{-0.09}$	$19.45^{+0.06}_{-0.08}$	mag

Note. [a] Adopting a distance of 77.6 kpc.

6 PROPERTIES OF DES J0222.7−5217

We obtained deeper photometric data for DES J0222.7−5217 with the SOAR telescope. Much like our SOAR imaging of DES 3, our SOAR imaging of DES J0222.7−5217 is ~ 1 mag deeper than the DES data. We apply the same methodology described in Section 5 to provide updated properties of DES J0222.7−5217.

Fig. 8 shows the binned elliptical density profile of DES J0222.7−5217 and the best-fitting exponential and Plummer models. We find that the two models yield very similar structural parameters for this object (see Table 3). Our half-light radius ($r_h \sim 0.'47$) estimate is ~ 12 per cent larger than the value determined by Bechtol et al. (2015, $r_h \simeq 0.'42$), but it is ~ 13 per cent smaller than that determined by Koposov et al. (2015a, $r_h \simeq 0.'54$). We find the system to be more elliptical ($\epsilon \sim 0.53$) and less rotated ($\theta \sim -84$ deg) when compared to the values previously determined ($\epsilon \simeq 0.27$ and $\theta \simeq -97$ deg; Koposov et al. 2015a). In general, our results are in agreement within 1σ with the literature. However, our deeper data has allowed us to better constrain the structural parameters of DES J0222.7−5217 thereby reducing significantly the uncertainties reported in previous work.

The CMD of DES J0222.7−5217 from the SOAR data is shown in the left panel of Fig. 9. The CMD, built with stars within an elliptical annulus of semimajor axis $a \sim 2r_h$ centred on the object, clearly shows MS, MSTO, blue straggler (BS), red giant branch (RGB), and HB stars. Note that there is a potential asymptotic giant branch (AGB) star. The middle panel of Fig. 9 shows the CMD of field stars contained in an elliptical annulus of equal area as the previous panel, whose inner semimajor axis is $a = 2.'5$. For comparison, in the right panel of Fig. 9, we show the CMD of stars within $r = 0.'9$ of the centre of DES J0222.7−5217 from the DES data. Much like SOAR data, this CMD shows BS, RGB, HB, and AGB stars, however, it does not provide enough information about the MSTO and MS stars. Therefore, the SOAR CMD is substantially more informative than the DES CMD.

The best-fitting model isochrone, determined from the our CMD fit method, estimates that DES J0222.7−5217 is located at a distance of $D_\odot \simeq 77.6$ kpc and its stellar population is old ($\simeq 12.6$ Gyr) and metal-poor ([Fe/H] $\simeq -2.01$). Again, the values of these parameters are consistent for both density profile models (see Table 3).

There is a moderate discrepancy between our heliocentric distance estimate and previous estimates of $D_\odot \simeq 95$ kpc (Bechtol et al. 2015) and $D_\odot \simeq 87$ kpc (Koposov et al. 2015a). In fact, this discrepancy may be due mainly to the limiting magnitude used in this work and those used by Bechtol et al. (2015) and Koposov et al. (2015a), since the resolution of the MS and MSTO allows for an improved distance measurement and estimations of the age and metallicity. Unfortunately, the metallicity and age values were not reported by these authors.

We estimate an absolute magnitude for DES J0222.7−5217 of $M_V = -2.6^{+0.5}_{-0.3}$ for the exponential profile and $M_V = -2.8^{+0.4}_{-0.3}$ for the Plummer profile. For these determinations, we used stars brighter than $r_{DES} = 24$ mag and the star counts were corrected for sample incompleteness. These results are in agreement (within 1σ) with those previously reported in the literature, $M_V \simeq -2.4$ (Bechtol et al. 2015) and $M_V \simeq -2.0$ (Koposov et al. 2015a).

With a half-light radius of $r_h \sim 10.5$ pc and a luminosity of $M_V \sim -2.7$, DES J0222.7−5217 lies in a region of size-luminosity space occupied by faint star clusters (see Fig. 7). Interestingly, the half-light radius, ellipticity and absolute magnitude of DES J0222.7−5217 are comparable to those for the star cluster DES 1 ($r_h \simeq 9.88$ pc, $\epsilon \simeq 0.53$ and $M_V \simeq -2.21$; Luque et al. 2016).

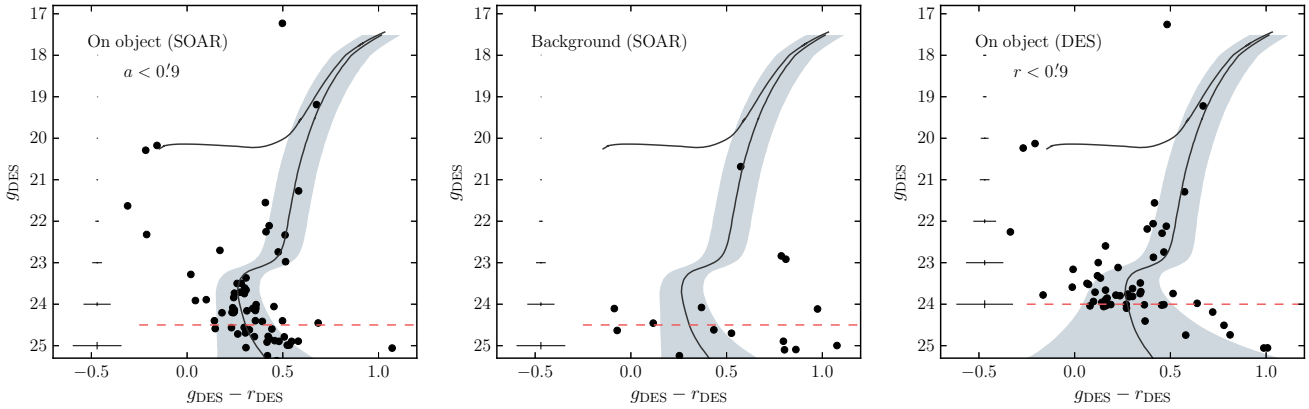

Figure 9. Left panel: CMD of DES J0222.7−5217 from the SOAR data. Only stars inside an ellipse with semi-major axis $a \sim 2r_{\rm h}$ from the centre of DES J0222.7−5217 are shown. In this and the other two panels, the best-fitting PARSEC (Bressan et al. 2012) isochrone derived from the SOAR data is shown. The isochrone filter (gray shaded area) based on photometric uncertainties contains the most likely members. Middle panel: CMD of field stars in an elliptical annulus of equal area on the sky as the previous panel. Right panel: CMD of DES stars within a circle with radius $r = 0.'9$ from the centre of DES J0222.7−5217. The horizontal dashed line in each panel indicates the faint magnitude limit used. The mean photometric errors in both colour and magnitude are shown in the extreme left of each panel.

7 CONCLUSIONS

In this paper, we announce the discovery of a new MW faint star cluster found in DES Y1A1 data, which we name DES 3. Its confirmation as a physical system required deep photometric imaging from the SOAR telescope. This new object adds to the 21 systems that have been found in the first two years of DES (Bechtol et al. 2015; Drlica-Wagner et al. 2015; Koposov et al. 2015a; Kim & Jerjen 2015b; Luque et al. 2016, 2017).

With a MCMC technique and two different density profile models (exponential and Plummer), we find that DES 3 is compact ($r_{\rm h} \sim 0.'3$) and slightly elongated ($\epsilon \sim 0.15$). The morphology of DES 3 does not suggest any evidence of on-going tidal disruption.

By means of an isochrone fit, we derive a distance of $\simeq 76.2$ kpc for DES 3. It is consistent with being dominated by an old ($\simeq 9.8$ Gyr) and metal-poor ([Fe/H] $\simeq -1.88$) population, as commonly observed in MW GCs found in the Galactic halo. However, its small physical size ($r_{\rm h} \sim 6.5$ pc) and low luminosity ($M_V \sim -1.9$) place DES 3 in the region occupied by faint star clusters as observed in Fig. 7. In fact, DES 3 is also one of the faint star clusters with smallest angular size known so far.

With deep SOAR data we found that DES J0222.7−5217 is located at a heliocentric distance of 77.6 kpc, and it hosts an old ($\simeq 12.6$ Gyr) and metal-poor ([Fe/H] $\simeq -2.01$) stellar population. Our best-fitting structural parameters for DES J0222.7−5217 are in general agreement (within 1σ) with the ones derived by Bechtol et al. (2015) and Koposov et al. (2015a), although the heliocentric distance determined in this work points to a closer object than previously reported. The half-light radius ($r_{\rm h} \sim 10.5$ pc) and luminosity ($M_V \sim -2.7$) of DES J0222.7−5217 suggest that it could be classified as a faint star cluster. However, the spectroscopic determination of the radial velocity of DES J0222.7−5217 will be very useful to confirm its nature.

Based on the Magellanic Stream (MS; Nidever et al. 2008) coordinates of DES 3, $(L_{\rm MS}, B_{\rm MS}) = -37.^{\circ}39, -31.^{\circ}69$ and DES J0222.7−5217, $(L_{\rm MS}, B_{\rm MS}) = -26.^{\circ}45, 8.^{\circ}25$, it is interesting to note that DES J0222.7−5217 is in a region where there is a high probability of finding objects associated with the Magellanic Clouds, while DES 3 lies close to a sequence of faint dwarf galaxies, some of which may also be associated with the Clouds (Fig. 10; Jethwa et al. 2016). However, DES 3 lies outside $\pm 20^{\circ}$ of the plane of the Magellanic Stream where the satellites of the LMC would be distributed (Jethwa et al. 2016).

Finally, the discovery of DES 3 in DES data indicates that the census of stellar systems, with characteristics of faint star clusters, is still incomplete. It is likely that additional new stellar systems will be found in future DES data. We have demonstrated the value of deeper imaging to improve the photometric errors and to detect stars at and below the MSTO. This greatly improves the fitting of isochrones, in particular tightening the constraints on the age. For many of these newly discovered objects a wide field is not needed and SOI on the SOAR telescope is an ideal instrument for follow-up studies.

ACKNOWLEDGEMENTS

This paper has gone through internal review by the DES collaboration.

Funding for the DES Projects has been provided by the U.S. Department of Energy, the U.S. National Science Foundation, the Ministry of Science and Education of Spain, the Science and Technology Facilities Council of the United Kingdom, the Higher Education Funding Council for England, the National Center for Supercomputing Applications at the University of Illinois at Urbana-Champaign, the Kavli Institute of Cosmological Physics at the University of Chicago, the Center for Cosmology and Astro-Particle Physics at the Ohio State University, the Mitchell Institute for Fundamental Physics and Astronomy at Texas A&M University, Financiadora de Estudos e Projetos, Fundação

Carlos Chagas Filho de Amparo à Pesquisa do Estado do Rio de Janeiro, Conselho Nacional de Desenvolvimento Científico e Tecnológico and the Ministério da Ciência, Tecnologia e Inovação, the Deutsche Forschungsgemeinschaft and the Collaborating Institutions in the Dark Energy Survey.

The Collaborating Institutions are Argonne National Laboratory, the University of California at Santa Cruz, the University of Cambridge, Centro de Investigaciones Energéticas, Medioambientales y Tecnológicas-Madrid, the University of Chicago, University College London, the DES-Brazil Consortium, the University of Edinburgh, the Eidgenössische Technische Hochschule (ETH) Zürich, Fermi National Accelerator Laboratory, the University of Illinois at Urbana-Champaign, the Institut de Ciències de l'Espai (IEEC/CSIC), the Institut de Física d'Altes Energies, Lawrence Berkeley National Laboratory, the Ludwig-Maximilians Universität München and the associated Excellence Cluster Universe, the University of Michigan, the National Optical Astronomy Observatory, the University of Nottingham, The Ohio State University, the University of Pennsylvania, the University of Portsmouth, SLAC National Accelerator Laboratory, Stanford University, the University of Sussex, Texas A&M University, and the OzDES Membership Consortium.

Based in part on observations at Cerro Tololo Inter-American Observatory, National Optical Astronomy Observatory, which is operated by the Association of Universities for Research in Astronomy (AURA) under a cooperative agreement with the National Science Foundation.

The DES data management system is supported by the National Science Foundation under Grant Numbers AST-1138766 and AST-1536171. The DES participants from Spanish institutions are partially supported by MINECO under grants AYA2015-71825, ESP2015-88861, FPA2015-68048, SEV-2012-0234, SEV-2016-0597, and MDM-2015-0509, some of which include ERDF funds from the European Union. IFAE is partially funded by the CERCA program of the Generalitat de Catalunya. Research leading to these results has received funding from the European Research Council under the European Union's Seventh Framework Program (FP7/2007-2013) including ERC grant agreements 240672, 291329, and 306478. We acknowledge support from the Australian Research Council Centre of Excellence for All-sky Astrophysics (CAASTRO), through project number CE110001020.

This manuscript has been authored by Fermi Research Alliance, LLC under Contract No. DE-AC02-07CH11359 with the U.S. Department of Energy, Office of Science, Office of High Energy Physics. The United States Government retains and the publisher, by accepting the article for publication, acknowledges that the United States Government retains a non-exclusive, paid-up, irrevocable, world-wide license to publish or reproduce the published form of this manuscript, or allow others to do so, for United States Government purposes.

Based on observations obtained at the Southern Astrophysical Research (SOAR) telescope, which is a joint project of the Ministério da Ciência, Tecnologia, e Inovação (MCTI) da República Federativa do Brasil, the U.S. National Optical Astronomy Observatory (NOAO), the University of North Carolina at Chapel Hill (UNC), and Michigan State University (MSU).

REFERENCES

Balbinot E., et al., 2013, ApJ, 767, 101
Balbinot E., et al., 2015, MNRAS, 449, 1129
Bechtol K., et al., 2015, ApJ, 807, 50
Belokurov V., et al., 2010, ApJ, 712, L103
Bertin E., 2011, in Evans I. N., Accomazzi A., Mink D. J., Rots A. H., eds, Astronomical Society of the Pacific Conference Series Vol. 442, Astronomical Data Analysis Software and Systems XX. p. 435
Bertin E., Arnouts S., 1996, A&AS, 117, 393
Bressan A., Marigo P., Girardi L., Salasnich B., Dal Cero C., Rubele S., Nanni A., 2012, MNRAS, 427, 127
Carraro G., Bensby T., 2009, MNRAS, 397, L106
Davis M., Efstathiou G., Frenk C. S., White S. D. M., 1985, ApJ, 292, 371
Desai S., et al., 2012, ApJ, 757, 83
Dooley G. A., Peter A. H. G., Carlin J. L., Frebel A., Bechtol K., Willman B., 2017, preprint, (arXiv:1703.05321)
Drlica-Wagner A., et al., 2015, ApJ, 813, 109
Drlica-Wagner A., et al., 2016, ApJ, 833, L5
Drlica-Wagner A., et al., 2017, preprint, (arXiv:1708.01531)
Fadely R., Willman B., Geha M., Walsh S., Muñoz R. R., Jerjen H., Vargas L. C., Da Costa G. S., 2011, AJ, 142, 88
Flaugher B., et al., 2015, AJ, 150, 150
Font A. S., et al., 2011, MNRAS, 417, 1260
Foreman-Mackey D., Hogg D. W., Lang D., Goodman J., 2013, PASP, 125, 306
Harris W. E., 2010, preprint, (arXiv:1012.3224)
Homma D., et al., 2016, ApJ, 832, 21
Homma D., et al., 2017, preprint, (arXiv:1704.05977)
Ibata R. A., Gilmore G., Irwin M. J., 1994, Nature, 370, 194
Ibata R., Nipoti C., Sollima A., Bellazzini M., Chapman S. C., Dalessandro E., 2013, MNRAS, 428, 3648
Jester S., et al., 2005, AJ, 130, 873
Jethwa P., Erkal D., Belokurov V., 2016, MNRAS, 461, 2212
Kim D., Jerjen H., 2015a, ApJ, 799, 73
Kim D., Jerjen H., 2015b, ApJ, 808, L39
Kim D., Jerjen H., Milone A. P., Mackey D., Da Costa G. S., 2015, ApJ, 803, 63
Kim D., Jerjen H., Mackey D., Da Costa G. S., Milone A. P., 2016a, ApJ, 820, 119
Kim D., et al., 2016b, ApJ, 833, 16
Koposov S., et al., 2007, ApJ, 669, 337
Koposov S. E., Belokurov V., Torrealba G., Evans N. W., 2015a, ApJ, 805, 130
Koposov S. E., et al., 2015b, ApJ, 811, 62
Koposov S. E., Belokurov V., Torrealba G., 2017, MNRAS, 470, 2702
Kroupa P., 2001, MNRAS, 322, 231
Laevens B. P. M., et al., 2014, ApJ, 786, L3
Laevens B. P. M., et al., 2015a, ApJ, 802, L18
Laevens B. P. M., et al., 2015b, ApJ, 813, 44
Law D. R., Majewski S. R., 2010, ApJ, 714, 229
Li T. S., et al., 2017, ApJ, 838, 8
Luque E., et al., 2016, MNRAS, 458, 603
Luque E., et al., 2017, MNRAS, 468, 97
Mackey A. D., Gilmore G. F., 2004, MNRAS, 355, 504
Mackey A. D., van den Bergh S., 2005, MNRAS, 360, 631
Marino A. F., Milone A. P., et al. 2014, MNRAS, 442, 3044
Marino A. F., et al., 2015, MNRAS, 450, 815
Martin N. F., de Jong J. T. A., Rix H.-W., 2008, ApJ, 684, 1075
Martin N. F., et al., 2015, ApJ, 804, L5
McConnachie A. W., 2012, AJ, 144, 4
Milone A. P., et al., 2014, ApJ, 785, 21
Mohr J. J., Armstrong R., Bertin E., et al. 2012, in Society of Photo-Optical Instrumentation Engineers (SPIE) Conference Series. p. 0 (arXiv:1207.3189), doi:10.1117/12.926785

Muñoz R. R., Geha M., Côté P., Vargas L. C., Santana F. A., Stetson P., Simon J. D., Djorgovski S. G., 2012, ApJ, 753, L15
Nidever D. L., Majewski S. R., Butler Burton W., 2008, ApJ, 679, 432
Odenkirchen M., Grebel E. K., Dehnen W., Rix H.-W., Wolf C., Rockosi C. M., 2002, in Grebel E. K., Brandner W., eds, Astronomical Society of the Pacific Conference Series Vol. 285, Modes of Star Formation and the Origin of Field Populations. p. 184
Pieres A., et al., 2016, MNRAS, 461, 519
Plummer H. C., 1911, MNRAS, 71, 460
Rockosi C. M., et al., 2002, AJ, 124, 349
Sales L. V., Navarro J. F., Kallivayalil N., Frenk C. S., 2017, MNRAS, 465, 1879
Schlegel D. J., Finkbeiner D. P., Davis M., 1998, ApJ, 500, 525
Sevilla I., Armstrong R., et al. 2011, preprint, (arXiv:1109.6741)
Simon J. D., et al., 2015, ApJ, 808, 95
Simon J. D., et al., 2017, ApJ, 838, 11
Szabo T., Pierpaoli E., Dong F., Pipino A., Gunn J., 2011, ApJ, 736, 21
The Dark Energy Survey Collaboration 2005, preprint, (arXiv:astro-ph/0510346)
Torrealba G., et al., 2016a, MNRAS,
Torrealba G., Koposov S. E., Belokurov V., Irwin M., 2016b, MNRAS, 459, 2370
Walker M. G., Mateo M., Olszewski E. W., Bailey III J. I., Koposov S. E., Belokurov V., Evans N. W., 2015, ApJ, 808, 108
Walker M. G., et al., 2016, ApJ, 819, 53
White S. D. M., Rees M. J., 1978, MNRAS, 183, 341
Willman B., Strader J., 2012, AJ, 144, 76
York D. G., Adelman J., Anderson Jr. J. E., Anderson S. F., et al. 2000, AJ, 120, 1579
Zinn R., 1985, ApJ, 293, 424
Zinn R., 1993, in Smith G. H., Brodie J. P., eds, Astronomical Society of the Pacific Conference Series Vol. 48, The Globular Cluster-Galaxy Connection. p. 38

[1] *Instituto de Física, UFRGS, Caixa Postal 15051, Porto Alegre, RS - 91501-970, Brazil*
[2] *Laboratório Interinstitucional de e-Astronomia - LIneA, Rua Gal. José Cristino 77, Rio de Janeiro, RJ - 20921-400, Brazil*
[3] *George P. and Cynthia Woods Mitchell Institute for Fundamental Physics and Astronomy, and Department of Physics and Astronomy, Texas A&M University, College Station, TX 77843, USA*
[4] *Fermi National Accelerator Laboratory, P. O. Box 500, Batavia, IL 60510, USA*
[5] *Kavli Institute for Cosmological Physics, University of Chicago, Chicago, IL 60637, USA*
[6] *Department of Physics, University of Surrey, Guildford GU2 7XH, UK*
[7] *Observatório Nacional, Rua Gal. José Cristino 77, Rio de Janeiro, RJ 20921-400, Brazil*
[8] *Cerro Tololo Inter-American Observatory, National Optical Astronomy Observatory, Casilla 603, La Serena, Chile*
[9] *Department of Physics & Astronomy, University College London, Gower Street, London, WC1E 6BT, UK*
[10] *Department of Physics and Electronics, Rhodes University, PO Box 94, Grahamstown, 6140, South Africa*
[11] *LSST, 933 North Cherry Avenue, Tucson, AZ 85721, USA*
[12] *CNRS, UMR 7095, Institut d'Astrophysique de Paris, F-75014, Paris, France*
[13] *Sorbonne Universités, UPMC Univ Paris 06, UMR 7095, Institut d'Astrophysique de Paris, F-75014, Paris, France*
[14] *Department of Astronomy, University of Illinois, 1002 W. Green Street, Urbana, IL 61801, USA*
[15] *National Center for Supercomputing Applications, 1205 West Clark St., Urbana, IL 61801, USA*
[16] *Institut de Física d'Altes Energies (IFAE), The Barcelona Institute of Science and Technology, Campus UAB, 08193 Bellaterra (Barcelona) Spain*
[17] *Institute of Space Sciences, IEEC-CSIC, Campus UAB, Carrer de Can Magrans, s/n, 08193 Barcelona, Spain*
[18] *Kavli Institute for Particle Astrophysics & Cosmology, P. O. Box 2450, Stanford University, Stanford, CA 94305, USA*
[19] *Department of Physics, California Institute of Technology, Pasadena, CA 91125, USA*
[20] *Jet Propulsion Laboratory, California Institute of Technology, 4800 Oak Grove Dr., Pasadena, CA 91109, USA*
[21] *Instituto de Fisica Teorica UAM/CSIC, Universidad Autonoma de Madrid, 28049 Madrid, Spain*
[22] *Department of Astronomy, University of Michigan, Ann Arbor, MI 48109, USA*
[23] *Department of Physics, University of Michigan, Ann Arbor, MI 48109, USA*
[24] *SLAC National Accelerator Laboratory, Menlo Park, CA 94025, USA*
[25] *Center for Cosmology and Astro-Particle Physics, The Ohio State University, Columbus, OH 43210, USA*
[26] *Department of Physics, The Ohio State University, Columbus, OH 43210, USA*
[27] *Astronomy Department, University of Washington, Box 351580, Seattle, WA 98195, USA*
[28] *Australian Astronomical Observatory, North Ryde, NSW 2113, Australia*
[29] *Institució Catalana de Recerca i Estudis Avançats, E-08010 Barcelona, Spain*
[30] *Institute of Cosmology & Gravitation, University of Portsmouth, Portsmouth, PO1 3FX, UK*
[31] *Centro de Investigaciones Energéticas, Medioambientales y Tecnológicas (CIEMAT), Madrid, Spain*
[32] *School of Physics and Astronomy, University of Southampton, Southampton, SO17 1BJ, UK*
[33] *Instituto de Física Gleb Wataghin, Universidade Estadual de Campinas, 13083-859, Campinas, SP, Brazil*
[34] *Computer Science and Mathematics Division, Oak Ridge National Laboratory, Oak Ridge, TN 37831*

This paper has been typeset from a TEX/LATEX file prepared by the author.

Capítulo 5

Considerações finais

Durante a realização deste trabalho, assumimos o desafio de desenvolver, otimizar e aplicar um algoritmo de busca por subestruturas (aglomerados estelares e galáxias anãs) fracas e ultra fracas da Galáxia em grandes levantamentos fotométricos. Um de nossos objetivos é aumentar o censo de satélites da MW e tentar reduzir a grande discrepância que existe entre o número de satélites previstos na literatura e os satélites conhecidos da Galáxia. Também estamos interessados na busca de aglomerados estelares, pois pode nos ajudar a entender o histórico de acúmulo de massa de nossa Galáxia e o sistema de aglomerados estelares associados. Em um esforço paralelo, foram desenvolvidas outras técnicas de busca por subestrutura dentro de nosso grupo de colaboração DES (Bechtol et al. 2015; Drlica-Wagner et al. 2015).

Como o algoritmo apresentado neste trabalho utiliza a rotina SExtractor para detectar sobredensidades nos mapas gerados pelo MF, os parâmetros de detecção do SExtractor são estabelecidos usando 17 objetos estelares (galáxias anãs e aglomerados estelares) previamente identificados nos dados do SDSS. Este conjunto de parâmetros nos permitiu detectar toda a nossa amostra de objetos entre os 10 primeiros lugares do *ranking*, que é baseado no número de vezes que um modelo de SSP é detectado nos mapas de densidade em cada região do céu e cada *kernel* de convolução. Portanto, a combinação do conjunto de parâmetros de detecção e os diferentes tamanhos de *kernel* de convolução são capazes de detectar objetos estelares compactos, assim como estendidos.

Mais tarde, ao aplicar este algoritmo nos dados do DES, o conjunto de parâmetros de detecção foi otimizado usando objetos simulados com características de sistemas estelares fracos. Além disso, um critério de seleção alternativo, com base na significância estatística, foi implementado para aumentar a probabilidade de detectar novos candidatos potenciais. Ambos os critérios de seleção nos fornecem centenas de candidatos que são cuidadosamente analisados para excluir falsos positivos devido a flutuações de campo ou simplesmente aglomerados de galáxias fracas que podem contaminar nossa amostra estelar.

Ao aplicar nosso algoritmo nos dois primeiros anos do DES, nós detectamos os 22 companheiros da MW que foram descobertos recentemente usando este conjunto de dados (Bechtol et al. 2015; Drlica-Wagner et al. 2015; Koposov et al. 2015a; Kim et al. 2015; Kim & Jerjen 2015b; Luque et al. 2016; Luque et al. 2017a; Luque et al.

2017b). Quatro destes sistemas estelares, DES 1, DES J0111−1341, DES J0225+0304, e DES 3, foram identificados apenas por SPARSEX. DES 3 é um dos vários candidatos potenciais selecionados por SPARSEX que exigiu imagens fotométricas mais profundas que as imagens do DES para ser confirmado como um objeto físico.

Através de nossos métodos de caracterização, baseados na máxima verossimilhança, nós estimamos que pelo menos três dos nossos objetos podem ser classificados como aglomerados estelares fracos, DES 1, DES J0111−1341 e DES 3. A natureza de DES J0225+0304 tem que ser confirmada através da determinação espectroscópica da massa dinâmica deste objeto. As nossas estimativas indicam que estes objetos são dominados por populações estelares velhas ($9.8 \lesssim \tau \lesssim 11.7$ G anos), pobres em metais ($-1.88 \lesssim$ [Fe/H] $\lesssim -1.26$) e estão localizados em um domínio de distâncias heliocêntricas entre $23.8 \lesssim D_{\odot} \lesssim 87.1$ kpc.

Foram encontradas várias evidências de uma possível associação de DES J0111−1341 e DES J0225+0304 com a corrente da galáxia anã de Sagitário. Se ambos os objetos forem confirmados como parte da família Sagitário através da determinação espectroscópica da velocidade radial e movimento própio destes sistemas, DES J0111−1341 e DES J0225+0304 seriam os primeiros objetos de baixa luminosidade associados com a corrente de Sagitário. Além disso, se DES J0225+0304 fosse de fato uma galáxia anã, este seria o primeiro caso de um satélite fraco de uma galáxia esferoidal. Este cenário seria muito interessante, pois confirmaria as previsões das simulações de N–corpos, onde sub-halos de matéria escura de baixa massa teriam sido formados. Mas, se isso fosse verdade, então, a seguinte questão poderia ser levantada: se os sub-halos de baixa massa não são eficientes na formação de estrelas, que mecanismos levaram a formação estelar neste sistema?

Embora seja verdade que ambos os critérios de seleção de candidatos levaram à descoberta de vários sistemas estelares, a fim de diminuir o número de falsos positivos selecionados como candidatos, é provável que alguns aperfeiçoamentos ou novos critérios de seleção alternativos possam ser implementados para otimizar ainda mais a detecção de objetos físicos.

Finalmente, na Figura 5.1 mostramos a distribuição dos companheiros da MW, galáxias anãs e aglomerados estelares, nos planos luminosidade vs tamanho e luminosidade vs distância heliocêntrica. Existem duas características importantes a serem observadas nesta figura. A primeira é a clara lacuna em tamanho entre os aglomerados globulares e as galáxias anãs brilhantes ($M_V \lesssim -5$), vista no painel 5.1a, a qual não mais aparece quando consideramos sistemas menos luminosos. Isso indica que a divisão entre aglomerados estelares e galáxias anãs é questionável neste regime de luminosidade. A segunda observação é que o censo de sistemas estelares da MW ainda está longe de ser completo. Isso porque há uma clara ausência de objetos estelares de baixo brilho superficial e/ou distantes e de baixa luminosidade, $D_{\odot} \gtrsim 110$ kpc e $M_V \gtrsim -3$, a qual é vista em ambos os paineis. É necessário mencionar que os sistemas estelares de baixa luminosidade ($M_V \gtrsim -3$) descobertos na área amostrada do DES atingem uma distância heliocêntrica limite da ordem

de $\sim$ 110 kpc. Portanto, segundo a Figura 5.1b, vários dos sistemas estelares de baixa luminosidade além de $\sim$ 110 kpc aguardam serem descobertos. Espera-se que os futuros levantamentos, especialmente o *Large Synoptic Survey Telescope* (LSST), aumente consideravelmente o número de satélites da Galáxia e o número de aglomerados estelares, aumentando, assim, a cobertura dos planos tamanho-luminosidade e distância-luminosidade.

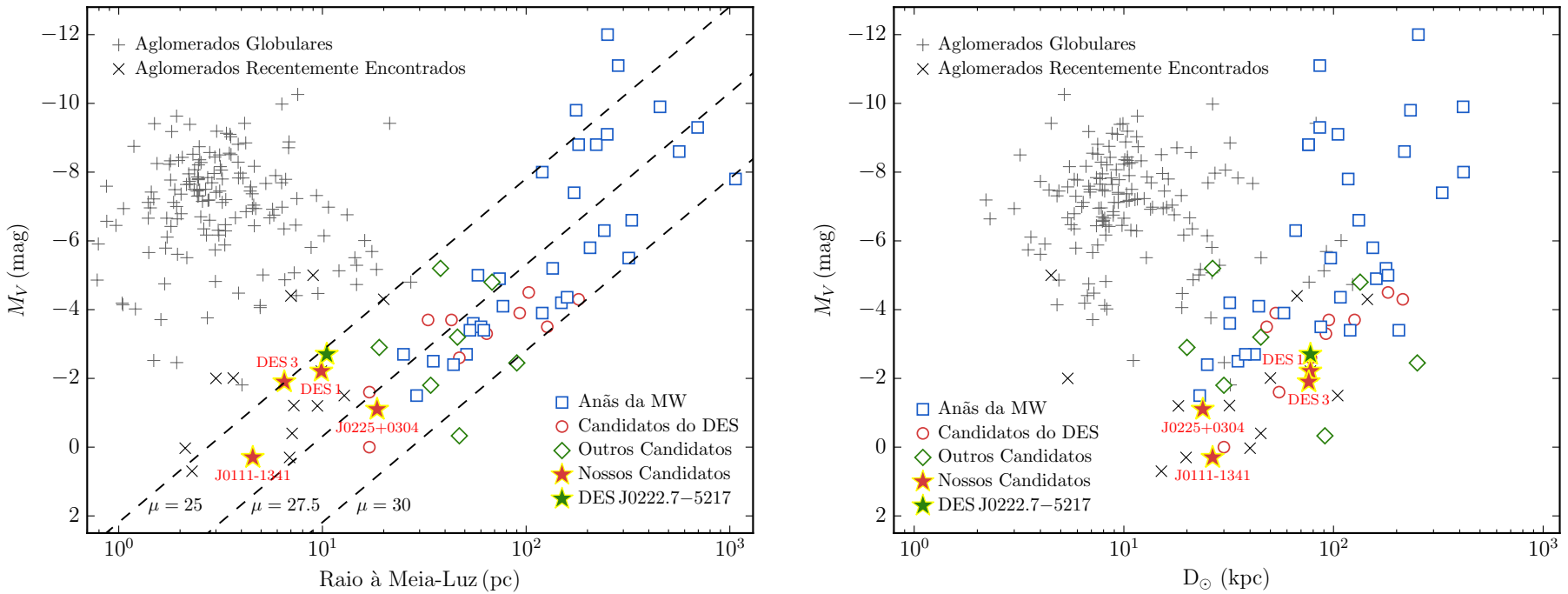

(A) Magnitude absoluta em função do raio à meia-luz

(B) Magnitude absoluta em função da distância heliocêntrica

FIGURA 5.1: Os paineis mostram os aglomerados globulares da MW (símbolos '+'; Harris 2010), aglomerados estelares recentemente encontrados ('×'; Koposov et al. 2007; Belokurov et al. 2010; Muñoz et al. 2012; Balbinot et al. 2013; Laevens et al. 2014; Laevens et al. 2015b; Kim & Jerjen 2015a; Kim et al. 2015; Kim et al. 2016a; Koposov, Belokurov, & Torrealba 2017), galáxias anãs da MW (quadrados azuis; McConnachie 2012; Bechtol et al. 2015, Drlica-Wagner et al. 2015; Koposov et al. 2015a; Kim et al. 2016b; Torrealba et al. 2016a; Torrealba et al. 2016b), candidatos a galáxias anãs previamente identificados na área amostrada do DES (círculos vermelhos; Bechtol et al. 2015; Drlica-Wagner et al. 2015; Koposov et al. 2015a; Kim & Jerjen 2015b), outros candidatos a galáxias anãs recentemente reportados (diamantes verdes; Martin et al. 2015; Laevens et al. 2015a; Laevens et al. 2015b; Drlica-Wagner et al. 2016; Homma et al. 2016; Homma et al. 2017), os nossos candidatos (estrelas vermelhas), e DES J0222.7−5217 (estrela verde). As linhas tracejadas no painel esquerdo indicam os contornos do brilho superficial constante em $\mu = \{25, 27.5, 30\}$ mag arcsec^{-2}.

Capítulo 6

Conclusões

Neste trabalho buscamos contribuir para a detecção de novas subestruturas da MW a fim de aumentar o censo de satélites da Galáxia e tentar reduzir a grande discrepância entre o número de satélites previstos pelas simulações de N–corpos e as galáxias satélites conhecidas. Do mesmo modo, procuramos aumentar o número de aglomerados estelares de baixa luminosidade recentemente descobertos. Para este propósito, nós implementamos um algoritmo estatístico eficiente para detectar subestruturas fracas da Galáxia. O código, chamado SPARSEX, foi validado e otimizado a partir de uma amostra de objetos estelares previamente identificados nos dados do SDSS e objetos simulados, os quais são distantes e fracos.

A aplicação do código SPARSEX nos dados dos dois primeiros anos do DES revelou centenas de candidatos a sistemas estelares. Dezessete desses candidatos foram detectados pelas três técnicas de busca por subestruturas desenvolvidas dentro da colaboração DES. Esses objetos foram publicados em três artigos em 2015 (Bechtol et al. 2015; Drlica-Wagner et al. 2015; Luque et al. 2016), os quais estão anexados neste trabalho. A maioria destes candidatos tem características de galáxias anãs. Até agora, observações estectroscópicas tem confirmado que Reticulum II, Horologium I, Tucana II, Grus I, Tucana III, e Eridanus II são de fato galáxias anãs.

Um dos candidatos selecionados apenas pelo SPARSEX nos dados do primeiro ano do DES é o aglomerado estelar DES 1. Este objeto foi detectado como uma sobredensidade estelar significativa tanto espacialmente quanto no CMD. Os ajustes de isócronas baseados em dois modelos diferentes de perfil de densidade mostram que esse objeto está composto de uma população estelar velha e pobre em metal, comumente observados nos GCs da MW que estão no halo Galáctico.

O ajuste do perfil de King para o DES 1, usando a máxima verossimilhança, leva a um raio de core de $r_c \simeq 0'.08$ e, conseqüentemente, um tamanho físico de $r_h \simeq 9.88\,\mathrm{pc}$. Sua distância heliocêntrica ($\simeq 77.6\,\mathrm{kpc}$) estimada coloca este candidato como um dos aglomerados estelares mais distantes do Sol. Utilizando um método semelhante ao descrito por Koposov et al. (2015a), nós determinamos uma magnitude absoluta de $M_V \simeq -2.21$ para DES 1. Em geral, seu tamanho físico e luminosidade colocam a DES 1 no lugar ocupado por aglomerados estelares de baixa luminosidade (Figura 4.3). DES 1 é também significativamente alongado ($\epsilon \sim 0.6$), o que é evidente não só em ambos perfis de densidade, mas também na distribuição

das estrelas no céu (Figuras 4.1 e 4.2). De fato, DES 1 está entre os aglomerados estelares mais alongados conhecidos até à data. A alta elipticidade inferida sugere que DES 1 está em processo dinâmico de dissolução por efeitos de maré, o que torna este objeto muito interessante para *follow-up* fotométrico e espectroscópico.

Adicionalmente, dois novos candidatos a sistemas estelares foram detectados nos dados dos dois primeiros anos do DES, DES J0111−1341 e DES J0225+0304. Com base em nossos resultados, DES J0111−1341 é um aglomerado estelar compacto ($r_{\rm h} \simeq 4.55\,{\rm pc}$) e ultra fraco ($M_V \simeq +0.3$), enquanto DES J0225+0304 é fraco ($M_V \simeq -1.1$) e tem um tamanho físico ($r_{\rm h} \simeq 18.55\,{\rm pc}$) comparável com uma galáxia anã fraca muito pequena (Figura 4.3). Estes novos sistemas estelares parecem estar a uma distância heliocêntrica de $D_\odot \sim 25\,{\rm kpc}$.

Existem várias linhas de evidências que sugerem que estes candidatos estão associados com a corrente de Sagitário: (1) eles se encontram nas bordas da corrente de Sagitário, como pode ser visto na Figura 4.4 (círculos vermelhos). (2) Os parâmetros do CMD (idade, metalicidade e distância) determinados para estes candidatos estão dentro do intervalo de metalicidade e idade determinada para a corrente de Sagitário usando os mesmos dados DES. (3) As distâncias dos nossos candidatos ao plano orbital de Sagitário, $\sim 1.73\,{\rm kpc}$ (DES J0111−1341) e $\sim 0.50\,{\rm kpc}$ (DES J0225+0304), são comparáveis com as $D_{\rm orb}$ dos GCs certamente associados com a anã de Sagitário, mais especificamente com Terzan 7 e NGC 6715 (Bellazzini, Ferraro, & Ibata 2003). Portanto, nós especulamos que estes candidatos provavelmente estão associados com a corrente de Sagitário. No entanto, a determinação espectroscópica da velocidade radial e movimento próprio destas subestruturas serão muito úteis para confirmar esta hipótese. Além disso, a massa dinâmica, derivada da dispersão da velocidade, nos ajudará a confirmar a natureza dos nossos candidatos. Se todas as nossas hipóteses são confirmadas, DES J0225+0304 seria a primeira galáxia anã fraca associada com a corrente da anã de Sagitário. Também seria o primeiro caso confirmado de um satélite fraco de uma galáxia anã esferoidal.

Quanto às propriedades da corrente em si, os histogramas da contagem de estrelas construídos através da corrente de Sagitário mostram um possível excesso de estrelas em $B \sim 8^\circ$. No entanto, esse excesso putativo é claramente visível apenas quando se utiliza um tamanho de bin de $0\overset{\circ}{.}6 \lesssim \Delta B \lesssim 0\overset{\circ}{.}7$; de outro modo, este último não é evidente. Portanto, neste trabalho, nós não afirmamos a ramificação da corrente. Além disso, nós não encontramos evidências diretas de subestruturas adicionais da corrente além das já existentes.

Os diagramas de Hess descontaminados da corrente de Sagitário permitiram determinar um espalhamento de metalicidade ($-2.18 \lesssim {\rm [Fe/H]} \lesssim -0.95$), bem como um gradiente de distância ($23\,{\rm kpc} \lesssim D_\odot \lesssim 29\,{\rm kpc}$). Isso sugere que a corrente é composto por mais de uma população estelar. Nossa determinação do gradiente de distância é consistente com aquele determinado por Koposov et al. (2012). No entanto, as determinações de metalicidade na literatura sugerem que a corrente de

Sagitário no equador celestial contém estrelas mais ricas em metais do que as determinadas neste trabalho (Koposov et al. 2012; De Boer, Belokurov, & Koposov 2015).

Recentemente, um novo aglomerado estelar foi detectado nos dados do primeiro ano do DES. A confirmação deste candidato como um sistema físico exigiu imagens fotométricas profundas do telescópio SOAR. Este novo objeto, o qual chamamos DES 3, agrega-se aos 21 sistemas estelares que foram encontrados nos dois primeiros anos de DES (Bechtol et al. 2015; Koposov et al. 2015a; Kim & Jerjen 2015b; Drlica-Wagner et al. 2015; Luque et al. 2016; Luque et al. 2017b). Usando o método de máxima verosimilhança e dois diferentes modelos de perfil de densidade (exponencial e Plummer), nós encontramos que o DES 3 é compacto ($r_{\rm h} \sim 0\farcm3$) e ligeiramente alongado ($\epsilon \sim 0.15$). A morfologia do DES 3 não sugere qualquer evidência de disrupção de maré. Por meio de ajustes de isócronas de PARSEC, nós derivamos uma distância de $\simeq 76.2$ kpc para DES 3. Este objeto é consistente com ser dominado por uma população estelar velha ($\simeq 9.8$ G anos) e pobre em metal ($[{\rm Fe/H}] \simeq -1.88$). Seu pequeno tamanho físico ($r_{\rm h} \sim 6.5$ pc) e baixa luminosidade ($M_V \sim -1.9$) colocam o DES 3 na região ocupada por aglomerados estelares fracos como é observado na Figura 4.3. Na verdade, o DES 3 também é um dos aglomerados estelares fracos com menor tamanho angular conhecido até à data.

Além disso, usando dados profundos do SOAR, nós encontramos que DES J0222.7−5217 (Eridanus III), objeto reportado no primeiro ano do DES (Bechtol et al. 2015; Koposov et al. 2015a), está localizado a uma distância heliocêntrica de 77.6 kpc e hospeda uma população estelar velha ($\simeq 12.6$ G anos) e pobre em metal ($[{\rm Fe/H}] \simeq -2.01$). Nossos melhores ajustes dos parâmetros estruturais para DES J0222.7−5217, em geral, estão de acordo (dentro de 1σ) com os aqueles derivados por Bechtol et al. (2015) e Koposov et al. (2015a), embora a distância heliocêntrica determinada neste trabalho aponte para um objeto mais próximo de nós do que o relatado anteriormente na literatura. O raio de à meia-luz ($r_{\rm h} \sim 10.5$ pc) e a luminosidade ($M_V \sim -2.7$) de DES J0222.7−5217 sugerem que este objeto poderia ser classificado como um aglomerado estelar fraco (Figura 4.3). No entanto, a determinação espectroscópica da massa dinâmica de DES J0222.7−5217 será muito útil para confirmar sua natureza.

A descoberta destes novos objetos nos dados do DES indica que o censo de sistemas estelares com baixa luminosidade ainda está incompleto. É provável que novos sistemas estelares adicionais sejam encontrados em futuros dados do DES.

Finalmente, pode-se concluir que o principal objetivo deste trabalho foi plenamente atingido, pois nosso algoritmo SPARSEX é extremamente eficiente em detectar subestruturas de diferente tamanho e de baixa luminosidade. Logicamente, o SPARSEX pode ser facilmente configurado para ser aplicado em futuros grandes levantamentos como o LSST, onde se espera aumentar significativamente o número de satélites da MW como previsto na literatura (Tollerud et al. 2008; Hargis, Willman, & Peter 2014).

Anexo A

Artigos publicados

A.1

Monthly Notices of the ROYAL ASTRONOMICAL SOCIETY

MNRAS **458,** 603–612 (2016) doi:10.1093/mnras/stw302
Advance Access publication 2016 February 9

Digging deeper into the Southern skies: a compact Milky Way companion discovered in first-year Dark Energy Survey data

E. Luque,[1,2⋆] A. Queiroz,[1,2] B. Santiago,[1,2⋆] A. Pieres,[1,2] E. Balbinot,[2,3] K. Bechtol,[4] A. Drlica-Wagner,[5] A. Fausti Neto,[2] L. N. da Costa,[2,6] M. A. G. Maia,[2,6] B. Yanny,[5] T. Abbott,[7] S. Allam,[5] A. Benoit-Lévy,[8] E. Bertin,[9,10] D. Brooks,[8] E. Buckley-Geer,[5] D. L. Burke,[11,12] A. Carnero Rosell,[2,6] M. Carrasco Kind,[13,14] J. Carretero,[15,16] C. E. Cunha,[11] S. Desai,[17,18] H. T. Diehl,[5] J. P. Dietrich,[17,18] T. F. Eifler,[19,20] D. A. Finley,[5] B. Flaugher,[5] P. Fosalba,[15] J. Frieman,[5,21] D. W. Gerdes,[22] D. Gruen,[23,24] G. Gutierrez,[5] K. Honscheid,[25,26] D. J. James,[7] K. Kuehn,[27] N. Kuropatkin,[5] O. Lahav,[8] T. S. Li,[28] M. March,[19] J. L. Marshall,[28] P. Martini,[25,29] R. Miquel,[16,30] E. Neilsen,[5] R. C. Nichol,[31] B. Nord,[5] R. Ogando,[2,6] A. A. Plazas,[20] A. K. Romer,[32] A. Roodman,[11,12] E. Sanchez,[33] V. Scarpine,[5] M. Schubnell,[22] I. Sevilla-Noarbe,[13,33] R. C. Smith,[7] M. Soares-Santos,[5] F. Sobreira,[2,5] E. Suchyta,[25,26] M. E. C. Swanson,[14] G. Tarle,[22] J. Thaler,[34] D. Tucker,[5] A. R. Walker[7] and Y. Zhang[22]

Affiliations are listed at the end of the paper

Accepted 2016 February 5. Received 2016 February 5; in original form 2015 August 8

ABSTRACT

We use the first-year Dark Energy Survey (DES) data down to previously unprobed photometric depths to search for stellar systems in the Galactic halo, therefore complementing the previous analysis of the same data carried out by our group earlier this year. Our search is based on a matched filter algorithm that produces stellar density maps consistent with stellar population models of various ages, metallicities, and distances over the survey area. The most conspicuous density peaks in these maps have been identified automatically and ranked according to their significance and recurrence for different input models. We report the discovery of one additional stellar system besides those previously found by several authors using the same first-year DES data. The object is compact, and consistent with being dominated by an old and metal-poor population. DES 1 is found at high significance and appears in the DES images as a compact concentration of faint blue point sources. Assuming different spatial profile parameterizations, the best-fitting heliocentric distance and total absolute magnitude in the range of 77.6–87.1 kpc and $-3.00 \lesssim M_V \lesssim -2.21$, respectively. The half-light radius of this object, $r_h \sim 10$ pc and total luminosity are consistent with it being a low-mass halo cluster. It is also found to have a very elongated shape ($\epsilon \sim 0.57$). In addition, our deeper probe of DES first-year data confirms the recently reported satellite galaxy candidate Horologium II as a significant stellar overdensity. We also infer its structural properties and compare them to those reported in the literature.

Key words: globular clusters: general – globular clusters: individual (DES 1) – galaxies: dwarf.

1 INTRODUCTION

The census of Milky Way (MW) satellites has grown rapidly over the past 15 yr. Several of these newly found objects are star systems with very low luminosities ($-3.0 \lesssim M_V \lesssim 0$) and small half-light radii

⋆ E-mail: elmer.luque@ufrgs.br (EL); basilio.santiago@ufrgs.br (BS)

(<10 pc), being more consistent with star clusters (Koposov et al. 2007; Belokurov et al. 2010; Fadely et al. 2011; Muñoz et al. 2012; Balbinot et al. 2013). These clusters are thought to be suffering stellar mass-loss via dynamical processes such as tidal disruption or evaporation (Koposov et al. 2007; Kim & Jerjen 2015a). The number of dwarf galaxies around the MW has also increased significantly, from the 11 classical dwarfs known until the late 1990s, up to a total of 27 which were known by early this year (McConnachie 2012), thanks in large part to the Sloan Digital Sky Survey (SDSS). Several of the dwarfs found with SDSS are very low-luminosity systems with high M/L, thus representing some of the most dark matter rich objects (Simon & Geha 2007).

At the larger luminosities typical of globular clusters (GCs), $-10 \lesssim M_V \lesssim -5$ mag, different cluster sub-populations classified by their position, kinematics, and horizontal branch (HB) morphology have been known for several decades (Zinn 1985, 1993; Milone et al. 2014). The so-called young halo clusters may have originated in dwarf galaxies accreted by the MW (Zinn 1993; Lee, Demarque & Zinn 1994; Marino et al. 2014, 2015). Both types of objects seem to share a vast planar structure around the Galaxy, which also encloses several stellar and gaseous streams of clusters and dwarf galaxies (Pawlowski, Pflamm-Altenburg & Kroupa 2012; Pawlowski, McGaugh & Jerjen 2015). The accretion origin of part of the MW system of GCs is also supported by the fact that several of them are found to have positions and kinematics that relate them to the Sagittarius dwarf galaxy (Law & Majewski 2010). On the other hand, at the much lower luminosities ($M_V \geq -7.4$ mag) of the recent satellite discoveries, the very distinction between star clusters and dwarf satellites may become less clear, as attested by their respective loci in size and luminosity space. It is therefore important to pursue a complete census of faint stellar systems inhabiting the Galactic halo, and to characterize them in terms of structure, stellar populations, and dark matter content. Extrapolations of the SDSS results over the entire sky and over the currently known luminosity function of MW dwarfs indicate that this census is still very incomplete (Tollerud et al. 2008; Hargis, Willman & Peter 2014).

A very recent boost to the number of known MW satellites has been brought by the Dark Energy Survey (DES; Abbott et al. 2005). Using the first internal release of DES co-add data (Y1A1), Bechtol et al. (2015) reported on the discovery of eight new MW satellites over a solid angle of 1800 deg^2 in the southern equatorial hemisphere. Six of these systems have sizes and optical luminosities clearly consistent with the low-luminosity dwarfs previously detected in SDSS. The case for the other two objects is less clear. In a parallel effort, Koposov et al. (2015) reported nine new MW satellites using the same DES imaging data, including the same eight and one additional object. One of the objects in common between these two searches, Kim 2, had in fact been previously found by Kim et al. (2015) using data from the Stromlo MW Satellite Survey. In addition to that, Kim & Jerjen (2015b) have discovered yet another object using Y1A1 data, Horologium II. The Panoramic Survey Telescope and Rapid Response System 1 and the Survey of the Magellanic Stellar History have also been responsible for several recent discoveries of MW satellites (Laevens et al. 2014, 2015a,b; Martin et al. 2015).

As described in Bechtol et al. (2015), several complementary search strategies have been implemented within the DES Collaboration to search for stellar sub-structures. In Bechtol et al. (2015), we used a conservative star selection to ensure high stellar purity and completeness as well as a uniform field density over the survey footprint. The present work extends the results presented in Bechtol et al. (2015) by including stars at fainter magnitudes and by considering a broader range of spatial extensions as well as ages and metallicities for the stellar populations composing new satellite systems. We also describe in detail the application of another search algorithm to the Y1A1 co-add data. Together, these analysis updates have enabled the discovery of a new candidate stellar cluster, DES J0034−4902, which we call DES 1, and the confirmation of Horologium II as a physical stellar system. In Section 2, we describe the first-year DES data used. In Section 3, we describe the matched-filter (MF) algorithm applied to find the new systems. The new discovery is presented in Section 4. In Section 5, we report on the detection and characterization of Horologium II. Our final remarks are given in Section 6.

2 DES DATA

DES is a wide-field imaging programme expected to cover about 5000 deg^2 in the *grizY* bands down to $\simeq$ 24.6th magnitude (at S/N $\simeq$ 10 for galaxies in g band; Abbott et al. 2005) in the southern equatorial hemisphere for a period of five years. It uses the Dark Energy Camera (DECam), a 3 deg^2 (2.°2 diameter) mosaic camera with 0.263 arcsec pixels on the prime focus of the Cerro Tololo Inter-American Observatory (CTIO) Blanco 4 m telescope (Flaugher et al. 2015). The DECam images are reduced by the DES Data Management (DESDM) team, which has developed a pipeline to process the data from basic single exposure instrumental corrections all the way to catalogue creation from calibrated co-added images. Here, we use the DES year one co-add catalogue data (Y1A1), taken from 2013 August to 2014 February. For more details on Y1A1 and DESDM, we refer to Sevilla et al. (2011), Mohr et al. (2012), and Gruendl et al., in preparation. The stellar sample used in this work was drawn using the SExtractor parameters `FLAGS`, `SPREAD_MODEL`, and point spread function (`PSF`) magnitudes (Bertin & Arnouts 1996; Desai et al. 2012; Bouy et al. 2013). We used a source quality criterion of `FLAGS` ≤ 3 over the *gri* filters. To avoid issues arising from fitting the `PSF` across variable-depth co-added images, we utilized the weighted-average (`WAVG`) of the `SPREAD_MODEL` measurements from the single-epoch exposures (for details, see Bechtol et al. 2015).

As mentioned above, Kim & Jerjen (2015b) have discovered one stellar object (Horologium II) in Y1A1 data that was not initially identified by Bechtol et al. (2015), or by Koposov et al. (2015). We believe that a primary reason for the non-detection of this object is that most of the probable member stars are fainter than $g \simeq 23$ mag, which is where Bechtol et al. (2015) set the faint-end threshold to search of stellar objects. This conservative threshold was set to ensure high stellar purity and completeness, as well as a uniform field density over the survey footprint.

In this work, we adopt a selection in `WAVG_SPREAD_MODEL` intended to increase stellar completeness relative to the analysis of Bechtol et al. (2015), specifically, i-band |`WAGV_SPREAD_MODEL`| < 0.003 + `WAVG_SPREADERR_MODEL`. A bright (faint) g magnitude limit of `WAVG_MAG_PSF` = 17 (`WAVG_MAG_PSF` = 24) was also applied. The faint limit is 1 mag deeper than used by Bechtol et al. (2015). In order to prevent point sources with extreme colours (including red dwarfs from the Galactic disc) from contaminating the sample, a colour cut at $-0.5 \leq g - r \leq 1.2$ was also used.

We estimated stellar completeness as follows. We first obtained a completeness curve that quantifies the stellar detection efficiency. This is determined by applying DAOPHOT to fields around DES 1 and Horologium II in the g and r filters. The fields selected are sub-regions of the co-added images encompassing

8.67 arcmin × 8.67 arcmin each. We then added sets of 450 artificial stars at a time, with 10 realizations for each filter from $\{g, r\} = 18$ mag down to 27 mag. These artificial stars were reduced in the same way as the real image, following the same IRAF tasks and PSF model. In addition, we have obtained a stellar completeness following the method described in Bechtol et al. (2015). This method basically quantifies the stellar classification efficiency. As in Bechtol et al. (2015), we have created a test sample of high stellar purity around from DES 1 and Horologium II using a colour-based selection ($r - i > 1.7$). We then applied the morphology-based star selection criteria (see above in the text) to evaluate the classification efficiency for the test sample. Our final stellar completeness was the product of the detection and classification efficiencies. The stellar completeness was found to be >90 per cent to $r \sim 23$ mag and falls to ∼80 per cent by $r \sim 24$ mag.

3 SEARCH METHOD

As discussed in Bechtol et al. (2015), several independent search methods were used in the original analysis of Y1A1 data. In this section, we describe in detail a different method, which was the one primarily used in this work.

3.1 Matched filter

The MF technique has several applications for signal processing. In the context of astronomy, it has been used to detect low-density features and populations in imaging data (Rockosi et al. 2002; Szabo et al. 2011). We here use it to search for new star clusters and dwarf galaxies following on the work by Balbinot et al. (2011).

The number of stars as a function of position on the sky (α,δ) and of colour (c) and magnitude (m) may be generally described as

$$n(\alpha, \delta, c, m) = n_{\rm cl}(\alpha, \delta, c, m) + n_{\rm bg}(\alpha, \delta, c, m). \quad (1)$$

The first term on the right-hand side corresponds to the contribution by the cluster (cl) we want to discover, whereas the second term represents the background (bg), which includes foreground halo stars and background unresolved galaxies. We then split these terms into a normalization term and a probability distribution function (PDF):

$$n_{\rm cl}(\alpha, \delta, c, m) = \zeta_{\rm cl}(\alpha, \delta) f_{\rm cl}(c, m), \quad (2)$$

where $\zeta_{\rm cl}$ and $f_{\rm cl}$ are the number normalization and PDF on the colour–magnitude diagram (CMD) plane, respectively, for the stellar population to be found. The stellar population may be extended in space (as in a stream), but we explicitly assume that its CMD is the same everywhere. As for the background stars, Galactic structure models show that both the number density and CMD vary as a function of position across the sky (Jurić et al. 2008). Therefore, we write

$$n_{\rm bg}(\alpha, \delta, c, m) = \zeta_{\rm bg}(\alpha, \delta) f_{\rm bg}(\alpha, \delta, c, m). \quad (3)$$

With the definitions above, equation (1) then becomes

$$n(\alpha, \delta, c, m) = \zeta_{\rm cl}(\alpha, \delta) f_{\rm cl}(c, m) + \zeta_{\rm bg}(\alpha, \delta) f_{\rm bg}(\alpha, \delta, c, m). \quad (4)$$

We bin stars into spatial pixels of area of 1.0 arcmin × 1.0 arcmin, indexed by i, and colour–magnitude bins of 0.01 mag × 0.05 mag, indexed by j. Details on the construction of the $f_{\rm cl}$ and $f_{\rm bg}$ PDFs are found in Section 3.2 and Section 3.3, respectively. With this notation,

$$n(i, j) = \zeta_{\rm cl}(i) f_{\rm cl}(j) + \zeta_{\rm bg}(i) f_{\rm bg}(i, j). \quad (5)$$

Table 1. Parameter grid used to simulate SSPs for the search of star systems in DES Y1 footprint.

Parameters	Lower limit	Upper limit	steps
log(Age)	9.0	10.2	0.3
Distance (kpc)	10	200	10
Metallicity, Z	0.0002, 0.001, and 0.007		

The left-hand side is the expected number of stars in a given spatial pixel and CMD bin. If the actual number of stars observed in a catalogue is $N(i, j)$, the variance between data and model is

$$s^2(i) = \sum_j \frac{[N(i, j) - \zeta_{\rm cl}(i) f_{\rm cl}(j) - \zeta_{\rm bg}(i) f_{\rm bg}(i, j)]^2}{\zeta_{\rm bg}(i) f_{\rm bg}(i, j)}. \quad (6)$$

The term in the denominator expresses the expected Poisson fluctuation in the star counts, which, for simplicity, we assume to be dominated by the background. Minimizing the variance and solving for $\zeta_{\rm cl}(i)$, we have the number of observed stars that, according to the model given by equation (4), are consistent with the model.

$$\zeta_{\rm cl}(i) = \frac{\sum_j N(i, j) f_{\rm cl}(j)/f_{\rm bg}(i, j)}{\sum_j f_{\rm cl}^2(j)/f_{\rm bg}(i, j)} - \frac{\zeta_{\rm bg}(i)}{\sum_j f_{\rm cl}^2(j)/f_{\rm bg}(i, j)}. \quad (7)$$

The output of the filter application is a stellar density map of stars which are probable cluster members stars, i.e. $\zeta_{\rm cl}(i)$. In practice, $f_{\rm bg}(i, j)$ is generated from our target stellar catalogue itself. We do that under the assumption that the contamination by any yet to be detected cluster, dwarf galaxy, or stellar stream, does not change the background PDF. As for the object PDF, we make use of simulated samples, as described in the next sub-section.

3.2 Model grid

Since we do not know a priori what stellar populations we will find, we create a grid of simple stellar populations (SSPs) with the code GENCMD.[1] GENCMD uses PARSEC isochrones by Bressan et al. (2012) for different assumed distances and randomly selects stellar masses following a predefined initial mass function (IMF). Currently, we are adopting a Kroupa (2001) IMF for that purpose. Given each stellar mass, we interpolate among the isochrone entries to draw absolute magnitudes in the desired filters. These are converted into *measured* apparent magnitudes using the assumed model distance, magnitude uncertainties taken from Y1A1, and the reddening map of Schlegel, Finkbeiner & Davis (1998). Positions on the sky may also be simulated assuming different profile models. We simulate several SSPs at various ages, metallicities and distances covering a broader range of isochrone choices, including younger and higher metallicity stellar populations, than those adopted in Bechtol et al. (2015). The parameter grid of these simulations is presented in Table 1.

3.3 Object detection

We apply the MF method as presented in Section 3.1 to the stellar catalogue using each of the SSPs in the model grid described in Section 3.2. In practice, the sky is partitioned into $\sim 10^\circ \times 10^\circ$ cells to account for local variations in the background CMD, which is empirically derived from the stars in each individual cell. This

[1] https://github.com/balbinot/gencmd

procedure generates one density map for every sky cell and for every point in the model grid.

The maps are then convolved with Gaussian spatial kernels of different sizes $\{\sigma = 0.0$ arcmin (no convolution) to $\sigma = 9.0$ arcmin$\}$ to highlight sub-structure on scales typical of star clusters and ultrafaint dwarf galaxies. In particular, smaller spatial kernels are suitable for the detection of more compact stellar systems. Our range of spatial kernel sizes complements those adopted by Bechtol et al. (2015).

As it is not practical to visually inspect all the resulting maps from the large number of combinations of sky cells, SSP models, and spatial convolution kernels, we use the SExtractor code to automatically search for density peaks. In fact, the convolution kernels are applied from within SExtractor itself as we run it on maps of different sky regions resulting from different SSP models. Any object found by SExtractor in each map is recorded. Objects are then ranked according to the number of times they are detected by SExtractor. This is done separately for each sky cell and convolution kernel. The SExtractor parameters for the search were defined as those that maximized the recovery of simulated objects of different sizes and richness inserted into the DES stellar catalogue.

The first 10 objects in each region of the sky and for each convolution kernel are visually inspected to identify the most likely candidates. We visually checked the stellar density map around them, the Poisson statistical significance above the background represented by their associated stellar peak, their number density profile and CMD. The density maps, significance and density profiles provide a basic assessment of the overdensities being found. The CMD helps us judge if this overdensity is consistent with a stellar population. All these diagnostic tools are shown in the next section for DES 1.

We validated the detection method described above, which we call sparsex, by applying it to simulated SSPs superposed on real SDSS and DES data. We also tried to recover faint MW satellites previously discovered in SDSS data. In particular, we have chosen 17 objects found in SDSS data (11 dwarf galaxies and six star clusters) that are characterized as distant and ultrafaint objects. sparsex detected all these stellar objects at the top of the object ranking lists. The rate of success for simulated stellar systems with similar properties was the same. Finally, sparsex detected all eight satellites reported by Bechtol et al. (2015) and Horologium II reported by Kim & Jerjen (2015b). The latter is discussed in more detail in Section 5. The ninth object detected by Koposov et al. (2015) is in a region of Y1 data that is not included in the Y1A1 co-add due to limited coverage in some of the DES filters.

Table 2 lists the central position (α_0, δ_0), the peak Poisson significance and ranking position of objects detected by sparsex in Y1A1 data. The objects reported by Bechtol et al. (2015), Koposov et al. (2015), and Kim & Jerjen (2015b) are shown in the top nine lines in Table 2. DES 1 is also included. The Poisson significance profile is built by taking the ratio of the number of stars internal to each radius[2] r and in excess of the background ($N_{\rm bgd}$), $N_{\rm obj}$, to the expected fluctuation in the same background, i.e., $N_{\rm obj}/\sqrt{N_{\rm bgd}}$. $N_{\rm obj} = (N_{\rm obs} - N_{\rm bgd})$, where $N_{\rm obs}$ is the total number of observed stars. $N_{\rm bgd}$ is computed within an annulus at 30.0 arcmin $< r <$ 34.0 arcmin from each object. To avoid a low stellar statistic, we have built the Poisson significance profile using a cumulative radius of 1.0 arcmin centred on the object.

[2] For the initial sub-structure search, we evaluate the detection significance assuming circular symmetry.

Table 2. sparsex validation in Y1A1 data. Column 1: name of object. Column 2: right ascension. Column 3: declination. Column 4: ranking position. Column 5: peak Poisson significance.

Name	α_0 (deg)	δ_0	Rank	Peak[a] significance
Ret II	53.92	−54.05	1.0	38.9
Eri II	56.09	−43.53	1.0	46.0
Tuc II	343.06	−58.57	1.0	9.1
Hor I	43.87	−54.11	1.0	24.1
Kim 2	317.20	−51.16	1.0	11.3
Pic I	70.95	−50.28	1.0	12.0
Phe II	354.99	−54.41	1.0	11.3
Eri III	35.69	−54.28	5.0	16.1
Hor II	49.12	−50.01	2.0	7.7
DES 1	8.50	−49.04	4.0	11.6

[a] Adopting a circular symmetry.

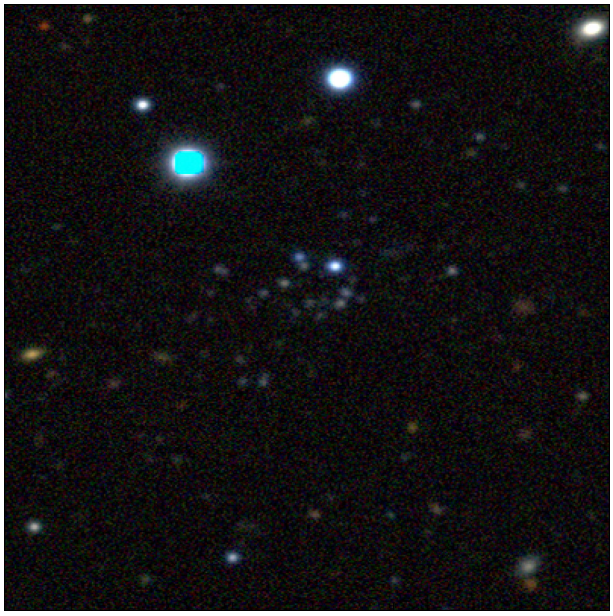

Figure 1. DES co-add image cutout of DES 1 taken from the DES Science portal. The image is 1.78 arcmin × 1.78 arcmin centred on DES 1. The R,G,B channels correspond to the i, r, g bands.

4 DES 1

DES 1 stands out as the most conspicuous new candidate from our search. It is also directly seen as an overdensity of blue stellar sources in the DES co-add images (Fig. 1). In Fig. 2, we show the number density of stars on the sky around this object (top panels). The left-hand panel shows all classified stellar sources, as described in Section 2, and the middle one shows only those close to the best-fitting isochrone (see Fig. 5 and associated discussion later in the text). A clear overdensity is seen in both. The elliptical Poisson significance profile[3] shows the higher peak at about 1.0 arcmin from the centre of DES 1 (see explanation in Section 3.3). This peak is clearly enhanced by filtering the stars according to our best-fitting

[3] The elliptical Poisson significance profile is built using the best-fitting structural parameters presented in this same section. Note that the semimajor axis of the ellipse, which we represent by the letter a, is equivalent to the elliptical radius defined in Martin, de Jong & Rix (2008).

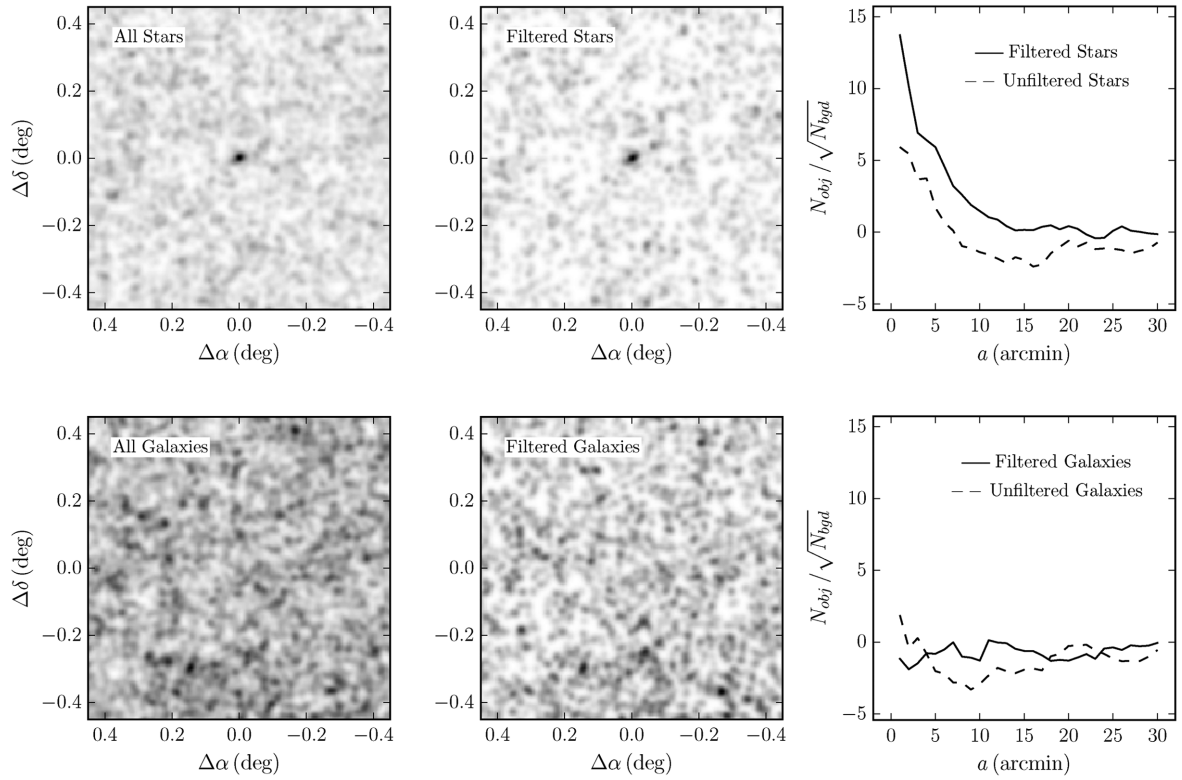

Figure 2. Top left panel: on-sky number density map of stellar sources around candidate DES 1. All stars are included. Top middle panel: similar to previous panel, but now only stars which lie close to the best-fitting isochrone shown in Fig. 5 are used. Density maps have been smoothed with a Gaussian kernel with standard deviation 0.′03. Top right panel: elliptical Poisson significance as a function of semimajor axis a from the centre of DES 1. The solid [dashed] line correspond to isochrone filtered [not pass the filter (unfiltered)] stars as indicated. The corresponding panels at the bottom show the same plots but using the distribution of sources classified as galaxies. *Note*. The centre was determined from the best-fitting exponential profile (see Table 3).

CMD model, discussed below. The bottom panels of Fig. 2 show that there is not an overdensity of galaxies at the position of DES 1, and therefore it is unlikely that misclassified galaxies can account for the apparent stellar overdensity.

We use a maximum-likelihood technique to infer structural and CMD parameters for DES 1. To estimate the structural properties for DES 1, we use two density profile models: exponential and empirical King (King 1962). The exponential profile has five free parameters: central RA (α_0) and Dec. (δ_0), position angle θ, ellipticity ϵ, and exponential scale r_e, whereas the King profile has six free parameters: α_0, δ_0, θ, ϵ, core radius r_c, and tidal radius r_t. We follow the same method as Martin et al. (2008) to find the best-fitting solution. For the parameter uncertainties, we follow a slight variant of Martin et al. (2008). The covariance between parameters is included in our uncertainty calculations via the profile likelihood technique (Sprott 2000, Section 4.5). We use 2σ (95.4 per cent confidence interval) to represent the structural and CMD parameter uncertainties.

The CMD fits weight each star by their membership probabilities p taken from the best profile fits. A threshold of $p \geq 1$ per cent is also adopted. We then use the CMDs of the most likely members of the system to fit an isochrone model, whose free parameters are: age, [Fe/H], $(m - M)_0$, and A_V. The method is based on finding the peak likelihood in a series of model grids, as described in detail by Pieres et al. (2015).

In Fig. 3, we show the results of the exponential profile fit to DES 1. The first three panels show the likelihood values projected on individual planes of this five-dimensional space, which all show well-defined peaks. The corresponding parameter values and their uncertainties (computed as discussed in Martin et al. 2008 and Pieres et al. 2015) are listed in Table 3. The last panel shows the individual stars coded by their membership probabilities. We note that DES 1 is a quite elongated object ($\epsilon \simeq 0.7$). Fig. 4 shows a binned density profile compared to the best-fitting exponential model. In both cases, we took into account the ellipticity. The central density of DES 1 is $\simeq 200$ stars arcmin^{-2}. A clear excess of stars relative to the background is seen out to $\simeq 2.0$ arcmin. In Fig. 4, we also show the best-fitting elliptical King profile. The set of structural parameters and their uncertainties determined by the maximum-likelihood fit are presented in Table 3. A visual inspection in Fig. 4 suggests that the King model best describes the central region and the excess stars seen out to $\simeq 2.0$ arcmin. We compute an estimate of half-mass radius[4] (r_h) for the King profile as follows. First, we have subtracted the expected number of field stars coinciding with DES 1, to obtain N_{DES1}, where N_{DES1} is the number of stars that belong to DES 1. We then compute r_h as the semimajor axis of the ellipse which contains $N_{DES1}/2$ stars (Balbinot et al. 2013). We obtain $r_h = 0.'39^{+0.13}_{-0.02}$ arcmin. The structural parameters determined by the exponential and King profiles agree within the uncertainties (see Table 3), confirming that DES 1 is a compact and quite elongated object.

The CMD for this candidate is shown on the left-hand panel of Fig. 5. Only stars inside an ellipse with semimajor axis $a = 2.0$ arcmin are shown. The middle panel shows the field

[4] To determine the half-mass radius, we have used the parameters determined from the best fit of King profile (see Table 3).

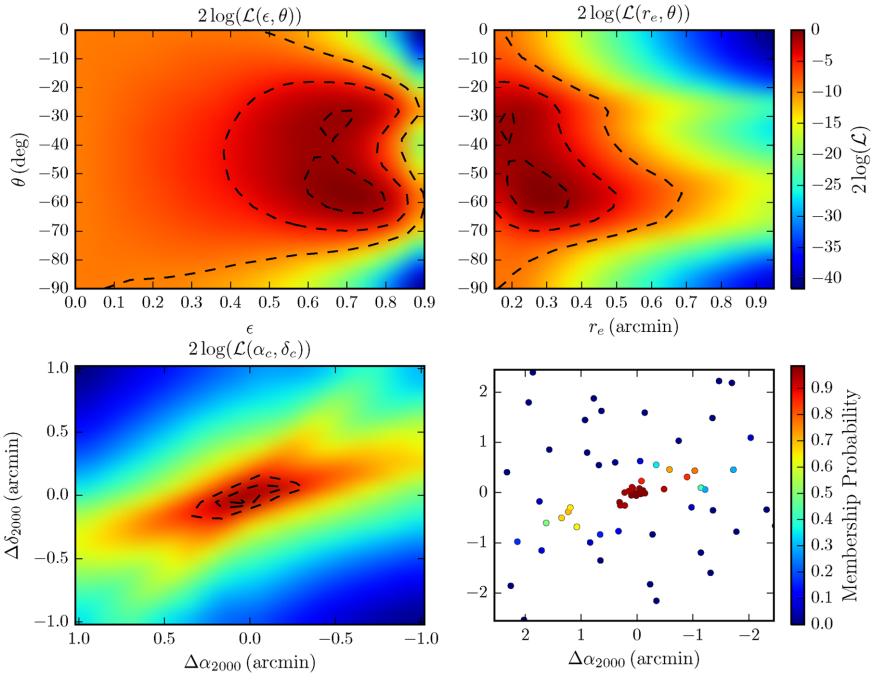

Figure 3. Upper left panel: likelihood map for DES 1 projected on to the position angle and eccentricity plane. Upper right: likelihood map for DES 1 projected on to the position angle and exponential scale plane. Lower left: likelihood map for DES 1 projected on to the central equatorial coordinates plane. The 1σ, 2σ and 3σ contour lines are shown. Lower right: spatial map of stars with probability larger than 1 per cent to belong to DES 1 colour-coded by probability. The best-fitting parameters are listed in Table 3.

Table 3. Properties of DES 1.

Parameters	Exponential profile	King profile
α_0 (J2000)	$00^h33^m59^s.7 \pm 9^s.4$	$00^h33^m59^s.6 \pm 1^s.4$
δ_0 (J2000)	$-49°02'20''.0 \pm 3''.6$	$-49°02'19''.8 \pm 2''.1$
$D_\odot$ (kpc)	∼87.1	∼77.6
r_e	$0'.23 \pm 0'.17$	–
θ (deg)	-57.9 ± 26.0	-52.5 ± 22.8
ϵ	0.69 ± 0.24	0.53 ± 0.22
Σ_c	204.98 ± 35.81	522.38 ± 88.30
Σ_{bgd}	2.02 ± 0.01	2.02 ± 0.01
r_h (arcmin)	0.39 ± 0.28^a	$0.39^{+0.13}_{-0.02}$
r_h (pc)	9.88 ± 7.09^b	$9.88^{+2.93}_{-0.45}{}^c$
M_V	$-3.00^{+0.66}_{-0.41}$	$-2.21^{+0.71}_{-0.48}$
TS	134.7	–
PS	13.7 ± 4.1	11.6 ± 3.9
r_c	–	$0'.08 \pm 0'.04$
r_t	–	$10'.75 \pm 5'.6$
[Fe/H]^d	-1.88 ± 0.25	-1.88 ± 0.05
log (Age)	10.00 ± 0.09	10.00 ± 0.06
A_V	0.0 ± 0.04	0.10 ± 0.07
$(m-M)_0$	19.70 ± 0.36	19.45 ± 0.11

[a]Using the relation, $r_h = 1.68 r_e$ (Martin et al. 2008).
[b]Adopting a distance of 87.1 kpc.
[c]Adopting a distance of 77.6 kpc.
[d]Adopting $Z_\odot = 0.0152$ (Bressan et al. 2012).
Note. Σ_c and Σ_{bgd} have units stars arcmin^{-2}.

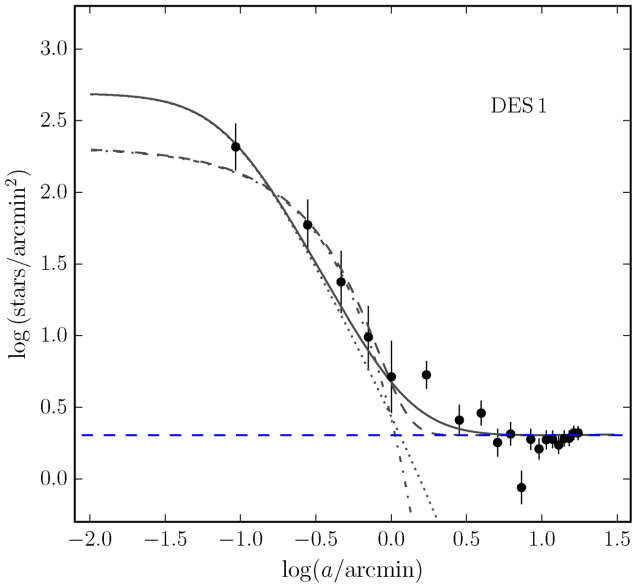

Figure 4. Solid points show a binned version of the density profile of DES 1, constructed in elliptical annuli using the derived structural parameters from the best-fit exponential profile (see Table 3). The error bars are 1σ Poisson uncertainties. Dot–dashed and dotted lines represent the best-fitting of exponential and King profiles, respectively. The horizontal dashed line shows the background level. Dashed and solid lines are the combination of the background level with the exponential and King profiles, respectively.

CMD in an elliptical annulus of equal area, whose inner semi-major axis is equal to 20.0 arcmin. The best-fitting isochrones derived from the likely members based on an exponential profile (solid line) and a King profile (dashed line) are also shown in Fig. 5; parameter values are listed in Table 3. Also shown are the sequences bracketing the best-fitting isochrone fit at a distance of $\sqrt{0.1^2 + \texttt{MAG\_ERR}^2 + \texttt{COL\_ERR}^2}$ on the CMD plane, where `MAG_ERR` and `COL_ERR` are the mean photometric uncertainties along the CMD axes. The 0.1 within the square root is a minimum isochrone mask width. It is meant to avoid

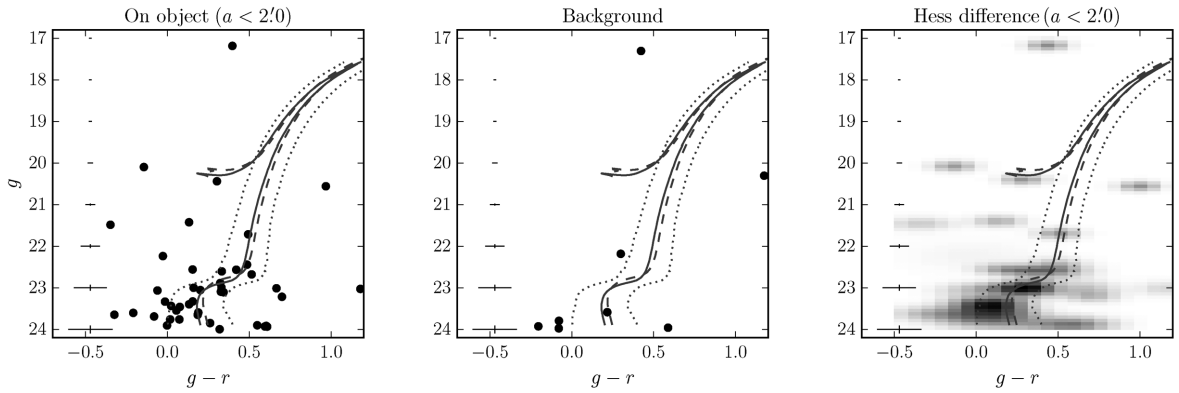

Figure 5. Left-hand panel: CMD of stars within an ellipse with semimajor axis $a = 2.0$ arcmin from the centre of DES 1. The best-fitting PARSEC isochrones (Bressan et al. 2012) are shown, along with ridge lines meant to bracket the most likely members. The best-fitting isochrone derived using the most likely stars as taken from an exponential profile is shown as a solid line, whereas the dashed line represents the best-fitting isochrone using the corresponding stars from a King profile. Middle panel: CMD of background stars in an elliptical annulus of equal area on the sky as the previous panel. Right-hand panel: Hess diagram of the CMD difference between stars within $a = 2.0$ arcmin and background stars (25.0 arcmin $< a <$ 40.0 arcmin). The mean photometric error is shown in the extreme left of each panel.

too narrow isochrone masks at the bright magnitudes, where uncertainties are small. We use the CMD space between them to filter the most likely cluster stars. See the middle and right-hand panels of Fig. 2 for a density map and an elliptical Poisson significance profile of objects inside this isochrone filter, respectively. The CMD difference relative to the background field, in their respective elliptical areas on the sky, is shown as the Hess diagram in the right-hand panel of Fig. 5. The main-sequence turn-off (MSTO) and sub-giant branch (SGB) are clearly visible.

As previously mentioned, we summarize the inferred properties of DES 1 in Table 3. The table lists positions, structural parameters, central (Σ_c) and background (Σ_{bgd}) densities, half-light radius (r_h), distance ($D_\odot$), absolute magnitude (M_V), test statistic (TS), peak Poisson significance (PS) value, core radius (r_c), and tidal radius (r_t), as well as best-fitting CMD parameters. The TS is based on the likelihood ratio between a hypothesis that includes an object versus a field-only hypothesis (see Bechtol et al. 2015).

In addition, we use Y2Q1[5] data to determine the properties of DES 1, but adopting a different magnitude threshold, $g < 23$ mag. By using a maximum-likelihood that simultaneously fits the profile (assuming a Plummer model) and the distance (but assuming an age of 12 Gyrs and a spread in metallicities), we obtain a distance modulus of $(m - M)_0 = 19.6$, in agreement with the method described earlier. The alternative r_h, however, is larger, $r_h \simeq 0.7$ arcmin. This value is marginally consistent with the previous ones reported here. Visual fits were also independently made to the object's CMD. Again, the results agree well with those from the maximum-likelihood fits shown on the table: log(Age) = 9.9, [Fe/H] = -1.88, $A_V = 0.03$, and $(m - M)_0 = 19.9$.

The quoted M_V estimate was computed by integrating overall masses along the best-fitting model isochrone assuming a Kroupa (2001) IMF, and normalizing the number of objects by those observed in the CMD with $r < 23$ mag and which fall in the isochrone filter. The star counts were corrected for sample incompleteness. As we count stars in $r < 23$ mag, the main source of uncertainty is due to small number of stars that are detected in the DES imaging.

[5] The Y2Q1 (year-two quick release) data set consists of exposures taken in the first and second years of DES. This data set is derived from single-epoch imaging instead (for details, see Drlica-Wagner et al. 2015).

We then calculate the uncertainty by estimating the upper and lower limits for the integrated V magnitude. We convert from DES g and r magnitudes to V magnitudes using

$$g_{SDSS} = g_{DES} + 0.104(g_{DES} - r_{DES}) - 0.01$$
$$r_{SDSS} = r_{DES} + 0.102(g_{DES} - r_{DES}) - 0.02$$
$$V = g_{SDSS} - 0.59(g_{SDSS} - r_{SDSS}) - 0.01. \quad (8)$$

This transform from DES g and r magnitudes to V-band magnitudes was derived using an SDSS stellar calibration sample and the equations from Jester et al. (2005) (see Bechtol et al. 2015).

5 HOROLOGIUM II

As mentioned earlier, Kim & Jerjen (2015b) report an additional MW satellite besides those found by Bechtol et al. (2015) and Koposov et al. (2015). Our reanalysis of Y1A1 presented here confirms this object, Horologium II, as a real stellar system. In fact, once we allow for a deeper magnitude threshold, as explained in Section 2, we detect it not only with the method described in Section 3 but also with the maximum-likelihood satellite search method described in Bechtol et al. (2015).

Fig. 6 shows the same information as Fig. 2, but now for Horologium II. A clear overdensity of stars is seen in the density map on the sky. The statistical significance of this overdensity is close to nine times the expected Poisson fluctuation in the background.

We have used the maximum-likelihood method to fit the spatial and CMD distributions as in the previous section. Table 4 lists the structural and isochrone parameters. The latter were derived from the most likely member stars when assuming an exponential profile.

The left-hand panel of Fig. 7 shows the CMD for Horologium II within an ellipse with semimajor axis $a = 3.0$ arcmin. The middle panel shows the background CMD in an elliptical annulus of equal area, whose inner semimajor axis is equal to 30.0 arcmin. The best-fitting PARSEC (Bressan et al. 2012) isochrone is shown. The sequences bracketing the best-fitting isochrone are also shown. The MSTO, SGB, and red giant branch are visible. Note that the CMD of Horologium II shows two stars that may belong to the HB. However, our maximum-likelihood fit assigns these stars a low probability of membership to Horologium II. The right-hand

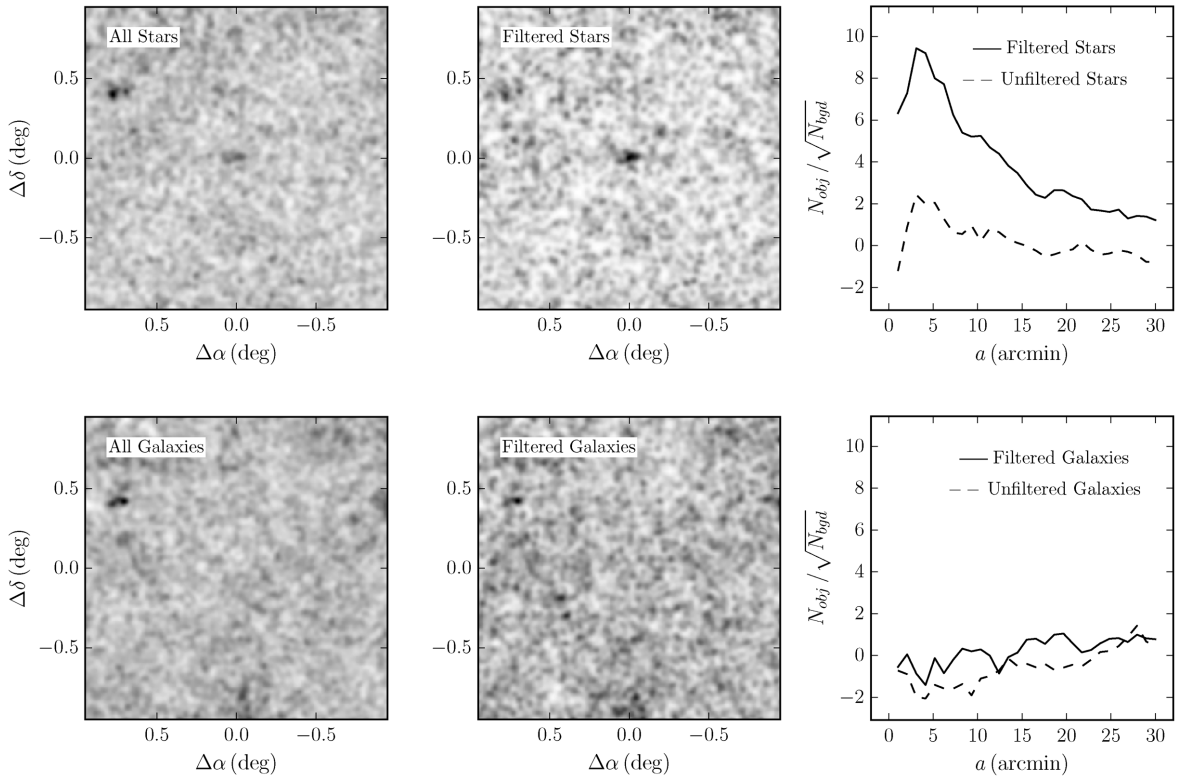

Figure 6. All panels are the same as those in Fig. 2 but now for the Horologium II satellite dwarf.

Table 4. Properties of Horologium II.

Parameters	Exponential profile
α_0 (J2000)	$03^h16^m27^s.6 \pm 39^s.3$
δ_0 (J2000)	$-50°00'36''.7 \pm 46''.7$
$D_\odot$ (kpc)	∼79.4
r_e	$1'.32 \pm 0'.45$
θ (deg)	106.3 ± 55.0
ϵ	0.57 ± 0.41
Σ_c (stars arcmin^{-2})	7.76 ± 1.29
Σ_{bgd} (stars arcmin^{-2})	1.80 ± 0.01
r_h	$2'.22 \pm 0'.76^a$
r_h (pc)	51.27 ± 17.55^b
M_V	$-2.72^{+0.67}_{-0.41}$
TS	52.3
PS	9.2 ± 2.7
[Fe/H]	-1.18 ± 0.24^c
log (Age)	9.88 ± 0.06
A_V	0.03 ± 0.11
$(m - M)_0$	19.50 ± 0.21

[a]Using the relation, $r_h = 1.68 r_e$ (Martin et al. 2008).
[b]Adopting a distance of 79.4 kpc.
[c]Adopting $Z_\odot = 0.0152$ (Bressan et al. 2012).

panel shows a binned elliptical density profile for Horologium II as a function of semimajor axis. For the centre of the overdensity, we adopt the value determined from the maximum-likelihood fit using an exponential profile. The best-fitting elliptical exponential profile is also overplotted.

Our distance, size, ellipticity, and absolute luminosity estimates are in good agreement (within 1σ) with those from the discovery paper by Kim & Jerjen (2015b). The position angle is within 2σ of its quoted value. The largest discrepancies occur for the isochrone parameters. We fit the observed CMD of Horologium II to a younger and more metal-rich PARSEC model than Kim & Jerjen (2015b). However, our likelihood function over the metallicity and age plane exhibits a tail of high-likelihood values towards lower Z and older ages. The discrepancy may also be related to the fact that our listed redenning value comes out of the maximum-likelihood CMD fit, whereas the values from Schlegel et al. (1998) maps (with corrections from Schlafly & Finkbeiner 2011) are used in the discovery paper.

6 CONCLUSIONS

In this paper, we make a deeper probe on the DES Y1A1 catalogue in search for additional Galactic satellites besides those previously reported by the collaboration (Bechtol et al. 2015). We report the discovery of a new stellar system in the MW halo, using catalogues based on first-year data from the DES. We have explored the data at least 1 mag deeper ($g < 24$ mag) than previously done in Bechtol et al. (2015). The candidate adds to the 11 previously identified systems found using DECam images (Bechtol et al. 2015; Kim & Jerjen 2015b; Kim et al. 2015; Koposov et al. 2015; Martin et al. 2015). We also confirm the dwarf galaxy candidate Horologium II, originally discovered by Kim & Jerjen (2015b), as a significant overdensity in the Y1A1 catalogue. Our best-fitting structural parameters for Horologium II are in general agreement with the ones derived by those authors, although the isochrone fit points to a younger and more metal-rich object than previously reported.

DES 1 is detected as a significant stellar overdensity both spatially and on the CMD plane. Isochrone fits based on two different methods show that it is made up of old and metal poor stars, as commonly observed in MW satellites found in the Galactic halo.

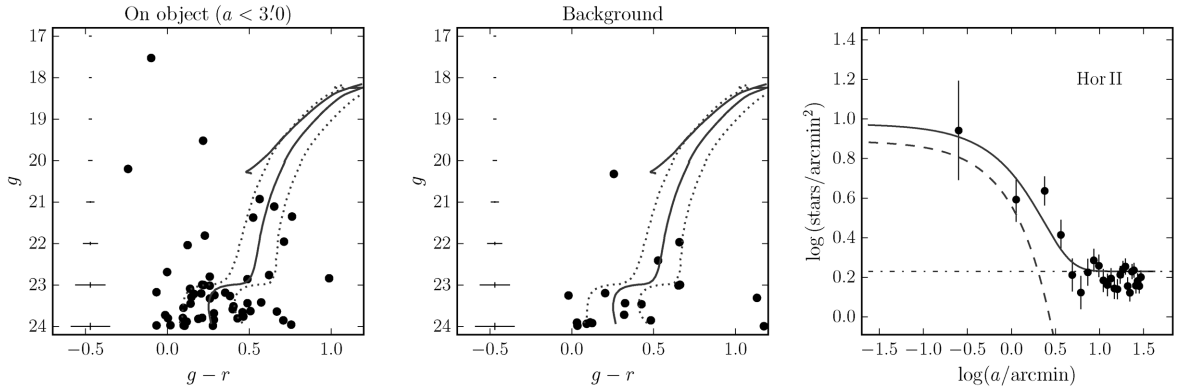

Figure 7. Left-hand panel: CMD of stars within an ellipse with semimajor axis $a = 3.0$ arcmin from the centre of Horologium II. The maximum-likelihood PARSEC (Bressan et al. 2012) isochrone fit is shown, along with ridge lines meant to bracket the most likely members. Middle panel: CMD of background stars in an elliptical annulus of equal area on the sky as the previous panel. The mean photometric error is shown in the extreme left of these panels. Right-hand panel: solid points show the binned density profile for Horologium II, constructed in elliptical annuli using the derived structural parameters from the best-fitting exponential profile (see Table 4). Error bars are based on a Poisson statistics. The dashed line shows the best fit of exponential profile, the horizontal dot–dashed line shows the background level, and the solid line represents the combination of both.

Maximum-likelihood fits of the King profile from DES 1 yield a core radius of $r_c \simeq 0.08$ arcmin, which at a distance $\simeq 77.6$ kpc corresponds to a physical size of $r_h \simeq 9.88$ pc. Its estimated distance places this faint cluster candidate as one of farthest away from the Sun. The absolute magnitude has been determined using a similar approach as Koposov et al. (2015), yielding $M_V \simeq -2.21$ for DES 1. Taken together, the physical size and luminosity place DES 1 in the locus occupied by low-luminosity star clusters. DES 1 is also significantly elongated [$\epsilon \simeq 0.69$ (Exponential), $\epsilon \simeq 0.53$ (King)], something that is apparent not only from the both profiles fit, but also from the distribution of the stars on the sky (Figs 1 and 3). It is, in fact, the most elongated halo cluster known to date, although, given the error bars, its ellipticity is marginally consistent with those of Kim 1, Laevens 3 (see Kim & Jerjen 2015a; Laevens et al. 2015b, respectively). The very high inferred ellipticity suggests that DES 1 is in dynamical process of tidal disruption, despite its large distance, and makes it a very interesting object for deeper imaging and spectroscopic follow up.

Due to the low number of probable member stars detected in the DES imaging, it is difficult to extract more reliable information about DES 1 at this stage. Steps to acquire deeper imaging of this object are already under way.

A search for satellites in data collected by the DES during its second season, including new areas sky, is under way. It is likely that additional new stellar systems will be discovered soon.

ACKNOWLEDGEMENTS

This paper has gone through internal review by the DES collaboration.

Funding for the DES Projects has been provided by the US Department of Energy, the US National Science Foundation, the Ministry of Science and Education of Spain, the Science and Technology Facilities Council of the United Kingdom, the Higher Education Funding Council for England, the National Center for Supercomputing Applications at the University of Illinois at Urbana-Champaign, the Kavli Institute of Cosmological Physics at the University of Chicago, the Center for Cosmology and Astro-Particle Physics at the Ohio State University, the Mitchell Institute for Fundamental Physics and Astronomy at Texas A&M University, Financiadora de Estudos e Projetos, Fundação Carlos Chagas Filho de Amparo à Pesquisa do Estado do Rio de Janeiro, Conselho Nacional de Desenvolvimento Científico e Tecnológico and the Ministério da Ciência, Tecnologia e Inovação, the Deutsche Forschungsgemeinschaft and the Collaborating Institutions in the DES. The DESDM system is supported by the National Science Foundation under Grant Number AST-1138766. The DES participants from Spanish institutions are partially supported by MINECO under grants AYA2012-39559, ESP2013-48274, FPA2013-47986, and Centro de Excelencia Severo Ochoa SEV-2012-0234, some of which include ERDF funds from the European Union.

The Collaborating Institutions are Argonne National Laboratory, the University of California at Santa Cruz, the University of Cambridge, Centro de Investigaciones Enérgeticas, Medioambientales y Tecnológicas-Madrid, the University of Chicago, University College London, the DES-Brazil Consortium, the University of Edinburgh, the Eidgenössische Technische Hochschule (ETH) Zürich, Fermi National Accelerator Laboratory, the University of Illinois at Urbana-Champaign, the Institut de Ciències de l'Espai (IEEC/CSIC), the Institut de Física d'Altes Energies, Lawrence Berkeley National Laboratory, the Ludwig-Maximilians Universität München and the associated Excellence Cluster Universe, the University of Michigan, the National Optical Astronomy Observatory, the University of Nottingham, The Ohio State University, the University of Pennsylvania, the University of Portsmouth, SLAC National Accelerator Laboratory, Stanford University, the University of Sussex, and Texas A&M University.

The DES data management system is supported by the National Science Foundation under Grant Number AST-1138766. The DES participants from Spanish institutions are partially supported by MINECO under grants AYA2012-39559, ESP2013-48274, FPA2013-47986, and Centro de Excelencia Severo Ochoa SEV-2012-0234.

Research leading to these results has received funding from the European Research Council under the European Union's Seventh Framework Programme (FP7/2007-2013) including ERC grant agreements 240672, 291329, and 306478.

EB acknowledges financial support from the European Research Council (ERC-StG-335936, CLUSTERS).

REFERENCES

Abbott T. et al., 2005, (arXiv:Astrophysics:e-prints)
Balbinot E., Santiago B. X., da Costa L. N., Makler M., Maia M. A. G., 2011, MNRAS, 416, 393
Balbinot E. et al., 2013, ApJ, 767, 101
Bechtol K. et al., 2015, ApJ, 807, 50
Belokurov V. et al., 2010, ApJ, 712, L103
Bertin E., Arnouts S., 1996, A&AS, 117, 393
Bouy H., Bertin E., Moraux E., Cuillandre J.-C., Bouvier J., Barrado D., Solano E., Bayo A., 2013, A&A, 554, A101
Bressan A., Marigo P., Girardi L., Salasnich B., Dal Cero C., Rubele S., Nanni A., 2012, MNRAS, 427, 127
Desai S. et al., 2012, ApJ, 757, 83
Drlica-Wagner A. et al., 2015, ApJ, 813, 109
Fadely R., Willman B., Geha M., Walsh S., Muñoz R. R., Jerjen H., Vargas L. C., Da Costa G. S., 2011, AJ, 142, 88
Flaugher B. et al., 2015, AJ, 150, 150
Hargis J. R., Willman B., Peter A. H. G., 2014, ApJ, 795, L13
Jester S. et al., 2005, AJ, 130, 873
Jurić M. et al., 2008, ApJ, 673, 864
Kim D., Jerjen H., 2015a, ApJ, 799, 73
Kim D., Jerjen H., 2015b, ApJ, 808, L39
Kim D., Jerjen H., Milone A. P., Mackey D., Da Costa G. S., 2015, ApJ, 803, 63
King I., 1962, AJ, 67, 471
Koposov S. et al., 2007, ApJ, 669, 337
Koposov S. E., Belokurov V., Torrealba G., Evans N. W., 2015, ApJ, 805, 130
Kroupa P., 2001, MNRAS, 322, 231
Laevens B. P. M. et al., 2014, ApJ, 786, L3
Laevens B. P. M. et al., 2015a, ApJ, 802, L18
Laevens B. P. M. et al., 2015b, ApJ, 813, 44
Law D. R., Majewski S. R., 2010, ApJ, 718, 1128
Lee Y.-W., Demarque P., Zinn R., 1994, ApJ, 423, 248
McConnachie A. W., 2012, AJ, 144, 4
Marino A. F. et al., 2014, MNRAS, 442, 3044
Marino A. F. et al., 2015, MNRAS, 450, 815
Martin N. F., de Jong J. T. A., Rix H.-W., 2008, ApJ, 684, 1075
Martin N. F. et al., 2015, ApJ, 804, L5
Milone A. P. et al., 2014, ApJ, 785, 21
Mohr J. J. et al., 2012, in Radziwill N. M., Chiozzi G., eds, Proc. SPIE Conf. Ser. Vol. 8451, Software and Cyberinfrastructure for Astronomy II. SPIE, Bellingham, p. 84510D
Muñoz R. R., Geha M., Côté P., Vargas L. C., Santana F. A., Stetson P., Simon J. D., Djorgovski S. G., 2012, ApJ, 753, L15
Pawlowski M. S., Pflamm-Altenburg J., Kroupa P., 2012, MNRAS, 423, 1109
Pawlowski M. S., McGaugh S. S., Jerjen H., 2015, MNRAS, 453, 1047
Pieres A. et al., 2015, preprint (arXiv:1512.01032)
Rockosi C. M. et al., 2002, AJ, 124, 349
Schlafly E. F., Finkbeiner D. P., 2011, ApJ, 737, 103
Schlegel D. J., Finkbeiner D. P., Davis M., 1998, ApJ, 500, 525
Sevilla I. et al., 2011, preprint (arXiv:1109.6741)
Simon J. D., Geha M., 2007, ApJ, 670, 313
Sprott D. A., 2000, Statistical Inference in Science. Springer-Verlag, Berlin
Szabo T., Pierpaoli E., Dong F., Pipino A., Gunn J., 2011, ApJ, 736, 21
Tollerud E. J., Bullock J. S., Strigari L. E., Willman B., 2008, ApJ, 688, 277
Zinn R., 1985, ApJ, 293, 424
Zinn R., 1993, in Smith G. H., Brodie J. P., eds, ASP Conf. Ser. Vol. 48, The Globular Cluster-Galaxy Connection. Astron. Soc. Pac., San Francisco, p. 38

[1]*Instituto de Física, UFRGS, Caixa Postal 15051, Porto Alegre, RS 91501-970, Brazil*
[2]*Laboratório Interinstitucional de e-Astronomia – LIneA, Rua Gal. José Cristino 77, Rio de Janeiro, RJ 20921-400, Brazil*
[3]*Department of Physics, University of Surrey, Guildford GU2 7XH, UK*
[4]*Kavli Institute for Cosmological Physics, University of Chicago, Chicago, IL 60637, USA*
[5]*Fermi National Accelerator Laboratory, PO Box 500, Batavia, IL 60510, USA*
[6]*Observatório Nacional, Rua Gal. José Cristino 77, Rio de Janeiro, RJ 20921-400, Brazil*
[7]*Cerro Tololo Inter-American Observatory, National Optical Astronomy Observatory, Casilla 603, La Serena, Chile*
[8]*Department of Physics and Astronomy, University College London, Gower Street, London WC1E 6BT, UK*
[9]*CNRS, UMR 7095, Institut d'Astrophysique de Paris, F-75014 Paris, France*
[10]*Sorbonne Universités, UPMC Univ Paris 06, UMR 7095, Institut d'Astrophysique de Paris, F-75014, Paris, France*
[11]*Kavli Institute for Particle Astrophysics & Cosmology, PO Box 2450, Stanford University, Stanford, CA 94305, USA*
[12]*SLAC National Accelerator Laboratory, Menlo Park, CA 94025, USA*
[13]*Department of Astronomy, University of Illinois, 1002 W. Green Street, Urbana, IL 61801, USA*
[14]*National Center for Supercomputing Applications, 1205 West Clark St, Urbana, IL 61801, USA*
[15]*Institut de Ciéncies de l'Espai, IEEC-CSIC, Campus UAB, Carrer de Can Magrans, s/n, E-08193 Bellaterra, Barcelona, Spain*
[16]*Institut de Física d'Altes Energies, Universitat Autònoma de Barcelona, E-08193 Bellaterra, Barcelona, Spain*
[17]*Excellence Cluster Universe, Boltzmannstr. 2, D-85748 Garching, Germany*
[18]*Faculty of Physics, Ludwig-Maximilians University, Scheinerstr. 1, D-81679 Munich, Germany*
[19]*Department of Physics and Astronomy, University of Pennsylvania, Philadelphia, PA 19104, USA*
[20]*Jet Propulsion Laboratory, California Institute of Technology, 4800 Oak Grove Dr., Pasadena, CA 91109, USA*
[21]*Kavli Institute for Cosmological Physics, University of Chicago, Chicago, IL 60637, USA*
[22]*Department of Physics, University of Michigan, Ann Arbor, MI 48109, USA*
[23]*Max Planck Institute for Extraterrestrial Physics, Giessenbachstrasse, D-85748 Garching, Germany*
[24]*Universitäts-Sternwarte, Fakultät für Physik, Ludwig-Maximilians Universität München, Scheinerstr. 1, D-81679 München, Germany*
[25]*Center for Cosmology and Astro-Particle Physics, The Ohio State University, Columbus, OH 43210, USA*
[26]*Department of Physics, The Ohio State University, Columbus, OH 43210, USA*
[27]*Australian Astronomical Observatory, North Ryde, NSW 2113, Australia*
[28]*George P. and Cynthia Woods Mitchell Institute for Fundamental Physics and Astronomy, and Department of Physics and Astronomy, Texas A&M University, College Station, TX 77843, USA*
[29]*Department of Astronomy, The Ohio State University, Columbus, OH 43210, USA*
[30]*Institució Catalana de Recerca i Estudis Avançats, E-08010 Barcelona, Spain*
[31]*Institute of Cosmology and Gravitation, University of Portsmouth, Portsmouth PO1 3FX, UK*
[32]*Department of Physics and Astronomy, Pevensey Building, University of Sussex, Brighton BN1 9QH, UK*
[33]*Centro de Investigaciones Energéticas, Medioambientales y Tecnológicas (CIEMAT), Madrid, Spain*
[34]*Department of Physics, University of Illinois, 1110 W. Green St, Urbana, IL 61801, USA*

This paper has been typeset from a TEX/LATEX file prepared by the author.

A.2

Monthly Notices of the ROYAL ASTRONOMICAL SOCIETY

MNRAS **468,** 97–108 (2017) doi:10.1093/mnras/stx405
Advance Access publication 2017 February 17

The Dark Energy Survey view of the Sagittarius stream: discovery of two faint stellar system candidates

E. Luque,[1,2⋆] A. Pieres,[1,2] B. Santiago,[1,2⋆] B. Yanny,[3] A. K. Vivas,[4] A. Queiroz,[1,2] A. Drlica-Wagner,[3] E. Morganson,[5] E. Balbinot,[6] J. L. Marshall,[7] T. S. Li,[7] A. Fausti Neto,[2] L. N. da Costa,[2,8] M. A. G. Maia,[2,8] K. Bechtol,[9] A. G. Kim,[10] G. M. Bernstein,[11] S. Dodelson,[3,9] L. Whiteway,[12] H. T. Diehl,[3] D. A. Finley,[3] T. Abbott,[4] F. B. Abdalla,[12,13] S. Allam,[3] J. Annis,[3] A. Benoit-Lévy,[12,14,15] E. Bertin,[14,15] D. Brooks,[12] D. L. Burke,[16,17] A. Carnero Rosell,[2,8] M. Carrasco Kind,[5,18] J. Carretero,[19,20] C. E. Cunha,[16] C. B. D'Andrea,[21,22] S. Desai,[23] P. Doel,[12] A. E. Evrard,[24,25] B. Flaugher,[3] P. Fosalba,[19] D. W. Gerdes,[25] D. A. Goldstein,[10,26] D. Gruen,[16,17] R. A. Gruendl,[5,18] G. Gutierrez,[3] D. J. James,[4] K. Kuehn,[27] N. Kuropatkin,[3] O. Lahav,[12] P. Martini,[28,29] R. Miquel,[20,30] B. Nord,[3] R. Ogando,[2,8] A. A. Plazas,[31] A. K. Romer,[32] E. Sanchez,[33] V. Scarpine,[3] M. Schubnell,[25] I. Sevilla-Noarbe,[33] R. C. Smith,[4] M. Soares-Santos,[3] F. Sobreira,[2,34] E. Suchyta,[35] M. E. C. Swanson,[5] G. Tarle,[25] D. Thomas[21] and A. R. Walker[4]

Affiliations are listed at the end of the paper

Accepted 2017 February 14. Received 2017 February 14; in original form 2016 August 13

ABSTRACT

We report the discovery of two new candidate stellar systems in the constellation of Cetus using the data from the first two years of the Dark Energy Survey (DES). The objects, DES J0111−1341 and DES J0225+0304, are located at a heliocentric distance of ∼25 kpc and appear to have old and metal-poor populations. Their distances to the Sagittarius orbital plane, ∼1.73 kpc (DES J0111−1341) and ∼0.50 kpc (DES J0225+0304), indicate that they are possibly associated with the Sagittarius dwarf stream. The half-light radius ($r_h \simeq 4.55$ pc) and luminosity ($M_V \simeq +0.3$) of DES J0111−1341 are consistent with it being an ultrafaint stellar cluster, while the half-light radius ($r_h \simeq 18.55$ pc) and luminosity ($M_V \simeq -1.1$) of DES J0225+0304 place it in an ambiguous region of size–luminosity space between stellar clusters and dwarf galaxies. Determinations of the characteristic parameters of the Sagittarius stream, metallicity spread ($-2.18 \lesssim$ [Fe/H] $\lesssim -0.95$) and distance gradient ($23\,\mathrm{kpc} \lesssim D_\odot \lesssim 29\,\mathrm{kpc}$), within the DES footprint in the Southern hemisphere, using the same DES data, also indicate a possible association between these systems. If these objects are confirmed through spectroscopic follow-up to be gravitationally bound systems and to share a Galactic trajectory with the Sagittarius stream, DES J0111−1341 and DES J0225+0304 would be the first ultrafaint stellar systems associated with the Sagittarius stream. Furthermore, DES J0225+0304 would also be the first confirmed case of an ultrafaint satellite of a satellite.

Key words: globular clusters: general – galaxies: dwarf.

1 INTRODUCTION

The Sagittarius dwarf galaxy was discovered relatively recently due to its position on the far side of the Milky Way (MW; Ibata, Gilmore & Irwin 1994). Its extended morphology towards the MW plane suggested the existence of extra tidal features (Johnston, Spergel

⋆ E-mail: elmer.luque@ufrgs.br. (EL); basilio.santiago@ufrgs.br (BS)

& Hernquist 1995; Lynden-Bell & Lynden-Bell 1995; Mateo et al. 1996). The Two Micron All-Sky Survey (2MASS) and the Sloan Digital Sky Survey (SDSS) made it clear that this dwarf is responsible for the most conspicuous tidal stellar substructure present in the Galactic halo (Newberg et al. 2002; Majewski et al. 2003).

Deeper photometric and spectroscopic data, specifically with SDSS, have allowed the morphological, structural and kinematic properties of the Sagittarius stream to be disentangled from MW substructure (Newberg et al. 2003, 2007; Belokurov et al. 2006, 2014; Yanny et al. 2009). This wealth of data was used by Law & Majewski (2010a) to model the MW gravitational potential and to find some evidence in favour of triaxiality (i.e. flattening).

Belokurov et al. (2006) demonstrated that the Sagittarius stream in the northern Galactic hemisphere bifurcates into brighter and fainter components separated by up to $\sim 15^\circ$ on the sky. More recently, Koposov et al. (2012) have shown that a bifurcation also appears in the Sagittarius tails in the southern Galactic hemisphere. This fainter branch had comparatively more metal-poor stars and a simpler mix of stellar populations than the main structure. The southern bifurcation, extending at least 30° on the sky, was confirmed using Panoramic Survey Telescope and Rapid Response System 1 (Pan-STARRS) data by Slater et al. (2013). The authors found evidence that the fainter substructure is 5 kpc closer to the Sun than the brighter one, similar to the behaviour seen in the northern Galactic hemisphere. They also argue that the distance between the streams agrees with the predictions of the *N*-body simulations presented by Law & Majewski (2010a). Based on their model, the same authors also identify MW satellites, dwarf galaxies and globular clusters (GCs) that may be physically associated with the Sagittarius dwarf. In particular, the Sagittarius dwarf has been observed to contain at least four GCs (NGC 6715, Arp 2, Terzan 7 and Terzan 8) within its main body (Da Costa & Armandroff 1995; Bellazzini, Ferraro & Ibata 2003). However, different studies have proposed several GCs to likely be associated with the Sagittarius stream (e.g. Bellazzini et al. 2003; Dotter et al. 2010; Forbes & Bridges 2010; Dotter, Sarajedini & Anderson 2011; Carballo-Bello et al. 2014; Sbordone et al. 2015). Even open clusters (OCs) have been suggested as members of the Sagittarius family (e.g. Carraro et al. 2004; Carraro & Bensby 2009). It is likely that additional GCs and OCs may have been stripped from Sagittarius during prolonged interaction with the MW and now lie scattered throughout the Galactic halo. In a recent analysis based on new models of the tidal disruption of the Sagittarius dwarf, Law & Majewski (2010b) found that several of the candidates proposed in the literature have non-negligible probability of belonging to the Sagittarius dwarf. However, calculating the expected quantity of false associations in the sample, they proposed that only five GCs (Arp 2, NGC 6715, NGC 5634, Terzan 8 and Whiting 1) are almost certainly associated with the Sagittarius dwarf; an additional four (Berkeley 29, NGC 5053, Pal 12 and Terzan 7) are moderately likely to be associated.

It now appears that stars left over from the accretion of the Sagittarius dwarf entirely wrap around the Galactic Centre. Recent spectroscopic analysis by Hyde et al. (2015), for instance, finds over 100 good stream candidates with metallicities in the range $-0.97 < [\mathrm{Fe/H}] < -0.59$ spread over 142°. De Boer, Belokurov & Koposov (2015) analyse the stream in the SDSS Stripe 82 region with both photometry and spectroscopy, finding a tight age–metallicity relation. They also show that the fainter branch is old (>9 Gyr) and metal-poor ($[\mathrm{Fe/H}] < -1.3$), while the dominant branch has stars covering large ranges in age and metallicity.

In this paper, we explore the tidal tails of Sagittarius within the Dark Energy Survey (DES; The Dark Energy Survey Collaboration 2005) footprint in the Southern hemisphere. This data set is $\sim$2 mag (in the *g* band) deeper than other large surveys covering this part of the sky (e.g. Pan-STARRS or SDSS). DES is a wide-field imaging survey of the Southern hemisphere that has recently finished its third year of data taking, from an expected total of 5 yr (Diehl et al. 2016). We also identify two previously undiscovered ultrafaint stellar systems whose inferred ages, metallicities and distances make it likely that they are associated with Sagittarius. In Section 2, we present the DES data. In Section 3, we discuss the properties of the Sagittarius stream as probed by those data. In Section 4, we present a method used to search for star clusters and other stellar systems in the DES footprint. In Section 5, we report on the identification of the two star system candidates whose properties make them likely to have been stripped from the Sagittarius dwarf. If DES J0111−1341 is confirmed to be a stellar cluster, it will be named DES 2, whereas DES J0225+0304 will be named Cetus III if found to be a dwarf galaxy. Our final remarks are then presented in Section 6.

2 DES DATA

DES is a wide-field optical imaging survey of 5000 deg^2 in the southern equatorial hemisphere in the *grizY* bands. DES is scheduled for 525 nights distributed over 5 yr. It uses the Dark Energy Camera (DECam), a 3 deg^2 ($2.^\circ2$ diameter) mosaic camera with 0.263 arcsec pixels on the prime focus of the 4-metre Blanco telescope at Cerro Tololo Inter-American Observatory (Flaugher et al. 2015). The DES data management (DESDM) uses an image-processing pipeline that consists of image detrending, astrometric calibration, nightly photometric calibration, global calibration, image coaddition and object catalogue creation. For a more detailed description, we refer to Sevilla et al. (2011), Desai et al. (2012) and Mohr et al. (2012). Here, we use DES Y2Q1 (year-two quick release) data derived from single-epoch imaging. This catalogue is derived from 26 590 DECam exposures taken during the first 2 yr of DES observing and has a median point-source depth at an S/N = 10 of $g = 23.4$, $r = 23.2$, $i = 22.4$, $z = 22.1$ and $Y = 20.7$. The resulting calibrated DES magnitudes are already corrected for Galactic reddening by the stellar locus regression (SLR) calibration (see Drlica-Wagner et al. 2015).

The stellar sample used in this work was drawn using SExtractor parameters `FLAGS`, `SPREAD_MODEL` and `PSF` magnitudes (Bertin & Arnouts 1996; Bertin 2011; Bouy et al. 2013). Briefly, `FLAGS` tells for instance if an object is saturated or has been truncated at the edge of the image, while `SPREAD_MODEL` is the main star/galaxy separator. We used the weighted average (`WAVG`) of the `SPREAD_MODEL` measurements from the individual exposures of each source. A source quality criterion of `FLAGS` < 4 over the *g* and *r* filters was also applied. To increase stellar completeness, we selected sources in the *r* band with |`WAVG_SPREAD_MODEL`| $<$ 0.003 + `SPREADERR_MODEL`. A bright (faint) *g* magnitude limit of `WAVG_MAG_PSF` $= 17$ (`WAVG_MAG_PSF` $= 24$) was also applied. In order to prevent point sources with extreme colours (including red dwarfs from the Galactic disc) from contaminating the sample, a colour cut at $-0.5 \leq g - r \leq 1.2$ was also used. Drlica-Wagner et al. (2015) show that our Y2Q1 stellar classification efficiency exceeds 90 per cent for $r < 23$ mag, and falls to $\sim$80 per cent by $r < 24$ mag, whereas contamination by galaxies is $\sim$40 per cent for 23 mag and increases to $\sim$60 per cent by $r < 24$ mag.

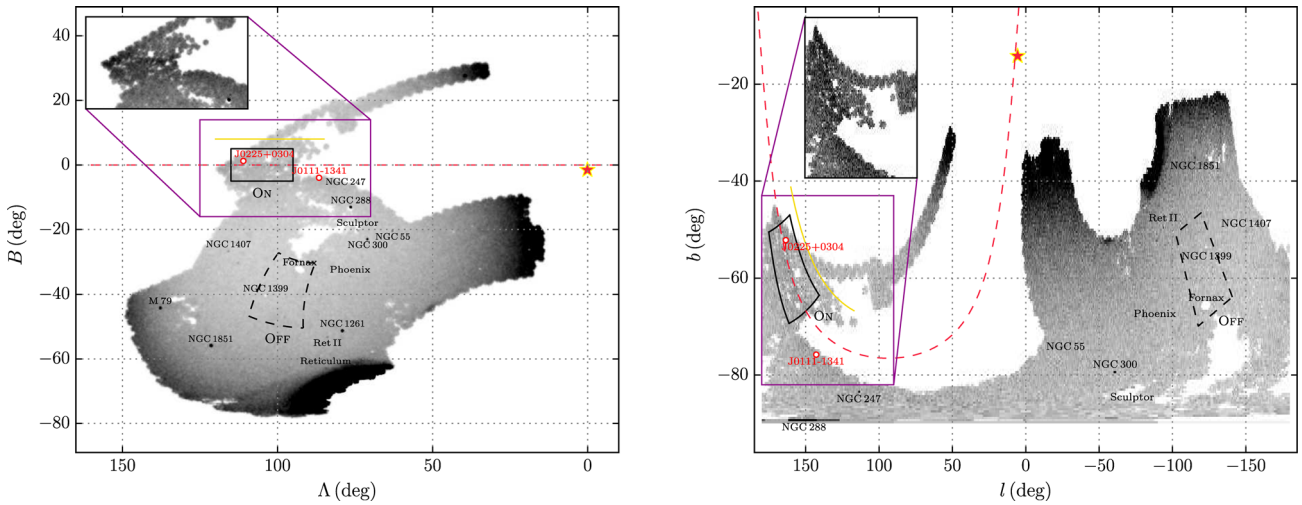

Figure 1. Density map of stars with $17 < g < 23$ and $-0.5 < g - r < 1.2$ from the DES Y2Q1 footprint in two different coordinate systems. The left-hand panel is shown in a coordinate system defined by the orbit of the Sagittarius dwarf (Majewski et al. 2003; Belokurov et al. 2014), while the right-hand panel is in Galactic coordinates (l, b). The current location of the Sagittarius dwarf is indicated by a red star. The red dashed line traces the Sagittarius tidal tail (Majewski et al. 2003). At the top left of each panel, we show an inset of the density map where the stream is more visible. Overdensities of some GCs (Harris 2010) and dwarf galaxies (McConnachie 2012; Bechtol et al. 2015; Koposov et al. 2015a) are also indicated. The new stellar system candidates discovered, DES J0111−1341 and DES J0225+0304, are marked with red circles. The ON region (solid lines) defined by $95° < \Lambda < 115°$ and $-5° < B < 5°$ represents the best-sampled region of the Sagittarius stream, whereas the OFF region (dashed lines) represents the region of stars used for the background with the same Galactic latitude as the ON region. The Fornax dwarf galaxy and NGC 1399 were masked to avoid overestimating the density of our sample of background stars (OFF region). These regions are used to construct the Hess diagrams in Figs 3 and 4. The yellow solid line, as shown in both panels, indicates the position of the faint branch of the Sagittarius stream in the DES footprint (see Section 3.1).

3 SAGITTARIUS STREAM IN THE SOUTHERN HEMISPHERE

In Fig. 1, we show a density map of stars with $17 < g < 23$ and $-0.5 < g - r < 1.2$ from the DES Y2Q1 footprint in two different coordinate systems. The colour cut was performed to exclude stars from the Galactic disc and possibly spurious objects that can contaminate our sample. The left-hand panel is in the coordinate system aligned with the Sagittarius stream (Λ, B) (Majewski et al. 2003; Belokurov et al. 2014), while the right-hand panel is in Galactic coordinates (l, b). Several overdensities are noticeable, such as some GCs (Harris 2010), dwarf galaxies (McConnachie 2012) and the recently discovered dwarf galaxy Reticulum II (Bechtol et al. 2015; Koposov et al. 2015a). The Sagittarius stream in the Southern hemisphere (trailing tail) is also visible between $90° \lesssim \Lambda \lesssim 120°$ and $-15° \lesssim B \lesssim 12°$ in Sagittarius coordinates and between $120° \lesssim l \lesssim 190°$ and $-80° \lesssim b \lesssim -45°$ in Galactic coordinates (see the inset maps on the top left of each panel). In the same figure, we show with red circles two new stellar system candidates, DES J0111−1341 and DES J0225+0304. Given their physical locations, these new candidates are possibly associated with the Sagittarius stream (discussed in Section 4). In this figure, we also show ON and OFF regions. The ON region (solid lines) defined by $95° \leq \Lambda \leq 115°$ and $-5° \leq B \leq 5°$ represents the best-sampled region of the Sagittarius stream, while the OFF region (dashed lines) represents the sample of background[1] stars located at the same Galactic latitude as the ON region. These regions are used in our colour–magnitude diagram (CMD) analysis presented in Sections 3.2 and 3.3. Finally, the yellow solid line represents the position of a possible secondary peak previously identified by Koposov et al. (2012, see discussion in the next section).

We emphasize that our analysis of the Sagittarius stream is focused on determining, using DES data, its basic characteristic parameters, such as metallicity, age and distance ranges so that they can be compared to the properties inferred for the newly discovered systems, DES J0111−1341 and DES J0225+0304. The compatibility between stream stars and these newly found systems helps shed light on their possible physical association.

3.1 Inferred number of stars

The Sagittarius stream is known to display substructures, like its bright and faint branches, in both the northern and southern Galactic hemispheres (Newberg et al. 2003; Belokurov et al. 2006; Yanny et al. 2009; Koposov et al. 2012). In particular, in the southern Galactic hemisphere, parallel to the bright branch, but ∼10° away, the faint branch is found (Koposov et al. 2012). We start by analysing variations in stellar number counts along and across the Sagittarius stream as covered by DES, in search for any clear branching of the stream in this region. In the left-hand panel of Fig. 1, we show the density map of the Sagittarius stream in the coordinate system approximately aligned with the orbit of Sagittarius (Λ, B) as described in Majewski et al. (2003) and Belokurov et al. (2014). We selected stars inside an area defined by $95° < \Lambda < 115°$ and $-15° < B < 12°$. We name this region the *stream sample*. This chosen region is a compromise between reaching a reasonably homogeneous stream coverage along both streams and still keeping a sizeable area within the DES footprint. To subtract the expected number of background stars coinciding with the *stream sample* region, we selected stars inside a region that is offset by $\Delta l = 80°$ with respect to the centre of the *stream sample* region. These regions[2]

[1] We refer to these stars as 'background', though they are dominantly composed of MW foreground stars.

[2] These two regions are not shown in Fig. 1 to avoid confusion with the ON and OFF regions used in Sections 3.2 and 3.3.

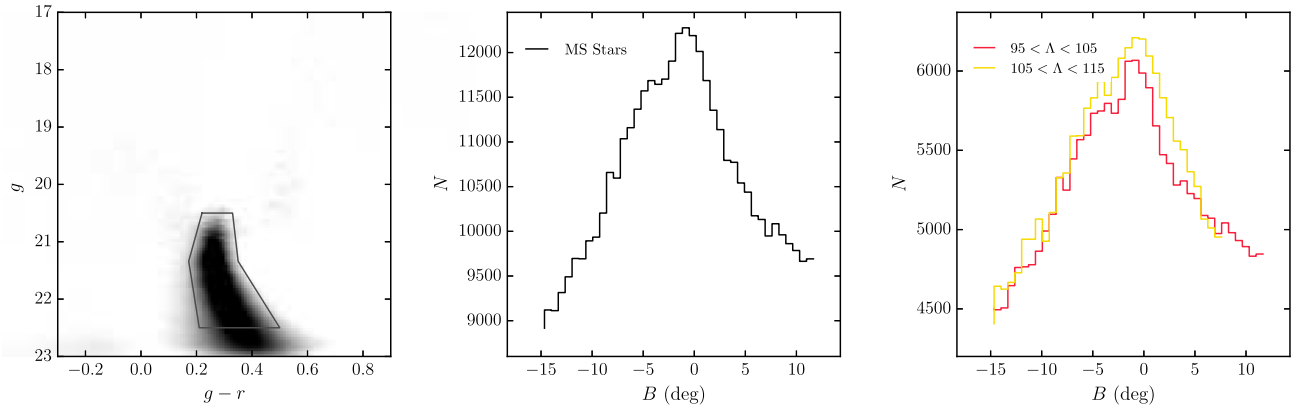

Figure 2. Left-hand panel: decontaminated Hess diagram constructed with stars within a region defined by $95^\circ < \Lambda < 115^\circ$ and $-15^\circ < B < 12^\circ$. The solid lines on the CMD plane are used to select MS stars belonging to the Sagittarius stream. Middle panel: number of MS stars (using the selected stars in the previous panel) along the Sagittarius stream ($95^\circ < \Lambda < 115^\circ$). The expected position of the faint stream (Koposov et al. 2012) is at $B \sim 8^\circ$. Right-hand panel: number of MS stars for two regions along the stream from $95^\circ < \Lambda < 105^\circ$ and $105^\circ < \Lambda < 115^\circ$ as indicated. The faint stream is seen only at $95^\circ < \Lambda < 105^\circ$ due to the current coverage of the DES footprint (see Fig. 1).

have approximately the same area and are from approximately the same Galactic latitude ($b \sim -59^\circ$) in order to maintain similar background density. For each region described above, we constructed the Hess diagram. In the left-hand panel of Fig. 2, we show the decontaminated Hess diagram calculated as the difference between the Hess diagrams of both regions weighted by their respective areas.[3] We use the HEALPIX software to determine the effective area in each region. In order to obtain a sample of representative stars of the Sagittarius stream, we weight each star of the *stream sample* region by its probability of being a member of the Sagittarius stream, $w = n_i/m_i$, where n_i (m_i) represents the number of stars in a given cell of the Hess diagram, with bins of 0.01 mag $\times$ 0.05 mag, after (before) subtracting the background stars. We consider that all the stars in a given cell of the Hess diagram have the same weight. The solid lines in the CMD plane on the left-hand panel of Fig. 2 select main-sequence (MS) stars associated with the stream. We then use the weights of these stars to analyse the variation of the number of stars along and across the stream. The results are shown in the middle and right-hand panels of Fig. 2. We use the HEALPIX software to compute the area actually covered by the Y2Q1 footprint and thus to compensate the number of stars for the area loss.

Koposov et al. (2012) find evidence for a faint stream at $B \sim 8^\circ$–10°. The DES footprint covers this area only from $95^\circ < \Lambda < 105^\circ$. The red histogram in the right-hand plot in Fig. 2 shows the number of MS stars within this region in bins of B; within this area, our data show a suggestion of an excess of stars that could be attributed to the faint stream. At Sagittarius longitudes $105^\circ < \Lambda < 115^\circ$, DES does not cover the secondary stream ($5^\circ < B < 12^\circ$); however, where DES has coverage ($-15^\circ < B < 5^\circ$), the number of MS stars (yellow histogram) is consistent with those at $95^\circ < \Lambda < 105^\circ$ (red histogram). Scaling the number of stars to the full range ($-15^\circ < B < 12^\circ$), we infer a number of MS stars for $95^\circ < \Lambda < 115^\circ$ as shown in the middle panel. The possible excess of stars observed at $B \sim 8^\circ$ (middle and right-hand panels in Fig. 2) only is visible when we use bin sizes between $0.^\circ6 \lesssim \Delta B \lesssim 0.^\circ7$; otherwise, this latter is not evident. Therefore, in this paper, we do not claim a detection of the branching of the stream.

[3] We replace negative values in the decontaminated Hess diagram by zero.

3.2 Metallicity spread

The Sagittarius stream in the northern Galactic hemisphere and the celestial equator (Stripe 82) is known for having a metallicity range (e.g. Koposov et al. 2012; De Boer et al. 2015; Hyde et al. 2015). In particular, using photometric and spectroscopic data within the SDSS Stripe 82 region (region in common with the DES footprint), Koposov et al. (2012) determined that the stars belonging to the bright and faint branches cover a metallicity range from $-2 \lesssim$ [Fe/H] $\lesssim 0$, while De Boer et al. (2015) determined a metallicity range from $-2.5 \lesssim$ [Fe/H] $\lesssim -0.3$. However, the brighter branch contains substantial numbers of metal-rich stars as compared to the fainter branch (Koposov et al. 2012).

We now turn to a global analysis of the stellar populations contributing to the Sagittarius stream. We first use the red giant branch (RGB) stars to find a spread in metallicity as follows. First, we selected stars inside a region defined by $95^\circ < \Lambda < 115^\circ$ and $-5^\circ < B < 5^\circ$ (ON region; left-hand panel of Fig. 1). The more restricted range in B is meant to further reduce sky coverage effects and to avoid any possible contamination by the faint branch. Using these stars, we have constructed and decontaminated a Hess diagram representative of the Sagittarius stream. The left-hand and middle panels of Fig. 3 show the Hess diagrams for the ON and OFF regions, respectively. They contain 185 558 and 117 860 stars (within an isochrone filter[4]), respectively. These regions are from approximately the same Galactic latitude (see right-hand panel of Fig. 1). The decontaminated Hess diagram shown in the right-hand panel of Fig. 3 was calculated as the difference between the Hess diagrams of the ON and OFF regions weighted by their respective areas. It contains a total of 87 810 stars. We use the HEALPIX software to determine the effective area in each region. In the decontaminated Hess diagram, we can identify MS, RGB and some younger population stars.

We select stars within the decontaminated CMD region defined by $0.4 < g - r < 0.8$ and $19.3 < g < 20.5$. For each interval of $\sim$0.4 mag along the CMD, we count stars as a function of colour and

[4] The isochrone filter is constructed by using the best-fitting isochrone determined for mean colour values (see Fig. 3). For isochrone filter details, we refer to Luque et al. (2016).

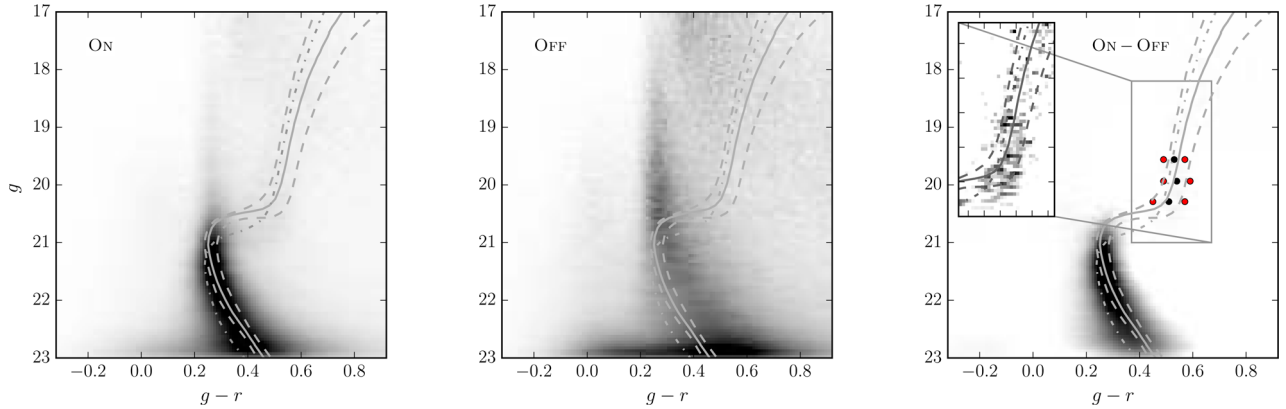

Figure 3. Left-hand panel: Hess diagram constructed with stars within a region of the Sagittarius stream defined by $95^\circ < \Lambda < 115^\circ$ and $-5^\circ < B < 5^\circ$ (ON region; Fig. 1). Middle panel: Hess diagram of the background constructed with stars within the OFF region (Fig. 1). Right-hand panel: difference Hess diagram between the ON and OFF regions. The solid black (red) circles represent the mean colour (standard deviation) values of RGB stars as a function of the colour $(g - r)$ for different ranges of magnitude. The mean colour value (μ) and standard deviation (σ) obtained from the Gaussian fit are $\mu = 0.527 \pm 0.002$ and $\sigma = 0.043 \pm 0.002$ (top circles), $\mu = 0.544 \pm 0.003$ and $\sigma = 0.051 \pm 0.005$ (middle circles), $\mu = 0.509 \pm 0.004$ and $\sigma = 0.061 \pm 0.006$ (lower circles). The solid line, in each panel, represents the best-fitting isochrone (Bressan et al. 2012) determined from mean colour values. The lower (top) dashed line represents the 1σ (-1σ) isochrone. From the bottom up, the isochrone parameters are $\log(\text{Age}) = 9.98$, $D_\odot = 24.5$ kpc and $[\text{Fe/H}] = -0.95$ (lower dashed line), $\log(\text{Age}) = 10.02$, $D_\odot = 24.5$ kpc and $[\text{Fe/H}] = -1.34$ (solid line), $\log(\text{Age}) = 10.12$, $D_\odot = 24.5$ kpc and $[\text{Fe/H}] = -2.18$ (top dashed line). In addition, an isochrone model with $[\text{Fe/H}] = -2.18$, $\log(\text{Age}) = 10.12$ and $(m - M)_0 = 17.31$ parameters is also overplotted on each panel (dot–dashed line; see Sections 3.2 and 3.3).

use the PYTHON package scipy.optimize[5] to fit a Gaussian distribution to determine the mean colour value and the associated standard deviation. The peak and 1σ deviations from it are shown as the black and red dots in the right-hand panel of Fig. 3. We then choose a set of PARSEC isochrone (Bressan et al. 2012) models that visually agree with the RGB mean and associated $\pm 1\sigma$ colours resulting from the Gaussian fits as well as the observed main-sequence turn-off (MSTO) and MS loci. This is done by imposing the following restrictions to the isochrones: (i) the model age and metallicity must respect the tight age–metallicity relation by De Boer et al. (2015) and (ii) a single distance must be used for the three sets of points along the RGB, MS and MSTO loci.

The best-fitting isochrones for the mean values and standard deviations (as described above) are shown in Fig. 3. Our results show that the stream population is old but displays a significant metallicity spread. While the peak RGB locus is consistent with $[\text{Fe/H}] = -1.34$, their redder and bluer ends are more metal-rich ($[\text{Fe/H}] = -0.98$) and metal-poor ($[\text{Fe/H}] = -2.18$), respectively. The metallicity spread found in this analysis is also much larger than the photometric errors ($\sigma_{g-r} \simeq 0.01$ for RGB stars at $g \simeq 20$) and uncertainty in calibration[6] [$\Delta(g - r) = 0.013$ for the ON region], which again attests to its reality. However, metallicity determinations in the literature (Koposov et al. 2012; De Boer et al. 2015) suggest that the Sagittarius stream in the Stripe 82 region contains more metal-rich stars than our determinations.

3.3 Distance gradient

Distance determinations for different regions of the Sagittarius stream in the northern Galactic hemisphere were performed by different authors (e.g. Belokurov et al. 2006; Correnti et al. 2010). Recent studies of the Sagittarius stream in the southern Galactic hemisphere were performed by Koposov et al. (2012) and Slater et al. (2013). Using SDSS Data Release 8, Koposov et al. (2012) determined a distance gradient from 22.08 ($\Lambda \simeq 97.^\circ5$) to 27.2 kpc ($\Lambda \simeq 112.^\circ5$), whereas Slater et al. (2013), using Pan-STARRS data, determined a distance gradient from 29.5 ($\Lambda \simeq 102^\circ$) to 33.1 kpc ($\Lambda \simeq 110^\circ$). We note a discrepancy in determining the distance gradient between the two groups. While it is true that both groups use red clump (RC) stars to determine the distance gradient along of the Sagittarius stream, the difference lies in the absolute magnitude value assumed in these determinations. To compare our results with the literature, we show only results within our region of analysis, $95^\circ < \Lambda < 115^\circ$. In this section, we perform an independent estimate of the distance gradient along the Sagittarius stream in the southern Galactic hemisphere, so as to compare it to those previous studies.

For each interval of $2.^\circ5$ in Λ, we construct a Hess diagram along the Sagittarius stream (ON region; left-hand panel of Fig. 1), eight in total. To decontaminate each one of the Hess diagrams by removing the background stars, we first divide the OFF region in subregions approximately equal to those used in the ON region, maintaining the same Galactic latitude. We then follow the same procedure described in Section 3.2. The results are shown in Fig. 4.

We estimated the distance gradient along the stream as follows. For each interval in Λ (see the text above), we first select CMD stars with $0.4 < g - r < 0.8$. For two intervals of magnitude, we count stars as a function of colour and fit a Gaussian distribution to determine the mean colour value (μ). The choice of only two intervals of magnitude is due to low statistics of RGB stars present in all the CMDs. By applying this restriction, we obtain ~150 stars in each magnitude interval. The peak values are shown as black solid dots in Fig. 4. We then use a set of PARSEC isochrone (Bressan et al. 2012) models that visually fit the RGB mean values resulting from the Gaussian fits as well as the observed MSTO and MS loci. This is done by again imposing the restriction that the model age and metallicity respect the age–metallicity relation by

[5] http://docs.scipy.org/doc/scipy-0.17.0/reference/optimize.html

[6] The uncertainty in calibration was determined by comparing the SLR calibration for Y2Q1 against external catalogues (2MASS and AAVSO Photometric All-Sky Survey, APASS-DR9). The latter transformed to DES filters.

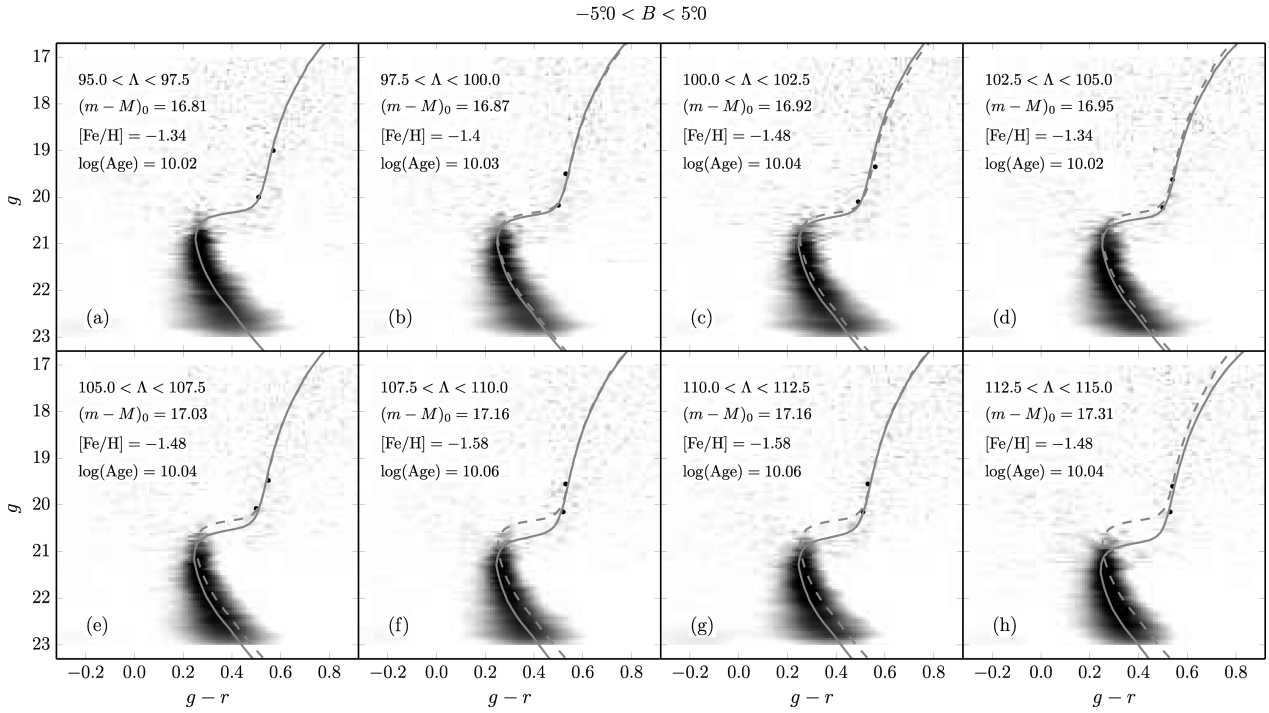

Figure 4. Hess diagrams, after decontamination from the background contribution, constructed along the Sagittarius stream (ON region) from 95° < Λ < 97.°5 to 112.°5 < Λ < 115° as indicated on each panel. The solid black dots represent the mean colour values of the Gaussian fit on RGB stars. The best-fitting isochrone (Bressan et al. 2012) using the method described in Section 3.3 is overplotted on each panel with a solid line. The isochrone parameters are also indicated on each panel. For comparison, in panels (b) through (h) is overplotted (with a dashed line) the nearest isochrone model [from panel (a)].

De Boer et al. (2015). The best-fitting isochrones using the method described above are superposed on to the decontaminated Hess diagrams (Fig. 4). Our best-fitting isochrones show a distance gradient along the Sagittarius stream from ∼23 kpc for 95° < Λ < 97.°5 and ∼29 kpc for 112.°5 < Λ < 115°. We estimate distance uncertainties in each Λ interval by varying the age and metallicity of the PARSEC isochrones around the best-fitting case (but still bound to the same age–metallicity relation) and redoing the visual isochrone fit. We estimate a mean distance uncertainty of ±0.3 kpc. Therefore, our results are in agreement with those obtained by Koposov et al. (2012).

To quantify the effect of the distance gradient along the stream on the metallicity spread (see Section 3.2), we overplotted in Fig. 3 the same isochrone model that best fits the -1σ Gaussian locus ([Fe/H] = −2.18, log (Age) = 10.12; dots shown on the blue side of the RGB locus), but now shifted to $(m - M)_0 = 17.31 = 29$ kpc (dot–dashed line). This distance corresponds to the maximum value determined in the analysis of the distance gradient. We conclude that a variation in distance as large as is inferred in this section does not account for the observed colour spread on the RGB (see Fig. 3).

4 SUBSTRUCTURE SEARCH AND OBJECT DETECTION

Many more than 17 objects were selected by our compact overdensity search techniques, stellar density maps, likelihood-based search and SPARSEX. Only 17 of them have been published[7] (Bechtol et al. 2015; Drlica-Wagner et al. 2015; Luque et al. 2016). A careful reanalysis of the promising candidates detected by the SPARSEX code has revealed two new candidate stellar systems in addition to those reported by Drlica-Wagner et al. (2015, see discussion in the next section). In this section, we briefly review SPARSEX.

The SPARSEX code is an overdensity detection algorithm, which is based on the matched-filter (MF) method (Balbinot et al. 2011; Luque et al. 2016). Briefly, we begin by binning stars into spatial pixels of 1.0 arcmin × 1.0 arcmin and colour–magnitude bins of 0.01 mag × 0.05 mag. We then create a grid of simple stellar populations (SSPs) with the code GENCMD.[8] We use GENCMD along with PARSEC isochrones (Bressan et al. 2012) and an initial mass function (IMF) of Kroupa (2001). We simulate several SSPs in a range of ages [9.0 ≤ log (Age) ≤ 10.2], metallicities ($Z = \{0.0002, 0.001, 0.007\}$) and distance ($10 \leq D_{\odot} \leq 200$ kpc). To account for local variations in the background CMD, we partition the sky into 10° × 10° regions. We then apply SPARSEX on the stellar catalogue in every sky region using the grid of the SSPs. This procedure generates one density map for each SSP model within a sky region.

To search for stellar clusters and dwarf galaxies, we convolved the set density maps with Gaussian spatial kernels of different sizes,[9] from $\sigma = 0$ (no convolution) to 9 arcmin. To automatically detect overdensities in each map, we use the SEXTRACTOR code (Bertin & Arnouts 1996). Finally, we selected stellar object candidates based

[7] Thus far, spectroscopic observations have confirmed that Reticulum II (Koposov et al. 2015b; Simon et al. 2015; Walker et al. 2015), Horologium I (Koposov et al. 2015b) and Tucana II (Walker et al. 2016) are indeed dwarf galaxies.

[8] https://github.com/balbinot/gencmd

[9] As mentioned in Luque et al. (2016), our range of spatial kernel sizes complements those adopted by the other two substructure search techniques. This range of kernel sizes and all possible combinations of parameters, age, metallicity and distance allows us to detect compact objects as GCs, as well as extended objects such as dwarf galaxies.

on two criteria: (1) according to the number of times that the SSP models are detected. In this case, the 10 highest ranked candidates in each region of the sky and each convolution kernel were visually analysed. (2) According to the statistical significance of the excess number of stars relative to the background: we built a significant profile in a cumulative way, in incremental steps of 1.0 arcmin in radius, centred on each candidate. We then applied a simple cut in significance. All candidates with significance thresholds $>5\sigma$ were visually analysed to discard artificial objects as well as contamination by faint galaxies (Luque et al. 2016).

Applying the method described above on DES Y2Q1 data, we successfully recovered with high significance all 19 stellar objects that have been recently reported in DES data (Bechtol et al. 2015; Drlica-Wagner et al. 2015; Kim & Jerjen 2015b; Kim et al. 2015; Koposov et al. 2015a; Luque et al. 2016). Additionally, we detected two new candidate stellar systems potentially associated with the Sagittarius stream, DES J0111−1341 and DES J0225+0304. The physical properties derived for DES J0111−1341 reveal that this candidate is consistent with being an ultrafaint stellar cluster, whereas DES J0225+0304 is more consistent with being a dwarf galaxy candidate (see discussion in the next section).

5 DES J0111−1341 AND DES J0225+0304

DES J0111−1341 and DES J0225+0304 were detected with high statistical significance, 8.2σ and 7.5σ, respectively. A Test Statistic (TS) for these candidates was also determined in an independent manner. The TS is based on the likelihood ratio between a hypothesis that includes an object versus a field-only hypothesis (Bechtol et al. 2015, equation 4). This analysis has revealed a TS ~ 15 ($\sim 4\sigma$) for both candidates. We do not observe an obvious overdensity of sources classified as galaxies, which reduces the possibility that the detected overdensities are caused by misclassified faint galaxies.

We use the maximum likelihood technique to determine the structural and CMD parameters. To estimate the structural parameters, we assume that the spatial distribution of stars of both objects follows an exponential profile model. Following the convention of Martin, de Jong & Rix (2008), we parametrize this model with six free parameters: central coordinates α_0 and δ_0, position angle θ, ellipticity ϵ, exponential scale radius r_e and background density Σ_{bgd}. For CMD fits, we first weighted each star by the membership probability p taken from the exponential density profile (Pieres et al. 2016). We then selected all the stars with a threshold of $p \geq 1$ per cent to fit an isochrone model. The free parameters age, $(m-M)_0$ and Z are simultaneously determined by this fitting method (for details, see Luque et al. 2016; Pieres et al. 2016). To explore the parameter space, we use the EMCEE module for Markov Chain Monte Carlo (MCMC; Foreman-Mackey et al. 2013)[10] sampling. We use MCMC to determine the best-fitting parameters for both the exponential profile and isochrone models. The absolute magnitudes were calculated using the prescription of Luque et al. (2016). The inferred properties of DES J0111−1341 and DES J0225+0304 are listed in Table 1.

5.1 DES J0111−1341

DES J0111−1341 is the candidate detected with most statistical significance ($\sim 8.2\sigma$) in our sample of promising candidates. In the top-left panel of Fig. 5, we show the density map constructed using stars inside the isochrone filter. For comparison, we show in the top middle panel the density map of objects classified as galaxies. Note the prominent stellar overdensity centred on DES J0111−1341. The top-right panel shows the elliptical significance profile. It is defined as the ratio of the number of stars inside a given ellipse and in excess of the background (N_{bgd}), N_{obj}, to the expected fluctuation in the same background, i.e. $N_{obj}/\sqrt{N_{bgd}}$. $N_{obj} = (N_{obs} - N_{bgd})$, where N_{obs} is the total number of observed stars. We build the elliptical significance profile using cumulative ellipses with semimajor axis a centred on the object. N_{bgd} is computed within an elliptical annulus at 30 arcmin $< a <$ 34 arcmin from DES J0111−1341 (Luque et al. 2016). Note that the higher peak of significance (PS) is clearly steeper for the filtered stars according to our best-fitting isochrone model. In the same figure, the CMD for DES J0111−1341 is shown in the bottom-left panel. Only stars inside an ellipse with semimajor axis $a = 2r_h$ are shown. The CMD shows predominantly MS stars. The bottom middle panel shows the CMD of background stars contained within an elliptical annulus of equal area as the previous panel. In both CMDs, we show the filter based on our best-fitting isochrone (see Luque et al. 2016). The Hess difference between the stars inside an ellipse with semimajor axis $a = 2r_h$ and background stars (20.0 arcmin $< a <$ 35.0 arcmin), this latter scaled to the same area, is shown in the bottom-right panel. In Fig. 6, we show the binned stellar density profile for DES J0111−1341. The best-fitting exponential model is also overplotted. In both cases, we took into account the ellipticity of the object.

The physical size ($r_h \sim 4.55$ pc) of DES J0111−1341 is comparable with the size of GCs associated with the Sagittarius stream]. However, its luminosity ($M_V \sim +0.3$) is inconsistent with this class of objects]. Therefore, its low luminosity and small size place DES J0111−1341 among the MW ultrafaint stellar clusters (see size–luminosity plane, Fig. 9). In particular, its luminosity is comparable to Kim 1 ($M_V \sim +0.3$; Kim & Jerjen 2015a). However, DES J0111−1341 is fainter than DES 1 (Luque et al. 2016),

Table 1. Properties of DES J0111−1341 and DES J0225+0304.

Parameters	DES J0111−1341	DES J0225+0304	Unit
α_0 (J2000)	$01:11:10.3^{+0.40}_{-0.48}$	$02:25:42.4^{+1.52}_{-1.60}$	h: m: s
δ_0 (J2000)	$-13:41:05.4^{+5.4}_{-6.6}$	$03:04:10.1^{+45.6}_{-39.6}$	◦: ′: ″
l	142.83	163.58	deg
b	−75.79	−52.20	deg
Λ	86.61	111.02	deg
B	−3.97	1.24	deg
θ	$-53.24^{+31.70}_{-23.24}$	$31.25^{+11.48}_{-13.39}$	deg
ϵ	$0.27^{+0.20}_{-0.17}$	$0.61^{+0.14}_{-0.23}$	
Σ_{bgd}	$1.040^{+0.001}_{-0.001}$	$1.679^{+0.002}_{-0.002}$	$\frac{\text{stars}}{\text{arcmin}^2}$
$D_\odot$	$26.5^{+1.3}_{-1.3}$	$23.8^{+0.7}_{-0.5}$	kpc
r_h[a]	$0.59^{+0.17}_{-0.12}$	$2.68^{+1.33}_{-0.70}$	arcmin
r_h	$4.55^{+1.33}_{-0.95}$[b]	$18.55^{+9.22}_{-4.86}$[c]	pc
M_V	$+0.3^{+0.9}_{-0.6}$	$-1.1^{+0.5}_{-0.3}$	mag
D_{orb}	∼1.73	∼0.50	kpc
[Fe/H][d]	$-1.38^{+0.07}_{-0.05}$	$-1.26^{+0.03}_{-0.03}$	
log (Age)	$10.06^{+0.02}_{-0.02}$	$10.07^{+0.01}_{-0.01}$	
$(m-M)_0$	$17.12^{+0.11}_{-0.11}$	$16.88^{+0.06}_{-0.05}$	

Notes. [a]Using the relation $r_h = 1.68 r_e$ (Martin et al. 2008).
[b]Adopting a distance of 26.5 kpc.
[c]Adopting a distance of 23.8 kpc.
[d]Adopting $Z_\odot = 0.0152$ (Bressan et al. 2012).

[10] http://dan.iel.fm/emcee/current/

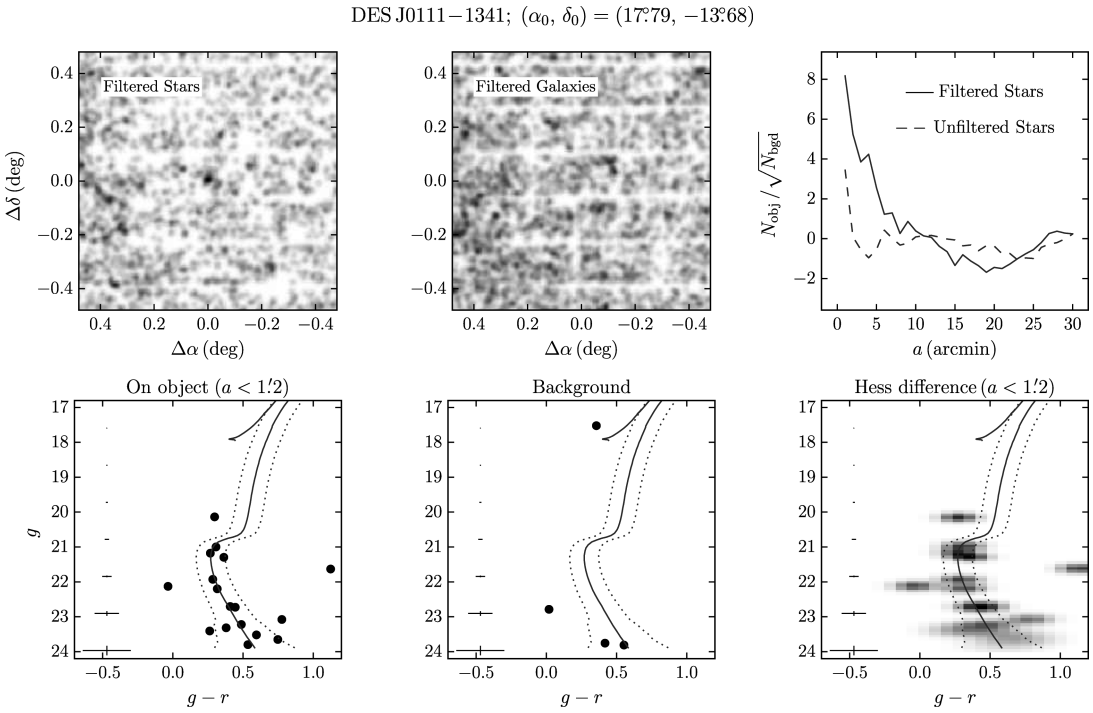

Figure 5. Top-left panel: on-sky number density map of stars around DES J0111−1341. Only stars that lie close to the best-fitting isochrone are included. Top middle panel: similar to the previous panel, but now for galaxies. Top-right panel: elliptical significance as a function of semimajor axis a from the centre of DES J0111−1341. The solid [dashed] line corresponds to isochrone-filtered [not pass the filter (unfiltered)] stars. Lower-left panel: CMD of stars within an ellipse with semimajor axis $a = 2r_h$ from the centre of DES J0111−1341. In this and the other two bottom panels, the best-fitting PARSEC isochrone (Bressan et al. 2012) is shown, along with ridge lines meant to bracket the most likely members. Lower middle panel: CMD of background stars in an elliptical annulus of equal area on the sky as the previous panel. Lower right panel: Hess diagram of the CMD difference between stars within $a = 2r_h$ and background stars (20.0 arcmin $< a <$ 35.0 arcmin). The mean photometric error is shown in the extreme left of each lower panel.

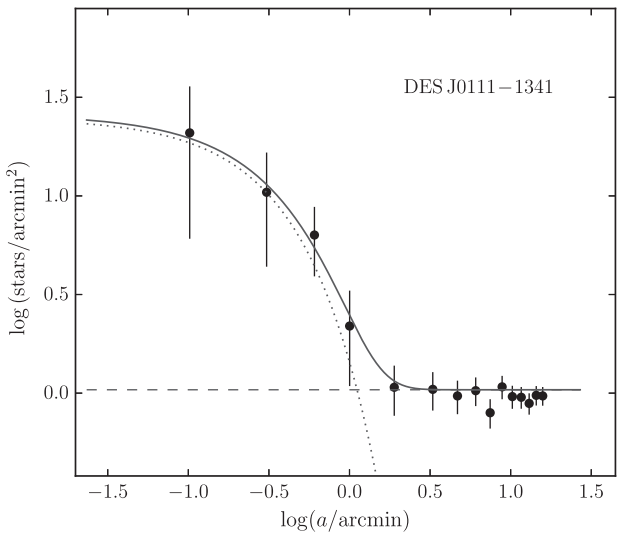

Figure 6. Solid points show a binned version of the density profile of DES J0111−1341, constructed in elliptical annuli using the derived structural parameters from the best-fitting exponential profile (see Table 1). The error bars are 1σ Poisson uncertainties. The dotted line represents the best-fitting exponential profile. The horizontal dashed line shows the background level. The solid line is the combination of the background level with the exponential profile.

Koposov 1, Koposov 2 (Koposov et al. 2007) and Muñoz 1 (Muñoz et al. 2012).

5.2 DES J0225+0304

Figs 7 and 8 show the analogous information as Figs 5 and 6 for DES J0225+0304. The physical size ($r_h \sim 18.55$ pc) and luminosity ($M_V \sim -1.1$) place it in an ambiguous region of size–luminosity space between stellar clusters and dwarf galaxies (see Fig. 9). DES J0225+0304 is elongated ($\epsilon \sim 0.61$) and has a physical size similar to an extended GC or a very small faint dwarf galaxy. In fact, the physical size, luminosity and ellipticity of DES J0225+0304 are comparable to the properties of the Tucana V stellar system ($r_h \simeq 17$ pc, $M_V \simeq -1.6$ and $\epsilon \simeq 0.7$; Drlica-Wagner et al. 2015).

5.3 Association with the Sagittarius stream

As mentioned in Section 3, DES J0111−1341 and DES J0225+0304 are probably associated with the Sagittarius dwarf stream. Their log (Age), [Fe/H] and $D_\odot$ (see Table 1) are well bracketed by the age, metallicity and distance ranges determined in Section 3.2 for the stream. In fact, the inferred ages and metallicities are very similar for both DES J0111−1341 and DES J0225+0304, and agree very well with the isochrone fit to the mean RGB colours of the stream, log (Age) = 10.02, [Fe/H] = −1.34 and $D_\odot = 24.5$ kpc.

To better explore this association, we estimate the distance of the two new candidates to the Sagittarius orbital plane (D_{orb}). For

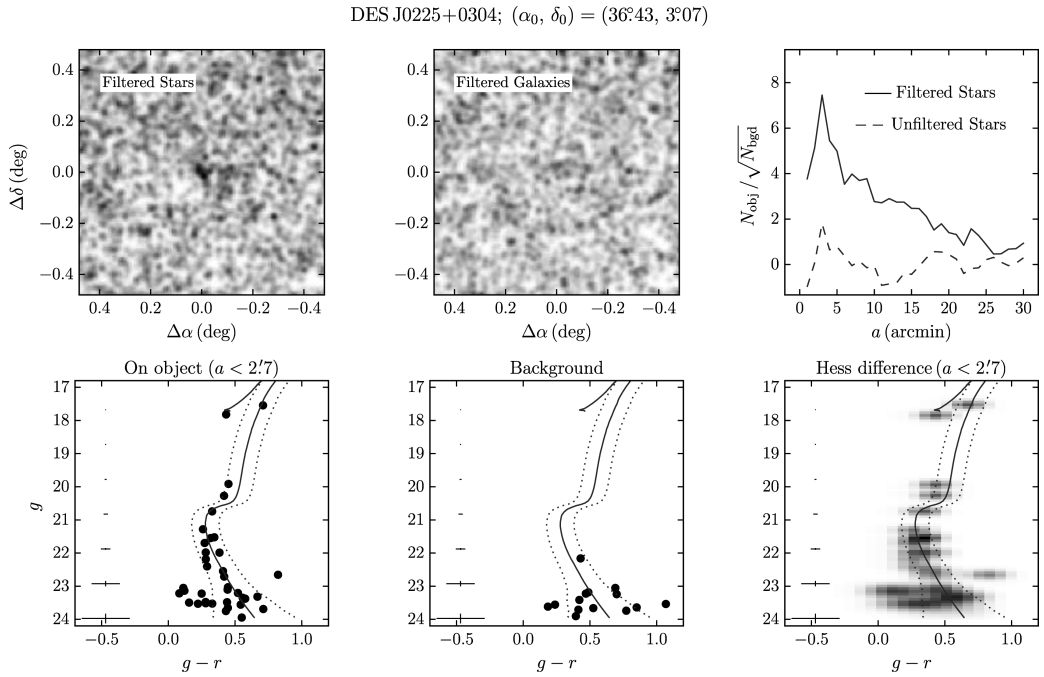

Figure 7. Top-left panel: on-sky number density map of stars around DES J0225+0304. Only stars that lie close to the best-fitting isochrone are included. Top middle panel: similar to the previous panel, but now for galaxies. Top-right panel: elliptical significance as a function of semimajor axis a from the centre of DES J0225+0304. The solid (dashed) line corresponds to isochrone-filtered [not pass the filter (unfiltered)] stars. Lower-left panel: CMD of stars within an ellipse with semimajor axis $a = 1r_{\rm h}$ from the centre of DES J0225+0304. In this and the other two bottom panels, the best-fitting PARSEC isochrone (Bressan et al. 2012) is shown, along with ridge lines meant to bracket the most likely members. Lower-middle panel: CMD of background stars in an elliptical annulus of equal area on the sky as the previous panel. Lower-right panel: Hess diagram of the CMD difference between stars within $a = 1r_{\rm h}$ and background stars (25.0 arcmin $< a <$ 45.0 arcmin). The mean photometric error is shown in the extreme left of each lower panel.

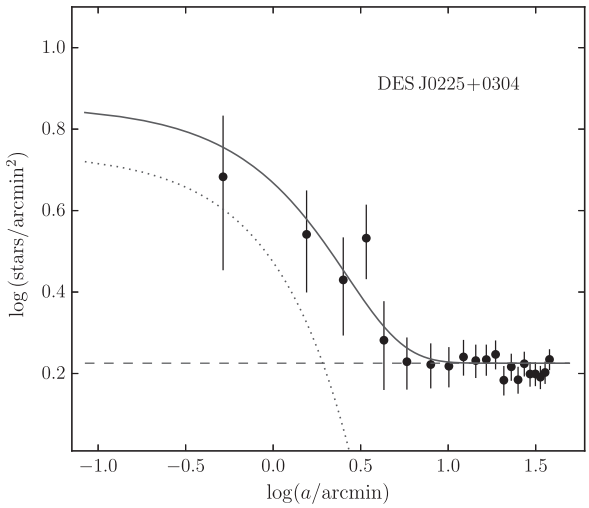

Figure 8. Solid points show a binned version of the density profile of DES J0225+0304, constructed in elliptical annuli using the derived structural parameters from the best-fitting exponential profile (see Table 1). The error bars are 1σ Poisson uncertainties. The dotted line represents the best-fitting exponential profile. The horizontal dashed line shows the background level. The solid line is the combination of the background level with the exponential profile.

this purpose, we use the best-fitting Sagittarius orbital plane[11] determined by Majewski et al. (2003). We then obtain a distance of ∼1.73 and ∼0.50 kpc for DES J0111−1341 and DES J0225+0304, respectively. When we compare the $D_{\rm orb}$ of the new candidates with the $D_{\rm orb}$ determined for GCs associated with the Sagittarius dwarf (Bellazzini et al. 2003, and references therein), we note that DES J0111−1341 has a $D_{\rm orb}$ similar to that of Terzan 7 (∼1.89 kpc), whereas the $D_{\rm orb}$ of DES J0225+0304 is comparable to that of NGC 6715 (∼0.45 kpc). These results indicate that both DES J0111−1341 and DES J0225+0304 are very close indeed to the Sagittarius plane, something that strongly increases the likelihood of their association with the Sagittarius stream. However, there are GCs spatially compatible with the orbit of Sagittarius (e.g. NCG 4147 and NGC 288) but not associated with Sagittarius when their radial velocities and proper motions are considered (Law & Majewski 2010b). This suggests that the spectroscopic determination of the radial velocity and the proper motion of these systems are both crucial to confirm that association.

We use a random sampling technique to give a statistical argument for this possible association. For this purpose, we use the sample of known star clusters and dwarf galaxies from various recent sources (Harris 2010; McConnachie 2012; Balbinot et al. 2013; Laevens et al. 2014, 2015a,b; Bechtol et al. 2015; Drlica-Wagner et al. 2015; Koposov et al. 2015a; Kim & Jerjen 2015a; Kim et al. 2015, 2016; Martin et al. 2015; Luque et al. 2016). The null hypothesis assumes that the stellar systems from our sample are not associated with the Sagittarius dwarf galaxy; thus, we removed the four GCs confirmed to be associated with the Sagittarius dwarf (NGC 6715, Arp 2, Terzan 7 and Terzan 8). First, we calculate the $D_{\rm orb}$ for each stellar system. We then randomly selecttwo systems from the sample, assigning an equal selection probability to each system. After performing 10^6 selections, we estimate a 0.08 probability of finding two stellar systems with $D_{\rm orb} \leq 1.73$ kpc. While it is true that this

[11] The best-fitting plane was performed by using M-giant stars detected in 2MASS data (for details, see Majewski et al. 2003).

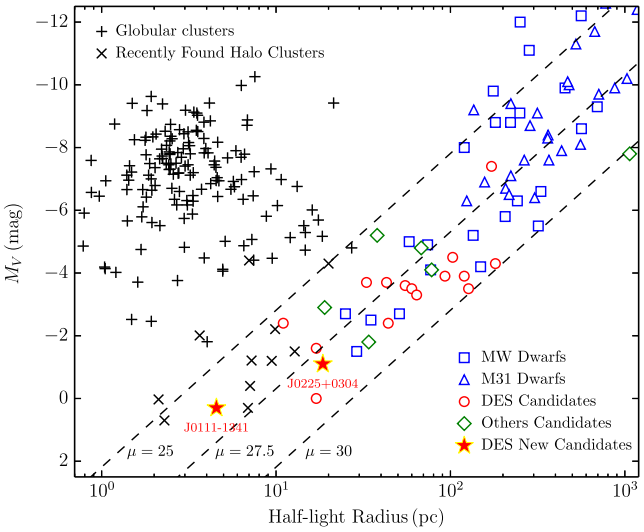

Figure 9. Absolute magnitude as a function of half-light radius. MW GCs ('+' symbols; Harris 2010), outer halo clusters with ambiguous classification ('×' symbols; Koposov et al. 2007; Belokurov et al. 2010; Muñoz et al. 2012; Balbinot et al. 2013; Laevens et al. 2014, 2015b; Kim & Jerjen 2015a; Kim et al. 2015, 2016; Luque et al. 2016), MW dwarf galaxies (blue squares; McConnachie 2012), M 31 dwarf galaxies (blue triangles; McConnachie 2012), previously reported dwarf galaxy candidates in the DES footprint (red circles; Bechtol et al. 2015; Drlica-Wagner et al. 2015), other recently reported dwarf galaxies (green diamond; Kim & Jerjen 2015a; Laevens et al. 2015a,b; Martin et al. 2015; Torrealba et al. 2016) and DES new candidates (red stars) are shown. Note that DES J0111−1341 clearly lies inside the region inhabited by ultrafaint stellar clusters, whereas DES J0225+0304 occupies the ambiguous region between stellar clusters and dwarf galaxies. The dashed lines indicate contours of constant surface brightness at $\mu = \{25, 27.5, 30\}$ mag arsec^{-2}.

probability value is not negligible, these randomly drawn pairs of objects are not necessarily as close to the Sagittarius orbit as our candidates.

6 CONCLUSIONS

In this paper, we report the discovery of two new candidate stellar systems in the constellation of Cetus using DES Y2Q1 data. These objects add to the 19 star systems that have been found in the first 2 yr of DES (Bechtol et al. 2015; Drlica-Wagner et al. 2015; Kim & Jerjen 2015b; Koposov et al. 2015a; Luque et al. 2016). DES J0111−1341 is a compact ($r_h \sim 4.55$ pc) and ultrafaint ($M_V \sim +0.3$) stellar cluster, whereas DES J0225+0304 is faint ($M_V \sim -1.1$) and has a physical size ($r_h \sim 18.55$ pc) comparable to a very small faint dwarf galaxy. These new stellar systems appear to be at a heliocentric distance $D_\odot \sim 25$ kpc.

There are several lines of evidence that suggest that our new candidates are associated with the Sagittarius stream: (i) they lie on the edges of the Sagittarius stream, as can be seen in Fig. 1 (red circles). (ii) The CMD parameters (age, metallicity and distance) determined for these new candidates lie within the metallicity and age range determined for the Sagittarius stream using the same DES data (Section 3.2). In particular, they are consistent with the parameters inferred by fitting the mean CMD locus of the stream stars. (iii) The distances D_{orb} of our candidates to the Sagittarius orbital plane, ∼1.73 kpc (DES J0111−1341) and ∼0.50 kpc (DES J0225+0304), are comparable to GCs previously associated with the Sagittarius dwarf, more specifically Terzan 7 and NGC 6715 (Bellazzini et al. 2003). Therefore, we speculate that these candidates are likely associated with the Sagittarius stream. However, the spectroscopic determination of the radial velocity and proper motion of these substructures will be very useful to confirm this hypothesis. Furthermore, the dynamic mass, derived from the velocity dispersion, will help to confirm the nature of our candidates. If all of our hypotheses are confirmed, DES J0225+0304 would be the first ultrafaint dwarf galaxy associated with the Sagittarius dwarf stream. It would also be the first confirmed case of an ultrafaint satellite of a satellite.

As for the properties of the stream itself, the star count histograms constructed across the Sagittarius stream show a possible excess of stars at $B \sim 8°$. However, this putative excess is only clearly visible when we use bin sizes of $0.^\circ6 \lesssim \Delta B \lesssim 0.^\circ7$. Therefore, we do not claim a detection of the branching of the stream. We found no further direct evidence of additional stream substructures to those already known to exist.

Finally, decontaminated Hess diagrams of the Sagittarius stream allowed us to determine a metallicity spread ($-2.18 \lesssim$ [Fe/H] $\lesssim -0.95$) as well as a distance gradient (23 kpc $\lesssim D_\odot \lesssim$ 29 kpc). This suggests that the stream is composed of more than one stellar population. Our determination of distance gradient is consistent with those determined by Koposov et al. (2012). However, metallicity determinations in the literature suggest that the stream in the celestial equator contains more metal-rich stars than those determined in this work (see e.g. Koposov et al. 2012; De Boer et al. 2015).

In the future, DES will acquire additional imaging data in this region, allowing even more significant studies of the region in which the Sagittarius stream crosses the equator.

ACKNOWLEDGEMENTS

This paper has gone through internal review by the DES collaboration.

Funding for the DES Projects has been provided by the US Department of Energy, the US National Science Foundation, the Ministry of Science and Education of Spain, the Science and Technology Facilities Council of the United Kingdom, the Higher Education Funding Council for England, the National Center for Supercomputing Applications at the University of Illinois at Urbana-Champaign, the Kavli Institute of Cosmological Physics at the University of Chicago, the Center for Cosmology and Astro-Particle Physics at the Ohio State University, the Mitchell Institute for Fundamental Physics and Astronomy at Texas A&M University, Financiadora de Estudos e Projetos, Fundação Carlos Chagas Filho de Amparo à Pesquisa do Estado do Rio de Janeiro, Conselho Nacional de Desenvolvimento Científico e Tecnológico and the Ministério da Ciência, Tecnologia e Inovação, the Deutsche Forschungsgemeinschaft and the Collaborating Institutions in the DES. The DES data management system is supported by the National Science Foundation under Grant Number AST-1138766. The DES participants from Spanish institutions are partially supported by MINECO under grants AYA2012-39559, ESP2013-48274, FPA2013-47986 and Centro de Excelencia Severo Ochoa SEV-2012-0234, some of which include ERDF funds from the European Union.

The Collaborating Institutions are Argonne National Laboratory, the University of California at Santa Cruz, the University of Cambridge, Centro de Investigaciones Enérgeticas, Medioambientales y Tecnológicas-Madrid, the University of Chicago, University College London, the DES-Brazil Consortium, the University of Edinburgh, the Eidgenössische Technische Hochschule

(ETH) Zürich, Fermi National Accelerator Laboratory, the University of Illinois at Urbana-Champaign, the Institut de Ciències de l'Espai (IEEC/CSIC), the Institut de Física d'Altes Energies, Lawrence Berkeley National Laboratory, the Ludwig-Maximilians Universität München and the associated Excellence Cluster Universe, the University of Michigan, the National Optical Astronomy Observatory, the University of Nottingham, the Ohio State University, the University of Pennsylvania, the University of Portsmouth, SLAC National Accelerator Laboratory, Stanford University, the University of Sussex and Texas A&M University.

The DES data management system is supported by the National Science Foundation under Grant Number AST-1138766. The DES participants from Spanish institutions are partially supported by MINECO under grants AYA2012-39559, ESP2013-48274, FPA2013-47986 and Centro de Excelencia Severo Ochoa SEV-2012-0234.

Research leading to these results has received funding from the European Research Council under the European Union's Seventh Framework Programme (FP7/2007-2013) including ERC grant agreements 240672, 291329 and 306478.

EB acknowledges financial support from the European Research Council (ERC-StG-335936, CLUSTERS).

REFERENCES

Balbinot E., Santiago B. X., da Costa L. N., Makler M., Maia M. A. G., 2011, MNRAS, 416, 393
Balbinot E. et al., 2013, ApJ, 767, 101
Bechtol K. et al., 2015, ApJ, 807, 50
Bellazzini M., Ferraro F. R., Ibata R., 2003, AJ, 125, 188
Belokurov V. et al., 2006, ApJ, 642, L137
Belokurov V. et al., 2010, ApJ, 712, L103
Belokurov V. et al., 2014, MNRAS, 437, 116
Bertin E., 2011, in Evans I. N., Accomazzi A., Mink D. J., Rots A. H., eds, ASP Conf. Ser. Vol. 442, Astronomical Data Analysis Software and Systems XX. Astron. Soc. Pac., San Francisco, p. 435
Bertin E., Arnouts S., 1996, A&AS, 117, 393
Bouy H., Bertin E., Moraux E., Cuillandre J.-C., Bouvier J., Barrado D., Solano E., Bayo A., 2013, A&A, 554, A101
Bressan A., Marigo P., Girardi L., Salasnich B., Dal Cero C., Rubele S., Nanni A., 2012, MNRAS, 427, 127
Carballo-Bello J. A., Sollima A., Martínez-Delgado D., Pila-Díez B., Leaman R., Fliri J., Muñoz R. R., Corral-Santana J. M., 2014, MNRAS, 445, 2971
Carraro G., Bensby T., 2009, MNRAS, 397, L106
Carraro G., Bresolin F., Villanova S., Matteucci F., Patat F., Romaniello M., 2004, AJ, 128, 1676
Correnti M., Bellazzini M., Ibata R. A., Ferraro F. R., Varghese A., 2010, ApJ, 721, 329
Da Costa G. S., Armandroff T. E., 1995, AJ, 109, 2533
De Boer T. J. L., Belokurov V., Koposov S., 2015, MNRAS, 451, 3489
Desai S. et al., 2012, ApJ, 757, 83
Diehl H. T. et al., 2016, in Peck A. B., Seaman R. L., Benn C. R., eds, Proc. SPIE Conf. Ser. Vol. 9910, Observatory Operations: Strategies, Processes, and Systems VI. SPIE, Bellingham, p. 99101D
Dotter A. et al., 2010, ApJ, 708, 698
Dotter A., Sarajedini A., Anderson J., 2011, ApJ, 738, 74
Drlica-Wagner A. et al., 2015, ApJ, 813, 109
Flaugher B. et al., 2015, AJ, 150, 150
Forbes D. A., Bridges T., 2010, MNRAS, 404, 1203
Foreman-Mackey D., Hogg D. W., Lang D., Goodman J., 2013, PASP, 125, 306
Harris W. E., 2010, preprint (arXiv:1012.3224)
Hyde E. A. et al., 2015, ApJ, 805, 189
Ibata R. A., Gilmore G., Irwin M. J., 1994, Nature, 370, 194
Johnston K. V., Spergel D. N., Hernquist L., 1995, ApJ, 451, 598
Kim D., Jerjen H., 2015a, ApJ, 799, 73
Kim D., Jerjen H., 2015b, ApJ, 808, L39
Kim D., Jerjen H., Milone A. P., Mackey D., Da Costa G. S., 2015, ApJ, 803, 63
Kim D., Jerjen H., Mackey D., Da Costa G. S., Milone A. P., 2016, ApJ, 820, 119
Koposov S. et al., 2007, ApJ, 669, 337
Koposov S. E. et al., 2012, ApJ, 750, 80
Koposov S. E., Belokurov V., Torrealba G., Evans N. W., 2015a, ApJ, 805, 130
Koposov S. E. et al., 2015b, ApJ, 811, 62
Kroupa P., 2001, MNRAS, 322, 231
Laevens B. P. M. et al., 2014, ApJ, 786, L3
Laevens B. P. M. et al., 2015a, ApJ, 802, L18
Laevens B. P. M. et al., 2015b, ApJ, 813, 44
Law D. R., Majewski S. R., 2010a, ApJ, 714, 229
Law D. R., Majewski S. R., 2010b, ApJ, 718, 1128
Luque E. et al., 2016, MNRAS, 458, 603
Lynden-Bell D., Lynden-Bell R. M., 1995, MNRAS, 275, 429
McConnachie A. W., 2012, AJ, 144, 4
Majewski S. R., Skrutskie M. F., Weinberg M. D., Ostheimer J. C., 2003, ApJ, 599, 1082
Martin N. F., de Jong J. T. A., Rix H.-W., 2008, ApJ, 684, 1075
Martin N. F. et al., 2015, ApJ, 804, L5
Mateo M., Mirabal N., Udalski A., Szymanski M., Kaluzny J., Kubiak M., Krzeminski W., Stanek K. Z., 1996, ApJ, 458, L13
Mohr J. J. et al., 2012, in Radziwill N. M., Chiozzi G., eds, Proc. SPIE Conf. Ser. Vol. 8451, Software and Cyberinfrastructure for Astronomy II. SPIE, Bellingham, p. 84510D
Muñoz R. R., Geha M., Côté P., Vargas L. C., Santana F. A., Stetson P., Simon J. D., Djorgovski S. G., 2012, ApJ, 753, L15
Newberg H. J. et al., 2002, ApJ, 569, 245
Newberg H. J. et al., 2003, ApJ, 596, L191
Newberg H. J., Yanny B., Cole N., Beers T. C., Re Fiorentin P., Schneider D. P., Wilhelm R., 2007, ApJ, 668, 221
Pieres A. et al., 2016, MNRAS, 461, 519
Sbordone L. et al., 2015, A&A, 579, A104
Sevilla I. et al., 2011, preprint (arXiv:1109.6741)
Simon J. D. et al., 2015, ApJ, 808, 95
Slater C. T. et al., 2013, ApJ, 762, 6
The Dark Energy Survey Collaboration, 2005, preprint (arXiv:e-prints)
Torrealba G., Koposov S. E., Belokurov V., Irwin M., 2016, MNRAS, 459, 2370
Walker M. G., Mateo M., Olszewski E. W., Bailey J. I., III, Koposov S. E., Belokurov V., Evans N. W., 2015, ApJ, 808, 108
Walker M. G. et al., 2016, ApJ, 819, 53
Yanny B. et al., 2009, ApJ, 700, 1282

[1]*Instituto de Física, UFRGS, Caixa Postal 15051, Porto Alegre, RS 91501-970, Brazil*
[2]*Laboratório Interinstitucional de e-Astronomia - LIneA, Rua Gal. José Cristino 77, Rio de Janeiro, RJ 20921-400, Brazil*
[3]*Fermi National Accelerator Laboratory, P. O. Box 500, Batavia, IL 60510, USA*
[4]*Cerro Tololo Inter-American Observatory, National Optical Astronomy Observatory, Casilla 603, La Serena, Chile*
[5]*National Center for Supercomputing Applications, 1205 West Clark St, Urbana, IL 61801, USA*
[6]*Department of Physics, University of Surrey, Guildford GU2 7XH, UK*
[7]*George P. and Cynthia Woods Mitchell Institute for Fundamental Physics and Astronomy, and Department of Physics and Astronomy, Texas A&M University, College Station, TX 77843, USA*
[8]*Observatório Nacional, Rua Gal. José Cristino 77, Rio de Janeiro, RJ 20921-400, Brazil*
[9]*Kavli Institute for Cosmological Physics, University of Chicago, Chicago, IL 60637, USA*

[10]*Lawrence Berkeley National Laboratory, 1 Cyclotron Road, Berkeley, CA 94720, USA*
[11]*Department of Physics and Astronomy, University of Pennsylvania, Philadelphia, PA 19104, USA*
[12]*Department of Physics & Astronomy, University College London, Gower Street, London WC1E 6BT, UK*
[13]*Department of Physics and Electronics, Rhodes University, PO Box 94, Grahamstown 6140, South Africa*
[14]*CNRS, UMR 7095, Institut d'Astrophysique de Paris, F-75014 Paris, France*
[15]*Sorbonne Universités, UPMC Univ Paris 06, UMR 7095, Institut d'Astrophysique de Paris, F-75014 Paris, France*
[16]*Kavli Institute for Particle Astrophysics & Cosmology, P. O. Box 2450, Stanford University, Stanford, CA 94305, USA*
[17]*SLAC National Accelerator Laboratory, Menlo Park, CA 94025, USA*
[18]*Department of Astronomy, University of Illinois, 1002 W. Green Street, Urbana, IL 61801, USA*
[19]*Institut de Ciències de l'Espai, IEEC-CSIC, Campus UAB, Carrer de Can Magrans, s/n, E-08193 Bellaterra, Barcelona, Spain*
[20]*Institut de Física d'Altes Energies (IFAE), The Barcelona Institute of Science and Technology, Campus UAB, E-08193 Bellaterra, Barcelona, Spain*
[21]*Institute of Cosmology & Gravitation, University of Portsmouth, Portsmouth PO1 3FX, UK*
[22]*School of Physics and Astronomy, University of Southampton, Southampton SO17 1BJ, UK*
[23]*Department of Physics, IIT Hyderabad, Kandi, Telangana 502285, India*
[24]*Department of Astronomy, University of Michigan, Ann Arbor, MI 48109, USA*
[25]*Department of Physics, University of Michigan, Ann Arbor, MI 48109, USA*
[26]*Department of Astronomy, University of California, Berkeley, 501 Campbell Hall, Berkeley, CA 94720, USA*
[27]*Australian Astronomical Observatory, North Ryde, NSW 2113, Australia*
[28]*Center for Cosmology and Astro-Particle Physics, The Ohio State University, Columbus, OH 43210, USA*
[29]*Department of Astronomy, The Ohio State University, Columbus, OH 43210, USA*
[30]*Institució Catalana de Recerca i Estudis Avançats, E-08010 Barcelona, Spain*
[31]*Jet Propulsion Laboratory, California Institute of Technology, 4800 Oak Grove Dr, Pasadena, CA 91109, USA*
[32]*Department of Physics and Astronomy, Pevensey Building, University of Sussex, Brighton BN1 9QH, UK*
[33]*Centro de Investigaciones Energéticas, Medioambientales y Tecnológicas (CIEMAT), E-28040 Madrid, Spain*
[34]*Universidade Federal do ABC, Centro de Ciências Naturais e Humanas, Av. dos Estados, 5001, Santo André, SP 09210-580, Brazil*
[35]*Computer Science and Mathematics Division, Oak Ridge National Laboratory, Oak Ridge, TN 37831, USA*

This paper has been typeset from a TEX/LATEX file prepared by the author.

A.3

The Astrophysical Journal, 813:109 (20pp), 2015 November 10 doi:10.1088/0004-637X/813/2/109

EIGHT ULTRA-FAINT GALAXY CANDIDATES DISCOVERED IN YEAR TWO OF THE DARK ENERGY SURVEY

A. Drlica-Wagner[1], K. Bechtol[2,3], E. S. Rykoff[4,5], E. Luque[6,7], A. Queiroz[6,7], Y.-Y. Mao[4,5,8], R. H. Wechsler[4,5,8], J. D. Simon[9], B. Santiago[6,7], B. Yanny[1], E. Balbinot[7,10], S. Dodelson[1,11], A. Fausti Neto[7], D. J. James[12], T. S. Li[13], M. A. G. Maia[7,14], J. L. Marshall[13], A. Pieres[6,7], K. Stringer[13], A. R. Walker[12], T. M. C. Abbott[12], F. B. Abdalla[15,16], S. Allam[1], A. Benoit-Lévy[15], G. M. Bernstein[17], E. Bertin[18,19], D. Brooks[15], E. Buckley-Geer[1], D. L. Burke[4,5], A. Carnero Rosell[7,14], M. Carrasco Kind[20,21], J. Carretero[22,23], M. Crocce[22], L. N. da Costa[7,14], S. Desai[24,25], H. T. Diehl[1], J. P. Dietrich[24,25], P. Doel[15], T. F. Eifler[17,26], A. E. Evrard[27,28], D. A. Finley[1], B. Flaugher[1], P. Fosalba[22], J. Frieman[1,11], E. Gaztanaga[22], D. W. Gerdes[28], D. Gruen[29,30], R. A. Gruendl[20,21], G. Gutierrez[1], K. Honscheid[31,32], K. Kuehn[33], N. Kuropatkin[1], O. Lahav[15], P. Martini[31,34], R. Miquel[23,35], B. Nord[1], R. Ogando[7,14], A. A. Plazas[26], K. Reil[5], A. Roodman[4,5], M. Sako[17], E. Sanchez[36], V. Scarpine[1], M. Schubnell[28], I. Sevilla-Noarbe[20,36], R. C. Smith[12], M. Soares-Santos[1], F. Sobreira[1,7], E. Suchyta[31,32], M. E. C. Swanson[21], G. Tarle[28], D. Tucker[1], V. Vikram[37], W. Wester[1], Y. Zhang[28], and J. Zuntz[38]

(The DES Collaboration)

[1] Fermi National Accelerator Laboratory, P.O. Box 500, Batavia, IL 60510, USA; kadrlica@fnal.gov
[2] Wisconsin IceCube Particle Astrophysics Center (WIPAC), Madison, WI 53703, USA; keith.bechtol@icecube.wisc.edu
[3] Department of Physics, University of Wisconsin–Madison, Madison, WI 53706, USA
[4] Kavli Institute for Particle Astrophysics & Cosmology, P.O. Box 2450, Stanford University, Stanford, CA 94305, USA
[5] SLAC National Accelerator Laboratory, Menlo Park, CA 94025, USA
[6] Instituto de Física, UFRGS, Caixa Postal 15051, Porto Alegre, RS-91501-970, Brazil
[7] Laboratório Interinstitucional de e-Astronomia—LIneA, Rua Gal. José Cristino 77, Rio de Janeiro, RJ-20921-400, Brazil
[8] Department of Physics, Stanford University, 382 Via Pueblo Mall, Stanford, CA 94305, USA
[9] Carnegie Observatories, 813 Santa Barbara St., Pasadena, CA 91101, USA
[10] Department of Physics, University of Surrey, Guildford GU2 7XH, UK
[11] Kavli Institute for Cosmological Physics, University of Chicago, Chicago, IL 60637, USA
[12] Cerro Tololo Inter-American Observatory, National Optical Astronomy Observatory, Casilla 603, La Serena, Chile
[13] George P. and Cynthia Woods Mitchell Institute for Fundamental Physics and Astronomy, and Department of Physics and Astronomy, Texas A&M University, College Station, TX 77843, USA
[14] Observatório Nacional, Rua Gal. José Cristino 77, Rio de Janeiro, RJ-20921-400, Brazil
[15] Department of Physics & Astronomy, University College London, Gower Street, London, WC1E 6BT, UK
[16] Department of Physics and Electronics, Rhodes University, P.O. Box 94, Grahamstown, 6140, South Africa
[17] Department of Physics and Astronomy, University of Pennsylvania, Philadelphia, PA 19104, USA
[18] CNRS, UMR 7095, Institut d'Astrophysique de Paris, F-75014, Paris, France
[19] Sorbonne Universités, UPMC Univ Paris 06, UMR 7095, Institut d'Astrophysique de Paris, F-75014, Paris, France
[20] Department of Astronomy, University of Illinois, 1002 W. Green Street, Urbana, IL 61801, USA
[21] National Center for Supercomputing Applications, 1205 West Clark St., Urbana, IL 61801, USA
[22] Institut de Ciències de l'Espai, IEEC-CSIC, Campus UAB, Carrer de Can Magrans, s/n, E-08193 Bellaterra, Barcelona, Spain
[23] Institut de Física d'Altes Energies, Universitat Autònoma de Barcelona, E-08193 Bellaterra, Barcelona, Spain
[24] Excellence Cluster Universe, Boltzmannstr. 2, D-85748 Garching, Germany
[25] Faculty of Physics, Ludwig-Maximilians University, Scheinerstr. 1, D-81679 Munich, Germany
[26] Jet Propulsion Laboratory, California Institute of Technology, 4800 Oak Grove Dr., Pasadena, CA 91109, USA
[27] Department of Astronomy, University of Michigan, Ann Arbor, MI 48109, USA
[28] Department of Physics, University of Michigan, Ann Arbor, MI 48109, USA
[29] Max Planck Institute for Extraterrestrial Physics, Giessenbachstrasse, D-85748 Garching, Germany
[30] Universitäts-Sternwarte, Fakultät für Physik, Ludwig-Maximilians Universität München, Scheinerstr. 1, D-81679 München, Germany
[31] Center for Cosmology and Astro-Particle Physics, The Ohio State University, Columbus, OH 43210, USA
[32] Department of Physics, The Ohio State University, Columbus, OH 43210, USA
[33] Australian Astronomical Observatory, North Ryde, NSW 2113, Australia
[34] Department of Astronomy, The Ohio State University, Columbus, OH 43210, USA
[35] Institució Catalana de Recerca i Estudis Avançats, E-08010 Barcelona, Spain
[36] Centro de Investigaciones Energéticas, Medioambientales y Tecnológicas (CIEMAT), Madrid, Spain
[37] Argonne National Laboratory, 9700 South Cass Avenue, Lemont, IL 60439, USA
[38] Jodrell Bank Center for Astrophysics, School of Physics and Astronomy, University of Manchester, Oxford Road, Manchester, M13 9PL, UK

Received 2015 August 14; accepted 2015 September 22; published 2015 November 4

ABSTRACT

We report the discovery of eight new ultra-faint dwarf galaxy candidates in the second year of optical imaging data from the Dark Energy Survey (DES). Six of these candidates are detected at high confidence, while two lower-confidence candidates are identified in regions of non-uniform survey coverage. The new stellar systems are found by three independent automated search techniques and are identified as overdensities of stars, consistent with the isochrone and luminosity function of an old and metal-poor simple stellar population. The new systems are faint ($M_V > -4.7$ mag) and span a range of physical sizes (17 pc $< r_{1/2} <$ 181 pc) and heliocentric distances (25 kpc $< D_\odot <$ 214 kpc). All of the new systems have central surface brightnesses consistent with known ultra-faint dwarf galaxies ($\mu \gtrsim 27.5$ mag arcsec^{-2}). Roughly half of the DES candidates are more distant, less luminous, and/or have lower surface brightnesses than previously known Milky Way satellite galaxies. Most of the

candidates are found in the southern part of the DES footprint close to the Magellanic Clouds. We find that the DES data alone exclude ($p < 10^{-3}$) a spatially isotropic distribution of Milky Way satellites and that the observed distribution can be well, though not uniquely, described by an association between several of the DES satellites and the Magellanic system. Our model predicts that the full sky may hold ∼100 ultra-faint galaxies with physical properties comparable to the DES satellites and that 20%–30% of these would be spatially associated with the Magellanic Clouds.

Key words: galaxies: dwarf – Local Group

1. INTRODUCTION

The population of Milky Way satellite galaxies includes the least luminous, least chemically enriched, and most dark matter dominated galaxies in the known universe (e.g., Simon & Geha 2007; Kirby et al. 2008). Although they are extreme systems from an observational perspective, low-luminosity dwarf spheroidal galaxies are likely to be the most common galaxy type by number. This duality places the emerging population of near-field galaxies in a unique position to allow the testing of models of galaxy formation and the cold dark matter paradigm (e.g., Bullock et al. 2001), and has motivated studies ranging from the physical conditions at the time of reionization (e.g., Bullock et al. 2000; Benson et al. 2002), to the particle properties of dark matter (e.g., Ackermann et al. 2015; Geringer-Sameth et al. 2015a).

Milky Way satellite galaxies are typically discovered as arcminute-scale statistical overdensities of individually resolved stars in wide-field optical imaging surveys (Willman 2010, and the references therein). Prior to 2005, there were 12 known "classical" Milky Way satellite galaxies with absolute magnitudes in the range $-8\,\mathrm{mag} \gtrsim M_V \gtrsim -18\,\mathrm{mag}$ (McConnachie 2012). From 2005 to 2014, 15 ultra-faint satellite galaxies with $M_V \gtrsim -8\,\mathrm{mag}$ were identified in Sloan Digital Sky Survey (SDSS; York et al. 2000) data through a combination of systematic searches (Willman et al. 2005a, 2005b; Belokurov et al. 2006, 2007, 2008, 2009, 2010; Grillmair 2006, 2009; Sakamoto & Hasegawa 2006; Zucker et al. 2006a, 2006b; Irwin et al. 2007; Walsh et al. 2007) and dedicated spectroscopic follow-up observations (Kleyna et al. 2005; Muñoz et al. 2006; Martin et al. 2007; Simon & Geha 2007; Adén et al. 2009; Belokurov et al. 2009; Carlin et al. 2009; Geha et al. 2009; Koch et al. 2009; Walker et al. 2009; Koposov et al. 2011; Simon et al. 2011; Willman et al. 2011; Kirby et al. 2013). Several outer halo star clusters and/or more compact stellar systems of uncertain classification were reported during roughly the same period (e.g., Koposov et al. 2007; Walsh et al. 2009; Belokurov et al. 2010, 2014; Muñoz et al. 2012; Balbinot et al. 2013; Laevens et al. 2014; Kim & Jerjen 2015a; Kim et al. 2015b). Dwarf galaxies are distinguished from star clusters by having a dynamical mass that is substantially larger than the mass inferred from the luminous stellar population and/or a significant dispersion in stellar metallicities indicative of multiple generations of star formation and a gravitational potential deep enough to retain supernova ejecta (Willman & Strader 2012).

Since the beginning of 2015, a combination of new optical imaging surveys and a reanalysis of SDSS data have resulted in the detection of 14 additional Milky Way companions, tentatively classified as dwarf galaxies (Bechtol et al. 2015; Kim & Jerjen 2015b; Kim et al. 2015a; Koposov et al. 2015a; Laevens et al. 2015a, 2015b; Martin et al. 2015). The new galaxy candidates have been examined for their (lack of) neutral gas (Westmeier et al. 2015), possible association with the Magellanic Clouds (Deason et al. 2015; Yozin & Bekki 2015), and spatial distribution within the Galactic halo (Pawlowski et al. 2015), and have become targets for indirect dark matter searches (Drlica-Wagner et al. 2015; Geringer-Sameth et al. 2015b; Hooper & Linden 2015). The provisional classification of these stellar systems as dwarf galaxies relies on their low surface brightnesses, large physical sizes, large ellipticities, and/or large heliocentric distances. However, some of these objects lie in a region of size–luminosity space where the distinction between dwarf galaxy and globular cluster is ambiguous. Thus far, spectroscopic observations have confirmed that three of the recently discovered satellites, Reticulum II (Koposov et al. 2015b; Simon et al. 2015; Walker et al. 2015), Horologium I (Koposov et al. 2015b), and Hydra II (Kirby et al. 2015) possess the kinematic and chemical signatures of galaxies.

The Dark Energy Survey (DES; Abbott et al. 2005), which began science operations in late 2013, has already had a large impact on our census of Milky Way substructures. In the first year of DES data, nine new dwarf galaxy candidates were discovered in a region spanning less than 10% of the southern hemisphere (Bechtol et al. 2015; Kim & Jerjen 2015b; Koposov et al. 2015a).[39] Here, we present an extension of the analysis described in Bechtol et al. (2015), incorporating the second year of DES observations to expand the survey coverage from $\sim 1800\,\mathrm{deg}^2$ to $\sim 5000\,\mathrm{deg}^2$ (Figure 1). In Section 2, we discuss the data reduction and catalog generation steps applied to the two-year DES data set and the resulting unique catalog of calibrated objects. We review the various algorithms applied to the DES data to search for ultra-faint galaxies in Section 3 and describe our candidate selection criteria in Section 4. The eight most significant stellar overdensities that are unassociated with previously known systems are reported in Section 5. If these objects are confirmed to be ultra-faint dwarf galaxies, they will be named after their resident constellations—Cetus II (DES J0117–1725), Columba I (DES J0531–2801), Grus II (DES J2204–4626), Indus II (DES J2038–4609).[40] Reticulum III (DES J0345–6026), Tucana III (DES J2356–5935), Tucana IV (DES J0002–6051), and Tucana V (DES J2337–6316)—and named DES 2 through *N* if found to be globular clusters (e.g., Luque et al. 2015). We place the DES candidates in context with other known Local Group galaxies and the Magellanic system in Section 6, and we conclude in Section 7.

[39] The system Kim 2/DES J2108.8–5109/Indus I was discovered independently in a separate data set by Kim et al. (2015b) slightly before the DES announcement. With deeper observations, Kim et al concluded that this object is likely a star cluster, and we do not include it in our count of dwarf galaxy candidates.

[40] To distinguish DES J2038–4609 from Kim 2/DES J2108.8–5109/Indus I, we suggest that the new system be designated Indus II if determined to be a dwarf galaxy.

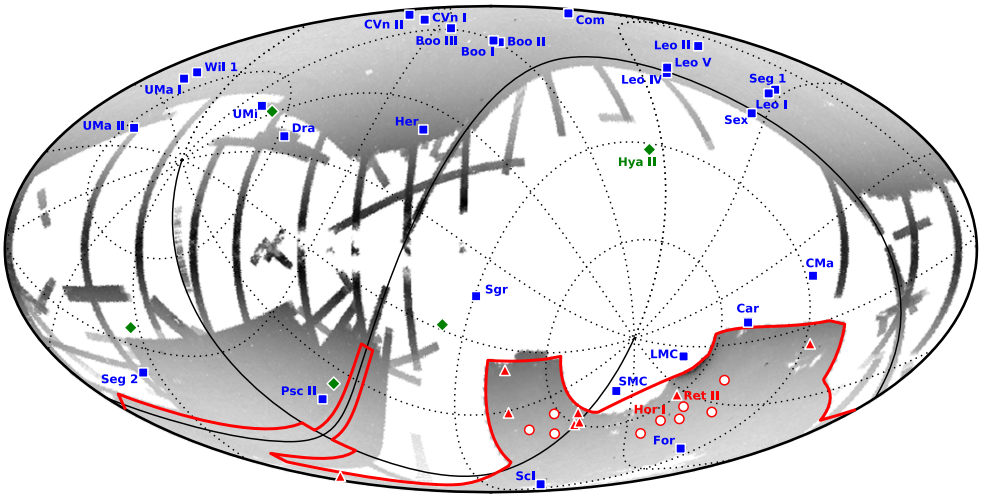

Figure 1. Locations of the eight new dwarf galaxy candidates reported here (red triangles) along with 9 previously reported dwarf galaxy candidates in the DES footprint (red circles; Bechtol et al. 2015; Kim & Jerjen 2015b; Koposov et al. 2015a), 5 recently discovered dwarf galaxy candidates located outside the DES footprint (green diamonds; Kim et al. 2015a; Laevens et al. 2015a, 2015b; Martin et al. 2015), and 27 Milky Way satellite galaxies known prior to 2015 (blue squares; McConnachie 2012). Systems that have been confirmed as satellite galaxies are individually labeled. The figure is shown in Galactic coordinates (Mollweide projection) with the coordinate grid marking the equatorial coordinate system (solid lines for the equator and zero meridian). The grayscale indicates the logarithmic density of stars with $r < 22$ from SDSS and DES. The two-year coverage of DES is $\sim$5000 deg^2 and nearly fills the planned DES footprint (outlined in red). For comparison, the Pan-STARRS 1 3π survey covers the region of sky with $\delta_{2000} > -30^\circ$ (Laevens et al. 2015a).

2. DATA SET

DES is an ongoing optical imaging survey of $\sim$5000 deg^2 in the south Galactic cap using the Dark Energy Camera (DECam; Flaugher et al. 2015) on the 4-m Blanco Telescope at Cerro Tololo Inter-American Observatory (CTIO). The DECam focal plane comprises 62 2k $\times$ 4k CCDs dedicated to science imaging and 12 2k $\times$ 2k CCDs for guiding, focus, and alignment. The DECam field of view covers 3 deg^2 with a central pixel scale of $0\farcs263$. DES is scheduled for 525 nights distributed over five years, during which period each point in the survey footprint will be imaged ten times in each of the *grizY* bands (Abbott et al. 2005).

The searches presented in Bechtol et al. (2015) and Luque et al. (2015) utilized an object catalog generated from the coadded images in the DES year-one annual release (Y1A1). To expedite the search for Milky Way satellites in year two, the present analysis uses data products derived from single-epoch imaging instead. This data set is referred to as the DES year-two quick release (Y2Q1), and its construction is summarized below.

2.1. DES Year-two Quick Release

Observations: The Y2Q1 data set consists of 26,590 DECam exposures taken during the first two years of DES observing that pass DES survey quality cuts. Slightly less than half of the DES survey area was observed during the first season (Y1; 2013 August 15–2014 February 9), with typically two to four overlapping exposures, referred to as "tilings," in each of the *grizY* filters. The second season (Y2; 2014 August 7–2015 February 15) covered much of the remaining survey area to a similar depth. Exposures taken in the *griz* bands are 90 s, while *Y*-band exposures are 45 s.

Image Reduction: The DES exposures were processed with the DES data management (DESDM) image detrending pipeline (Sevilla et al. 2011; Desai et al. 2012; Mohr et al. 2012; R.A. Gruendl et al. 2015, in preparation). This pipeline corrects for cross-talk between CCD amplifier electronics, bias level variations, and pixel-to-pixel sensitivity variations (flat-fielding). Additional corrections are made for nonlinearity, fringing, pupil, and illumination. Both the Y1 and Y2 exposures were reduced with the same image detrending pipeline used to process Y1A1.

Single-epoch Catalog Generation: Astronomical source detection and photometry were performed on a per exposure basis using the `PSFex` and `SExtractor` routines (Bertin & Arnouts 1996; Bertin 2011) in an iterative process (Mohr et al. 2012; R.A. Gruendl et al. 2015, in preparation). As part of this step, astrometric calibration was performed with `SCAMP` (Bertin 2006) by matching objects to the UCAC-4 catalog (Zacharias et al. 2013). The `SExtractor` source detection threshold was set at a signal-to-noise ratio (S/N) of S/N > 10 for the Y1 exposures, while for Y2 this threshold was lowered to S/N > 5 (the impact of this change on the stellar completeness is discussed in Section 2.2). During the catalog generation process, we flagged problematic images (e.g., CCDs suffering from reflected light, imaging artifacts, point-spread function (PSF) mis-estimation, etc.) and excluded the affected objects from subsequent analyses. The resulting photometric catalogs were ingested into a high-performance relational database system. Throughout the rest of this paper, photometric fluxes and magnitudes refer to `SExtractor` output for the PSF model fit.

Photometric Calibration: Photometric calibration was performed using the stellar locus regression technique (SLR: Ivezić et al. 2004; MacDonald et al. 2004; High et al. 2009; Gilbank et al. 2011; Coupon et al. 2012; Desai et al. 2012; Kelly et al. 2014). Our reference stellar locus was empirically derived from the globally calibrated DES Y1A1 stellar objects in the region of the Y1A1 footprint with the smallest $E(B-V)$ value from the Schlegel et al. (SFD; 1998) interstellar extinction map. We performed a $1''$ match on all Y1 and Y2 objects with S/N > 10 observed in *r*-band and at least one other band. We then applied a high-purity stellar selection

based on the weighted average of the spread_model quantity for the matched objects ($|$wavg_spread_model_$r|$ < 0.003; see below). The average zero point measured in Y1A1, $ZP_{grizY} = \{30.0, 30.3, 30.2, 29.9, 28.0\}$, was assigned to each star as an initial estimate. Starting from this coarse calibration, we began an iterative procedure to fix the color uniformity across the survey footprint. We segmented the sky into equal-area pixels using the HEALPix scheme (Górski et al. 2005). For each ∼0.2 deg^2 (resolution nside = 128) HEALPix pixel, we chose the DES exposure in each band with the largest coverage and ran a modified version of the Big MACS SLR code (Kelly et al. 2014)[41] to calibrate each star from the reference exposure with respect to the empirical stellar locus. These stars became our initial calibration standards. We then adjusted the zero points of other CCDs so that the magnitudes of the matched detections agreed with the calibration set from the reference exposure. CCDs with fewer than 10 matched stars or with a large dispersion in the magnitude offsets of matched stars ($\sigma_{ZP} > 0.1$ mag) were flagged. For each calibration star, we computed the weighted-average magnitude in each band using these new CCD zero points; this weighted-average magnitude was used as the calibration standard for the next iteration of the SLR. In the first iteration, we assigned SLR zero points to the calibration stars based on the HEALPix pixel within which they reside. In subsequent iterations, we assigned SLR zero points to the calibration stars based on a bi-linear interpolation of their positions onto the HEALPix grid of SLR zero points. After the second iteration, the color zero points were stable at the 1–2 mmag level. The absolute calibration was set against the 2MASS J-band magnitude of matched stars (making use of the stellar locus in color-space), which were de-reddened using the SFD map with a reddening law of $A_J = 0.709 \times E(B-V)_{SFD}$ from Schlafly & Finkbeiner (2011). The resulting calibrated DES magnitudes are thus already corrected for Galactic reddening by the SLR calibration.

Unique Catalog Generation: There is significant imaging overlap within the DES footprint. For our final high-level object catalog, we identified unique objects by performing a 0.″5 spatial match across all five bands. For each unique object, we calculated the magnitude in each filter in two ways: (1) taking the photometry from the single-epoch detection in the exposure with the largest effective depth,[42] and (2) calculating the weighted average (wavg) magnitude from multiple matched detections. During the catalog generation stage, we kept all objects detected in any two of the five filters (this selection is later restricted to the g- and r-band for our dwarf galaxy search). The process of combining catalog-level photometry increases the photometric precision, but does not increase the detection depth.

The resulting Y2Q1 catalog covers ∼5100 deg^2 in any single band, ∼5000 deg^2 in both the g- and r-bands, and ∼4700 deg^2 in all five bands. The coverage of the Y2Q1 data set is shown in Figure 1. The Y2Q1 catalog possesses a median relative astrometric precision of ∼40 mas per coordinate and a median absolute astrometric uncertainty of ∼140 mas per coordinate when compared against UCAC-4. The median absolute photometric calibration agrees within ∼3% with the de-reddened global calibration solution of Y1A1 in the overlap region in the $griz$ bands. When variations in the reddening law are allowed, this agreement improves to $\lesssim$1%. The color uniformity of the catalog is ∼1% over the survey footprint (tested independently with the red sequence of galaxies). The Y2Q1 catalog has a median point-source depth at an S/N = 10 of $g = 23.4$, $r = 23.2$, $i = 22.4$, $z = 22.1$, and $Y = 20.7$.

2.2. Stellar Object Sample

We selected stars observed in both the g- and r-bands from the Y2Q1 unique object catalog following the common DES prescription based on the wavg_spread_model and spreaderr_model morphological quantities (e.g., Chang et al. 2015; Koposov et al. 2015a). Specifically, our stellar sample consists of well-measured objects with $|$wavg_spread_model_$r| < 0.003 +$ spreaderr_model_r, flags_$\{g, r\} < 4$, and magerr_psf_$\{g, r\} < 1$. By incorporating the uncertainty on spread_model, it is possible to maintain high stellar completeness at faint magnitudes while achieving high stellar purity at bright magnitudes. We sacrificed some performance in our stellar selection by using the r-band spread_model, which has a slightly worse PSF than the i-band; however, relaxing the requirement on i-band coverage increased the accessible survey area.

The stellar completeness is the product of the object detection efficiency and the stellar classification efficiency. As described in Section 2.1, different source detection thresholds were applied to the individual Y1 and Y2 exposures, and accordingly, the detection efficiency for faint objects in Y2Q1 varies across the survey footprint. We used a region of the DES Science Verification data set (SVA1), imaged to full survey depth (i.e., ∼10 overlapping exposures in each of $grizY$), to estimate the object detection completeness using the individual Y1 exposures. For the Y2 exposures, we instead compared to publicly available catalogs from the Canada–France–Hawaii Telescope Lensing Survey (CFHTLenS; Erben et al. 2013). In both cases, the imaging for the reference catalog is ∼2 mag deeper than the Y2Q1 catalog. These comparisons show that the Y2Q1 object catalog is >90% complete at about 0.5 mag brighter than the S/N = 10 detection limit.

We estimated the stellar classification efficiency by comparing to CFHTLenS and by using statistical estimates from the Y2Q1 data alone. For the CFHTLenS matching, we identified probable stars in the CFHTLenS catalog using a combination of the class_star output from SExtractor and the fitclass output from the lensfit code (Heymans et al. 2012). Specifically, our CFHTLenS stellar selection was (fitclass = 1) OR (class_star > 0.98), and our galaxy selection was (fitclass = 0) OR (class_star < 0.2). Comparing against the DES stellar classification based on spread_model, we found that the Y2Q1 stellar classification efficiency exceeds 90% for $r < 23$ mag, and falls to ∼80% by $r = 24$ (Figure 2). We independently estimated the stellar classification efficiency by creating a test sample of Y2Q1 objects with high stellar purity using the color-based selection $r - i > 1.7$. We then applied the spread_model morphological stellar selection to evaluate the stellar completeness for the test sample. The stellar selection efficiency determined by the color-based selection test is in good agreement with that from the CFHTLenS comparison.

For a typical field at high Galactic latitude, the stellar purity is ∼50% at $r = 22.5$ mag, and falls to ∼10% at the faint magnitude limit (Figure 2). In other words, the majority of faint objects in the "stellar sample" are misclassified galaxies rather

[41] https://code.google.com/p/big-macs-calibrate/

[42] The effective depth is calculated from the exposure time, sky brightness, seeing, and atmospheric transmission (Neilsen et al. 2015).

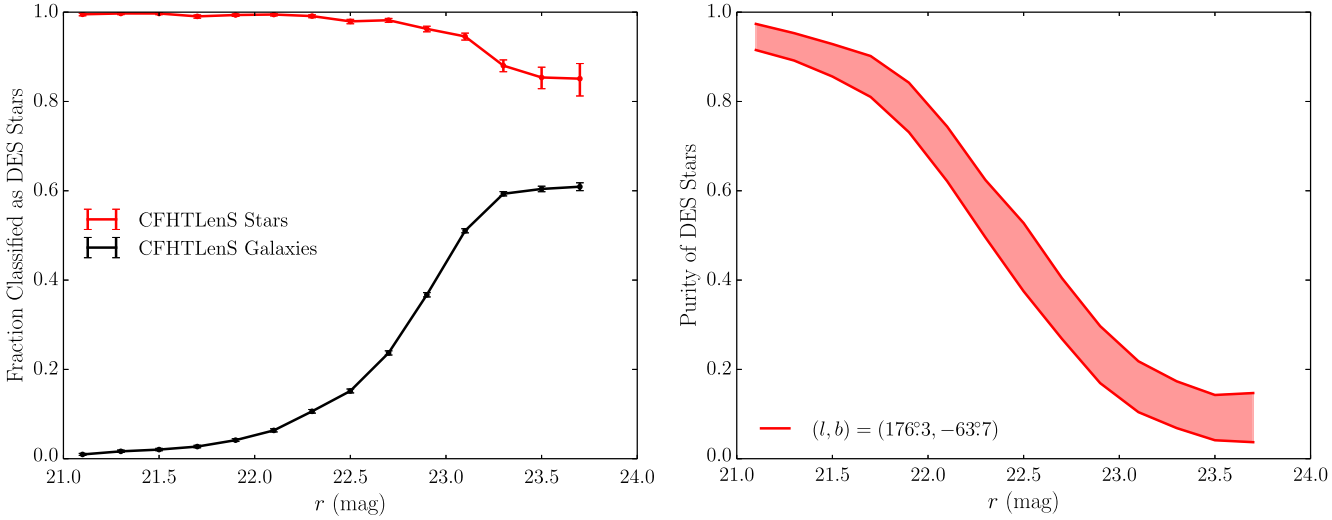

Figure 2. Performance of the morphological stellar classification based on |wavg_spread_model_r| < 0.003 + spreaderr_model_r was evaluated by comparing against deeper CFHTLenS imaging (Section 2.2). Left: fraction of CFHTLenS-classified stars and galaxies that pass our DES stellar selection criteria. Right: stellar purity evaluated in a typical high-Galactic latitude field centered at Galactic coordinates (l, b) = (176.°3, −63.°7). The shaded region represents the uncertainty associated with objects that are not confidently classified as either stars or galaxies with CFHTLenS. If a large fraction of these ambiguous objects are true stars, the inferred stellar purity for DES is near the upper bound of the indicated range.

than foreground halo stars.[43] This transition can be seen in the color–magnitude distribution diagnostic plots for individual candidates (Section 6.1).

3. SEARCH METHODS

In this section we describe three complementary search strategies that were used to identify overdensities of individually resolved stars matching the old and metal-poor populations that are characteristic of ultra-faint galaxies. Each technique used a different method to estimate the spatially varying field density and to select potential satellite member stars. The output of each search method was a set of seed coordinates, (α_{2000}, δ_{2000}, $m - M$), corresponding to statistical excesses relative to the local field density. These seeds were cross-matched between methods and examined in greater detail (Section 5).

When searching for new stellar systems, each detection algorithm applied a deep magnitude threshold ($g < 23.5$ mag or $g < 24$ mag depending on the search technique). At these faint magnitudes, our stellar sample is far from complete (Section 2.2). However, real stellar systems are dominated by faint stars, and the signal-to-noise ratio for satellite discovery can increase by including objects that are fainter than the stellar completeness limit. After candidate systems were identified, we applied a brighter magnitude threshold ($g < 23$ mag) to avoid biasing the fit results during object characterization (Section 5).

One potential concern when extending our search to very faint magnitudes is the increased contamination from misclassified galaxies (Section 2.2). However, as long as the contaminating objects have a similar statistical distribution in the target region and the surrounding area, each technique naturally incorporates the increased object density into the background estimate. There are situations where the assumption of uniformity does not apply (e.g., clusters of galaxies, variations in survey depth, gaps in coverage, etc.); therefore, when assembling our candidate list, we also examined the distribution of probable galaxies as well as stars with colors far from the expected isochrone (Section 5).

We briefly describe our three search strategies below.

3.1. Stellar Density Maps

Our most straightforward and model-independent search technique used a simple isochrone filter to facilitate visual inspection of the stellar density field. The specific algorithm was a variant of the general approach described in Section 3.1 of Bechtol et al. (2015) and follows from the methods of Koposov et al. (2008), Walsh et al. (2009), and Kim & Jerjen (2015a).

We first increased the contrast of putative satellite galaxies by selecting stars that were consistent with the isochrone of an old ($\tau = 12$ Gyr) and metal-poor ($Z = 0.0001$) stellar population (Dotter et al. 2008). Specifically, we selected stars within 0.1 mag of the isochrone locus in color–magnitude space, enlarged by the photometric measurement uncertainty of each star added in quadrature. After isochrone filtering, we smoothed the stellar density field with a $2'$ Gaussian kernel. For each density peak in the smoothed map, we scanned over a range of radii ($1'$–$18'$) and computed the Poisson significance of finding the observed number of stars within each circle centered on the density peak given the local field density. This process was repeated for stellar populations at a range of distance moduli (16 mag $\leqslant m - M \leqslant$ 24 mag) and diagnostic plots were automatically generated for each unique density peak. Our nominal magnitude threshold for this search was $g < 24$ mag; however, in regions on the periphery of the survey with large variations in coverage we used a brighter threshold of $g < 23$ mag.

3.2. Matched-filter Search

Our second search strategy utilized a matched-filter algorithm (Balbinot et al. 2011, 2013; Luque et al. 2015). We began by binning objects in our stellar sample with 17 mag

[43] This conclusion differs from that of Koposov et al. (2015a), who state that low levels of contamination are observed to the magnitude limit of DES.

$< g < 24$ mag into $1' \times 1'$ spatial pixels and g versus $g-r$ color–magnitude bins of 0.01 mag $\times$ 0.05 mag. We then created a grid of possible simple stellar populations modeled with the isochrones of Bressan et al. (2012) and populated according to a Chabrier (2001) initial mass function to use as signal templates. The model grid spanned a range of distances (10 kpc $< D <$ 200 kpc), ages ($9 < \log_{10}\tau < 10.2$), and metallicities ($Z = \{0.0002, 0.001, 0.007\}$). The color–magnitude distribution of the field population was empirically determined over larger $10^\circ \times 10^\circ$ regions. For each isochrone in the grid, we then fit the normalization of the simple stellar population in each spatial pixel to create a corresponding density map for the full Y2Q1 area.

The set of pixelized density maps do not assume a spatial model for the stellar system, and can be used to search for a variety of stellar substructures (e.g., streams and diffuse clouds). To search specifically for dwarf galaxies, we convolved the density maps with Gaussian kernels having widths ranging from $0'$ (no convolution) to $9'$ and used `SExtractor` to identify compact stellar structures in those maps. This convolution and search was performed on each map for our grid of isochrones. The resulting seeds were ranked according to their statistical significance and by the number of maps in which they appeared, i.e., the number of isochrones for which an excess was observed.

3.3. Likelihood-based Search

Our third search technique was a maximum-likelihood-based algorithm that simultaneously used the full spatial and color–magnitude distribution of stars, as well as photometric uncertainties and information about the survey coverage. The likelihood was constructed from the product of Poisson probabilities for detecting each individual star given its measured properties and the parameters that describe the field population and putative satellite (Section 3.2 of Bechtol et al. 2015). When searching for new stellar systems, we used a spherically symmetric Plummer model as the spatial kernel, and a composite isochrone model consisting of four isochrones of different ages, $\tau = \{12\,\mathrm{Gyr}, 13.5\,\mathrm{Gyr}\}$, and metallicities, $Z = \{0.0001, 0.0002\}$, to bracket a range of possible stellar populations (Bressan et al. 2012). We scanned the Y2Q1 data testing for the presence of a satellite galaxy at each location on a multi-dimensional grid of sky position ($0.^\circ7$ resolution; `HEALPix` nside = 4096), distance modulus (16 mag $< m - M <$ 23 mag), and kernel half-light radius ($r_h = \{0.^\circ03, 0.^\circ1, 0.^\circ3\}$). For the likelihood search, we restricted our magnitude range to 16 mag $< g <$ 23.5 mag as a compromise between survey depth and stellar completeness. The statistical significance of a putative galaxy at each grid point was expressed as a test statistic (TS) based on the likelihood ratio between a hypothesis that includes a satellite galaxy versus a field-only hypothesis (Equation (4) of Bechtol et al. 2015). As a part of the model fitting, the satellite membership probability is computed for every star in the region of interest. These photometric membership probabilities can be used to visualize which stars contribute to the candidate detection significance (Section 5) and have previously been used to select targets for spectroscopic follow-up (Simon et al. 2015; Walker et al. 2015).

4. CANDIDATE SELECTION

The search methods described in Section 3 each produced a set of seed locations (α_{2000}, δ_{2000}, $m - M$) for overdensities in the stellar field and a significance associated with each seed. Before performing a computationally intensive multi-parameter likelihood fit to characterize each seed, we applied a set of simple selection cuts to remove seeds that are unlikely to be new Milky Way satellites. We set detection significance thresholds at $>5.5\sigma$ for the stellar density map search and TS > 45 ($\sim 6\sigma$) for the maximum-likelihood search. For the matched-filter method, the ten highest-ranked seeds were selected from each $10^\circ \times 10^\circ$ search region. After thresholding, the union of all three search techniques yielded several hundred unique seeds. Many of these seeds were attributed to steep gradients in the stellar density field, numerical effects near the survey boundaries, and imaging artifacts. We also compared against catalogs of other astrophysical objects that produce false positives, such as large nearby galaxies (Nilson 1973; Corwin 2004) and galaxy clusters (Rykoff et al. 2014). These objects were removed from our list of candidates and we did not pursue investigation at lower significance thresholds due to an increased false positive rate.

The resulting list of seeds was matched against catalogs of known Local Group galaxies (McConnachie 2012) and star clusters (Harris 1996, 2010 edition; Kharchenko et al. 2013). Some of the most prominent stellar systems in our list of seeds were the Fornax, Phoenix, Sculptor,[44] and Tucana dwarf galaxies, and the globular clusters AM 1, Eridanus, Reticulum, Whiting 1, NGC 288, NGC 1261, NGC 1851, NGC 1904, and NGC 7089. Additionally, seed locations were compared against other stellar overdensities recently reported in the DES footprint (Bechtol et al. 2015; Kim et al. 2015b; Koposov et al. 2015a; Kim & Jerjen 2015b; Luque et al. 2015) and all 11 objects were recovered with high significance. The locations of previously known stellar systems in the DES footprint are shown in Figure 3.

As an additional test of the physical nature of the $\sim$30 highest significance unassociated seeds, we explored the posterior probability density of the likelihood with an affine invariant Markov Chain Monte Carlo (MCMC) ensemble sampler (MCMC; Foreman-Mackey et al. 2013).[45] This step was meant as a preliminary investigation of whether the posterior distribution was well-constrained by the data. We fixed the distance modulus of each object at the value that maximized the likelihood in the grid search (Section 16) and sampled the morphological parameters (center position, extension, ellipticity, and position angle) along with the richness of the putative stellar system. We imposed a Jeffreys' prior on the extension ($\mathcal{P}(a_h) \propto 1/a_h$) and flat priors on all other parameters. The posterior probability was sampled with 2.5×10^5 steps and we rejected seeds that lacked a well-defined maximum in the posterior.

The process described above resulted in the selection of eight candidate stellar systems. Six of these candidates, DES J2204–4626 (Gru I), DES J2356–5935 (Tuc III), DES J0531–2801 (Col I), DES J0002–6051 (Tuc IV), DES J0345–6026 (Ret III), and DES J2337–6316 (Tuc V), are high-confidence detections in clean regions of the survey. The additional two candidates,

[44] The center of Sculptor lies in a hole in Y2Q1 coverage, though the outskirts are still detected at high significance.
[45] `emcee` v2.1.0: http://dan.iel.fm/emcee/

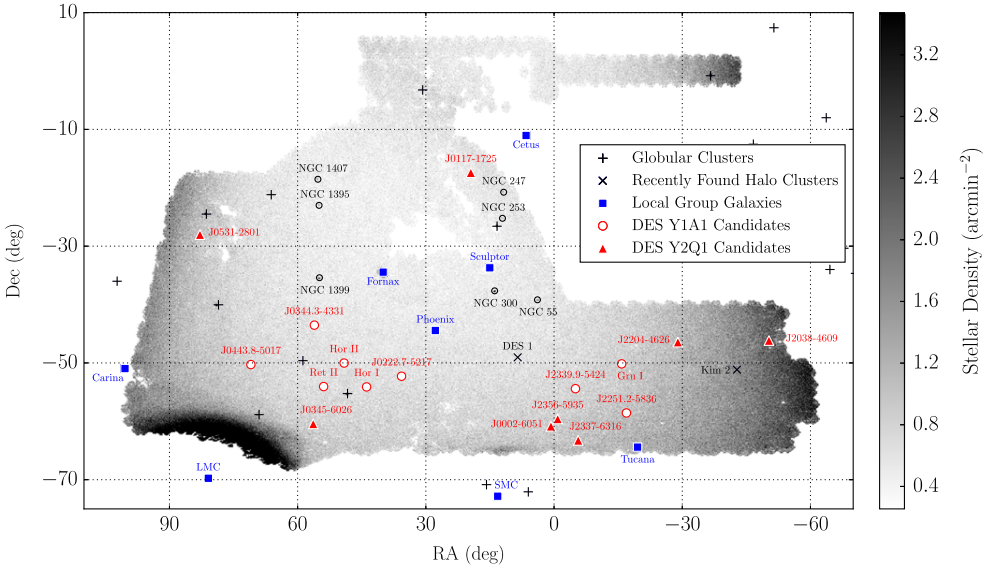

Figure 3. Cartesian projection of the density of stars observed in both the g- and r-bands with $g < 23$ and $g - r < 1$ over the DES Y2Q1 footprint (∼5000 deg^2). Globular clusters are marked with "+" symbols (Harris 1996, 2010 edition), two faint outer halo clusters are marked with "×" symbols (Kim et al. 2015b; Luque et al. 2015), Local Group galaxies known prior to DES are marked with blue squares (McConnachie 2012), dwarf galaxy candidates discovered in Y1 DES data are marked with red outlined circles, and the Y2 stellar systems are marked with red triangles. The periphery of the LMC can be seen in the southeast corner of the footprint, while the Galactic stellar disk can be seen on the eastern and western edges.

Table 1
Detection of Ultra-faint Galaxy Candidates

Name	α_{2000} (deg)	δ_{2000} (deg)	$m - M$	r_h ($'$)	a_h ($'$)	ϵ	ϕ	Map Sig. (σ)	TS Scan	$\sum p_i$
DES J2204–4626 (Gru II)	331.02	−46.44	18.62 ± 0.21	$6.0^{+0.9}_{-0.5}$	…	<0.2	…	15.7	369	161
DES J2356–5935 (Tuc III)[a]	359.15	−59.60	17.01 ± 0.16	$6.0^{+0.8}_{-0.6}$	…	…	…	11.1	390	168
DES J0531–2801 (Col I)[b]	82.86	−28.03	21.30 ± 0.22	$1.9^{+0.5}_{-0.4}$	…	<0.2	…	10.5	71	33
DES J0002–6051 (Tuc IV)	0.73	−60.85	18.41 ± 0.19	$9.1^{+1.7}_{-1.4}$	$11.8^{+2.2}_{-1.8}$	$0.4^{+0.1}_{-0.1}$	11 ± 9	8.7	287	134
DES J0345–6026 (Ret III)[b]	56.36	−60.45	19.81 ± 0.31	$2.4^{+0.9}_{-0.8}$	…	<0.4	…	8.1	56	22
DES J2337–6316 (Tuc V)	354.35	−63.27	18.71 ± 0.34	$1.0^{+0.3}_{-0.3}$	$1.8^{+0.5}_{-0.6}$	$0.7^{+0.1}_{-0.2}$	30 ± 5	8.0	129	24
DES J2038–4609 (Ind II)[b]	309.72	−46.16	21.65 ± 0.16	$2.9^{+1.1}_{-1.0}$	…	<0.4	…	6.0	32	22
DES J0117–1725 (Cet II)	19.47	−17.42	17.38 ± 0.19	$1.9^{+1.0}_{-0.5}$	…	<0.4	…	5.5	53	21

Notes. Characteristics of satellite galaxy candidates discovered in DES Y2 data. Best-fit parameters from the maximum-likelihood analysis assume a Bressan et al. (2012) isochrone. Uncertainties come from the highest density interval containing 68% of the posterior distribution. The uncertainty on the distance modulus ($m - M$) also includes systematic uncertainties coming from the choice of theoretical isochrone and photometric calibration (Section 5). The azimuthally averaged half-light radius (r_h) is quoted for all candidates. For systems with evidence for asphericity (Bayes' factor > 3), we quote the ellipticity (ϵ), the position angle (ϕ), and the length of the semimajor axis of the ellipse containing half of the light ($a_h = r_h/\sqrt{1-\epsilon}$). Upper limits on the ellipticity are quoted for other candidates at 84% confidence. "Map Sig." refers to detection significance of the candidate from the stellar density map search method (Section 3.1). "TS Scan" refers to the significance (Equation (4) in Bechtol et al. 2015) from the likelihood scan (Section 3.3). Σp_i is the estimated number of satellite member stars in the DES Y2Q1 catalog with $g < 23$ mag.
[a] Fit with a spherically symmetric Plummer profile due to the possible presence of tidal tails (Section 6.1).
[b] Fit with a composite isochrone: $\tau = \{12\,\mathrm{Gyr}, 13.5\,\mathrm{Gyr}\}$, $Z = \{0.0001, 0.0002\}$ (Section 5).

DES J2038–4609 (Ind II) and DES J0117–1725 (Cet II), are lower confidence and reside in more complicated regions. In Table 1 we report the coordinates and detection significances of each of these objects.

5. CANDIDATE CHARACTERIZATION

In this section, we describe the iterative procedure used to characterize each of the eight candidate stellar systems. When fitting the new candidates, we applied a brighter magnitude threshold, $g < 23$ mag, to mitigate the impact of stellar incompleteness. The results of our characterization are shown in Tables 1 and 2.

We began by simultaneously fitting the morphological parameters and distance modulus of each candidate following the procedure described in Section 4. Best-fit values were derived from the marginalized posterior distribution and the morphological parameters were temporarily fixed at these values. We then ran a MCMC chain simultaneously sampling the distance, age, metallicity, and richness, assuming flat priors on each parameter. Significant correlations between these parameters were found, and in some cases the age and metallicity were poorly constrained (see below). To assess the error contribution from intrinsic uncertainty in the isochrone, we resample the posterior distribution using the Dartmouth isochrone family (Dotter et al. 2008). In general, the best-fit distance moduli agree to within 0.1 mag when the data were fit

Table 2
Derived Properties of Ultra-faint Galaxy Candidates

Name	ℓ (deg)	b (deg)	Distance (kpc)	M_* (10^3 $M_\odot$)	M_V (mag)	$r_{1/2}$ (pc)	τ (Gyr)	Z
DES J2204–4626 (Gru II)	351.15	−51.94	53 ± 5	$3.4^{+0.3}_{-0.4}$	−3.9 ± 0.22	93 ± 14	12.5	0.0002
DES J2356–5935 (Tuc III)[a]	315.38	−56.19	25 ± 2	$0.8^{+0.1}_{-0.1}$	−2.4 ± 0.42	44 ± 6	10.9	0.0001
DES J0531–2801 (Col I)[b]	231.62	−28.88	182 ± 18	$6.2^{+1.9}_{-1.0}$	−4.5 ± 0.17	103 ± 25	…	…
DES J0002–6051 (Tuc IV)	313.29	−55.29	48 ± 4	$2.2^{+0.4}_{-0.3}$	−3.5 ± 0.28	127 ± 24	11.6	0.0001
DES J0345–6026 (Ret III)[b]	273.88	−45.65	92 ± 13	$2.0^{+0.6}_{-0.7}$	−3.3 ± 0.29	64 ± 24	…	…
DES J2337–6316 (Tuc V)	316.31	−51.89	55 ± 9	$0.5^{+0.1}_{-0.1}$	−1.6 ± 0.49	17 ± 6	10.9	0.0003
DES J2038–4609(Ind II)[b]	353.99	−37.40	214 ± 16	$4.9^{+1.8}_{-1.6}$	−4.3 ± 0.19	181 ± 67	…	…
DES J0117–1725 (Cet II)	156.48	−78.53	30 ± 3	$0.1^{+0.04}_{-0.04}$	0.0 ± 0.68	17 ± 7	10.9	0.0002

Notes. Derived properties of the DES Y2 satellite candidates. Stellar masses (M_*) are computed for a Chabrier (2001) initial mass function. The absolute visual magnitude is derived via the procedure of Martin et al. (2008) using the transformation equations from Bechtol et al. (2015). The uncertainty on the azimuthally averaged physical half-light radius ($r_{1/2}$) includes the uncertainty in the projected half-light radius and distance. Age (τ) and metallicity (Z) values come from the peak of the posterior distribution.
[a] Fit with a spherically symmetric Plummer profile due to the possible presence of tidal tails (Section 6.1).
[b] Fit with a composite isochrone: $\tau = \{12\,\mathrm{Gyr}, 13.5\,\mathrm{Gyr}\}$, $Z = \{0.0001, 0.0002\}$ (Section 5).

by these two isochrone classes. To determine the uncertainty on the distance modulus quoted in Table 1 we started with the highest posterior density interval from the Bressan et al. (2012) isochrone fit. We then calculated a systematic component from the difference in the best-fit distance modulus derived with Bressan et al. (2012) and Dotter et al. (2008) isochrones. An additional ±0.03 mag uncertainty was added to account for uncertainty in the photometric calibration. The age and metallicity values were taken from the peak of the marginalized posterior density from the Bressan et al. (2012) isochrone fit.

For the distant systems (i.e., DES J0531–2801, DES J2038–4609, and DES J0345–6026), the main-sequence turnoff (MSTO) is fainter than the $g < 23$ mag limit imposed for our fit. In these systems, the data provide weaker constraints on the age and metallicity. We therefore fit the distance modulus using a composite of four Bressan et al. (2012) isochrones with fixed ages, $\tau = \{12\,\mathrm{Gyr}, 13.5\,\mathrm{Gyr}\}$, and metallicities, $Z = \{0.0001, 0.0002\}$. We followed the procedure above to incorporate systematic uncertainties from the choice of theoretical isochrone family and from the calibration.[46]

Fixing the distance, age, and metallicity at the values derived in the previous step, we then re-fit the morphological parameters. The best-fit values of the morphological parameters and their highest posterior density intervals are listed in Table 1. The majority of objects show no significant evidence for ellipticity, which is confirmed by calculating the Bayes factor (BF) via the Savage–Dickey density ratio (Dickey 1971; Trotta 2007). For objects with evidence for asphericity (BF > 3), we report both the elliptical Plummer radius, a_h, and the position angle, ϕ. For all objects, we report the azimuthally averaged half-light radius, r_h. In the region of DES J2356–5935 there is a linear structure visible in the filtered stellar density map, consistent with a set of tidal tails (Section 6.1). We require the spatial profile of DES J2356–5935 to be azimuthally symmetric in the MCMC fit and analyze this linear feature separately.

The best-fit parameters derived from our iterative MCMC analysis along with several additional derived properties are reported in Tables 1 and 2. The physical size of each object was calculated by propagating the uncertainty from the distance and azimuthally averaged half-light radius. Absolute magnitudes were calculated according to the prescription of Martin et al. (2008) and do not include the distance uncertainty.

The two lower-confidence candidates are located in complicated regions of the survey. DES J0117–1725 is located in a region of sparse coverage and is close to both a CCD chip gap and a larger hole in the survey. DES J2038–4609 is located in a region of non-uniform depth at the interface of Y1 and Y2 observations. Although we have attempted to account for these issues in the likelihood fit, we caution that the parameters derived for these systems may be less secure than for the other candidates.

As a final note, the iterative MCMC fitting procedure described above was also applied to the satellite galaxy candidate Grus I (Koposov et al. 2015a). Grus I was identified in Y1A1 imaging data, but was located close to a CCD chip gap in a region with sparse coverage. We reanalyzed Grus I with the additional Y2 exposures and found that its structural parameters are consistent within uncertainties with those reported by Koposov et al. (2015a).

6. DISCUSSION

Spectroscopic observations are needed to definitively classify the newly discovered stellar systems as either star clusters or ultra-faint dwarf galaxies based upon their stellar dynamics and/or metallicity dispersions. However, the distances, physical sizes, and luminosities derived from DES photometry (Table 2) already suggest a galactic classification for many of the new candidates. In Figures 4 and 5, we show the distributions of physical half-light radius heliocentric distance versus absolute magnitude for Milky Way globular clusters (Harris 1996, 2010 edition) and Local Group galaxies (McConnachie 2012). We find that all of the systems discovered in Y2Q1 fall along the established locus for nearby galaxies. Several of the new systems possess lower surface brightnesses than any confirmed ultra-faint galaxy,[47] supporting earlier conclusions that the threshold in surface brightness was an observational selection effect (Koposov et al. 2008;

[46] One notable exception is the case of DES J2038–4609, where significant constraining power comes from a set of horizontal branch (HB) stars. For DES J2038–4609 we estimated the distance uncertainty from the Bressan et al. (2012) isochrone analysis alone.

[47] A potential exception to this statement is the large, faint, and perhaps tidally disrupted object Böotes III (Carlin et al. 2009).

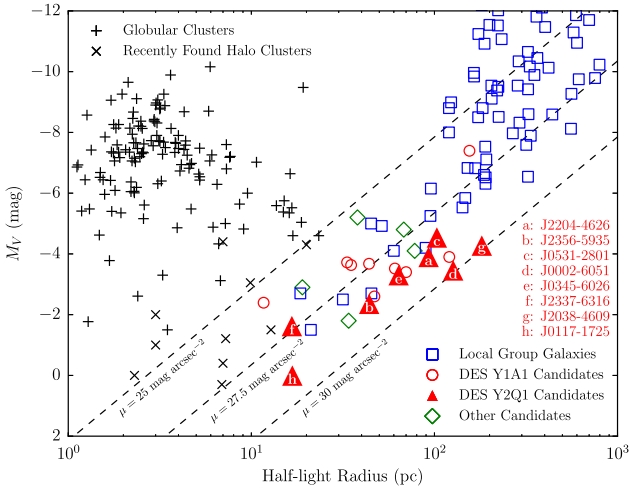

Figure 4. Local Group galaxies (McConnachie 2012) and globular clusters (Harris 1996, 2010 edition) occupy distinct regions in the plane of physical half-light radius (azimuthally averaged) and absolute magnitude. The majority of DES satellite candidates (red triangles and circles) are more consistent with the locus of Local Group galaxies (blue squares) than with the population of Galactic globular clusters (black "+"). Other recently reported dwarf galaxy candidates (green diamonds) include Hydra II (Martin et al. 2015), Triangulum II (Laevens et al. 2015b), Pegasus III (Kim et al. 2015a), Draco II, and Sagittarius II (Laevens et al. 2015a). Several outer halo star clusters and systems of ambiguous classification are indicated with "×" symbols: Koposov 1 and Koposov 2 (Koposov et al. 2007; Paust et al. 2014), Segue 3 (Belokurov et al. 2010; Fadely et al. 2011; Ortolani et al. 2013), Muñoz 1 (Muñoz et al. 2012), Balbinot 1 (Balbinot et al. 2013), Laevens 1 (Belokurov et al. 2014; Laevens et al. 2014), Laevens 3 (Laevens et al. 2015a), Kim 1 and Kim 2 (Kim & Jerjen 2015a; Kim et al. 2015b), and DES 1(Luque et al. 2015). The dashed lines indicate contours of constant surface brightness at $\mu = \{25, 27.5, 30\}$ magarcsec^{-2}.

Walsh et al. 2009). Finally, globular clusters generally have small ellipticities, $\epsilon \lesssim 0.2$ (van den Bergh 2008), while dwarf galaxies are commonly more elliptical (Martin et al. 2008). However, the ellipticities of many of the new objects are not well-constrained by the DES data and thus do not provide a strong indicator of the nature of these objects.

The spatial distribution of the new candidates within the DES footprint is suggestive of an association with the Magellanic Clouds (Section 6.3). When discussing this scenario, the coordinates of the Large Magellanic Cloud (LMC) are taken to be α_{2000}, δ_{2000}, $D_\odot$ = (80.°89, −69.°76, 49.89 kpc) (distance from de Grijs et al. 2014) and the coordinates of the Small Magellanic Cloud (SMC) are taken to be (α_{2000}, δ_{2000}, $D_\odot$) = (13.°19, − 72.°83, 61.94 kpc) (distance from de Grijs & Bono 2015).[48] While the new DES candidates reside in a region close to the Magellanic Stream, no candidate is found to be coincident with the main filament of the Stream. A similar observation was made by Koposov et al. (2015a) for the DES stellar systems discovered in Y1.

We also investigate a potential group of satellites in the constellation Tucana, consisting of DES J0002–6051 and DES J2337–6316, and the object DES J2251.2–5836 (Tuc II) discovered in Y1 data (Bechtol et al. 2015; Koposov et al. 2015a). The centroid of the Tucana group is at (α_{2000}, δ_{2000}, $D_\odot$) = (351.°90, −61.°06, 53.63 kpc), and the separation of each member from the centroid is $\lesssim$7 kpc (Table 3). This grouping of objects is projected onto a region of H I gas that is likely a secondary filament or high-velocity cloud associated with the head of the Magellanic Stream (Putman et al. 2003; McClure-Griffiths et al. 2009).

[48] Sky coordinates taken from NED: https://ned.ipac.caltech.edu

Table 3
Physical Separations of Ultra-faint Galaxy Candidates

Name	$D_\odot$ (kpc)	D_{GC} (kpc)	D_{LMC} (kpc)	D_{SMC} (kpc)	D_{Tuc} (kpc)
DES J2204–4626 (Gru II)	53	49	46	33	18
DES J2356–5935 (Tuc III)	25	23	32	38	28
DES J0531–2801 (Col I)	182	186	149	157	168
DES J0002–6051 (Tuc IV)	48	46	27	18	7
DES J0345–6026 (Ret III)	92	92	45	40	53
DES J2337–6316 (Tuc V)	55	52	29	14	3
DES J2038–4609 (Ind II)	214	208	193	170	169
DES J0117–1725 (Cet II)	30	32	46	51	40
DES J2251.2–5836 (Tuc II)	58	54	37	20	7

Note. Three-dimensional physical separation between DES satellite candidates and the LMC and SMC. Also listed is the heliocentric distance, the Galactocentric distance, and the separation to the centroid of the proposed Tucana group comprising DES J2251.2–5836, DES J0002–6051, and DES J2337–6316.

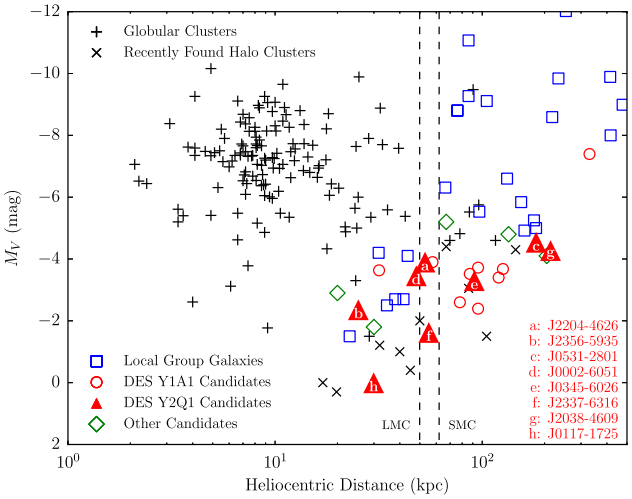

Figure 5. DES satellite galaxy candidates (red circles and triangles) have comparable luminosities to known Local Group galaxies (blue squares; McConnachie 2012) and other newly discovered galaxy candidates (green diamonds), but are typically found at larger distances. The dashed lines indicate the heliocentric distances of the LMC and SMC. Globular clusters (black "+" symbols, Harris 1996) and outer halo star clusters ("×" symbols) have been detected at comparable luminosities and distances due to their more compact nature. The constituents of each source class can be found in Figure 4.

6.1. Review of Individual Candidates

1. *DES J2204–4626* (Grus II, Figure 6): As the most significant new candidate, DES J2204–4626 has ∼161 probable member stars with $g < 23$ mag in the DES imaging. The large physical size of this system (93 pc) allows it to be tentatively classified as an ultra-faint dwarf galaxy. A clear red giant branch (RGB) and MSTO are seen in the color–magnitude diagram of DES J2204–4626. Several likely blue horizontal branch (BHB) members are seen at $g \sim 19$ mag. There is a small gap in survey coverage ∼0.°5 from the centroid of

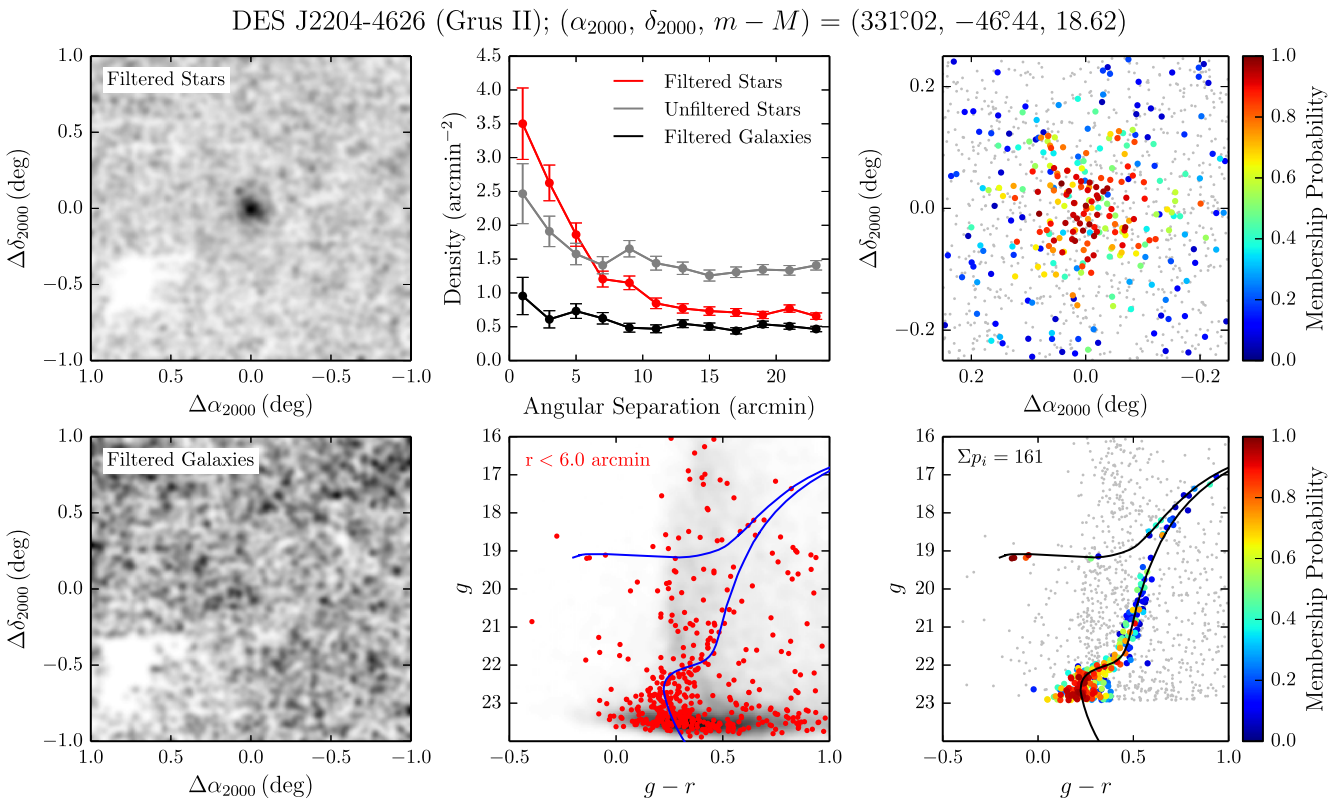

Figure 6. Stellar density and color–magnitude diagrams for DES J2204–4626 (Grus II). Top left: spatial distribution of stellar objects with $g < 24$ mag that pass the isochrone filter (see text). The field of view is $2° \times 2°$ centered on the candidate and the stellar distribution has been smoothed by a Gaussian kernel with standard deviation $1\farcm2$. Top center: radial distribution of objects with $g - r < 1$ mag and $g < 24$ mag: stars passing the isochrone filter (red), stars excluded from the isochrone filter (gray), and galaxies passing the isochrone filter (black). Top right: spatial distribution of stars with high membership probabilities within a $0\fdg5 \times 0\fdg5$ field of view. Small gray points indicate stars with membership probability less than 5%. *Bottom left*: same as top left panel, but for probable galaxies that pass the isochrone filter. Bottom center: the color–magnitude distributions of stars within $0\fdg1$ of the centroid are indicated with individual points. The density of the field within an annulus from radii of $0\fdg5$–$1\fdg0$ is represented by the background two-dimensional histogram in grayscale. The blue curve shows the best-fit isochrone as described in Tables 1 and 2. Bottom right: color–magnitude distribution of high membership probability stars.

DES J2204–4626, but this is accounted for in the maximum-likelihood analysis and should not significantly affect the characterization of this rich satellite.

DES J2204–4626 is from the LMC (46 kpc) and from the Galactic center (49 kpc). It is slightly closer to the SMC (33 kpc) and intriguingly close to the the group of stellar systems in Tucana (∼18 kpc). While it is unlikely that DES J2204–4626 is currently interacting with any of the other known satellites, we cannot preclude the possibility of a past association.

2. *DES J2356–5935* (Tucana III, Figure 7): DES J2356–5935 is another highly significant stellar system that presents a clearly defined main sequence and several RGB stars. The physical size and luminosity of DES J2356–5935 ($r_{1/2} = 44$ pc, $M_V = -2.4$ mag) are comparable to that of the recently discovered dwarf galaxy Reticulum II. At a distance of 25 kpc, DES J2356–5935 would be among the nearest ultra-faint satellite galaxies known, along with Segue 1 (23 kpc), Reticulum II (32 kpc), and Ursa Major II (32 kpc). The relative abundance of bright stars in DES J2356–5935 should allow for an accurate spectroscopic determination of both its velocity dispersion and metallicity. DES J2356–5935 is reasonably close to the LMC and SMC (32 kpc and 38 kpc, respectively), and measurements of its systemic velocity will help to elucidate a physical association.

As mentioned in Section 5, there is an additional linear feature in the stellar density field around DES J2356–5935 that strongly influences the fitted ellipticity of this galaxy candidate. In Figure 8, we show the $6° \times 6°$ region centered on DES J2356–5935, which contains this linear feature. Selecting stars with the same isochrone filter used to increase the contrast of DES J2356–5935 relative to the field population, we found a faint stellar overdensity extending ∼2° on both sides of DES J2356–5935. This feature has an FWHM of $\sim 0\fdg3$ (i.e., projected dimensions of 1.7 kpc × 130 pc at a distance of 25 kpc) and is oriented ∼85° east of north. The length of the feature and the smooth density field observed with an inverted isochrone filter support the conclusion that this is a genuine stellar structure associated with DES J2356–5935.

One interpretation is that DES J2356–5935 is in the process of being tidally stripped by the gravitational potential of the Milky Way. The relatively short projected length of the putative tails may imply that DES J2356–5935 is far from its orbital pericenter (where tidal effects are strongest) and/or that stripping began recently. Despite the possible presence of tidal tails, the

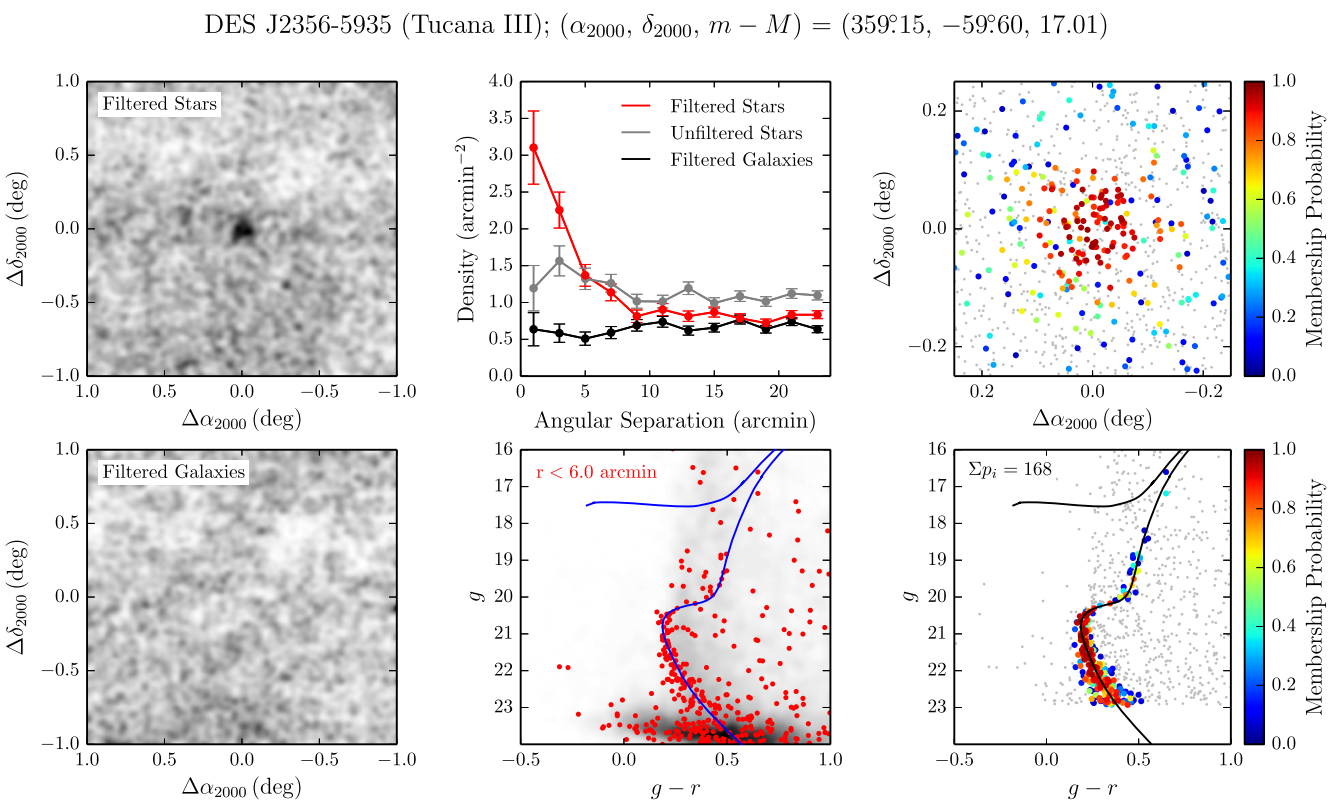

Figure 7. Analogous to Figure 6 but for DES J2356–5935 (Tucana III).

main body of DES J2356–5935 appears to be relatively round. While the proximity of DES J2356–5935 might make it an important object for indirect dark matter searches, evidence of tidal stripping would suggest that a large fraction of its outer dark matter halo has been removed. However, the mass within the stellar core (and therefore the dark matter content in the central region) can still likely be determined accurately (Oh et al. 1995; Muñoz et al. 2008; Peñarrubia et al. 2008).

3. *DES J0531–2801* (Columba I, Figure 9): DES J0531–2801 is the second most distant of the Y2 DES candidates (182 kpc) and is detected as a compact cluster of RGB stars. Both the BHB and red horizontal branch (RHB) appear to be well-populated. The distance, physical size (103 pc), and luminosity ($M_V = -4.5$ mag) of DES J0531–2801 place it in the locus of Local Group dwarf galaxies, comparable to Leo IV and CVn II (Belokurov et al. 2007). DES J0531–2801 is isolated from the other new DES systems and is likely not associated with the Magellanic system.
4. *DES J0002–6051* (Tucana IV, Figure 10): DES J0002–6051 has the largest angular size of the candidates ($r_h = 9.'1$), which at a distance of 48 kpc corresponds to a physical size of $r_{1/2} \sim 127$ pc. This large half-light radius is inconsistent with the sizes of known globular clusters (Harris 1996, 2010 edition), thus making it very likely that DES J0002–6051 is a dwarf galaxy. The measured ellipticity of DES J0002–6051, $\epsilon = 0.4$, is also consistent with a galactic classification. DES J0002–6051 is found to be 27 kpc from the LMC and 18 kpc from the SMC. DES J0002–6051 is one of the proposed members of the Tucana group, with a centroid separation of 7 kpc. Measurements of the radial velocity and proper motion of DES J0002–6051 will provide strong clues as to whether it was accreted as part of a system of satellites. Similar to DES J2356–5935 and DES J2204–4626, the MSTO of DES J0002–6051 is well-populated and clearly visible. Several possible member stars can also be seen along the HB.
5. *DES J0345–6026* (Reticulum III, Figure 11): DES J0345–6026 appears to be similar to DES J2204–4626 in its structural properties, but is more distant (heliocentric distance of 92 kpc). Like DES J2204–4626, DES J0345–6026 can be tentatively classified as a dwarf galaxy based on its physical size and low surface brightness. There is some indication of asphericity for this object; however, the ellipticity is not significantly constrained by the DES data. DES J0345–6026 has a sparsely populated RGB, a few possible RHB members, and two possible BHB members. The MSTO for DES J0345–6026 is slightly fainter than our fitting threshold of $g < 23$ mag, thus its age is poorly constrained.
6. *DES J2337–6316* (Tucana V, Figure 12): DES J2337–6316 is the second new system in the Tucana group and is the closest to the group's centroid (3 kpc). At a heliocentric distance of 55 kpc, DES J2337–6316 is also located 29 kpc from the LMC and 14 kpc from the SMC. The physical size (17 pc) and luminosity ($M_V \sim -1.6$ mag) place DES J2337–6316 in a region of the size–luminosity plane close to Segue 1, Willman 1, and Kim 2. Segue 1 and Willman 1 have sizes similar to the most extended globular clusters, but are approximately an order of magnitude less luminous. On the other hand, deep imaging of Kim 2 has led Kim et al. (2015b) to

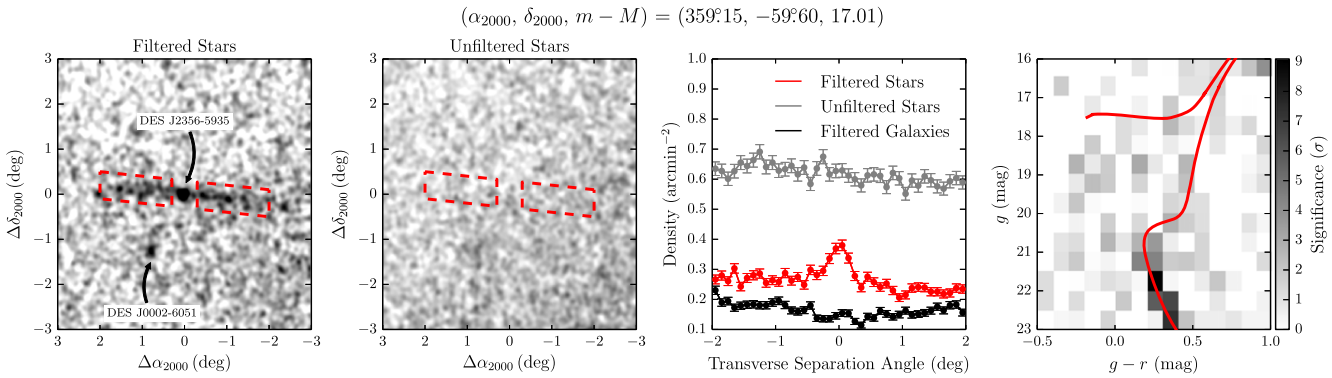

Figure 8. Possible tidal tails around DES J2356–5935 (Tucana III). Left: spatial distribution of stellar objects with $g < 23$ mag that pass the same isochrone filter as applied to visualize DES J2356–5935 (Figure 7). Red boxes highlight the positions of the tidal tails. Middle left: spatial distribution of stellar objects with $g - r < 1$ mag and $g < 23$ mag not passing the isochrone filter. Middle right: average density profiles transverse to the tidal tail axis: stars passing the isochrone filter (red), other unfiltered stars (gray), and galaxies passing the isochrone filter (black). For the density calculation, the range of included angles parallel to the tidal tails is $\pm 2.^{\circ}0$, excluding the region within $0.^{\circ}3$ of DES J2356–5935. Right: binned significance diagram representing the Poisson probability of detecting the observed number of stars within $0.^{\circ}2$ of the tidal tail axis (excluding the region within $0.^{\circ}3$ of DES J2356–5935) for each bin of the color–magnitude space given the local field density.

conclude that it is very likely a star cluster. DES J2337–6316 is one of the few new objects for which the DES data places a constraint on ellipticity. The high ellipticity, $\epsilon = 0.7$, supports a galactic classification for DES J2337–6316. Most of the high probability member stars for DES J2337–6316 are on the main sequence and fainter than $g \sim 22.5$ mag. As with other similarly faint objects, a few stars situated close to the lower RGB are also likely members. A system similar to DES J2337–6316 would have been difficult to detect in SDSS with a threshold at $r < 22$.

7. *DES J2038–4609* (Indus II, Figure 13): DES J2038–4609 is the first of the two lower-confidence candidates. The detection of this object comes predominantly from a tight clump of BHB stars at $g \sim 22$ mag and $g-r \sim 0$ mag. Three of the potential HB members are clustered within a spatial region of radius $\sim 10'$. Several additional HB and RGB stars are assigned non-zero membership probabilities by the likelihood fit, enlarging the best-fit size of this system. DES J2038–4609 is located at a boundary between the Y1 and Y2 imaging, and the effect of the deeper Y2 source detection threshold is visible when extending to magnitudes of $g > 23$ mag. The best-fit physical size of DES J2038–4609 (181 pc) would place it among the population of Local Group galaxies. Deeper imaging is needed to better characterize this candidate since the MSTO is fainter than the current DES detection threshold.
8. *DES J0117–1725* (Cetus II, Figure 14): DES J0117–1725 is the second lower-confidence candidate, being the least luminous ($M_V = 0.0 \pm 0.68$ mag) and most compact ($r_{1/2} = 17$ pc) of the new stellar systems. DES J0117–1725 is nearly two orders of magnitude fainter than globular clusters with comparable half-light radii. At a heliocentric distance of 30 kpc, DES J0117–1725 is the second nearest of the new systems. DES J0117–1725 is detected predominantly by its main sequence stars and has one potential HB member. The lack of strong features in the color–magnitude distribution of stars associated with DES J0117–1725 leads to a large degeneracy between the distance, age, and metallicity of this system. If determined to be a dwarf galaxy, DES J0117–1725 would be the least luminous known galaxy; however, the current classification of this object is ambiguous.

There are several gaps in the Y2Q1 coverage $\sim 0.^{\circ}1$ from DES J0117–1725; however, DES J0117–1725 is sufficiently compact that few member stars are expected in the region of missing coverage. These gaps are incorporated into the likelihood analysis and should have a minimal impact on the fit. The region around DES J0117–1725 was imaged in only a single r-band exposure; however, there are two to three overlapping exposures in each of the g- and i-bands. We have verified that the stellar overdensity is also apparent in the $g-i$ filter combination. Nonetheless, the properties of DES J0117–1725 should be interpreted with caution until additional imaging is acquired.

6.2. Satellite Detection Completeness

Many studies of the Milky Way satellite galaxy population require knowledge of the detection efficiency for satellites as a function of luminosity, heliocentric distance, physical size, and sky position in order to account for observational selection effects. To quantify our search sensitivity with the Y2Q1 data set, we follow the approach that Bechtol et al. (2015) applied to the DES Y1A1 coadd data. Briefly, we generated many realizations of satellite galaxies with different structural properties that are spread uniformly throughout the survey footprint, excluding regions of high stellar density near to the LMC. We then applied the map-based search algorithm to estimate the likelihood of a high-confidence detection. In the present implementation, the detection significance was evaluated as the Poisson probability of finding the "observed" number of stars within a circular region matched to the half-light radius of the simulated satellite given the effective local field density after the isochrone selection (see Section 3.1). Realizations that yield at least 10 detectable stars and produce a $>5.50\sigma$ overdensity within the half-light radius are considered "detected."

An essential input to the completeness calculation is the magnitude threshold for individual stars. For the searches described in Section 3, we used deeper magnitude thresholds (e.g., $g < 24$ mag) in order to maximize the discovery potential. A more conservative threshold, $g < 23$ mag, is selected to estimate the completeness in detecting new stellar systems

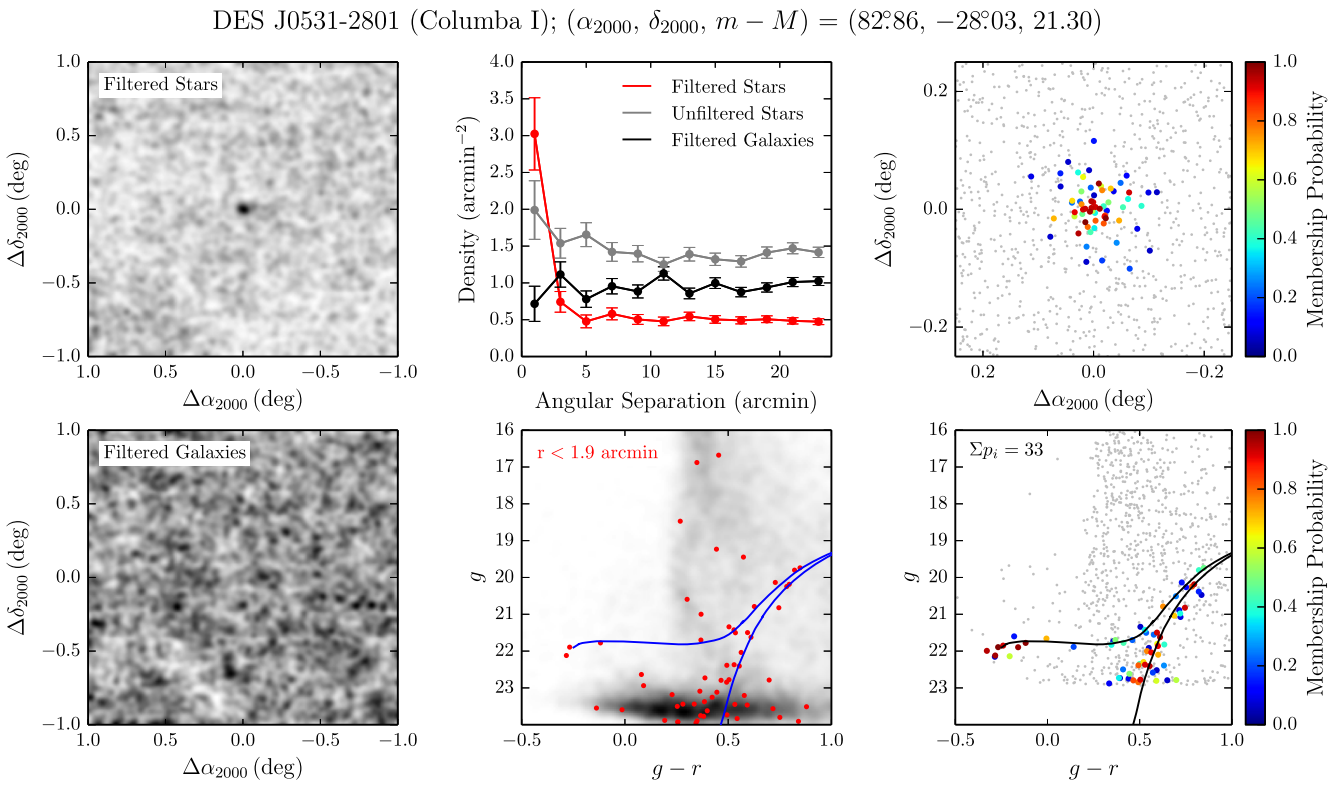

Figure 9. Analogous to Figure 6 but for DES J0531–2801 (Columba I).

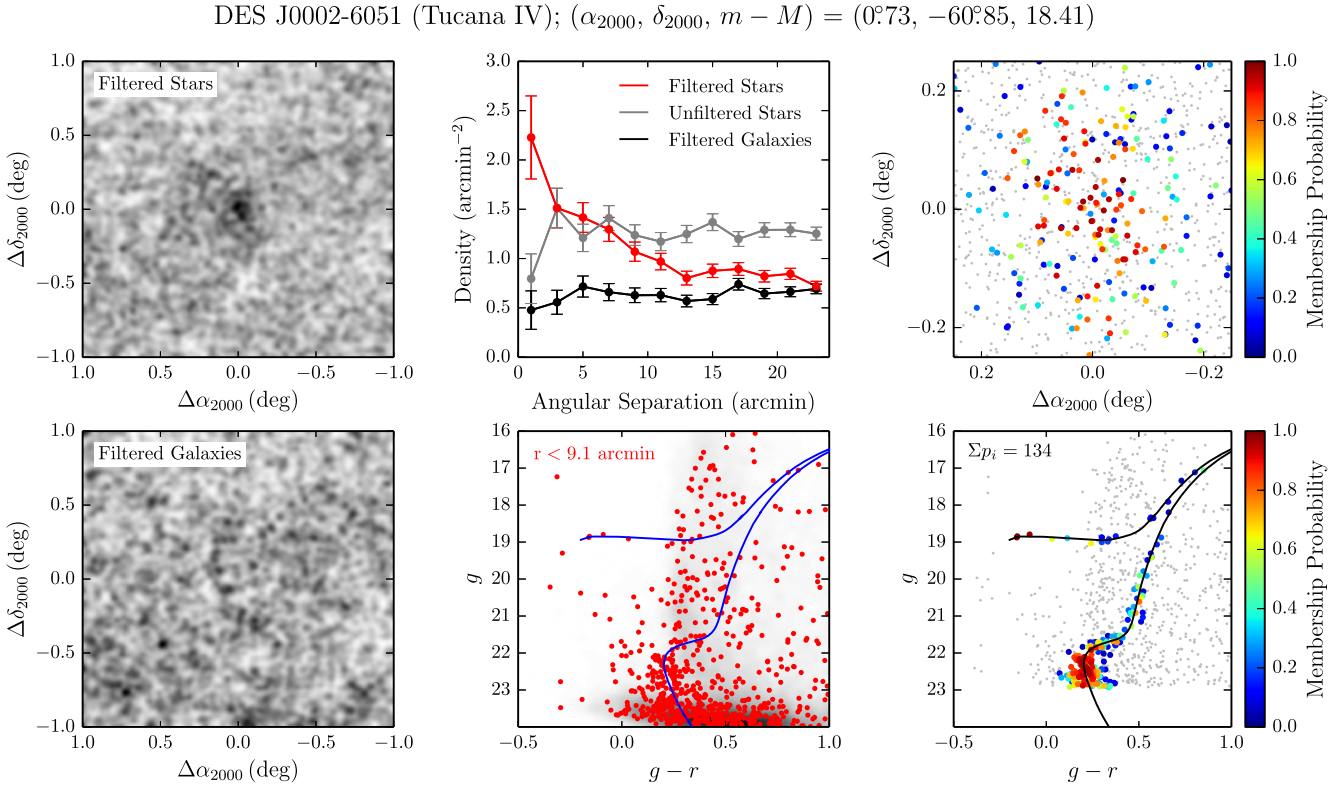

Figure 10. Analogous to Figure 6 but for DES J0002–6051 (Tucana IV).

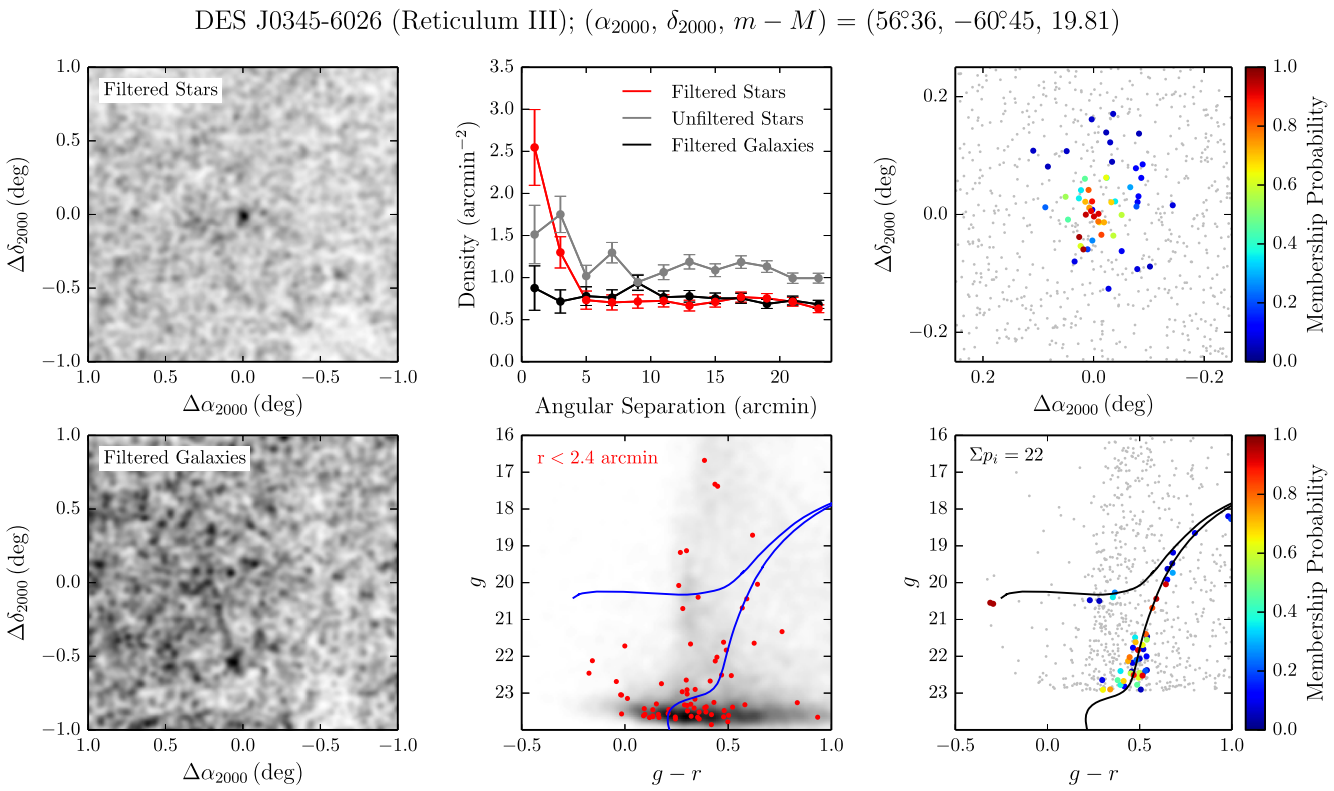

Figure 11. Analogous to Figure 6 but for DES J0345–6026 (Reticulum III).

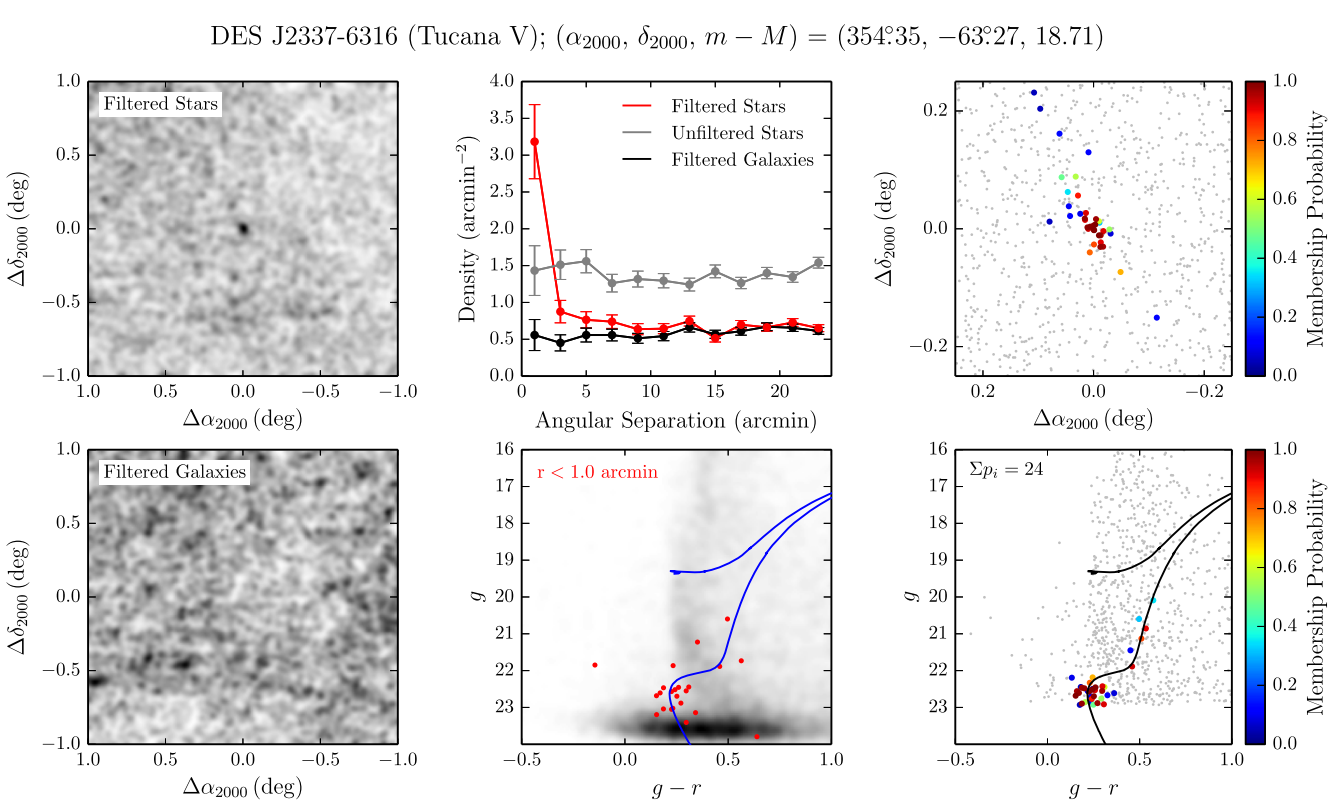

Figure 12. Analogous to Figure 6 but for DES J2337–6316 (Tucana V).

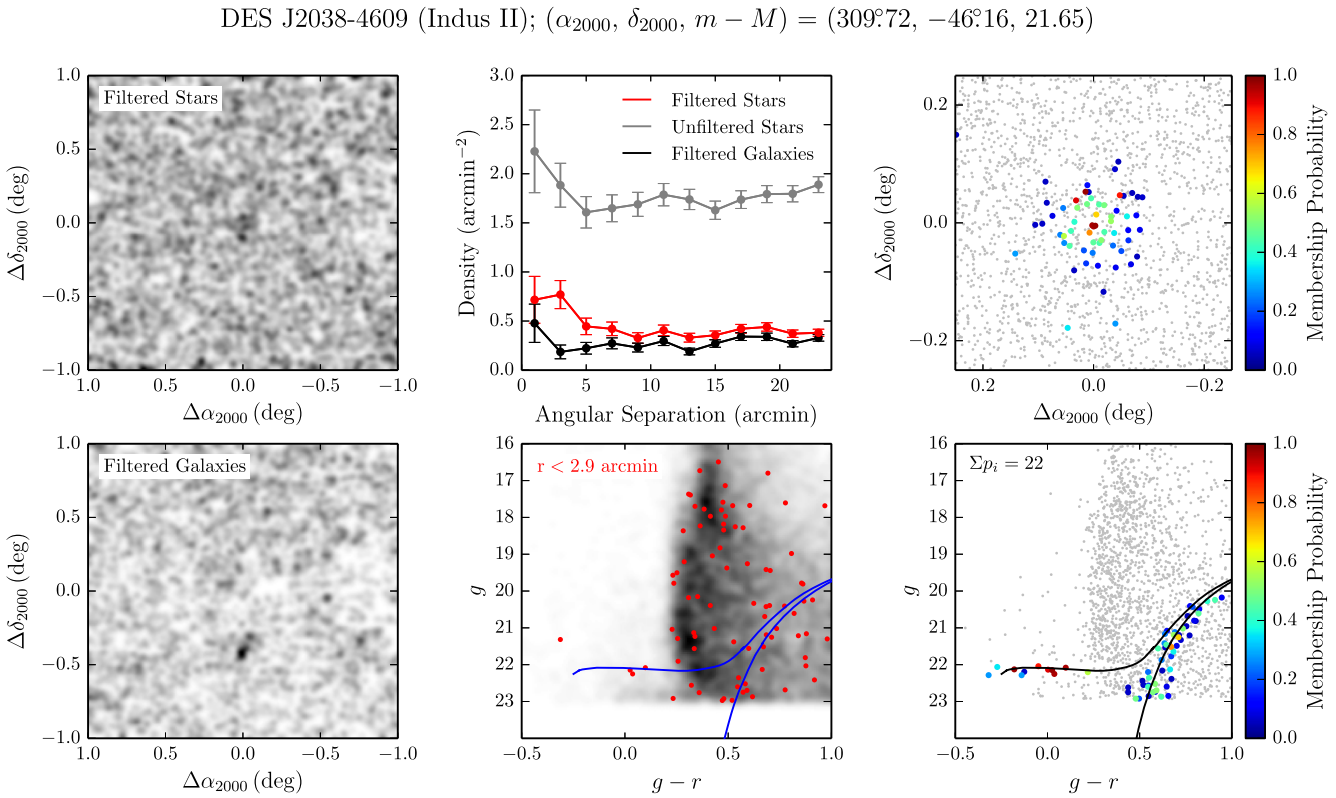

Figure 13. Analogous to Figure 6 but for DES J2038–4609 (Indus II). Note that the magnitude threshold for the smoothed counts maps and radial profiles has been raised to $g < 23$ mag due to non-uniform imaging depth in this region. DES J2038–4609 is detected primarily by a cluster of potential BHB members.

based on the following considerations. First, the Y2Q1 stellar sample is expected to be nearly complete for both Y1 and Y2 exposures at magnitudes $g \lesssim 23$ mag. Figure 3 shows that the measured stellar density in this magnitude range varies smoothly over the Y2Q1 footprint. At fainter magnitudes, discontinuities in the field density can occur in regions where exposures from Y1 and Y2 overlap (typically, more faint objects are detected in the Y2 exposures). Second, the field population with $g \gtrsim 23$ mag in high Galactic latitude regions is likely dominated by misclassified galaxies rather than halo stars, and therefore the assumption of isotropy on arcminute angular scales is compromised due to galaxy clustering. The adopted magnitude threshold matches that used in Bechtol et al. (2015), and in this case, the sensitivity estimates obtained in the prior work can be approximately scaled to the enlarged effective solid angle of the Y2Q1 data set, ∼5000 deg^2.

In Table 4, we list the expected detection efficiencies for the DES ultra-faint galaxy candidates using magnitude thresholds of $g < 23$ mag and $g < 22$ mag, which roughly correspond to the stellar completeness limits of Y2Q1 and SDSS, respectively. For the brighter threshold, several of the DES candidates have substantially reduced detection probabilities.

We note that all of the faint stellar systems that were discovered in the Y1A1 data set are also significantly detected using the Y2Q1 data set, suggesting that our present search has sensitivity comparable to previous studies.

6.3. Total Number and Distribution of Milky Way Satellite Galaxies

The detection of 17 candidate ultra-faint galaxies in the first two years of DES data is consistent with the range of predictions based on the standard cosmological model (Tollerud et al. 2008; Hargis et al. 2014). These predictions model the spatial distribution of luminous satellites from the locations of dark matter subhalos in cosmological *N*-body simulations of Local Group analogs. Significant anisotropy in the distribution of satellites is expected (Tollerud et al. 2008; Hargis et al. 2014) and likely depends on the specific accretion history of the Milky Way (Deason et al. 2015).

The proximity of the DES footprint to the Magellanic Clouds is noteworthy when considering an anisotropic distribution of satellites. The possibility that some Milky Way satellites are or were associated with the Magellanic system has been discussed for some time (Lynden-Bell 1976; D'Onghia & Lake 2008; Nichols et al. 2011; Sales et al. 2011), and the recent DES results have renewed interest in this topic (Deason et al. 2015; Koposov et al. 2015a; Wheeler et al. 2015; Yozin & Bekki 2015). The existence of structures on mass scales ranging from galaxy clusters to ultra-faint satellite galaxies is a generic prediction of hierarchical galaxy formation in the cold dark matter paradigm. However, specific predictions for the number of observable satellites of the LMC and SMC depend on the still unknown efficiency of galaxy formation in low-mass subhalos. Identifying satellites of satellites within the Local Group would support the standard cosmological model, and may provide a new opportunity to test the impact of environment on the formation of the least luminous galaxies (Wetzel et al. 2015).

Based on a study of Milky Way–LMC analogs in *N*-body simulations, Deason et al. (2015) propose a method to evaluate the probability that a given satellite was at one time associated with the LMC based upon the present three-dimensional

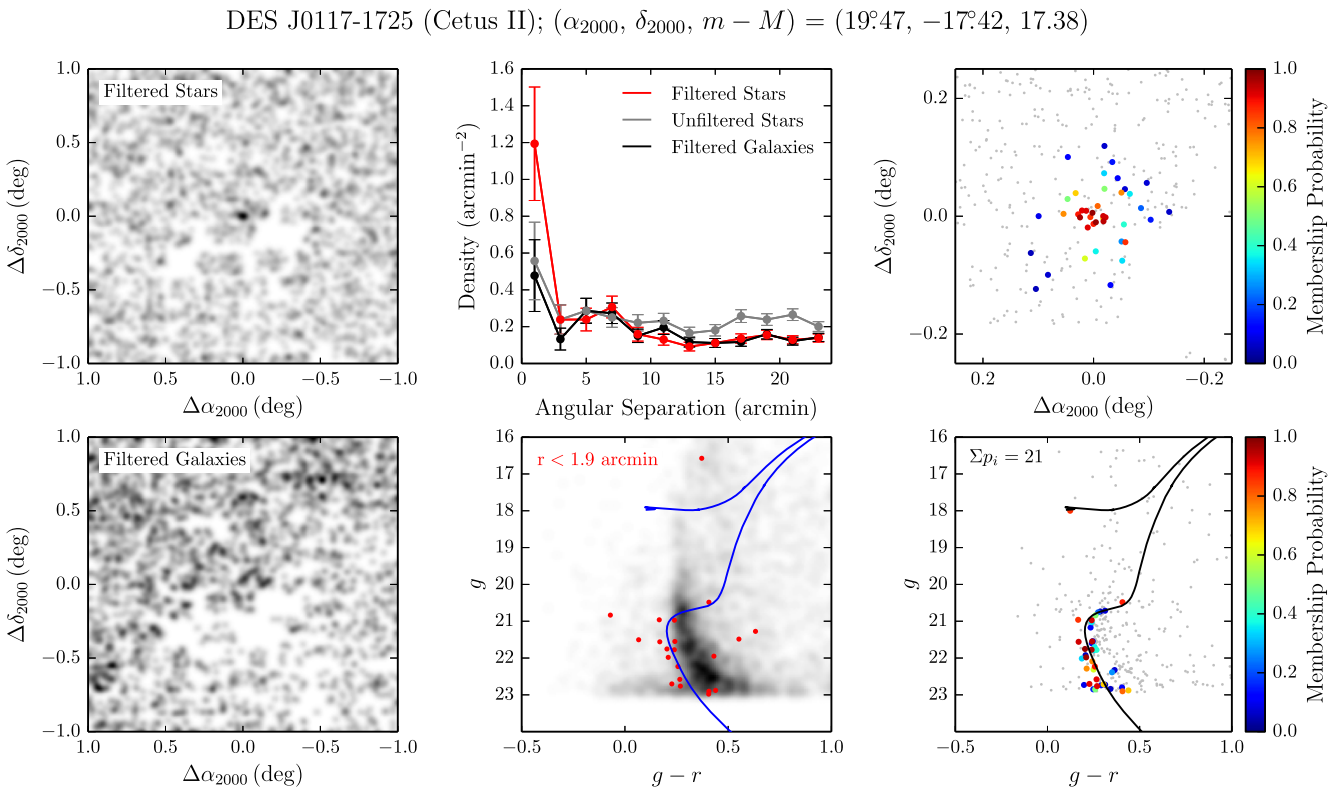

Figure 14. Analogous to Figure 6 but for DES J0117–1725 (Cetus II). Note that the magnitude threshold for the smoothed counts maps and radial profiles has been raised to $g < 23$ mag due to incomplete coverage in this region.

Table 4
Expected Detection Efficiencies for Ultra-faint Galaxy Candidates

Name	M_V	Distance (kpc)	r_h (arcmin)	Efficiency ($g < 23$ mag)	Efficiency ($g < 22$ mag)
DES J2204–4626 (Gru II)	−3.9	53	6.0	1.00	0.39
DES J2356–5935 (Tuc III)	−2.4	25	6.0	1.00	0.94
DES J0531–2801 (Col I)	−4.5	182	1.9	0.95	0.86
DES J0002–6051 (Tuc IV)	−3.5	48	9.1	0.98	0.05
DES J0345–6026 (Ret III)	−3.3	92	2.4	0.33	0.05
DES J2337–6316 (Tuc V)	−1.6	55	1.0	0.94	0.01
DES J2038–4609 (Ind II)	−4.3	214	2.9	0.26	0.00
DES J0117–1725 (Cet II)	0.0	30	1.9	0.38	0.01
Ret II	−3.6	32	6.0	1.00	1.00
DES J0344.3–4331 (Eri II)	−7.4	330	1.8	1.00	1.00
DES J2251.2–5836 (Tuc II)	−3.9	58	7.2	1.00	0.07
Hor I	−3.5	87	2.4	0.66	0.14
DES J0443.8–5017 (Pic I)	−3.7	126	1.2	0.85	0.47
DES J0222.7–5217 (Eri III)	−2.4	95	0.4	0.41	0.04
DES J2339.9–5424 (Phe II)	−3.7	95	1.2	0.99	0.77
Gru I	−3.4	120	2.0	0.21	0.04
Hor II	−2.6	78	2.1	0.26	0.01

Note. Expected detection efficiencies are provided for two magnitude thresholds roughly corresponding to the stellar completeness depths of DES Y2Q1 ($g < 23$ mag) and SDSS ($g < 22$ mag). The detection efficiencies are estimated from multiple realizations of each candidate within the DES footprint using the best-fit luminosity M_V, heliocentric distance, and azimuthally averaged half-light radius r_h, which were then analyzed with the map-based detection algorithm described in Section 3.1. The average detection probability ratio between the two threshold choices is ∼50%, implying that roughly half of the DES candidates would have been detected if they were located in the SDSS footprint.

separation between the two (Table 3). This prescription predicts that two to four of the Y2 DES candidates were associated with the LMC before infall, in addition to the two to four potentially associated satellites found in Y1 DES data. Deason et al. further suggest that a grouping of satellites near the LMC in both physical separation and velocity would imply that the Magellanic system was recently accreted onto the Milky Way since members of this group would disperse within a few Gyr.

As a population, the new DES satellite galaxy candidates do appear to be unevenly distributed within the survey footprint;

15 are located at $\delta_{2000} < -40°$, close to the Magellanic Clouds (Figure 3). A Kolmogorov–Smirnov test, shown in Figure 15, significantly rejects the hypothesis of a uniform distribution ($p = 4.3 \times 10^{-4}$). One possible explanation for non-uniformity is that some of the new systems are satellites of the LMC or SMC. Below we introduce a simple model to test this hypothesis.

We began by modeling the probability distribution for detecting a satellite galaxy as a function of sky position. In this analysis, we excluded classical Milky Way satellites and considered only satellites that have similar characteristics to those discovered by DES (i.e., are detectable at the DES Y2Q1 depth). The underlying luminosity function and the completeness as a function of luminosity, heliocentric distance, and physical size were all simplified into a two-dimensional probability distribution.

We modeled this two-dimensional probability distribution with three components: (i) an isotropic distribution of satellites associated with the main halo of the Milky Way, (ii) a population of satellites spatially associated with the LMC halo, and (iii) a population of satellites spatially associated with the SMC halo. The first component was uniform on the sky, and the latter two components were spatially concentrated around the Magellanic Clouds. We assumed spherically symmetric three-dimensional distributions of satellites centered around each of the Magellanic Clouds having power-law radial profiles with slope $\alpha = -1$ and truncation radius $r_t = 35$ kpc. These distributions were then projected onto the sky to create two-dimensional predicted density maps.

Several underlying assumptions went into this simple model. First, we assumed that the Magellanic components were concentrated enough that variations in the completeness with respect to heliocentric distance would not substantially alter the projected density maps. Second, we assumed that the truncation radii of the LMC and SMC are the same, but later test the sensitivity of our results to this choice. Third, we assumed that smaller satellites of the Milky Way do not have their own associated satellites. We note that a power-law radial profile with slope $\alpha = -1$ can be viewed as a very extended Navarro–Frenk–White profile (Navarro et al. 1997). Since the DES footprint does not cover the central regions of the Magellanic Clouds, this shallow profile yields a conservative estimate on the fraction of satellites associated with the Magellanic system.

We performed an unbinned maximum-likelihood fit of our three-component model to the distribution of observed satellites. The parameters of the likelihood function are the total number of satellites and the relative normalizations of the three components. The likelihood is defined as the product of the probabilities to detect each observed satellite given its sky position. When presenting our results, we marginalized over the ratio of the LMC component to the SMC component. This ratio is not strongly constrained by our analysis; however, there is a slight preference for a larger SMC component.

The left panel of Figure 16 shows the constraints using the sky positions of the seventeen DES satellite galaxy candidates. We find that the DES data alone reject a uniform distribution of satellites at $>3\sigma$ confidence when compared to our best-fit model. This again implies that there is either a clear overdensity of satellites around the Magellanic Clouds or that the initial assumption of isotropy around the main halo is incorrect. In Figure 15, we show the distribution of declinations for our best-fit three-component model and find good agreement with the observations ($p = 0.7$).

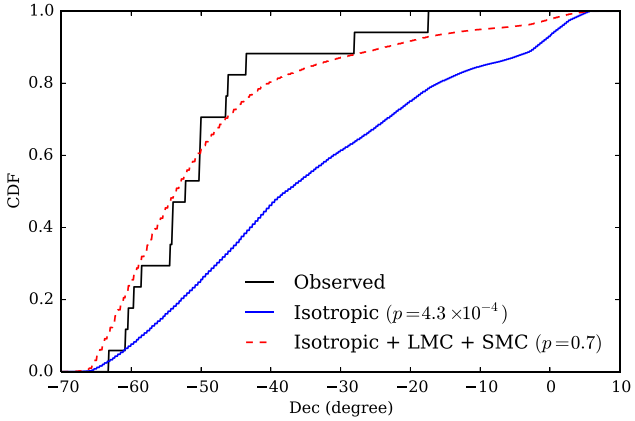

Figure 15. Cumulative distribution functions of declination values for the 17 observed satellites in the DES footprint (black), a uniform distribution given the shape of DES footprint (blue), and the best-fit model for a uniform distribution and Magellanic Cloud components (red dashed). See Section 6.3.

We next tested the sensitivity of our result to the assumed distribution of satellites around the LMC and SMC. The central panel of Figure 16 shows the 1σ contours for three different values of $r_t = \{25, 35, 45\,\mathrm{kpc}\}$, and two values of the slope, $\alpha = \{-1, -2\}$. Despite slight changes in the likelihood contours, in each case >10% of Milky Way satellites are likely to be spatially associated with the Magellanic Clouds.

We further examined the satellite population by simultaneously considering the 16 ultra-faint satellites observed in the SDSS DR10 footprint.[49] To fully combine DES and SDSS observations we would need to model the detection efficiency of SDSS relative to DES as a function of satellite distance, size, and luminosity. However, since the SDSS DR10 footprint only overlaps with the isotropic component in our model, we can again fold the complications of detection efficiency into a constant detection ratio. Our fiducial calculation assumes that 50% of the satellites discovered in DES would be detectable by SDSS, which agrees with the relative detection efficiency of the 17 DES satellites at the depth of SDSS (Table 4). The right panel of Figure 16 shows that the DES+SDSS constraints are in agreement with those from DES data alone, though the fraction of LMC and SMC satellites is more tightly constrained by including information from a large region widely separated from the Magellanic Clouds. The combined results imply that there are ∼100 satellites over the full sky that are detectable at DES Y2Q1 depth, and that 20%–30% of these might be associated with the Magellanic Clouds. Importantly, this prediction does not attempt to model the full population of Milky Way satellites beyond the DES Y2Q1 sensitivity and ignores the diminished detection efficiency close to the Galactic plane.

The Pan-STARRS team has recently identified three candidate Milky Way satellite galaxies in their 3π survey (Laevens et al. 2015a, 2015b). If this search is complete to the depth of SDSS over its full area, it is notable that so few candidates have been found. This observation alone could imply anisotropy without requiring the influence of the Magellanic Clouds. However, much of the Pan-STARRS area

[49] We include Pegasus III (Kim et al. 2015a) in the list of ultra-faint satellites from SDSS.

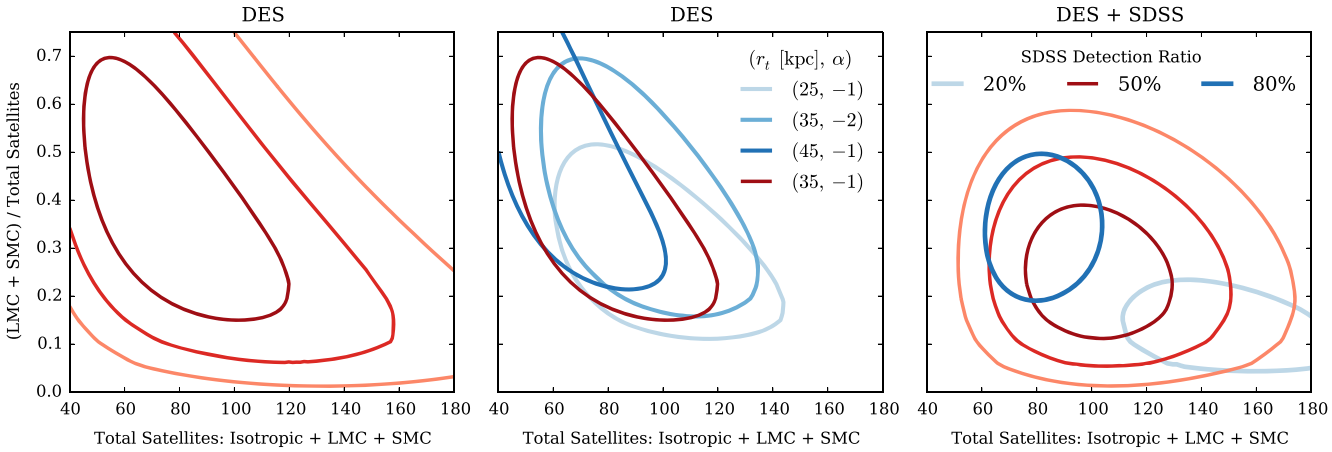

Figure 16. Maximum-likelihood fit to the spatial distribution of satellites for a model including isotropic, LMC, and SMC components (Section 6.3). The horizontal axis represents the total number of satellites detectable at DES Y2Q1 depth integrated over the entire sky (not including the classical dwarf galaxies and detection inefficiency near the Galactic plane). The vertical axis represents the fraction of these satellites associated with the Magellanic Clouds. Left: the 1σ, 2σ, and 3σ likelihood contours when considering only DES data. Center: 1σ contours for different values of the LMC and SMC truncation radius (r_t) and the slope of the radial profile (α). Right: contours of the likelihood function when SDSS observations are included. Red contours (1σ, 2σ, 3σ) assume that 50% of the satellites discovered in DES would have been detected if they were located in the SDSS footprint. This value matches the estimated detection efficiency from Table 4. We show the sensitivity of our results to the SDSS/DES detection ratio with the dark blue contour (80% detection ratio) and the light blue contour (20% detection ratio).

is located at low Galactic latitudes where the elevated foreground stellar density and interstellar extinction may present additional challenges. Under the assumption that Pan-STARRS covers the full sky with $\delta_{2000} > -30°$, $\sim$2000 deg^2 overlap with DES Y2Q1. This area of the DES footprint includes two new candidates, one of which has a large enough surface brightness to likely have been detected at SDSS depth (DES J0531–2801, see Table 4). These two candidates are located in a region of the sky that would be observed at a relatively high airmass by Pan-STARRS and may suffer from decreased detection efficiency.

From this analysis, we conclude that the distribution of satellites around the Milky Way is unlikely to be isotropic, and that a plausible component of this anisotropy is a population of satellites associated with the Magellanic Clouds. However, several alternative explanations for anisotropy in the Milky Way satellite distribution exist. For example, Milky Way satellites could be preferentially located along a three-dimensional planar structure, as has been suggested by many authors, starting with Lynden-Bell (1976). This proposed planar structure encompasses the Magellanic Clouds and many of the classical and SDSS satellites. Pawlowski et al. (2015) suggest that the satellites discovered in Y1 DES data are also well aligned with this polar structure. We note that the Y2 discoveries presented here include several objects near the SMC and may reduce the fraction of objects in close proximity to the proposed plane. An additional possibility is that the satellites are associated with the orbit of the Magellanic System and are not isotropically distributed around the Magellanic Clouds themselves (Yozin & Bekki 2015). The DES footprint covers only a fraction of the region surrounding the Magellanic Clouds and additional sky coverage may yield more satellites with similar proximity to the Magellanic system and/or help to distinguish between these various scenarios. Measurements of the relative motions of the satellites and further theoretical work will also help clarify the physical relationships between these stellar systems.

7. CONCLUSIONS

We report the discovery of six new ultra-faint galaxy candidates in a combined data set from the first two years of DES covering $\sim$5000 deg^2 of the south Galactic cap. Two additional candidates are identified in regions with incomplete or non-uniform coverage and should be viewed with lower confidence until additional imaging is obtained. The new satellites are faint ($M_V > -4.7$ mag) and span a wide range of physical sizes (17 pc $< r_{1/2} <$ 181 pc) and heliocentric distances (25 kpc $< D_\odot <$ 214 kpc). All are low surface brightness systems similar to the known ultra-faint satellite galaxies of the Milky Way, and most possess physical sizes that are large enough (>40 pc) to be provisionally classified as galaxies. Spectroscopic observations are needed to better understand and unambiguously classify the new stellar systems. A total of 17 confirmed and candidate ultra-faint galaxies have been found in the first two years of DES. Roughly half of the DES systems are sufficiently distant and/or faint to have eluded detection at survey depths comparable to SDSS.

The DES satellites are concentrated in the southern half of the survey footprint in proximity to the Magellanic Clouds. In addition, we find three satellites clustered in a Tucana group, each of which is within <10 kpc of the group centroid. We find that the DES data alone exclude ($p < 10^{-3}$) an isotropic distribution of satellites within the Milky Way halo, and that the observed distribution can be well, although not uniquely, explained by a model in which several of the observed DES satellites are associated with the Magellanic system. Under the assumption that the total satellite population can be modeled by isotropic distributions around the Milky Way, LMC, and SMC, we estimate that a total of $\sim$100 ultra-faint satellites with comparable physical characteristics to those detected by DES might exist over the full sky, with 20%–30% of these systems being spatially associated with the Magellanic Clouds.

Milky Way satellite galaxies are considered a unique population for studying the particle nature of dark matter due to their proximity, characteristically large mass-to-light ratios,

and lack of intrinsic astrophysical backgrounds. Although the dark matter content of the new stellar systems has not yet been spectroscopically confirmed, the possibility that some are dark matter dominated galaxies makes them interesting targets for indirect dark matter searches via gamma rays. No gamma-ray sources from the third *Fermi*-LAT source catalog (3FGL; Acero et al. 2015) are located within $0.^{\circ}5$ of any of the new candidates. A follow-up gamma-ray analysis of these ultra-faint galaxy candidates will be presented separately.

Future seasons of DES will not significantly increase the DES sky coverage. However, there will be considerable gains in depth from the expected 10 tilings per filter relative to the two to four in the Y2Q1 data set. This increased depth will expand the effective volume of the survey. In addition, we expect the survey uniformity to improve with the coming seasons, resulting in a cleaner list of seeds with fewer false positives. Star-galaxy separation may become a limiting factor at the future depth of DES, motivating the development of improved classification algorithms (e.g., Fadely et al. 2012; Soumagnac et al. 2015), as well as alternative search strategies, involving, for instance, the time domain (Baker & Willman 2015) or stellar velocities (Antoja et al. 2015). While it is likely that the most conspicuous Milky Way satellites in the DES footprint have been found, the most exciting phase of Milky Way science with DES is likely still to come. The wide area and growing sensitivity of DES will enable the discovery of dwarf galaxies that are fainter, farther, and have lower surface brightness.

This work made use of computational resources at SLAC National Accelerator Laboratory and the University of Chicago Research Computing Center. Some of the results in this paper have been derived using the `HEALPix` (Górski et al. 2005) package. This research made use of Astropy, a community-developed core Python package for Astronomy (Astropy Collaboration et al. 2013). We thank the anonymous referee for helpful suggestions. A.D.W. thanks Ellen Bechtol for her generous hospitality during the preparation of this manuscript. E.B. acknowledges financial support from the European Research Council (ERC-StG-335936, CLUSTERS).

Funding for the DES Projects has been provided by the U.S. Department of Energy, the U.S. National Science Foundation, the Ministry of Science and Education of Spain, the Science and Technology Facilities Council of the United Kingdom, the Higher Education Funding Council for England, the National Center for Supercomputing Applications at the University of Illinois at Urbana-Champaign, the Kavli Institute of Cosmological Physics at the University of Chicago, the Center for Cosmology and Astro-Particle Physics at the Ohio State University, the Mitchell Institute for Fundamental Physics and Astronomy at Texas A&M University, Financiadora de Estudos e Projetos, Fundação Carlos Chagas Filho de Amparo à Pesquisa do Estado do Rio de Janeiro, Conselho Nacional de Desenvolvimento Científico e Tecnológico and the Ministério da Ciência, Tecnologia e Inovação, the Deutsche Forschungsgemeinschaft and the Collaborating Institutions in the Dark Energy Survey.

The Collaborating Institutions are Argonne National Laboratory, the University of California at Santa Cruz, the University of Cambridge, Centro de Investigaciones Energéticas, Medioambientales y Tecnológicas-Madrid, the University of Chicago, University College London, the DES-Brazil Consortium, the University of Edinburgh, the Eidgenössische Technische Hochschule (ETH) Zürich, Fermi National Accelerator Laboratory, the University of Illinois at Urbana-Champaign, the Institut de Ciències de l'Espai (IEEC/CSIC), the Institut de Física d'Altes Energies, Lawrence Berkeley National Laboratory, the Ludwig-Maximilians Universität München and the associated Excellence Cluster universe, the University of Michigan, the National Optical Astronomy Observatory, the University of Nottingham, The Ohio State University, the University of Pennsylvania, the University of Portsmouth, SLAC National Accelerator Laboratory, Stanford University, the University of Sussex, and Texas A&M University.

The DES data management system is supported by the National Science Foundation under grant Number AST-1138766. The DES participants from Spanish institutions are partially supported by MINECO under grants AYA2012-39559, ESP2013-48274, FPA2013-47986, and Centro de Excelencia Severo Ochoa SEV-2012-0234. Research leading to these results has received funding from the European Research Council under the European Union's Seventh Framework Programme (FP7/2007-2013), including ERC grant agreements 240672, 291329, and 306478.

REFERENCES

Abbott, T., Aldering, G., Annis, J., et al. 2005, arXiv:astro-ph/0510346
Acero, F., Ackermann, M., Ajello, M., et al. 2015, ApJS, 218, 23
Ackermann, M., et al. 2015, PRL, in press (arXiv:1503.02641)
Adén, D., Feltzing, S., Koch, A., et al. 2009, A&A, 506, 1147
Antoja, T., Mateu, C., Aguilar, L., et al. 2015, MNRAS, 453, 541
Astropy Collaboration, Robitaille, T. P., Tollerud, E. J., et al. 2013, A&A, 558, A33
Baker, M., & Willman, B. 2015, AJ, in press (arXiv:1507.00734)
Balbinot, E., Santiago, B. X., da Costa, L. N., Makler, M., & Maia, M. A. G. 2011, MNRAS, 416, 393
Balbinot, E., Santiago, B. X., da Costa, L., et al. 2013, ApJ, 767, 101
Bechtol, K., Drlica-Wagner, A., Balbinot, E., et al. 2015, ApJ, 807, 50
Belokurov, V., Irwin, M. J., Koposov, S. E., et al. 2014, MNRAS, 441, 2124
Belokurov, V., Walker, M. G., Evans, N. W., et al. 2008, ApJL, 686, L83
Belokurov, V., Walker, M. G., Evans, N. W., et al. 2009, MNRAS, 397, 1748
Belokurov, V., Walker, M. G., Evans, N. W., et al. 2010, ApJL, 712, L103
Belokurov, V., Zucker, D. B., Evans, N. W., et al. 2006, ApJL, 647, L111
Belokurov, V., Zucker, D. B., Evans, N. W., et al. 2007, ApJ, 654, 897
Benson, A. J., Frenk, C. S., Lacey, C. G., Baugh, C. M., & Cole, S. 2002, MNRAS, 333, 177
Bertin, E. 2006, in ASP Conf. Ser. 351, Astronomical Data Analysis Software and Systems XV, ed. C. Gabriel et al. (San Francisco, CA: ASP), 112
Bertin, E. 2011, in ASP Conf. Ser. 442, Astronomical Data Analysis Software and Systems XX, ed. I. N. Evans et al. (San Francisco, CA: ASP), 435
Bertin, E., & Arnouts, S. 1996, A&AS, 117, 393
Bressan, A., Marigo, P., Girardi, L., et al. 2012, MNRAS, 427, 127
Bullock, J. S., Kravtsov, A. V., & Weinberg, D. H. 2000, ApJ, 539, 517
Bullock, J. S., Kravtsov, A. V., & Weinberg, D. H. 2001, ApJ, 548, 33
Carlin, J. L., Grillmair, C. J., Muñoz, R. R., Nidever, D. L., & Majewski, S. R. 2009, ApJL, 702, L9
Chabrier, G. 2001, ApJ, 554, 1274
Chang, C., Busha, M. T., Wechsler, R. H., et al. 2015, ApJ, 801, 73
Corwin, H. G. 2004, yCat, 7239, 0
Coupon, J., Kilbinger, M., McCracken, H. J., et al. 2012, A&A, 542, A5
de Grijs, R., & Bono, G. 2015, AJ, 149, 179
de Grijs, R., Wicker, J. E., & Bono, G. 2014, AJ, 147, 122
Deason, A. J., Wetzel, A. R., Garrison-Kimmel, S., & Belokurov, V. 2015, MNRAS, 453, 3568
Desai, S., Armstrong, R., Mohr, J. J., et al. 2012, ApJ, 757, 83
Dickey, J. M. 1971, Ann. Math. Statist., 42, 204
D'Onghia, E., & Lake, G. 2008, ApJL, 686, L61
Dotter, A., Chaboyer, B., Jevremović, D., et al. 2008, ApJS, 178, 89
Drlica-Wagner, A., Albert, A., Bechtol, K., et al. 2015, ApJL, 809, L4
Erben, T., Hildebrandt, H., Miller, L., et al. 2013, MNRAS, 433, 2545
Fadely, R., Hogg, D. W., & Willman, B. 2012, ApJ, 760, 15

Fadely, R., Willman, B., Geha, M., et al. 2011, AJ, 142, 88
Flaugher, B., Diehl, H. T., Honscheid, K., et al. 2015, AJ, submitted (arXiv:1504.02900)
Foreman-Mackey, D., Hogg, D. W., Lang, D., & Goodman, J. 2013, PASP, 125, 306
Geha, M., Willman, B., Simon, J. D., et al. 2009, ApJ, 692, 1464
Geringer-Sameth, A., Koushiappas, S. M., & Walker, M. G. 2015a, PhRvD, 91, 083535
Geringer-Sameth, A., Walker, M. G., Koushiappas, S. M., et al. 2015b, PhRvL, 115, 081101
Gilbank, D. G., Gladders, M. D., Yee, H. K. C., & Hsieh, B. C. 2011, AJ, 141, 94
Górski, K. M., Hivon, E., Banday, A. J., et al. 2005, ApJ, 622, 759
Grillmair, C. J. 2006, ApJL, 645, L37
Grillmair, C. J. 2009, ApJ, 693, 1118
Hargis, J. R., Willman, B., & Peter, A. H. G. 2014, ApJL, 795, L13
Harris, W. E. 1996, AJ, 112, 1487
Heymans, C., van Waerbeke, L., Miller, L., et al. 2012, MNRAS, 427, 146
High, F. W., Stubbs, C. W., Rest, A., Stalder, B., & Challis, P. 2009, AJ, 138, 110
Hooper, D., & Linden, T. 2015, arXiv:1503.06209
Irwin, M. J., Belokurov, V., Evans, N. W., et al. 2007, ApJL, 656, L13
Ivezić, Ž., Lupton, R. H., Schlegel, D., et al. 2004, AN, 325, 583
Kelly, P. L., von der Linden, A., Applegate, D. E., et al. 2014, MNRAS, 439, 28
Kharchenko, N. V., Piskunov, A. E., Schilbach, E., Röser, S., & Scholz, R.-D. 2013, A&A, 558, A53
Kim, D., & Jerjen, H. 2015a, ApJ, 799, 73
Kim, D., & Jerjen, H. 2015b, ApJL, 808, L39
Kim, D., Jerjen, H., Mackey, D., da Costa, G. S., & Milone, A. P. 2015a, ApJL, 804, L44
Kim, D., Jerjen, H., Milone, A. P., Mackey, D., & da Costa, G. S. 2015b, ApJ, 803, 63
Kirby, E. N., Boylan-Kolchin, M., Cohen, J. G., et al. 2013, ApJ, 770, 16
Kirby, E. N., Simon, J. D., & Cohen, J. G. 2015, ApJ, 810, 56
Kirby, E. N., Simon, J. D., Geha, M., Guhathakurta, P., & Frebel, A. 2008, ApJL, 685, L43
Kleyna, J. T., Wilkinson, M. I., Evans, N. W., & Gilmore, G. 2005, ApJL, 630, L141
Koch, A., Wilkinson, M. I., Kleyna, J. T., et al. 2009, ApJ, 690, 453
Koposov, S., Belokurov, V., Evans, N. W., et al. 2008, ApJ, 686, 279
Koposov, S., de Jong, J. T. A., Belokurov, V., et al. 2007, ApJ, 669, 337
Koposov, S. E., Belokurov, V., Torrealba, G., & Evans, N. W. 2015a, ApJ, 805, 130
Koposov, S. E., Casey, A. R., Belokurov, V., et al. 2015b, ApJ, in press (arXiv:1504.07916)
Koposov, S. E., Gilmore, G., Walker, M. G., et al. 2011, ApJ, 736, 146
Laevens, B. P. M., Martin, N. F., Bernard, E. J., et al. 2015a, ApJ, submitted (arXiv:1507.07564)
Laevens, B. P. M., Martin, N. F., Ibata, R. A., et al. 2015b, ApJL, 802, L18
Laevens, B. P. M., Martin, N. F., Sesar, B., et al. 2014, ApJL, 786, L3
Luque, E., Queiroz, A., Santiago, B., et al. 2015, MNRAS, in press (arXiv:1508.02381)
Lynden-Bell, D. 1976, MNRAS, 174, 695
MacDonald, E. C., Allen, P., Dalton, G., et al. 2004, MNRAS, 352, 1255
Martin, N. F., de Jong, J. T. A., & Rix, H.-W. 2008, ApJ, 684, 1075
Martin, N. F., Ibata, R. A., Chapman, S. C., Irwin, M., & Lewis, G. F. 2007, MNRAS, 380, 281
Martin, N. F., Nidever, D. L., Besla, G., et al. 2015, ApJL, 804, L5
McClure-Griffiths, N. M., Pisano, D. J., Calabretta, M. R., et al. 2009, ApJS, 181, 398
McConnachie, A. W. 2012, AJ, 144, 4
Mohr, J. J., Armstrong, R., Bertin, E., et al. 2012, Proc. SPIE, 8451, 84510D
Muñoz, R. R., Carlin, J. L., Frinchaboy, P. M., et al. 2006, ApJL, 650, L51
Muñoz, R. R., Geha, M., Côté, P., et al. 2012, ApJL, 753, L15
Muñoz, R. R., Majewski, S. R., & Johnston, K. V. 2008, ApJ, 679, 346
Navarro, J. F., Frenk, C. S., & White, S. D. M. 1997, ApJ, 490, 493
Neilsen, E., Bernstein, G., Gruendl, R., & Kent, S. 2015, Limiting Magnitude, τ, $T_{\rm eff}$, and Image Quality in DES Year 1, Tech. Rep. FERMILAB-TM-2610-AE-CD (Batavia, IL: Fermi National Accelerator Laboratory)
Nichols, M., Colless, J., Colless, M., & Bland-Hawthorn, J. 2011, ApJ, 742, 110
Nilson, P. 1973, Uppsala General Catalogue of Galaxies (Uppsala: Royal Society of Sciences in Uppsala)
Oh, K. S., Lin, D. N. C., & Aarseth, S. J. 1995, ApJ, 442, 142
Ortolani, S., Bica, E., & Barbuy, B. 2013, MNRAS, 433, 1966
Paust, N., Wilson, D., & van Belle, G. 2014, AJ, 148, 19
Pawlowski, M. S., McGaugh, S. S., & Jerjen, H. 2015, MNRAS, 453, 1047
Peñarrubia, J., Navarro, J. F., & McConnachie, A. W. 2008, ApJ, 673, 226
Putman, M. E., Staveley-Smith, L., Freeman, K. C., Gibson, B. K., & Barnes, D. G. 2003, ApJ, 586, 170
Rykoff, E. S., Rozo, E., Busha, M. T., et al. 2014, ApJ, 785, 104
Sakamoto, T., & Hasegawa, T. 2006, ApJL, 653, L29
Sales, L. V., Navarro, J. F., Cooper, A. P., et al. 2011, MNRAS, 418, 648
Schlafly, E. F., & Finkbeiner, D. P. 2011, ApJ, 737, 103
Schlegel, D. J., Finkbeiner, D. P., & Davis, M. 1998, ApJ, 500, 525
Sevilla, I., Armstrong, R., Bertin, E., et al. 2011, in Proc. DPF-2011 Conf., Providence, RI, 8–13 August 2011
Simon, J., Drlica-Wagner, A., Li, T. S., et al. 2015, ApJ, 808, 95
Simon, J. D., & Geha, M. 2007, ApJ, 670, 313
Simon, J. D., Geha, M., Minor, Q. E., et al. 2011, ApJ, 733, 46
Soumagnac, M. T., Abdalla, F. B., Lahav, O., et al. 2015, MNRAS, 450, 666
Tollerud, E. J., Bullock, J. S., Strigari, L. E., & Willman, B. 2008, ApJ, 688, 277
Trotta, R. 2007, MNRAS, 378, 72
van den Bergh, S. 2008, AJ, 135, 1731
Walker, M. G., Belokurov, V., Evans, N. W., et al. 2009, ApJL, 694, L144
Walker, M. G., Mateo, M., Olszewski, E. W., et al. 2015, ApJ, 808, 108
Walsh, S. M., Jerjen, H., & Willman, B. 2007, ApJL, 662, L83
Walsh, S. M., Willman, B., & Jerjen, H. 2009, AJ, 137, 450
Westmeier, T., Staveley-Smith, L., Calabretta, M., et al. 2015, MNRAS, 453, 338
Wetzel, A. R., Deason, A. J., & Garrison-Kimmel, S. 2015, ApJ, 807, 49
Wheeler, C., Oñorbe, J., Bullock, J. S., et al. 2015, MNRAS, 453, 1305
Willman, B. 2010, AdAst, 2010, 21
Willman, B., Blanton, M. R., West, A. A., et al. 2005a, AJ, 129, 2692
Willman, B., Dalcanton, J. J., Martinez-Delgado, D., et al. 2005b, ApJL, 626, L85
Willman, B., Geha, M., Strader, J., et al. 2011, AJ, 142, 128
Willman, B., & Strader, J. 2012, AJ, 144, 76
York, D. G., Adelman, J., Anderson, J. E., Jr., et al. 2000, AJ, 120, 1579
Yozin, C., & Bekki, K. 2015, MNRAS, 453, 2302
Zacharias, N., Finch, C. T., Girard, T. M., et al. 2013, AJ, 145, 44
Zucker, D. B., Belokurov, V., Evans, N. W., et al. 2006a, ApJL, 650, L41
Zucker, D. B., Belokurov, V., Evans, N. W., et al. 2006b, ApJL, 643, L103

A.4

The Astrophysical Journal, 807:50 (16pp), 2015 July 1 doi:10.1088/0004-637X/807/1/50

EIGHT NEW MILKY WAY COMPANIONS DISCOVERED IN FIRST-YEAR DARK ENERGY SURVEY DATA

K. Bechtol[1], A. Drlica-Wagner[2], E. Balbinot[3,4], A. Pieres[4,5], J. D. Simon[6], B. Yanny[2], B. Santiago[4,5], R. H. Wechsler[7,8,9], J. Frieman[1,2], A. R. Walker[10], P. Williams[1], E. Rozo[9,11], E. S. Rykoff[9], A. Queiroz[4,5], E. Luque[4,5], A. Benoit-Lévy[12], D. Tucker[2], I. Sevilla[13,14], R. A. Gruendl[13,15], L. N. da Costa[4,16], A. Fausti Neto[4], M. A. G. Maia[4,16], T. Abbott[10], S. Allam[2,17], R. Armstrong[18], A. H. Bauer[19], G. M. Bernstein[18], R. A. Bernstein[6], E. Bertin[20,21], D. Brooks[12], E. Buckley-Geer[2], D. L. Burke[9], A. Carnero Rosell[4,16], F. J. Castander[19], R. Covarrubias[15], C. B. D'Andrea[22], D. L. DePoy[23], S. Desai[24,25], H. T. Diehl[2], T. F. Eifler[18,26], J. Estrada[2], A. E. Evrard[27], E. Fernandez[28,29], D. A. Finley[2], B. Flaugher[2], E. Gaztanaga[19], D. Gerdes[27], L. Girardi[16], M. Gladders[1,28], D. Gruen[30,31], G. Gutierrez[2], J. Hao[2], K. Honscheid[32,33], B. Jain[18], D. James[10], S. Kent[2], R. Kron[1], K. Kuehn[34,35], N. Kuropatkin[2], O. Lahav[12], T. S. Li[23], H. Lin[2], M. Makler[36], M. March[18], J. Marshall[23], P. Martini[33,37], K. W. Merritt[2], C. Miller[27,38], R. Miquel[29,39], J. Mohr[24], E. Neilsen[2], R. Nichol[22], B. Nord[2], R. Ogando[4,16], J. Peoples[2], D. Petravick[15], A. A. Plazas[26,40], A. K. Romer[41], A. Roodman[7,10], M. Sako[18], E. Sanchez[14], V. Scarpine[2], M. Schubnell[27], R. C. Smith[10], M. Soares-Santos[2], F. Sobreira[2,4], E. Suchyta[32,33], M. E. C. Swanson[15], G. Tarle[27], J. Thaler[42], D. Thomas[22], W. Wester[2], and J. Zuntz[43]

(The DES Collaboration)

[1] Kavli Institute for Cosmological Physics, University of Chicago, Chicago, IL 60637, USA; bechtol@kicp.uchicago.edu, kadrlica@fnal.gov
[2] Fermi National Accelerator Laboratory, P.O. Box 500, Batavia, IL 60510, USA
[3] Department of Physics, University of Surrey, Guildford GU2 7XH, UK
[4] Laboratório Interinstitucional de e-Astronomia—LIneA, Rua Gal. José Cristino 77, Rio de Janeiro, RJ—20921-400, Brazil
[5] Instituto de Física, UFRGS, Caixa Postal 15051, Porto Alegre, RS—91501-970, Brazil
[6] Carnegie Observatories, 813 Santa Barbara St., Pasadena, CA 91101, USA
[7] Kavli Institute for Particle Astrophysics & Cosmology, P.O. Box 2450, Stanford University, Stanford, CA 94305, USA
[8] Department of Physics, Stanford University, 382 Via Pueblo Mall, Stanford, CA 94305, USA
[9] SLAC National Accelerator Laboratory, Menlo Park, CA 94025, USA
[10] Cerro Tololo Inter-American Observatory, National Optical Astronomy Observatory, Casilla 603, La Serena, Chile
[11] University of Arizona, Department of Physics, 1118 E. Fourth St., Tucson, AZ 85721, USA
[12] Department of Physics & Astronomy, University College London, Gower Street, London, WC1E 6BT, UK
[13] Department of Astronomy, University of Illinois, 1002 W. Green Street, Urbana, IL 61801, USA
[14] Centro de Investigaciones Energéticas, Medioambientales y Tecnológicas (CIEMAT), Madrid, Spain
[15] National Center for Supercomputing Applications, 1205 West Clark St., Urbana, IL 61801, USA
[16] Observatório Nacional, Rua Gal. José Cristino 77, Rio de Janeiro, RJ—20921-400, Brazil
[17] Space Telescope Science Institute, 3700 San Martin Drive, Baltimore, MD 21218, USA
[18] Department of Physics and Astronomy, University of Pennsylvania, Philadelphia, PA 19104, USA
[19] Institut de Ciències de l'Espai, IEEC-CSIC, Campus UAB, Facultat de Ciències, Torre C5 par-2, E-08193 Bellaterra, Barcelona, Spain
[20] Sorbonne Universités, UPMC Univ Paris 06, UMR 7095, Institut d'Astrophysique de Paris, F-75014, Paris, France
[21] CNRS, UMR 7095, Institut d'Astrophysique de Paris, F-75014, Paris, France
[22] Institute of Cosmology & Gravitation, University of Portsmouth, Portsmouth, PO1 3FX, UK
[23] George P. and Cynthia Woods Mitchell Institute for Fundamental Physics and Astronomy, and Department of Physics and Astronomy, Texas A&M University, College Station, TX 77843, USA
[24] Department of Physics, Ludwig-Maximilians-Universitat, Scheinerstr.1, D-81679 Munich, Germany
[25] Excellence Cluster universe, Boltzmannstr.2, D-85748 Garching, Germany
[26] Jet Propulsion Laboratory, California Institute of Technology, 4800 Oak Grove Dr., Pasadena, CA 91109, USA
[27] Department of Physics, University of Michigan, Ann Arbor, MI48109, USA
[28] Department of Astronomy and Astrophysics, University of Chicago, Chicago IL 60637, USA
[29] Institució Catalana de Recerca i Estudis Avançats, E-08010, Barcelona, Spain
[30] Max Planck Institute for Extraterrestrial Physics, Giessenbachstrasse, D-85748 Garching, Germany
[31] University Observatory Munich, Scheinerstrasse 1, D-81679 Munich, Germany
[32] Department of Physics, The Ohio State University, Columbus, OH 43210, USA
[33] Center for Cosmology and Astro-Particle Physics, The Ohio State University, Columbus, OH 43210, USA
[34] Australian Astronomical Observatory, North Ryde, NSW 2113, Australia
[35] Argonne National Laboratory, 9700 S. Cass Avenue, Lemont IL 60639 USA
[36] ICRA, Centro Brasileiro de Pesquisas Físicas, Rua Dr. Xavier Sigaud 150, CEP 22290-180, Rio de Janeiro, RJ, Brazil
[37] Department of Astronomy, The Ohio State University, Columbus, OH 43210, USA
[38] Department of Astronomy, University of Michigan, Ann Arbor, MI, 48109, USA
[39] Institut de Física d'Altes Energies, Universitat Autònoma de Barcelona, E-08193 Bellaterra, Barcelona, Spain
[40] Brookhaven National Laboratory, Bldg 510, Upton, NY 11973, USA
[41] Astronomy Centre, University of Sussex, Falmer, Brighton, BN1 9QH, UK
[42] Department of Physics, University of Illinois, 1110 W. Green St., Urbana, IL 61801, USA
[43] Jodrell Bank Center for Astrophysics, School of Physics and Astronomy, University of Manchester, Oxford Road, Manchester, M13 9PL, UK

Received 2015 March 9; accepted 2015 April 30; published 2015 June 30

ABSTRACT

We report the discovery of eight new Milky Way companions in $\sim$1800 deg^2 of optical imaging data collected during the first year of the Dark Energy Survey (DES). Each system is identified as a statistically significant overdensity of individual stars consistent with the expected isochrone and luminosity function of an old and metal-poor stellar population. The objects span a wide range of absolute magnitudes (M_V from -2.2 to -7.4 mag), physical

sizes (10−170 pc), and heliocentric distances (30−330 kpc). Based on the low surface brightnesses, large physical sizes, and/or large Galactocentric distances of these objects, several are likely to be new ultra-faint satellite galaxies of the Milky Way and/or Magellanic Clouds. We introduce a likelihood-based algorithm to search for and characterize stellar over-densities, as well as identify stars with high satellite membership probabilities. We also present completeness estimates for detecting ultra-faint galaxies of varying luminosities, sizes, and heliocentric distances in the first-year DES data.

Key words: galaxies: dwarf – Local Group

1. INTRODUCTION

Milky Way satellite galaxies provide a unique opportunity to study the low-luminosity threshold of galaxy formation and to better connect the baryonic component of galaxies with the dark matter halos in which they reside. Prior to the Sloan Digital Sky Survey (SDSS), the faintest known galaxies had luminosities of $\sim 10^5\ L_\odot$, and it was clear that the population of 12 "classical" Milky Way satellites was orders of magnitude smaller than would be naively expected in the cold dark matter paradigm (Klypin et al. 1999; Moore et al. 1999). Over the past decade, systematic searches of wide-field SDSS imaging have revealed 15 additional arcminute-scale, resolved stellar over-densities (Willman et al. 2005a, 2005b; Belokurov et al. 2006, 2007, 2008, 2009, 2010; Grillmair 2006, 2009; Sakamoto & Hasegawa 2006; Zucker et al. 2006a, 2006b; Irwin et al. 2007; Walsh et al. 2007) that have been either photometrically classified or spectroscopically confirmed as gravitationally bound "ultra-faint" galaxies (Kleyna et al. 2005; Muñoz et al. 2006; Martin et al. 2007; Simon & Geha 2007; Adén et al. 2009; Belokurov et al. 2009; Carlin et al. 2009; Geha et al. 2009; Koch et al. 2009; Walker et al. 2009; Koposov et al. 2011; Simon et al. 2011; Willman et al. 2011; Kirby et al. 2013). These ultra-faint galaxies are the smallest, least luminous, least chemically enriched, and most dark matter dominated galaxies in the known universe.

Since all known ultra-faint Milky Way satellite galaxies were discovered in SDSS, the census of these objects is almost certainly incomplete due to the partial sky coverage ($\sim 14,000\ \mathrm{deg}^2$) and photometric magnitude limit (95% complete to $r \sim 22$ mag) of that survey. While only 27 Milky Way satellite galaxies are currently known, extrapolations of the luminosity function suggest that hundreds of luminous Milky Way satellites remain to be found in current and near-future wide-field optical imaging surveys (Tollerud et al. 2008; Hargis et al. 2014; He et al. 2015).

The Dark Energy Survey (DES) is in the process of imaging $5000\ \mathrm{deg}^2$ of the southern Galactic cap in five photometric bands (Abbott et al. 2005; Diehl et al. 2014). The deep photometry of DES ($r \sim 24$ mag) will enable the detection of the faintest known satellite galaxies out to ∼120 kpc (compared to the SDSS limit of ∼50 kpc), and more luminous satellite galaxies out to the Milky Way virial radius (Rossetto et al. 2011). We have completed an initial search of the first year of DES data and report here on the eight most significant dwarf galaxy candidates discovered therein (Table 1). Since the physical nature of these candidates cannot be definitively determined with photometry alone, we refer to them by their discovery coordinates. If these candidates are later confirmed to be Local Group galaxies, they should be renamed after the constellation in which they reside: DES J0335.6−5403 (Reticulum II), DES J0344.3−4331 (Eridanus II), DES J2251.2−5836 (Tucana II), DES J0255.4−5406 (Horologium I), DES J2108.8−5109 (Indus I), DES J0443.8−5017 (Pictor I), DES J2339.9−5424 (Phoenix II), and DES J0222.7−5217 (Eridanus III). If any are instead globular clusters, they would be known as DES 1 through N. After the completion of this work, we learned that DES J2108.8−5109 was previously identified by Kim et al. (2015) in data from the Stromlo Milky Way Satellite Survey and designated as a likely star cluster, Kim 2.

2. DATA SET

DES is a wide-field optical imaging survey in the *grizY* bands performed with the Dark Energy Camera (DECam; Flaugher et al. 2010, 2015; Diehl 2012). The DECam focal plane comprises 74 CCDs: 62 2k × 4k CCDs dedicated to science imaging and 12 2k × 2k CCDs for guiding, focus, and alignment. DECam is installed at the prime focus of the 4 m Blanco telescope at Cerro Tololo Inter-American Observatory. In this configuration, DECam has a hexagonal 2°.2-wide field of view and a central pixel scale of 0.263 arcseconds. The full DES survey is scheduled for 525 nights distributed over 5 years. Here, we consider data collected between 2013 August 15 and 2014 February 9 during the first year of DES.

The first internal annual release of DES data (Y1A1) consists of ∼12,000 science exposures processed by the DES data management (DESDM) infrastructure (R. A. Gruendl et al. 2015, in preparation).[44] Most of the Y1A1 footprint is covered by 2–4 overlapping exposures, or "tilings," in each filter. Single exposures in a tiling are 90 s in *griz* and 45 s in *Y*. Here, we rely on the *g*- and *r*-band images for photometry, and use the *i*-band for star–galaxy separation.

The DESDM image processing pipeline consists of image detrending, astrometric calibration, nightly photometric calibration, global calibration, image coaddition, and object catalog creation, as recently summarized in Balbinot et al. (2015). We refer to Sevilla et al. (2011), Desai et al. (2012), and Mohr et al. (2012) for a more detailed description of the DES single-epoch and coadd image processing. The `SExtractor`toolkit is used to create object catalogs from the processed and coadded images (Bertin & Arnouts 1996; Bertin et al. 2011). The Y1A1 data release contains a catalog of ∼131 million unique objects detected in the coadd imaging which are distributed over $1800\ \mathrm{deg}^2$. This area includes $\sim 200\ \mathrm{deg}^2$ overlapping with the Stripe 82 region of SDSS, as well as a contiguous region of $\sim 1600\ \mathrm{deg}^2$ overlapping the South Pole Telescope (SPT) footprint (Carlstrom et al. 2011). The DES imaging in the SPT region is unprecedented in depth. Figure 1 shows the coverage of Y1A1 in Galactic coordinates.

We selected stars from the Y1A1 coadd object catalog based on the *spread_model* quantity output by `SExtractor` (Desai et al. 2012). To avoid issues arising from fitting the point-spread function (PSF) across variable-depth coadded images,

[44] http://data.darkenergysurvey.org/aux/releasenotes/DESDMrelease.html

Table 1
Detection of New Satellite Galaxy Candidates in DES Y1A1

Name	α_{2000} (deg)	δ_{2000} (deg)	$m-M$	Map Sig (σ)	TS Scan	TS Fit	r_h (deg)	ϵ	ϕ (deg)	Σp_i
DES J0335.6–5403 (Ret II)	53.92	−54.05	17.5	24.6	1466	1713	$0.10^{+0.01}_{-0.01}$	$0.6^{+0.1}_{-0.2}$	72^{+7}_{-7}	338.1
DES J0344.3–4331 (Eri II)	56.09	−43.53	22.6	23.0	322	512	$0.03^{+0.01}_{-0.01}$	$0.19^{+0.16}_{-0.16}$	90^{+30}_{-30}	96.9
DES J2251.2–5836 (Tuc II)	343.06	−58.57	18.8	6.4	129	167	$0.12^{+0.03}_{-0.03}$	⋯	⋯	114.9
DES J0255.4–5406 (Hor I)	43.87	−54.11	19.7	8.2	55	81	$0.04^{+0.05}_{-0.02}$	⋯	⋯	30.6
DES J2108.8–5109 (Ind I)	317.20	−51.16	19.2	5.5	⋯	75	$0.010^{+0.002}_{-0.002}$	⋯	⋯	26.6
DES J0443.8–5017 (Pic I)	70.95	−50.28	20.5	7.1	⋯	63	$0.02^{+0.07}_{-0.01}$	⋯	⋯	19.1
DES J2339.9–5424 (Phe II)	354.99	−54.41	19.9	5.1	⋯	61	$0.02^{+0.01}_{-0.01}$	⋯	⋯	19.4
DES J0222.7–5217 (Eri III)	35.69	−52.28	19.9	5.4	⋯	57	$0.007^{+0.005}_{-0.003}$	⋯	⋯	8.9

Note. Best-fit parameters from the maximum-likelihood fit assuming the composite isochrone described in Section 3.2. Uncertainties are calculated from the the highest density interval containing 90% of the posterior distribution. "Map Sig" refers to detection significance of the candidate from the stellar density map search method (Section 3.1). "TS Scan" refers to the significance (Equation (4)) from the likelihood scan using a Plummer model spatial kernel with half-light radius $r_h = 0.^\circ 1$ (Section 3.2). "TS Fit" denotes the significance of the likelihood method using the set of best-fit parameters. Ellipticities and position angles are not quoted for lower significance candidates where they are not well constrained by the data. For objects with significant ellipticity, the half-light radius is measured along the elliptical semimajor axis. Σp_i is the estimated number of satellite member stars with $g < 23$ in the stellar catalog.

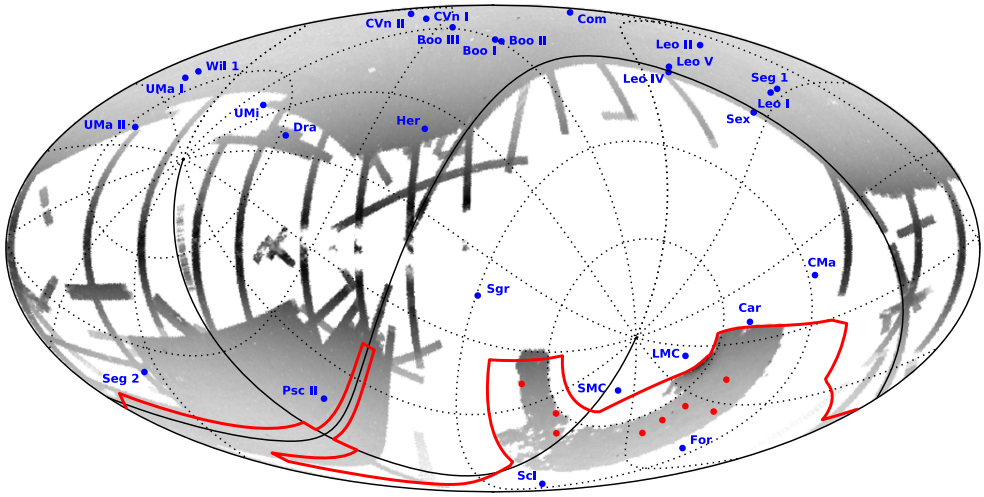

Figure 1. Locations of 27 known Milky Way satellite galaxies (blue; McConnachie 2012a) and eight DES dwarf galaxy candidates (red) in Galactic coordinates (Mollweide projection). The coordinate grid shows the equatorial coordinate system with solid lines for the equator and zero meridian. The gray scale indicates the logarithmic density of stars with $r < 22$ from SDSS and DES. The large contiguous region in the northern equatorial hemisphere shows the coverage of SDSS (Ahn et al. 2014). The full DES footprint is outlined in red, and is now partially filled in by a region of ∼1600 deg^2 near to the Magellanic Clouds and a region of ∼200 deg^2 overlapping with the SDSS Stripe 82 field along the celestial equator. Both fields were observed during the first year of DES and that compose the Y1A1 data set.

we utilized the weighted-average (*wavg*) of the *spread_model* measurements from the single-epoch exposures. Our stellar sample consists of well-measured objects with $|wavg\_spread\_model\_i| < 0.003$, $flags\_\{g, r, i\} < 4$, and $magerr\_auto\_\{g, r, i\} < 1$. We also removed objects for which the *mag_psf* and *mag_auto* measurements differ by more than 0.5 mag because this is indicative of poor object characterization.

We estimated the stellar completeness on a statistical basis over the full Y1A1 footprint by creating a test sample of high stellar purity using a color-based selection of $r - i > 1.7$. We then applied the morphology-based star selection criteria above that uses imaging in only a single band to evaluate the stellar completeness for the test sample. This approach is unbiased since the two star selection criteria are orthogonal, and benefits from a large statistical sample that is representative of the full Y1A1 data set. The stellar completeness was found to be >90% to $g \sim 22$ mag and falls to ∼50% by $g \sim 23$ mag. We validated this completeness estimate with matched spectroscopic data in the overlap region between Y1A1 and SDSS Stripe 82. Based on studies with the DAOPHOT[45] software package optimized for photometry in crowded stellar fields, we do not expect this stellar completeness to be reduced in the vicinity of DES satellite galaxy candidates relative to the Y1A1 footprint at large.

For point-like objects and a well-estimated PSF, the SExtractor *mag_psf* variables are expected to give the best measurement of stellar fluxes. However, due to the aforementioned difficulties with PSF estimation on deep coadded images, we chose instead to use the *mag_auto* measurements. The *mag_auto* measurements are found to give a less biased estimate of flux when compared to a stellar calibration sample from Pan-STARRS (Schlafly et al. 2012). Measured magnitudes are extinction corrected using the

[45] http://www.star.bris.ac.uk/~mbt/daophot/

$E(B-V)$ dust maps from Schlegel et al. (1998). The relative calibration uncertainties are estimated via stellar-locus regression (Kelly et al. 2014) and are found to be ∼2% across the survey footprint. Uncertaities in the offsets between the DES photometric system and the AB system are estimated to be ∼1%.

3. SEARCH METHODS

Ultra-faint galaxies are discovered as arcminute-scale over-densities of individually resolved stars. The Y1A1 stellar object catalog is of such quality and depth that numerous stellar over-densities are immediately apparent from a visual scan. Several of these over-densities are not associated with any known star cluster, globular cluster, or satellite galaxy. To formalize the process of identifying new candidate satellite galaxies, we applied both (1) a simple spatial binning algorithm to facilitate inspection of the stellar density field, and (2) a matched-filter maximum-likelihood technique. These complementary approaches validated one another and the resultant list of candidates was vetted by both methods.

3.1. Stellar Density Maps

Several independent searches of the stellar density field were conducted. One approach involved direct visual inspection of coadded images. Other searches used binned stellar density maps constructed from the coadd object catalogs. As an example, we detail below how one of these maps was built and analyzed.

We began by spatially binning the stellar catalog into equal-area pixels using the `HEALPix` scheme (Górski et al. 2005).[46] We considered `HEALPix` pixel sizes of $\sim 0\overset{\circ}{.}06$ (nside = 1024) and $\sim 0\overset{\circ}{.}11$ (nside = 512) to optimize sensitivity to satellites possessing different angular sizes. Since the stellar density is greatly enhanced in regions of the Y1A1 footprint near the LMC and Galactic plane, we further grouped the stars into larger regions of ∼13 deg^2 (nside = 16) to estimate the local field density of stars. We corrected the effective solid angle of each pixel using the survey coverage, as estimated by `mangle` as part of DESDM processing (Swanson et al. 2008).[47] Several conspicuous stellar over-densities were immediately apparent after this simple spatial binning procedure.

We increase our sensitivity to ultra-faint satellite galaxies by focusing our search on regions of color–magnitude space populated by old, low-metallicity stellar populations (Koposov et al. 2008; Walsh et al. 2009). As a template, we used a `PARSEC` isochrone corresponding to a stellar population of age 12 Gyr and metallicity $Z = 0.0002$ (Bressan et al. 2012). Sensitivity to satellites at varying distances was enhanced by considering 20 logarithmically spaced steps in heliocentric distance ranging from 20 to 400 kpc (distance moduli $16.5 < M - m < 23.0$). For each step in distance, all stars within 0.2 mag of the isochrone in magnitude–magnitude space were retained while those outside the isochrone template were discarded. We then created a significance map for each ∼13 deg^2 region by computing the Poisson likelihood of finding the observed number of stars in each map pixel given a background level characterized by the local field density.

[46] http://healpix.sourceforge.net
[47] http://space.mit.edu/~molly/mangle/

3.2. Matched-filter Maximum-likelihood Method

The simple approach described above is computationally efficient and easily generalizable. However, a more sensitive search can be performed by simultaneously modeling the spatial and photometric distributions of stars and incorporating detailed characteristics of the survey (variable depth, photometric uncertainty, etc.). One way to incorporate this information is through a maximum-likelihood analysis (Fisher 1925; Edwards 1972). Likelihood-based analyses have found broad applicability in studies of Milky Way satellites (e.g., Dolphin 2002; Martin et al. 2008a). Here we extend the maximum-likelihood approach to a wide-area search for Milky Way satellites. Similar strategies have been applied to create catalogs of galaxy clusters over wide-field optical surveys (e.g., Rykoff et al. 2014).

Our maximum-likelihood search begins by assuming that the stellar catalog in a small patch of sky represents a Poisson realization of (1) a field contribution including Milky Way foreground stars, mis-classified background galaxies, and imaging artifacts, and (2) a putative satellite galaxy. The unbinned Poisson log-likelihood function is given by

$$\log \mathcal{L} = -f\lambda + \sum_i \big(1 - p_i\big), \tag{1}$$

where i indexes the objects in the stellar sample. The value p_i can be interpreted as the probability that star i is a member of the satellite, and is computed as

$$p_i \equiv \frac{\lambda u_i}{\lambda u_i + b_i}. \tag{2}$$

Here, u represents the signal probability density function (PDF) for the satellite galaxy and is normalized to unity over the spatial and magnitude domain, $\mathcal{S}$; specifically, $\int_{\rm all} u\, d\mathcal{S} = 1$. The corresponding background density function for the field population is denoted by b.

We define the richness, λ, to be a normalization parameter representing the total number of satellite member stars with mass $>0.1 M_\odot$. In Equation (1), $f \equiv \int_{\rm obs} u\, d\mathcal{S}$ represents the fraction of satellite member stars that are within the *observable* spatial and magnitude domain of the survey, and $f\lambda$ denotes the expected number of observable satellite member stars.[48] Maximizing the likelihood with respect to the richness implies $f\lambda = \sum_i p_i$. This condition makes clear that the satellite membership probability for each star in the catalog is a natural product of the maximum-likelihood approach. These membership probabilities can be used to prioritize targeting when planning spectroscopic follow-up observations. Figure 2 highlights the use of membership probabilities to visualize a low-surface-brightness satellite galaxy candidate.

To characterize a candidate satellite galaxy, we explore the likelihood of the data, $\mathcal{D}$, as a function of a set of input model parameters, $\boldsymbol{\theta}$. The signal PDF is assumed to be separable into two independent components,

$$u\big(\mathcal{D}_i \,|\boldsymbol{\theta}\big) = u_s\big(\mathcal{D}_{s,i} \,|\boldsymbol{\theta}_s\big) \times u_c\big(\mathcal{D}_{c,i} \,|\boldsymbol{\theta}_c\big). \tag{3}$$

[48] `Mangle` maps of the survey coverage are used in the calculation of the observable fraction at each position in the sky.

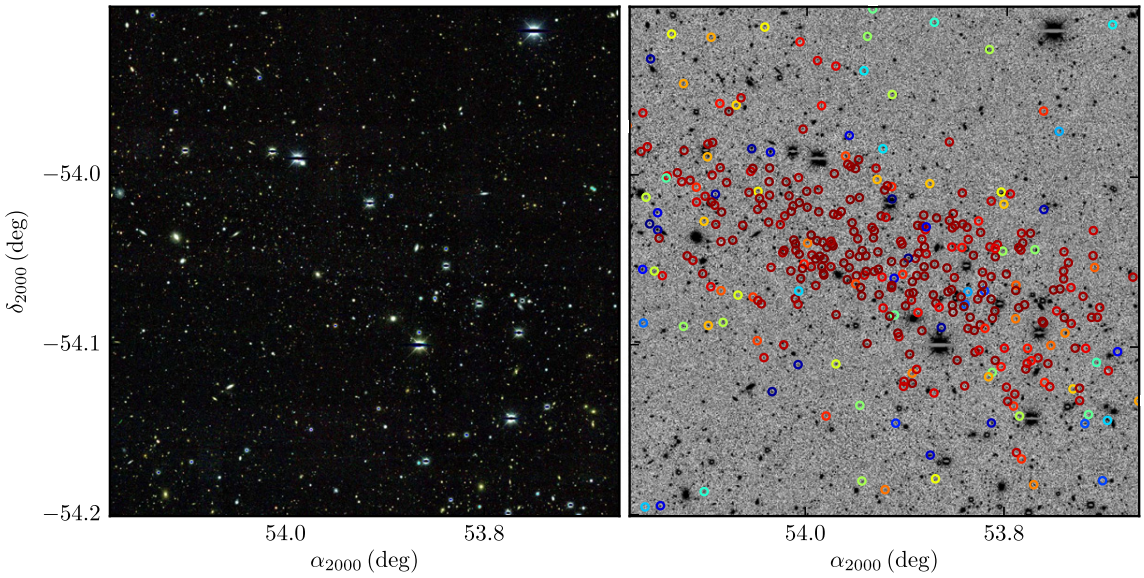

Figure 2. Left: false color *gri* coadd image of the $0.^{\circ}3 \times 0.^{\circ}3$ region centered on DES J0335.6−5403. Right: stars in the same field of view with membership probability $p_i > 0.01$ are marked with colored circles. In this color map, red signifies high-confidence association with DES J0335.6−5403 and blue indicates lower membership probability. The membership probabilities have been evaluated using Equation (2) for the best-fit model parameters listed in Table 1.

The first component, u_s, depends only on the spatial properties, while the second component, u_c, depends only on the distribution in color–magnitude space.

We modeled the spatial distribution of satellite member stars with an elliptical Plummer profile (Plummer 1911), following the elliptical coordinate prescription of Martin et al. (2008a). The Plummer profile is sufficient to describe the spatial distribution of stars in known ultra-faint galaxies (Muñoz et al. 2012b). The spatial data for catalog object i consist of spatial coordinates, $\boldsymbol{D}_{s,i} = \{\alpha_i, \delta_i\}$, while the parameters of our elliptical Plummer profile are the centroid coordinates, half-light radius, ellipticity, and position angle, $\boldsymbol{\theta}_s = \{\alpha_0, \delta_0, r_{\rm h}, \epsilon, \phi\}$.

We modeled the color–magnitude component of the signal PDF with a set of representative isochrones for old, metal-poor stellar populations, specifically by taking a grid of isochrones from Bressan et al. (2012) spanning $0.0001 < Z < 0.001$ and $1\ {\rm Gyr} < \tau < 13.5\ {\rm Gyr}$. Our spectral data for star i consist of the magnitude and magnitude error in each of two filters, $\boldsymbol{D}_{c,i} = \{g_i, \sigma_{g,i}, r_i, \sigma_{r,i}\}$, while the model parameters are composed of the distance modulus, age, and metallicity describing the isochrone, $\boldsymbol{\theta}_c = \{M - m, \tau, Z\}$. To calculate the spectral signal PDF, we weight the isochrone by a Chabrier (2001) initial mass function (IMF) and densely sample in magnitude–magnitude space. We then convolve the photometric measurement PDF of each star with the PDF of the weighted isochrone. The resulting distribution represents the predicted probability of finding a star at a given position in magnitude–magnitude space given a model of the stellar system.

The background density function of the field population is empirically determined from a circular annulus surrounding each satellite candidate ($0.^{\circ}5 < r < 2.^{\circ}0$). The inner radius of the annulus is chosen to be sufficiently large that the stellar population of the candidate satellite does not bias the estimate of the field population. Stellar objects in the background annulus are binned in color–magnitude space using a cloud-in-cells algorithm and are weighted by the inverse solid angle of the annulus. The effective solid angle of the annulus is corrected to account for regions that are masked or fall below our imposed magnitude limit of $g < 23$ mag. The resulting two-dimensional histogram for the field population provides the number density of stellar objects as a function of observed color and magnitude (${\rm deg}^{-2}\ {\rm mag}^{-2}$). This empirical determination of the background density incorporates contamination from unresolved galaxies and imaging artifacts.

The likelihood formalism above was applied to the Y1A1 data set via an automated analysis pipeline.[49] For the search phase of the algorithm, we used a radially symmetric Plummer model with half-light radius $r_{\rm h} = 0.^{\circ}1$ as the spatial kernel, and a composite isochrone model consisting of four isochrones bracketing a range of ages, $\tau = \{12, 13.5\ {\rm Gyr}\}$, and metallicities, $Z = \{0.0001, 0.0002\}$, to bound a range of possible stellar populations. We then tested for a putative satellite galaxy at each location on a three-dimensional grid of sky position (0.7 arcmin resolution; nside = 4096) and distance modulus ($16 < M - m < 24$; 16−630 kpc).

The statistical significance at each grid point can be expressed as a Test Statistic (TS) based on the likelihood ratio between a hypothesis that includes a satellite galaxy versus a field-only hypothesis:

$$\mathrm{TS} = 2\Big[\log \mathcal{L}\Big(\lambda = \hat{\lambda}\Big) - \log \mathcal{L}\Big(\lambda = 0\Big)\Big]. \quad (4)$$

Here, $\hat{\lambda}$ is the value of the stellar richness that maximizes the likelihood. In the asymptotic limit, the null-hypothesis distribution of the TS will follow a $\chi^2/2$ distribution with one bounded degree of freedom (Chernoff 1954). We have verified that the output distribution of our implementation agrees well with the theoretical expectation by testing on simulations of the stellar field. In this case, the *local* statistical significance of a given stellar over-density, expressed in

[49] The Ultra-faint Galaxy Likelihood (UGALI) code; detailed methodology and performance to be presented elsewhere.

Table 2
Properties of DES Satellite Galaxy Candidates

Name	Distance (kpc)	M_* ($10^3 M_\odot$)	M_V (mag)	$r_{1/2}$ (pc)	$\log_{10}(\tau)$ $\log_{10}$(Gyr)	Z
DES J0335.6–5403 (Ret II)	32	$2.6^{+0.2}_{-0.2}$	-3.6 ± 0.1	55^{+5}_{-5}	10.08 ± 0.21	<0.0003
DES J0344.3–4331 (Eri II)	330	83^{+17}_{-14}	-7.4 ± 0.1	172^{+57}_{-57}	10.10 ± 0.23	<0.0006
DES J2251.2–5836 (Tuc II)	58	3^{+7}_{-1}	-3.9 ± 0.2	120^{+30}_{-30}	…	…
DES J0255.4–5406 (Hor I)	87	$2.4^{+1.4}_{-0.7}$	-3.5 ± 0.3	60^{+76}_{-30}	9.96 ± 0.21	<0.0005
DES J2108.8–5109 (Ind I)	69	$0.8^{+0.4}_{-0.4}$	-2.2 ± 0.5	12^{+2}_{-2}	…	…
DES J0443.8–5017 (Pic I)	126	$2.8^{+5.0}_{-1.7}$	-3.7 ± 0.4	43^{+153}_{-21}	10.00 ± 0.16	<0.0004
DES J2339.9–5424 (Phe II)	95	$2.8^{+1.2}_{-0.7}$	-3.7 ± 0.4	33^{+20}_{-11}	…	…
DES J0222.7–5217 (Eri III)	95	$0.9^{+0.9}_{-0.7}$	-2.4 ± 0.6	11^{+8}_{-5}	…	…

Note. Uncertainties are calculated from the the highest density interval containing 90% of the posterior distribution. Stellar masses are computed for a Chabrier initial mass function.

Gaussian standard deviations, is approximately the square root of the TS.

4. CANDIDATE SELECTION AND CHARACTERIZATION

The two search methods described in Section 3 each produce significance maps of the full Y1A1 footprint, where peaks in these maps represent the three-dimensional seed positions (α_{2000}, δ_{2000}, $M - m$) of possible satellite galaxies. Seeds were selected from the union of the search methods. Statistical significance thresholds were set at $>5\sigma$ for the stellar density map method and TS > 45 for the matched-filter maximum-likelihood method, yielding $\sim$50 seeds. Most of these were discarded as being attributed to steep gradients in the stellar density field, numerical effects near the survey boundaries, imaging artifacts, and large nearby galaxies resolved into multiple closely spaced catalog objects. For this reason, we did not pursue investigation at lower significance thresholds.

The resulting seed list was compared against catalogs of known star clusters (Harris 1996, 2010 edition; Kharchenko et al. 2013) and Milky Way satellite galaxies (McConnachie 2012a) as well as catalogs of other astrophysical objects that can produce false positives, such as large nearby galaxies (Nilson 1973; Corwin 2004) or galaxy clusters (Rykoff et al. 2014). Associated seeds include the Reticulum globular cluster, the Phoenix dwarf galaxy, AM 1, NGC 1261, NGC 1291, NGC 1553, NGC 1851, NGC 7089, NGC 7424, ESO 121-SC 003, and ESO 201-SC 010.

We explored the multi-dimensional parameter space for each unassociated seed using the `emcee` module for Markov Chain Monte Carlo (MCMC; Foreman-Mackey et al. 2013),[50] and the likelihood function described in Section 3.2 with flat priors on each of the input parameters. For each seed, we ran an MCMC chain with 100 walkers that each make 1000 steps including a burn-in stage of 50 steps. This is sufficient to sample the region of parameter space near the maximum-likelihood estimate. Only seeds with well-constrained posterior distributions enter our candidate list of new Milky Way companions.

Table 1 presents the eight most significant stellar over-densities in the Y1A1 data set consistent with being previously unknown dwarf galaxies. When comparing the significances obtained with the map-based and likelihood scan algorithms, it is worth noting that the two methods were applied assuming different size scales for the target satellites, and that kernel assumed for the likelihood scan ($r_h = 0.^\circ 1$) is larger than the majority of candidates listed in Table 1. After fitting the spatial parameters of the candidates, all are detected with high significance using the likelihood-based method. The dependence of detection efficiency on assumed kernel size is discussed is Section 5.2.

The physical characteristics of these objects, as determined by the follow-up MCMC likelihood analysis, are summarized in Table 2. The best-fit values and uncertainties are determined from the peak of the posterior distribution and the 90% highest posterior density interval (Box & Tiao 1973). A significant correlation was observed between the age of the stellar isochrone and the heliocentric distance—a degeneracy that may be expected given the evolution of the main sequence turnoff. For some DES candidates, the posterior distribution for the distance is multi-modal. The distance estimates provided in Table 2 indicate the peaks in the posterior distribution.

To compare with previously known Milky Way satellite galaxies, we convert from DES g- and r-band magnitudes to visual magnitudes using

$$\begin{aligned} g_{\rm DES} &= g_{\rm SDSS} - 0.104\left(g_{\rm SDSS} - r_{\rm SDSS}\right) + 0.01 \text{ mag} \\ r_{\rm DES} &= r_{\rm SDSS} - 0.102\left(g_{\rm SDSS} - r_{\rm SDSS}\right) + 0.02 \text{ mag} \\ \Rightarrow V &= g_{\rm DES} - 0.487\left(g_{\rm DES} - r_{\rm DES}\right) - 0.025 \text{ mag}. \end{aligned} \quad (5)$$

This transform from DES g and r magnitudes to V-band magnitudes was derived using an SDSS stellar calibration sample and the equations from Jester et al. (2005). The absolute magnitude of each satellite is calculated using the sampling formalism of Martin et al. (2008a). For bright satellites, this formalism yields a very similar estimate to the integration of the stellar luminosity function for the best-fit model. However, for fainter satellites, the uncertainty in the total magnitude can be dominated by shot noise arising from sparse sampling of the stellar population. In this case, the additional association of a single bright star can have a strong influence on the measured magnitude of a satellite. Similarly, the evolution of individual member stars can substantially change the total luminosity. To quantify the impact of shot noise on the derived luminosity estimates, we use a representative isochrone weighted by a Chabrier IMF to simulate an ensemble of satellites with similar characteristics to the observed candidates. The quoted uncertainty on the

[50] `emcee` v2.1.0: http://dan.iel.fm/emcee/current/.

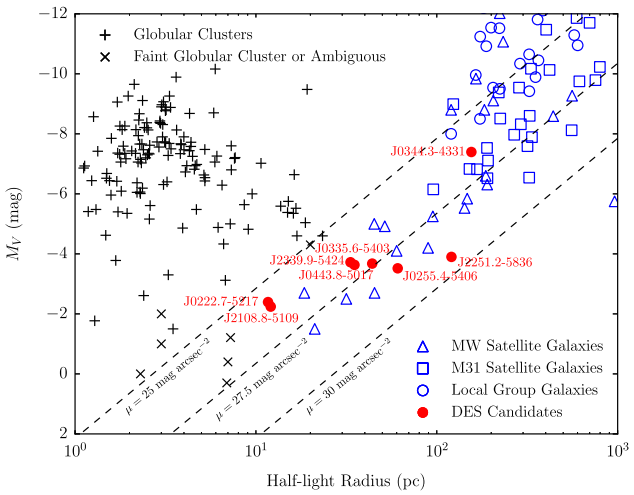

Figure 3. Local Group galaxies (McConnachie 2012a) and globular clusters (Harris 1996, 2010 edition) occupy distinct regions in the plane of physical half-light radius (geometric mean of the major and minor axes) and absolute luminosity. The majority of DES satellite candidates (red dots) are more consistent with the locus of Local Group galaxies (empty blue shapes) than with the population of Galactic globular clusters (black crosses). Several of the faintest globular clusters and systems of ambiguous classification are indicated with×marks: Koposov 1 and Koposov 2 (Koposov et al. 2007; Paust et al. 2014), Segue 3 (Belokurov et al. 2010; Fadely et al. 2011; Ortolani et al. 2013), Muñoz 1 (Muñoz et al. 2012a), Balbinot 1 (Balbinot et al. 2013), PSO J174.0675–10.8774/Crater I (Laevens et al. 2014; Belokurov et al. 2014), and Kim 1 (Kim & Jerjen 2015). Dashed lines indicate contours of constant surface brightness at $\mu = \{25, 27.5, 30\}$ mag arcsec^{-2}.

luminosity reflects the expected shot noise from stars in the magnitude range visible to DES, 17 mag $< g <$ 23 mag.

The angular and physical half-light radii listed in Tables 1 and Table 2 are both given as two-dimensional quantities. The deprojected (three-dimensional) half-light radius is a factor ∼1.3 larger than the projected half-light radius for a variety of common density profiles (Wolf et al. 2010). For objects with measured ellipticity, we report the half-light radius measured along the semimajor axis.

As illustrated in Figure 1, the DES candidates are distributed throughout the Y1A1 footprint and occupy a portion of the celestial sphere in the direction of the Magellanic Clouds where no ultra-faint galaxies were previously known. The DES candidates are widely distributed in heliocentric distance from ∼30 kpc (DES J0335.6−5403) to >300 kpc (DES J0344.3−4331).

5. DISCUSSION

Galaxies are distinguished from star clusters by having a dynamical mass that is substantially larger than the mass inferred from the luminous stellar population and/or a significant dispersion in metallicities indicative of multiple generations of star formation and a deep enough gravitational potential to retain supernova ejecta (Willman & Strader 2012). While devoted spectroscopic follow up observations are necessary to unambiguously classify these objects, the properties given in Table 2 already provide strong clues as to which candidates are most likely to be galaxies. First, the large physical sizes of most of these objects are more consistent with the locus occupied by known satellite galaxies of the Local Group than with globular clusters of the Milky Way, as shown in Figure 3. All of the DES candidates are of comparable surface brightness to the ultra-faint galaxies detected in SDSS (McConnachie 2012a). The two most compact systems, DES J2108.8−5109 and DES J0222.7−5217, fall in between the known ultra-faint galaxies and the faintest Milky Way star clusters, e.g., Koposov 1 and Koposov 2 (Koposov et al. 2007; Paust et al. 2014), Segue 3 (Belokurov et al. 2010; Fadely et al. 2011; Ortolani et al. 2013), Muñoz 1 (Muñoz et al. 2012a), Balbinot 1 (Balbinot et al. 2013), and Kim 1 (Kim & Jerjen 2015). For the most significant DES candidates, it is possible to estimate the ellipticity. Whereas globular clusters tend to have ellipticity $\lesssim$0.2 (Martin et al. 2008a; van den Bergh 2008), the best measured candidate, DES J0335.6−5403, has an ellipticity ∼0.6, which is more consistent with the population of known ultra-faint galaxies.

Further insight can be gained by fitting isochrones to the observed stellar distribution in color–magnitude space. Two independent maximum-likelihood implementations confirm that the DES candidates are generally consistent with old ($\tau \gtrsim 10$ Gyr) and metal-poor stellar populations ($Z \sim 0.0002$). The first of these analyses is the pipeline described in Section 3.2 used in a mode that varies age and metallicity in addition to spatial parameters and distance modulus in a simultaneous fit. The second color–magnitude fitting procedure adopts a similar likelihood formalism, but fits the spatial and photometric distributions of the stars in two separate phases. Instead of assuming an IMF, the second method weights the stars according to their proximity to the best-fit centroid location, and then evaluates the consistency between each star and a given isochrone in color–magnitude space given the photometric uncertainty for that star. The second method is more robust to complications that might arise from stellar incompleteness and/or imperfect modeling of the IMF. Age estimates and metallicity upper limits for four of the more significant DES candidates are reported in Table 2. Like the previously known ultra-faint dwarfs, the new DES systems are old and metal-poor (e.g., Brown et al. 2014). The latter fitting procedure has also been applied to non-extinction corrected magnitudes to independently validate the extinction values from Schlegel et al. (1998).

5.1. Review of Individual Candidates.

Brief comments on the individual galaxy candidates are provided below, and spatial maps and color–magnitude diagrams for each candidate are provided in Figures 4–11. The rightmost panels of these Figures show the satellite membership probabilities of individual stars that are assigned by the likelihood fit using a single representative isochrone with $\tau = 13.5$ Gyr and $Z = 0.0001$. Stars with high membership probabilities contribute most to the statistical significance of each candidate. The constellation designation, should these candidates be confirmed as dwarf galaxies, is listed in parenthesis.

1. *DES J0335.6–5403* (Reticulum II, Figure 4): as the nearest and most significant candidate, DES J0335.6−5403 is highly conspicuous in the Y1A1 stellar density maps, with ∼300 member stars brighter than $g \sim 23$ mag. In fact, an over-density of faint stars at this position is even visible in the much shallower Digitized Sky Survey images, although it was not detected by Whiting et al. (2007) and other searches of photographic material. Note that like the previously known ultra-faint dwarfs, DES J0335.6−5403 very likely contains several blue horizontal branch stars identified by the likelihood

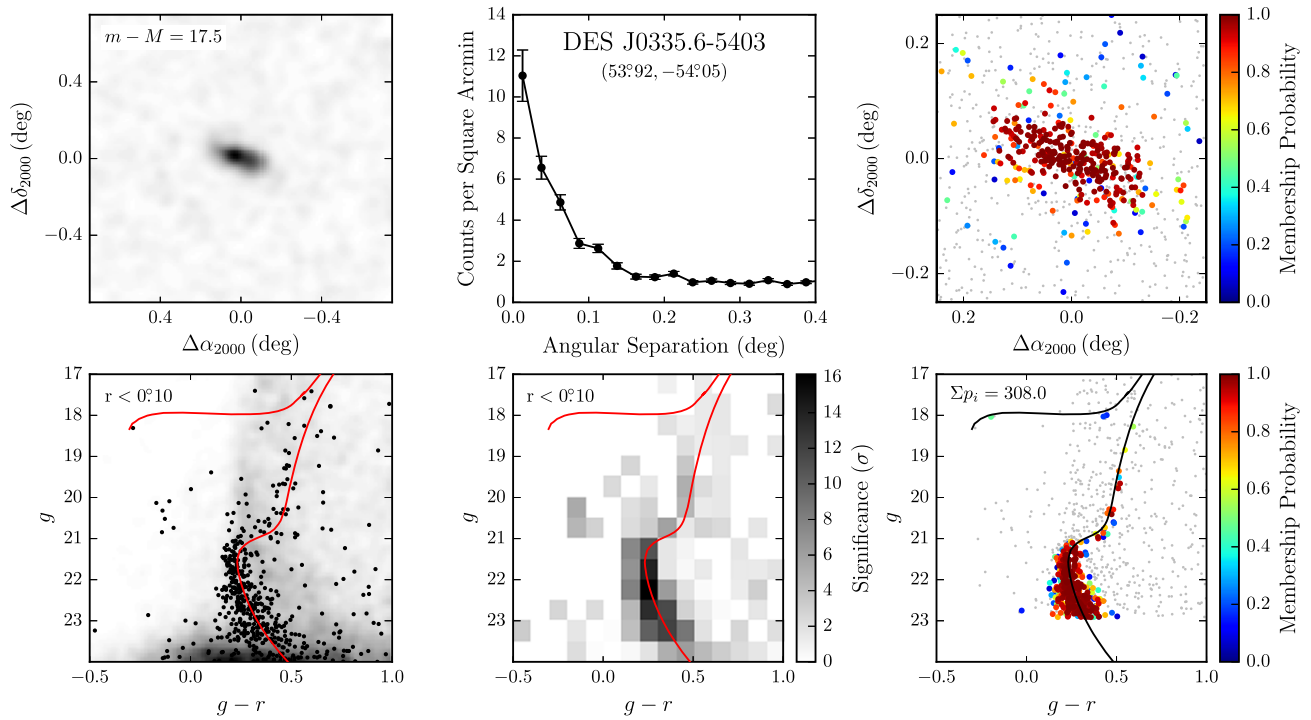

Figure 4. Stellar density and color–magnitude diagrams for DES J0335.6–5403. Top left: spatial distribution of stars with $g < 24$ mag that are within 0.1 mag of the isochrone displayed in the lower panels. The field of view is $1.^\circ5 \times 1.^\circ5$ centered on the candidate and the stellar distribution has been smoothed with a Gaussian kernel with standard deviation $0.^\circ027$. Top center: radial distribution of stars with $g - r < 1$ mag and $g < 24$ mag. Top right: spatial distribution of stars with high membership probabilities within a $0.^\circ5 \times 0.^\circ5$ field of view. Small gray points indicate stars with membership probability less than 5%. Bottom left: the color–magnitude distribution of stars within $0.^\circ1$ of the centroid are indicated with individual points. The density of the field within a 1° annulus is represented by the background two-dimensional histogram in grayscale. The red curve shows a representative isochrone for a stellar population with $\tau = 13.5$ Gyr and $Z = 0.0001$ located at the best-fit distance modulus listed in the upper left panel. Bottom center: binned significance diagram representing the Poisson probability of detecting the observed number of stars within the central $0.^\circ1$ for each bin of the color–magnitude space given the local field density. Bottom right: color–magnitude distribution of high membership probability stars.

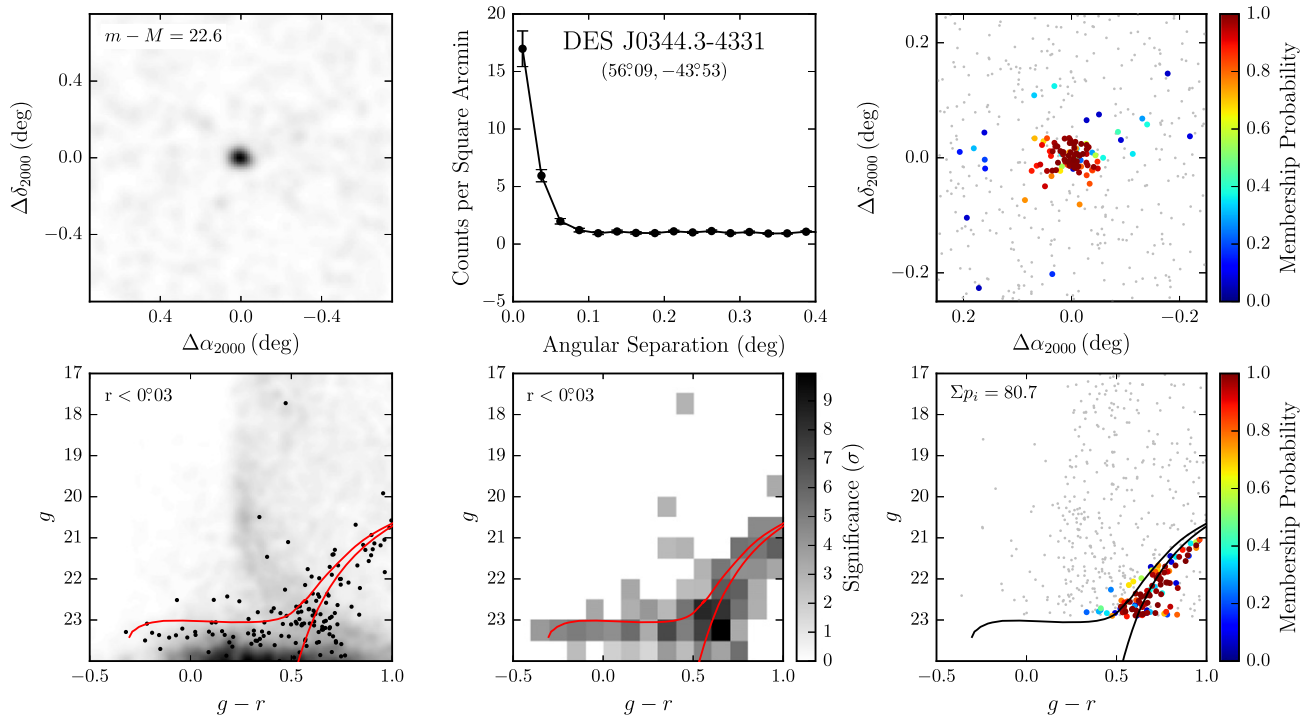

Figure 5. Analogous to Figure 4 but for DES J0344.3–4331. A large number of stars, including several probable horizontal branch members, are present at magnitudes fainter than the $g < 23$ mag threshold of our likelihood analysis. This threshold was set by the rapidly decreasing stellar completeness at fainter magnitudes. However, it is likely that extending to fainter magnitudes would cause the best-fit distance modulus of DES J0344.3–4331 to increase. Better constraints on the properties of DES J0344.3–4331 require the stellar completeness to be robustly quantified in this regime.

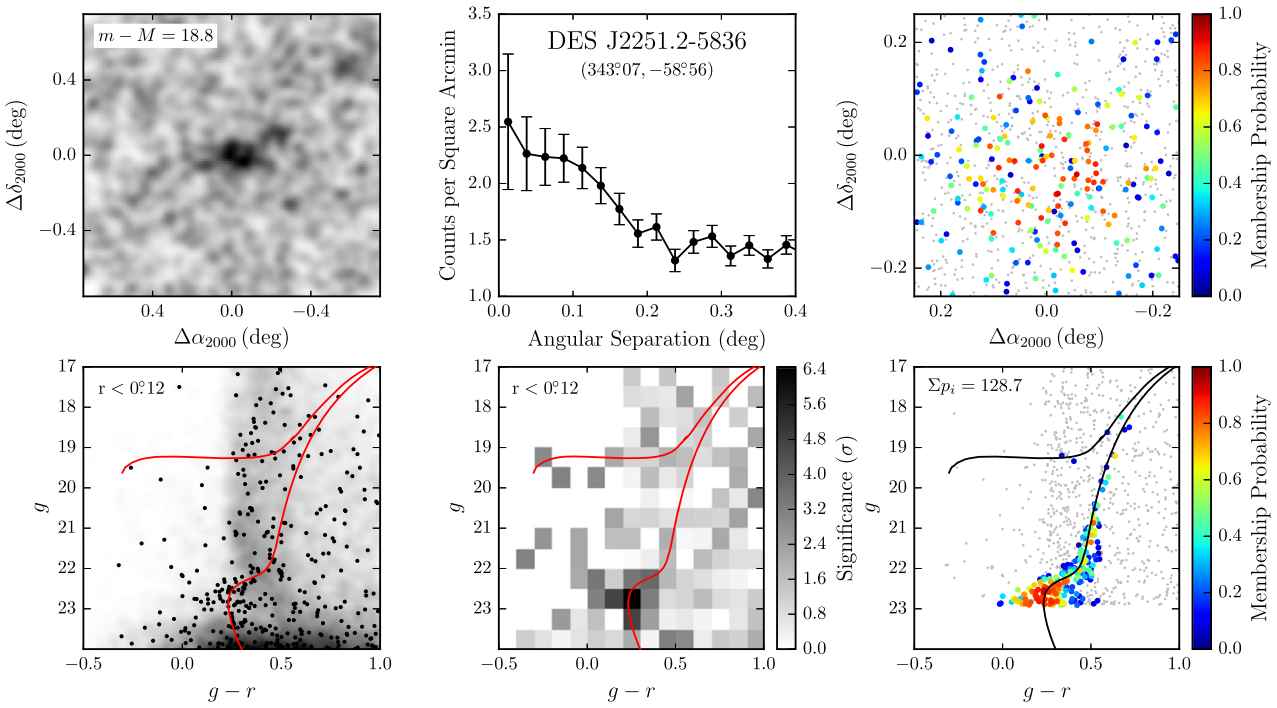

Figure 6. Analogous to Figure 4 but for DES J2251.2−5836.

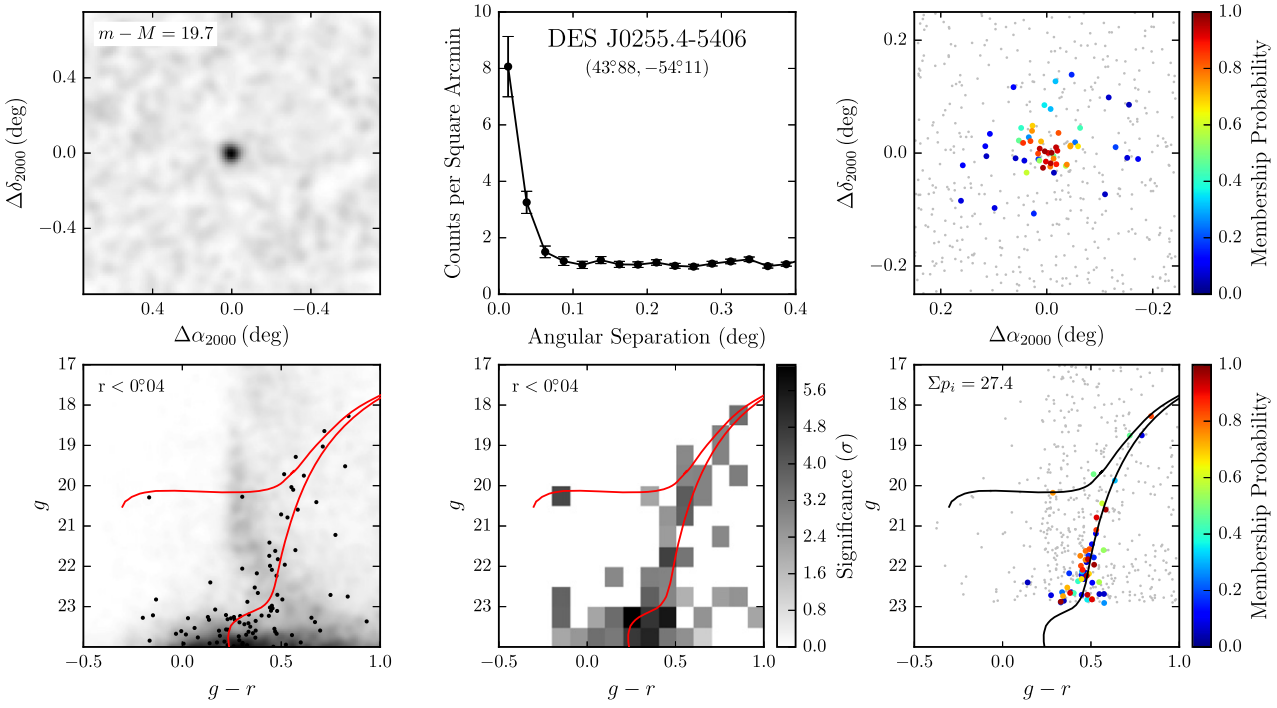

Figure 7. Analogous to Figure 4 but for DES J0255.4−5406.

procedure, two of which are relatively far from the center of the object. Given its luminosity, radius, and ellipticity, DES J0335.6−5403 is almost certainly a dwarf galaxy rather than a globular cluster. As illustrated in Figure 3, it is significantly more extended than any known faint globular cluster, and its elongated shape would also make it an extreme outlier from the Milky Way cluster population. Among known dwarfs, DES J0335.6−5403 appears quite comparable to Ursa Major II (Zucker et al. 2006a; Muñoz et al. 2010). DES J0335.6−5403 is only ∼23 kpc from the LMC, and measurements of its radial velocity and proper motion will provide strong

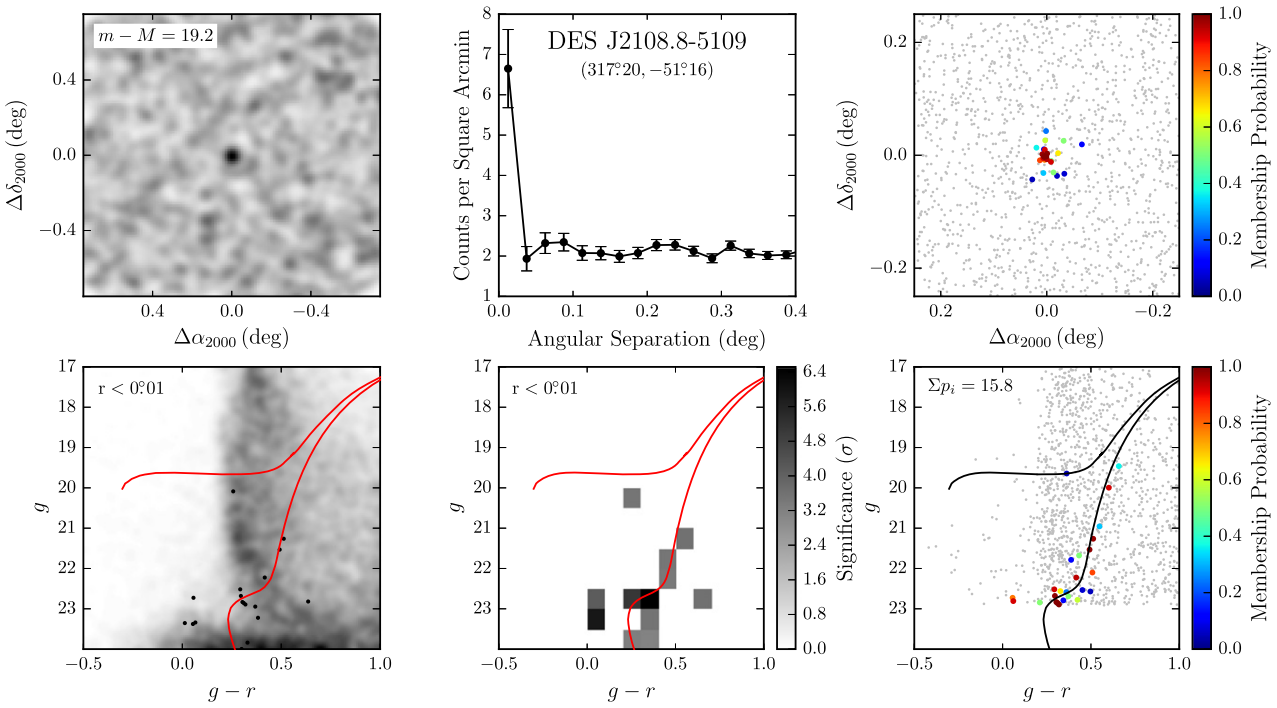

Figure 8. Analogous to Figure 4 but for DES J2108.8–5109.

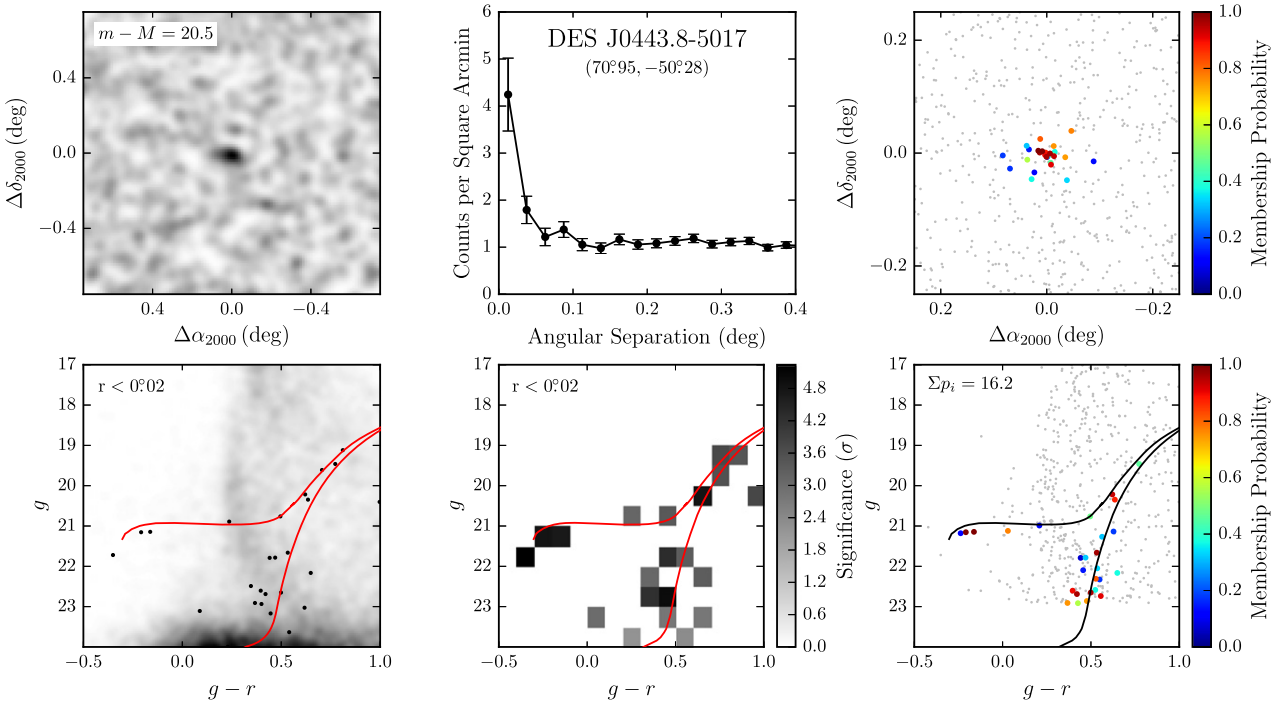

Figure 9. Analogous to Figure 4 but for DES J0443.8–5017.

clues as to whether it originated as a Milky Way satellite or fell into the Milky Way halo as part of a Magellanic group.

2. *DES J0222.7–5217* (Eridanus II, Figure 5): at a distance of >330 kpc, DES J0344.3–4331 is nearly a factor of three more distant than any known outer halo globular cluster, and its half-light radius of ∼170 pc is inconsistent with the sizes of globular clusters. It is therefore very likely that this object is a new dwarf galaxy. The color–magnitude diagram of DES J0344.3–4331 closely resembles that of another distant Milky Way satellite, Canes Venatici I, with a well-populated horizontal branch

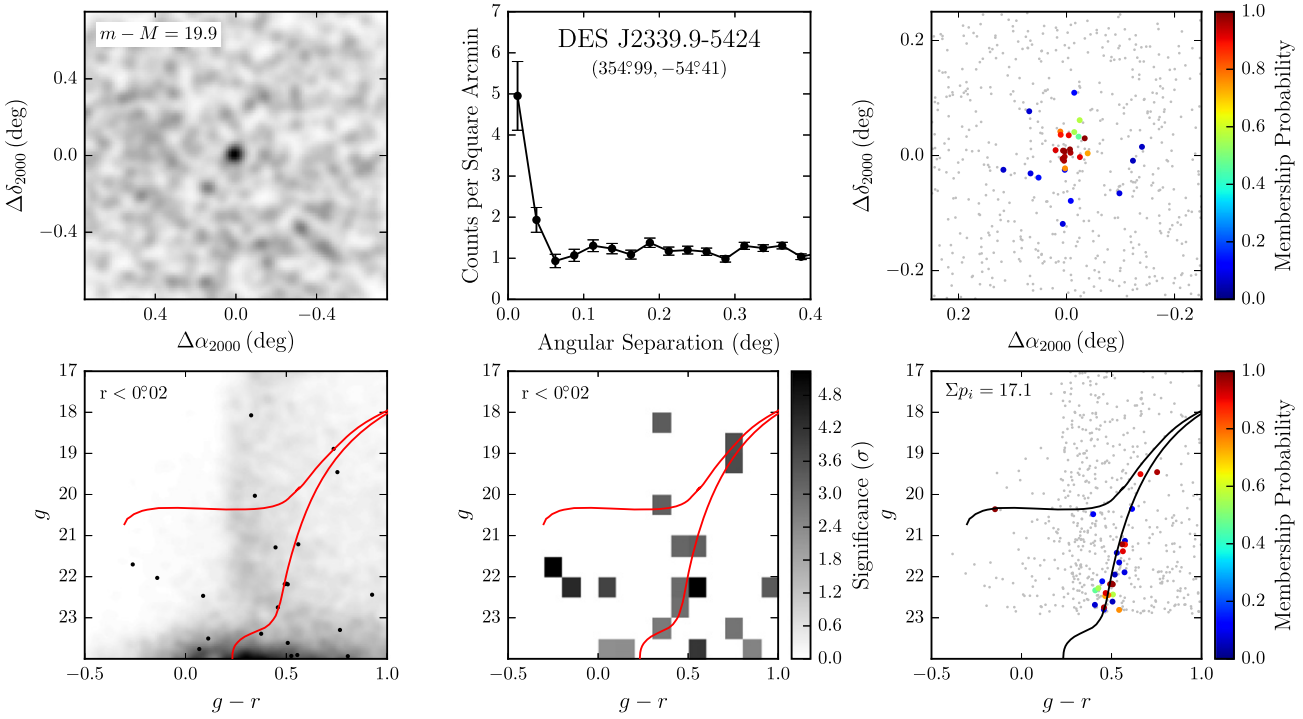

Figure 10. Analogous to Figure 4 but for DES J2339.9–5424.

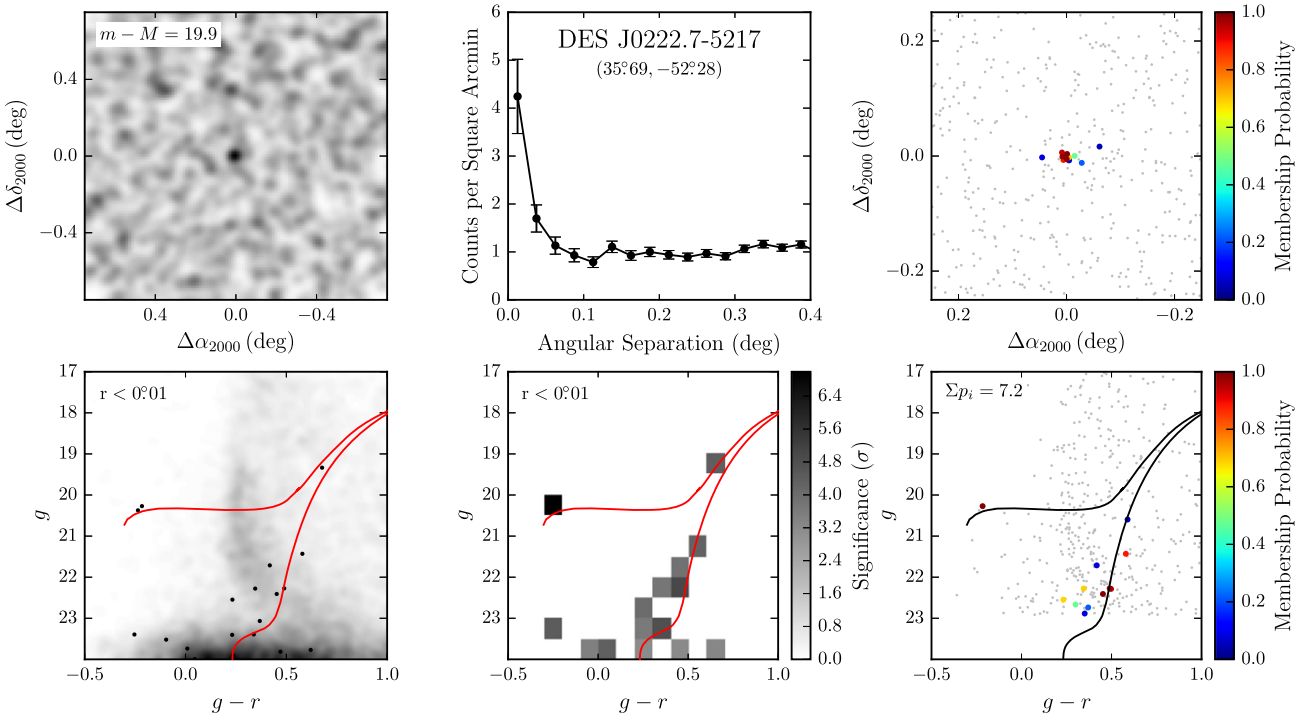

Figure 11. Analogous to Figure 4 but for DES J0222.7–5217.

covering a wide range of colors (Zucker et al. 2006b; Martin et al. 2008b; Okamoto et al. 2012). Its large distance places DES J0344.3–4331 in a very intriguing range of parameter space for studying the quenching and loss of gas in dwarf galaxies. As has been known for many years, dwarf galaxies within ∼250 kpc of the Milky Way and M31 are almost exclusively early-type galaxies with no gas or recent star formation, while dwarfs beyond that limit often have irregular morphologies, contain gas, and/or are still forming stars (e.g., Einasto et al. 1974; Blitz & Robishaw 2000; Grcevich & Putman 2009; Spekkens et al. 2014). The next most distant Milky Way dwarf galaxy, Leo T, is gas-rich and has hosted recent star formation (de Jong et al. 2008; Ryan-Weber et al.

2008); deeper optical and H I imaging to search for neutral gas and young stars in DES J0344.3−4331 has the potential to provide new insight into how gas is stripped from low-mass dwarfs and reveal the minimum mass for maintaining star formation over many Gyr. A radial velocity measurement will also shed light on if DES J0344.3−4331 has already passed close to the Milky Way or whether it is infalling for the first time. Given its distance, it is unlikely to be associated with the Magellanic Clouds. Like DES J0335.6−5403, DES J0344.3−4331 is clearly detected in Digitized Sky Survey images dating as far back as 1976.

3. *DES J2251.2-5836* (Tucana II, Figure 6): DES J2251.2−5836 is the third new satellite with a large enough size (120 pc) to be tentatively identified as a dwarf galaxy with DES multi-band photometry alone. It has a similar luminosity to DES J0335.6−5403, but is a much lower surface brightness system and is a factor of ∼2 farther away. DES J2251.2−5836 is ∼19 kpc from the LMC and ∼37 kpc from the SMC, making it a strong candidate for another member of the Magellanic group. In the surface density map in the upper left panel of Figure 6, the outer regions of DES J2251.2−5836 appear elongated and distorted. However, these features are likely a result of noise rather than real distortions (Martin et al. 2008a; Muñoz et al. 2010). The distribution of likely member stars in the upper right panel is much rounder. The high detection significance of this object demonstrates the power of the likelihood analysis to simultaneously combine spatial and color–magnitude information.
4. *DES J0255.4–5406* (Horologium I, Figure 7): DES J0255.4−5406, at a distance of ∼87 kpc, has only a sparse population of red giant branch and horizontal-branch stars visible in the DES photometry (a hint of the main sequence turnoff may be present at the detection limit). Given the small number of stars visible in the DES data, deeper imaging and spectroscopy will be needed to characterize the system more fully. Its Plummer radius of ∼60 pc establishes it as a likely dwarf galaxy, twice as extended as the largest globular clusters with comparable luminosities. DES J0255.4−5406 (perhaps along with DES J0443.8−5017 and DES J2339.9−5424; see below) is significantly farther from the Milky Way than any previously known dwarf galaxy with $M_V \lesssim -4$, suggesting that tidal stripping may not be needed to explain the low luminosities of the faintest dwarfs. On its own, the Galactocentric distance is not necessarily a good indicator of the past importance of Galactic tides in shaping the photometric and spectroscopic properties of satellites. The most important factor is the peri-Galacticon distance, which is not yet known for the new satellites. DES J0255.4−5406 is ∼40 kpc away from the Magellanic Clouds and a factor ∼2 closer to them than to the Milky Way, making it a potential Magellanic satellite. If it is (or was) associated with the Magellanic group, it is possible that tides from the LMC could have been relevant to its evolution. A measurement of the systemic velocity will help clarify whether DES J0255.4−5406 is currently near apocenter, infalling, or associated with the Magellanic system.
5. *DES J2108.8–5109* (Indus I, Figure 8): we identify DES J2108.8−5109 with Kim 2 (Kim et al. 2015). DES J2108.8−5109 is one of the faintest ($M_V \sim -2.2$ mag) and most compact ($r_h \sim 12$ pc) of the satellites discussed here. The object is visible in the coadded DES images. If it is a globular cluster, as argued by Kim et al. (2015), DES J2108.8−5109 is fainter and more extended than most of the other outer halo clusters, such as AM 1, Eridanus, Pal 3, Pal 4, and Pal 14. DES J2108.8−5109 is ∼37 kpc from the SMC, ∼55 kpc from the LMC, and ∼69 kpc from the much more massive Milky Way, so it is more likely a satellite of the Milky Way than of the Magellanic Clouds.
6. *DES J0443.8-5017* (Pictoris I, Figure 9): DES J0443.8−5017 has a large enough radius to be a likely dwarf galaxy, but the uncertainty on the radius measurement is large enough to make it also consistent with the globular cluster population. DES J0443.8−5017 has a prominent blue horizontal branch and hints of an elliptical shape, but fewer member stars are detected in the DES data. More accurate measurements of size and shape from deeper imaging, and kinematics and chemical abundances from spectroscopy, will be required to determine the nature of this object. The large distance of DES J0443.8−5017 places it far enough behind the Magellanic Clouds that it is less likely to be a Magellanic satellite than many of the other new discoveries.
7. *DES J2339.9–5424* (Phoenix II, Figure 10): DES J2339.9−5424 is quite similar to DES J0443.8−5017, but slightly smaller and closer. Again, we cannot draw firm conclusions on its nature without additional data, At ∼43 kpc from the SMC and ∼65 kpc from the LMC, it is unclear whether DES J2339.9−5424 could plausibly be a Magellanic satellite.
8. *DES J0222.7–5217* (Eridanus III, Figure 11): DES J0222.7−5217 is the most compact of the newly discovered objects in both angular and physical units. Along with DES J2108.8−5109, it is the most likely of the new discoveries to be a distant globular cluster rather than a dwarf galaxy. However, they could also be consistent with an extension of the dwarf galaxy locus to fainter magnitudes and smaller sizes. Even though it is one of the lowest luminosity system identified in the DES data so far, its compactness gives it a relatively high surface brightness, and like DES J2108.8−5109 and DES J0443.8−5017, it is clearly visible in coadded images. However, only a handful of likely member stars are resolved at the depth of the Y1A1 data, and significantly deeper imaging will be needed to better constrain its physical properties and stellar population.

5.2. Detection Completeness

Given that no additional ultra-faint Milky Way satellite galaxies have been confirmed outside of the SDSS DR7 footprint, despite the large areas of sky subsequently observed by SDSS and Pan-STARRS, it is interesting that multiple candidates have been found within the comparatively small area explored by DES thus far.[51] Without definite classifications, it is difficult to incorporate the DES candidates into

[51] The classification of PSO J174.0675−10.8774/Crater I as a globular cluster or dwarf galaxy is currently ambiguous (Belokurov et al. 2014; Laevens et al. 2014).

constraints on the luminosity function of Milky Way satellite galaxies. However, it is still possible to quantify the sensitivity of the first-year DES search using simple semi-analytic estimates of the completeness.

First, we calculated the probability that each new satellite could have been detected in the Y1A1 data. We began by generating a large number of realizations of each galaxy candidate distributed uniformly over the Y1A1 footprint. The candidates were modeled using radially symmetric Plummer profiles and the realizations included shot noise due to the limited number of stars expected to be in the observable magnitude range of DES. We then applied the simple map-based detection algorithm described in Section 3.1 to evaluate the detection efficiency. To be "detected," the satellite must possess at least 10 stars brighter than our imposed magnitude limit ($g < 23$) and a large enough surface brightness to pass the visual search selection criteria. Specifically, we considered extraction of varying sizes and computed the Poisson probability of detecting $n_{\rm satellite} + n_{\rm field}$ stars when expecting $n_{\rm field}$ stars based on the local field surface density. We tested extraction regions with sizes corresponding to the pixel areas in the map-based search algorithm ($r_{\rm ext} = \{0.^\circ029, 0.^\circ057\}$; Section 3.1) and the kernel size from the likelihood scan ($r_{\rm ext} = 0.^\circ1$; Section 3.2), as well as an extraction radius set to the angular half-light radius of the simulated satellite. When computing the local field density, we selected only stars along the isochrone at the distance of the satellite with $\tau = 12$ Gyr and $Z = 0.0002$ (see Section 3.1). Table 3 summarizes the expected detection efficiencies for the DES candidates when applying a 5σ statistical significance threshold, as in our seed selection procedure for the map-based search. The results show that all of the DES candidates would have been identified over a substantial fraction of the Y1A1 footprint with non-negligible probability, and for several candidates, near certainty.

Table 3 also shows that the detection efficiency is sensitive to the size of the extraction region. Extended systems such as DES J2251.2−5836 are unlikely to found using the smallest extraction regions considered here, whereas the reverse is true for compact systems such as DES J0222.7−5217 and DES J2108.8−5109. This size dependence accounts for the low significance of the two most compact candidates, DES J0222.7−5217 and DES J2108.8−5109, in the likelihood scan (Table 1). After allowing their spatial extensions to be fit, the detection significances of these candidates increase to a level well above the our imposed threshold.

For comparison, Table 3 also provides detection efficiency estimates for previously known ultra-faint galaxies (assuming they were located in the SPT region of Y1A1 instead of their actual locations). We find that all of the SDSS ultra-faint galaxies, with the exception of the highly extended Boötes III, could have been readily detected in Y1A1. We attribute these high detection efficiencies to the deeper imaging of DES relative to SDSS and note that DES J2251.2−5836, DES J0255.4−5406, DES J2108.8−5109, and DES J0222.7−5217 have a substantially reduced detection probability when the magnitude limit is raised to $r < 22$ mag, comparable to the stellar completeness limit of SDSS.

Our Y1A1 search sensitivity can be quantified in a more general way by considering an ensemble of satellites spanning a range of luminosities, physical sizes, and heliocentric distances. Figure 12 presents the discovery potential of our Y1A1 search expressed as the detection efficiency with respect to these galaxy properties, estimated by the same method described above with $r_{\rm ext} = r_{\rm h}$. Nearby, luminous, and compact objects have a high probability of being significantly detected whereas objects that are more distant, faint, and extended are less likely to be found. The detection threshold in the plane of physical size and luminosity is nearly parallel to contours of constant surface brightness, and is weakly dependent on the distance, provided that a sufficient number of stars are detected.

Since the Y1A1 search procedure described in Section 3 is a combination of the map-based and likelihood-based search techniques, the actual completeness of our search is likely slightly higher than estimated here. We expect the likelihood method to be more sensitive to extended low surface brightness systems because it combines spatial and color–magnitude information simultaneously. As the depth of DES imaging increases (2 to 4 tilings in Y1A1 compared to 10 tilings planned after 5 years) and more advanced techniques are applied to separate stars and galaxies at faint magnitudes (e.g., Fadely et al. 2012; Soumagnac et al. 2013), we anticipate that lower surface brightness satellites will become accessible. Our present study is optimized for the detection of relatively compact ($r_0 \lesssim 0.^\circ2$) and radially symmetric stellar overdensities. The search for extended low surface brightness features in the stellar distribution will be the focus of future work.

5.3. Total Number and Spatial Distribution of Milky Way Satellite Galaxies

The discovery of eight new dwarf galaxy candidates in $\sim$1600 deg^2 of Y1A1 not overlapping with SDSS Stripe 82 is consistent with expectations from the literature (Tollerud et al. 2008; Rossetto et al. 2011; Hargis et al. 2014; He et al. 2015). By empirically modeling the incompleteness of SDSS, Tollerud et al. 2008 predicted that 19–37 satellite galaxies could be found over the full DES footprint. More recent estimates based on high-resolution *N*-body simulations (Hargis et al. 2014) and semi-analytic galaxy formation models that include baryonic physics (He et al. 2015) predict $\sim$10 new detectable satellite galaxies in DES. Large uncertainties are associated with each of these estimates due to weak constraints on the luminosity function in the ultra-faint regime. Additionally, as noted in Section 5.1, some of the DES candidates may be globular clusters or may be associated with the Magellanic Clouds. In the latter case, it becomes more challenging to directly compare our results to the predictions above, which assume an isotropic distribution of Milky Way satellite galaxies.

A number of studies, beginning with Lynden-Bell (1976), note that many Milky Way satellite galaxies appear to be distributed on the sky along a great circle, indicating a planar three-dimensional structure rather than an ellipsoidal or spherical distribution. This great circle has a polar orientation relative to the disk of the Milky Way. The discovery of most of the SDSS ultra-faint dwarfs in the north Galactic cap region increased the apparent significance of this alignment. However, since the primary region surveyed by SDSS is located in the direction of this so-called vast polar structure (Pawlowski et al. 2012), the true anisotropy of the Milky Way satellite population is not yet clear. The next generation of deep wide-field surveys should be able to address this issue with wider sky coverage.

In this context, it is interesting to consider the locations of the eight new satellites reported here, which may increase the known Milky Way dwarf galaxy population by $\sim$30%. The

Table 3
Expected Detection Efficiencies for Milky Way Companions in DES Y1A1

Name	M_V	Distance (kpc)	r_h (deg)	Efficiency ($r_{ext} = 0.^\circ029$)	Efficiency ($r_{ext} = 0.^\circ057$)	Efficiency ($r_{ext} = 0.^\circ1$)	Efficiency ($r_{ext} = r_h$)
DES-J0335.6–5403 (Ret II)	−3.6	32	0.100	1.00	1.00	1.00	1.00
DES-J0344.3–4331 (Eri II)	−7.4	330	0.030	1.00	1.00	1.00	1.00
DES-J2251.2–5836 (Tuc II)	−3.9	58	0.120	0.25	0.98	1.00	1.00
DES-J0255.4–5406 (Hor I)	−3.5	87	0.040	0.62	0.78	0.55	0.78
DES-J2108.8–5109 (Ind I)	−2.2	69	0.010	0.96	0.69	0.18	0.97
DES-J0443.8–5017 (Pic I)	−3.7	126	0.020	0.92	0.74	0.30	0.89
DES-J2339.9–5424 (Phe II)	−3.7	95	0.020	1.00	0.96	0.74	0.99
DES-J0222.7–5217 (Eri III)	−2.4	95	0.007	0.24	0.06	0.00	0.28
Segue 1	−1.5	23	0.073	0.72	0.99	0.99	0.99
Ursa Major II	−4.2	32	0.267	0.06	0.97	1.00	1.00
Bootes II	−2.7	42	0.070	0.94	1.00	1.00	1.00
Segue 2	−2.5	35	0.057	1.00	1.00	1.00	1.00
Willman 1	−2.7	38	0.038	1.00	1.00	1.00	1.00
Coma Berenices	−4.1	44	0.100	1.00	1.00	1.00	1.00
Bootes III	−5.8	47	1.666	0.00	0.00	0.00	0.96
Bootes I	−6.3	66	0.210	1.00	1.00	1.00	1.00
Sextans	−9.3	86	0.463	1.00	1.00	1.00	1.00
Ursa Major I	−5.5	97	0.188	0.00	0.30	0.90	0.98
Hercules	−6.6	132	0.143	0.86	1.00	1.00	1.00
Leo IV	−5.8	154	0.077	1.00	1.00	1.00	1.00
Canes Venatici II	−4.9	160	0.027	1.00	1.00	1.00	1.00
Leo V	−5.2	178	0.043	1.00	1.00	1.00	1.00
Pisces II	−5.0	182	0.018	1.00	1.00	1.00	1.00
Canes Venatici I	−8.6	218	0.148	1.00	1.00	1.00	1.00

Note. Detection efficiencies are calculated from many realizations of satellites with the properties (luminosity M_V, distance, Plummer profile angular half-light radius r_h) of a given ultra-faint galaxy/candidate as they would have been observed in DES Y1A1. The simulated satellites are uniformly distributed throughout the SPT region of the Y1A1 footprint, excluding regions of high stellar density near to the LMC, i.e., $\sim$1600 deg^2. The rightmost columns list the detection efficiencies for extraction regions of different radii, r_{ext}. Here, a detection constitutes $>5\sigma$ stellar excess with $g < 23$ within the extraction region given the local density of the stellar field, after selecting stars that are consistent with the isochrone of an old and metal-poor stellar population at the satellite distance (i.e., following the map-based detection algorithm described in Section 3.1). The extraction region radii are choosen to reflect size scales used in the map-based search ($r_{ext} = \{0.^\circ029, 0.^\circ057\}$), likelihood scan ($r_{ext} = 0.^\circ1$; Section 3.2), and matched to the size of the satellite ($r_{ext} = r_h$). Data for previously known satellites are taken from references compiled by McConnachie (2012b).

thickness of the vast polar structure defined by Pawlowski et al. (2012) is 29 kpc, and we find that the DES satellites have a dispersion of $\sim$28 kpc from this plane. This result is perhaps not surprising given their proximity to the Magellanic Clouds, which played a large role in defining the original Lynden-Bell plane. In fact, the entire Y1A1 search area (with the exception of Stripe 82) is located quite close to the previously known plane of satellites. Thus, any satellite galaxies identified in this data set are necessarily close to the plane, and a selection of eight random positions within this area would likely have a similar dispersion relative to the polar structure. A more quantitative characterization of the distribution of Milky Way satellites awaits the completion of the DES survey, including areas farther away from the vast polar structure, as well as future results from Pan-STARRS.

6. CONCLUSIONS

We report on the discovery of eight new dwarf galaxy candidates associated with the Milky Way and/or Magellanic Clouds found in $\sim$1800 deg^2 of imaging data collected during the first year of DES. These satellites span a wide range of absolute magnitudes (−2.2 to −7.4 mag), physical sizes (10–170 pc), and heliocentric distances 30−330 kpc). The projected positions of the DES candidates are in close proximity to the Magellanic Clouds, and it is possible that some may be associated with the Magellanic system.

The nature of these systems cannot be conclusively determined with photometry alone. However, judging from their low surface brightnesses, ellipticities, and/or large distances, it is likely that several are new dwarf galaxies, in particular, DES J0335.6−5403, DES J0344.3−4331, and DES J2251.2−5836. If spectroscopically confirmed, the DES candidates may become the first ultra-faint galaxies identified outside the SDSS footprint, and would significantly increase the population of Local Group galaxies in the southern hemisphere. The proximity of DES J0335.6−5403, at $\sim$30 kpc, suggests that it may be an interesting target for indirect dark matter searches using gamma-ray telescopes (e.g., Ackermann et al. 2014). The implications of these candidate galaxies for indirect dark matter searches are discussed in a separate paper (Drlica-Wagner et al. 2015).

The second year of the DES survey was completed on 2015 February 15. In addition to filling in regions of non-uniform coverage in the western portion of the Y1A1 footprint, the second season expands the DES survey to encompass over 4000 deg^2. The sensitivity to ultra-faint satellite galaxies achieved with first-year DES data already exceeds that of SDSS (Section 5.2), and over the next five years, DES is expected to make an important contribution to our understanding of the Milky Way environment.

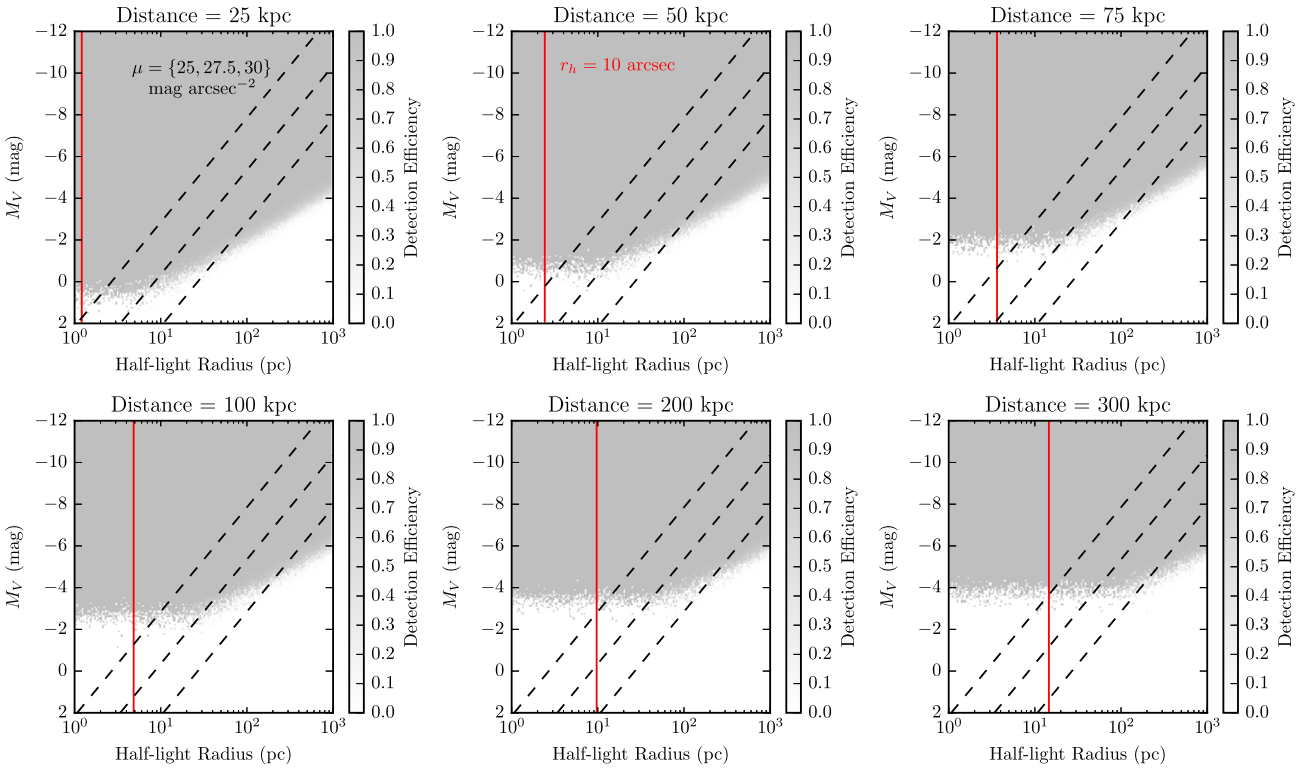

Figure 12. Sensitivity of the our Y1A1 search expressed as the detection efficiency as a function of satellite luminosity, physical size, and heliocentric distance. Each panel corresponds to a different heliocentric distance. Contours of constant surface density are indicated with dashed black lines: $\mu = \{25, 27.5, 30\}$ mag arcsec^{-2}.

During the preparation of this manuscript, we were sent an independent study by Koposov et al. using publicly released images from the first year of DES. Koposov et al. (2015) identify nine candidate satellites of the Milky Way and/or Magellanic Clouds, including eight that overlap with candidates presented here. The candidate that Koposov et al. refer to as Grus I is located outside the Y1A1 footprint in a region that was observed during the first year of DES with good image quality, but which did not have sufficient coverage in all bands to enter the coaddition stage of the standard DESDM pipeline. Therefore, the stars that comprise Grus I are not in the coadd object catalog that was used for this analysis.

We note that we have not used the coordinates shared by Koposov et al. as seeds in our analysis, nor have we tuned our search algorithms based on knowledge of the candidates reported in their work. The search methods presented here yield significance maps of the entire Y1A1 footprint, and the reported detections are the most significant points in the maps unassociated with known objects. While our final choice of 5σ for the significance threshold for reportable galaxy candidates was made after our knowledge of the results from Koposov et al., the threshold was chosen to provide as much timely information to the astronomical community as possible with minimal likelihood of false positives, rather than for agreement with the Koposov et al. detections. We conclude that the independent discovery of these Milky Way companions by two separate teams using distinct object catalogs and search algorithms strengthens the case for follow-up by the astronomical community.

We thank Sergey Koposov and collaborators for sending a copy of their submitted paper with their nine discoveries, and Helmut Jerjen for pointing out the association between Kim 2 and DES J2108.8−5109. Marla Geha provided useful comments on the presentation of these results. K.B. and A.D.W. thank Beth Willman for advice regarding the search for ultra-faint galaxies. A.D.W. thanks Ellen Bechtol for her generous hospitality during the preparation of this manuscript. We acknowledge helpful suggestions from the anonymous referee. This work made use of computational resources at the SLAC National Accelerator Laboratory and University of Chicago Research Computing Center. This material is based upon work supported by the National Science Foundation under Grant Number (1138766). A.C.R. acknowledges financial support provided by the PAPDRJ CAPES/FAPERJ Fellowship. A.A.P. was supported by DOE grant DE-AC02-98CH10886 and by JPL, run by Caltech under a contract for NASA. Funding for the DES Projects has been provided by the U.S. Department of Energy, the U.S. National Science Foundation, the Ministry of Science and Education of Spain, the Science and Technology Facilities Council of the United Kingdom, the Higher Education Funding Council for England, the National Center for Supercomputing Applications at the University of Illinois at Urbana-Champaign, the Kavli Institute of Cosmological Physics at the University of Chicago, the Center for Cosmology and Astro-Particle Physics at the Ohio State University, the Mitchell Institute for Fundamental Physics and Astronomy at Texas A&M University, Financiadora de Estudos e Projetos, Fundação Carlos Chagas Filho de Amparo à Pesquisa do Estado do Rio de Janeiro, Conselho Nacional de Desenvolvimento Científico e Tecnológico and the Ministério da Ciência, Tecnologia e Inovação, the Deutsche Forschungsgemeinschaft and the Collaborating Institutions in the Dark Energy Survey. The DES data management system is supported by the National Science Foundation under Grant Number AST-1138766. The

DES participants from Spanish institutions are partially supported by MINECO under grants AYA2012-39559, ESP2013-48274, FPA2013-47986, and Centro de Excelencia Severo Ochoa SEV-2012-0234, some of which include ERDF funds from the European Union. The Collaborating Institutions are Argonne National Laboratory, the University of California at Santa Cruz, the University of Cambridge, Centro de Investigaciones Enérgeticas, Medioambientales y Tecnológicas-Madrid, the University of Chicago, University College London, the DES-Brazil Consortium, the University of Edinburgh, the Eidgenössische Technische Hochschule (ETH) Zürich, Fermi National Accelerator Laboratory, the University of Illinois at Urbana-Champaign, the Institut de Ciències de l'Espai (IEEC/CSIC), the Institut de Física d'Altes Energies, Lawrence Berkeley National Laboratory, the Ludwig-Maximilians Universität München and the associated Excellence Cluster universe, the University of Michigan, the National Optical Astronomy Observatory, the University of Nottingham, The Ohio State University, the University of Pennsylvania, the University of Portsmouth, SLAC National Accelerator Laboratory, Stanford University, the University of Sussex, and Texas A&M University.

REFERENCES

Abbott, T., Aldering, G., Annis, J., et al. 2005, arXiv:astro-ph/0510346
Ackermann, M., Albert, A., Anderson, B., et al. 2014, PhRvD, 89, 042001
Adén, D., Feltzing, S., Koch, A., et al. 2009, A&A, 506, 1147
Ahn, C. P., Alexandroff, R., Allende Prieto, C., et al. 2014, ApJS, 211, 17
Balbinot, E., Santiago, B. X., da Costa, L., et al. 2013, ApJ, 767, 101
Balbinot, E., Santiago, B. X., Girardi, L., et al. 2015, MNRAS, 449, 1129
Belokurov, V., Irwin, M. J., Koposov, S. E., et al. 2014, MNRAS, 441, 2124
Belokurov, V., Zucker, D. B., Evans, N. W., et al. 2006, ApJL, 647, L111
Belokurov, V., Zucker, D. B., Evans, N. W., et al. 2007, ApJ, 654, 897
Belokurov, V., Walker, M. G., Evans, N. W., et al. 2008, ApJL, 686, L83
Belokurov, V., Walker, M. G., Evans, N. W., et al. 2009, MNRAS, 397, 1748
Belokurov, V., Walker, M. G., Evans, N. W., et al. 2010, ApJL, 712, L103
Bertin, E. 2011, in ASP Conf. Ser. 442, Astronomical Data Analysis Software and Systems XX, ed. I. N. Evans et al. (San Francisco, CA: ASP), 435
Bertin, E., & Arnouts, S. 1996, A&AS, 117, 393
Blitz, L., & Robishaw, T. 2000, ApJ, 541, 675
Box, G., & Tiao, G. 1973, Bayesian Inference in Statistical Analysis (Reading, MA: Addison-Wesley)
Bressan, A., Marigo, P., Girardi, L., et al. 2012, MNRAS, 427, 127
Brown, T. M., Tumlinson, J., Geha, M., et al. 2014, ApJ, 796, 91
Carlin, J. L., Grillmair, C. J., Muñoz, R. R., Nidever, D. L., & Majewski, S. R. 2009, ApJL, 702, L9
Carlstrom, J., Ade, P., Aird, K., et al. 2011, PASP, 123, 568
Chabrier, G. 2001, ApJ, 554, 1274
Chernoff, H. 1954, AnMat, 25, 573
Corwin, H. G. 2004, yCat, 7239, 0
de Jong, J. T. A., Harris, J., Coleman, M. G., et al. 2008, ApJ, 680, 1112
Desai, S., Armstrong, R., Mohr, J. J., et al. 2012, ApJ, 757, 83
Diehl, H. T., Abbott, T. M. C., Annis, J., et al. 2014, Proc. SPIE, 9149, 0
Diehl, T. 2012, PhPro, 37, 1332
Dolphin, A. E. 2002, MNRAS, 332, 91
Drlica-Wagner, A., Albert, A., Bechtol, K., et al. 2015, ApJL, submitted (arXiv:1503.02632)
Edwards, A. 1972, Likelihood: An Account of the Statistical Concept of Likelihood and Its Application to Scientific Inference (Cambridge: Cambridge Univ. Press)
Einasto, J., Saar, E., Kaasik, A., & Chernin, A. D. 1974, Natur, 252, 111
Fadely, R., Hogg, D. W., & Willman, B. 2012, ApJ, 760, 15
Fadely, R., Willman, B., Geha, M., et al. 2011, AJ, 142, 88
Fisher, R. A. 1925, PCPS, 22, 700
Flaugher, B., Diehl, H. T., Honscheid, K., et al. 2015, AJ, submitted (arXiv:1504.02900)
Flaugher, B. L., Abbott, T. M. C., Annis, J., et al. 2010, Proc. SPIE, 7735, 0
Foreman-Mackey, D., Hogg, D. W., Lang, D., & Goodman, J. 2013, PASP, 125, 306
Geha, M., Willman, B., Simon, J. D., et al. 2009, ApJ, 692, 1464
Górski, K. M., Hivon, E., Banday, A. J., et al. 2005, ApJ, 622, 759
Grcevich, J., & Putman, M. E. 2009, ApJ, 696, 385
Grillmair, C. J. 2006, ApJL, 645, L37
Grillmair, C. J. 2009, ApJ, 693, 1118
Hargis, J. R., Willman, B., & Peter, A. H. G. 2014, ApJL, 795, L13
Harris, W. E. 1996, AJ, 112, 1487
He, C., Bechtol, K., Hearin, A. P., & Hooper, D. 2015, PhRvD, 91, 063515
Irwin, M. J., Belokurov, V., Evans, N. W., et al. 2007, ApJL, 656, L13
Jester, S., Schneider, D. P., Richards, G. T., et al. 2005, AJ, 130, 873
Kelly, P. L., von der Linden, A., Applegate, D. E., et al. 2014, MNRAS, 439, 28
Kharchenko, N. V., Piskunov, A. E., Schilbach, E., Röser, S., & Scholz, R.-D. 2013, A&A, 558, A53
Kim, D., & Jerjen, H. 2015, ApJ, 799, 73
Kim, D., Jerjen, H., Milone, A. P., Mackey, D., & da Costa, G. S. 2015, ApJ, 803, 63
Kirby, E. N., Boylan-Kolchin, M., Cohen, J. G., et al. 2013, ApJ, 770, 16
Kleyna, J. T., Wilkinson, M. I., Evans, N. W., & Gilmore, G. 2005, ApJL, 630, L141
Klypin, A., Kravtsov, A. V., Valenzuela, O., & Prada, F. 1999, ApJ, 522, 82
Koch, A., Wilkinson, M. I., Kleyna, J. T., et al. 2009, ApJ, 690, 453
Koposov, S., Belokurov, V., Evans, N. W., et al. 2008, ApJ, 686, 279
Koposov, S., de Jong, J. T. A., Belokurov, V., et al. 2007, ApJ, 669, 337
Koposov, S. E., Belokurov, V., Torrealba, G., & Evans, N. W. 2015, ApJ, 805, 130
Koposov, S. E., Gilmore, G., Walker, M. G., et al. 2011, ApJ, 736, 146
Laevens, B. P. M., Martin, N. F., Sesar, B., et al. 2014, ApJL, 786, L3
Lynden-Bell, D. 1976, MNRAS, 174, 695
Martin, N. F., de Jong, J. T. A., & Rix, H.-W. 2008a, ApJ, 684, 1075
Martin, N. F., Ibata, R. A., Chapman, S. C., Irwin, M., & Lewis, G. F. 2007, MNRAS, 380, 281
Martin, N. F., Coleman, M. G., de Jong, J. T. A., et al. 2008b, ApJL, 672, L13
McConnachie, A. W. 2012a, AJ, 144, 4
McConnachie, A. W. 2012b, AJ, 144, 4
Mohr, J. J., Armstrong, R., Bertin, E., et al. 2012, Proc. SPIE, 8451, 84510D
Moore, B., Ghigna, S., Governato, F., et al. 1999, ApJL, 524, L19
Muñoz, R. R., Carlin, J. L., Frinchaboy, P. M., et al. 2006, ApJL, 650, L51
Muñoz, R. R., Geha, M., Côté, P., et al. 2012a, ApJL, 753, L15
Muñoz, R. R., Geha, M., & Willman, B. 2010, AJ, 140, 138
Muñoz, R. R., Padmanabhan, N., & Geha, M. 2012b, ApJ, 745, 127
Nilson, P. 1973, Uppsala General Catalogue of Galaxies
Okamoto, S., Arimoto, N., Yamada, Y., & Onodera, M. 2012, ApJ, 744, 96
Ortolani, S., Bica, E., & Barbuy, B. 2013, MNRAS, 433, 1966
Paust, N., Wilson, D., & van Belle, G. 2014, AJ, 148, 19
Pawlowski, M. S., Pflamm-Altenburg, J., & Kroupa, P. 2012, MNRAS, 423, 1109
Plummer, H. C. 1911, MNRAS, 71, 460
Rossetto, B. M., Santiago, B. X., Girardi, L., et al. 2011, AJ, 141, 185
Ryan-Weber, E. V., Begum, A., Oosterloo, T., et al. 2008, MNRAS, 384, 535
Rykoff, E. S., Rozo, E., Busha, M. T., et al. 2014, ApJ, 785, 104
Sakamoto, T., & Hasegawa, T. 2006, ApJL, 653, L29
Schlafly, E. F., Finkbeiner, D. P., Jurić, M., et al. 2012, ApJ, 756, 158
Schlegel, D. J., Finkbeiner, D. P., & Davis, M. 1998, ApJ, 500, 525
Sevilla, I., Armstrong, R., Bertin, E., et al. 2011, arXiv:1109.6741
Simon, J. D., & Geha, M. 2007, ApJ, 670, 313
Simon, J. D., Geha, M., Minor, Q. E., et al. 2011, ApJ, 733, 46
Soumagnac, M. T., Abdalla, F. B., Lahav, O., et al. 2013, arXiv:1306.5236
Spekkens, K., Urbancic, N., Mason, B. S., Willman, B., & Aguirre, J. E. 2014, ApJL, 795, L5
Swanson, M. E. C., Tegmark, M., Hamilton, A. J. S., & Hill, J. C. 2008, MNRAS, 387, 1391
Tollerud, E. J., Bullock, J. S., Strigari, L. E., & Willman, B. 2008, ApJ, 688, 277
van den Bergh, S. 2008, AJ, 135, 1731
Walker, M. G., Belokurov, V., Evans, N. W., et al. 2009, ApJL, 694, L144
Walsh, S. M., Jerjen, H., & Willman, B. 2007, ApJL, 662, L83
Walsh, S. M., Willman, B., & Jerjen, H. 2009, AJ, 137, 450
Whiting, A. B., Hau, G. K. T., Irwin, M., & Verdugo, M. 2007, AJ, 133, 715
Willman, B., Geha, M., Strader, J., et al. 2011, AJ, 142, 128
Willman, B., & Strader, J. 2012, AJ, 144, 76
Willman, B., Blanton, M. R., West, A. A., et al. 2005a, AJ, 129, 2692
Willman, B., Dalcanton, J. J., Martinez-Delgado, D., et al. 2005b, ApJL, 626, L85
Wolf, J., Martinez, G. D., Bullock, J. S., et al. 2010, MNRAS, 406, 1220
Zucker, D. B., Belokurov, V., Evans, N. W., et al. 2006a, ApJL, 650, L41
Zucker, D. B., Belokurov, V., Evans, N. W., et al. 2006b, ApJL, 643, L103

Referências

Abell, G. O. (1958). "The Distribution of Rich Clusters of Galaxies." Em: *ApJS* 3, p. 211.

Alam, S. et al. (2015). "The Eleventh and Twelfth Data Releases of the Sloan Digital Sky Survey: Final Data from SDSS-III". Em: *ApJS* 219, 12, p. 12. arXiv: 1501.00963 [astro-ph.IM].

Balbinot, E. et al. (2011). "The tidal tails of NGC 2298". Em: *MNRAS* 416, pp. 393–402. arXiv: 1105.1933 [astro-ph.GA].

Balbinot, E. et al. (2013). "A New Milky Way Halo Star Cluster in the Southern Galactic Sky". Em: *ApJ* 767, 101, p. 101. arXiv: 1212.5952.

Balbinot, E. et al. (2015). "The LMC geometry and outer stellar populations from early DES data". Em: *MNRAS* 449, pp. 1129–1145. arXiv: 1502.05050.

Balbinot, E. et al. (2016). "The Phoenix Stream: A Cold Stream in the Southern Hemisphere". Em: *ApJ* 820, 58, p. 58. arXiv: 1509.04283.

Battaglia, G. et al. (2011). "VizieR Online Data Catalog: CaII triplet in Sextans dSph galaxy (Battaglia+, 2011)". Em: *VizieR Online Data Catalog* 741.

Bechtol, K. et al. (2015). "Eight New Milky Way Companions Discovered in First-year Dark Energy Survey Data". Em: *ApJ* 807, 50, p. 50. arXiv: 1503.02584.

Bellazzini, M., F. R. Ferraro, & R. Ibata (2003). "Building Up the Globular Cluster System of the Milky Way: The Contribution of the Sagittarius Galaxy". Em: *AJ* 125, pp. 188–196. eprint: astro-ph/0210596.

Belokurov, V. et al. (2006). "The Field of Streams: Sagittarius and Its Siblings". Em: *ApJL* 642, pp. L137–L140. eprint: astro-ph/0605025.

Belokurov, V. et al. (2010). "Big Fish, Little Fish: Two New Ultra-faint Satellites of the Milky Way". Em: *ApJL* 712, pp. L103–L106. arXiv: 1002.0504.

Belokurov, V. et al. (2014). "Precession of the Sagittarius stream". Em: *MNRAS* 437, pp. 116–131. arXiv: 1301.7069 [astro-ph.GA].

Bertin, E. (2011). "Automated Morphometry with SExtractor and PSFEx". Em: *Astronomical Data Analysis Software and Systems XX*. Ed. by I. N. Evans et al. Vol. 442. Astronomical Society of the Pacific Conference Series, p. 435.

Bertin, E. & S. Arnouts (1996). "SExtractor: Software for source extraction." Em: *A&AS* 117, pp. 393–404.

Bertone, G., D. Hooper, & J. Silk (2005). "Particle dark matter: evidence, candidates and constraints". Em: *PhR* 405, pp. 279–390. eprint: hep-ph/0404175.

Binney, J. & S. Tremaine (2008). *Galactic Dynamics*. 2nd. Princeton Series in Astrophysics. Princeton University Press.

Bouy, H. et al. (2013). "Dynamical analysis of nearby clusters. Automated astrometry from the ground: precision proper motions over a wide field". Em: *A&A* 554, A101, A101. arXiv: 1306.4446 [astro-ph.IM].

Bragaglia, A. et al. (2006). "BVI photometry of the very old open cluster Berkeley 17*". Em: *MNRAS* 368, pp. 1971–1981. eprint: astro-ph/0603050.

Bressan, A. et al. (2012). "PARSEC: stellar tracks and isochrones with the PAdova and TRieste Stellar Evolution Code". Em: *MNRAS* 427, pp. 127–145. arXiv: 1208.4498 [astro-ph.SR].

Brodie, J. P. & J. Strader (2006). "Extragalactic Globular Clusters and Galaxy Formation". Em: *ARA&A* 44, pp. 193–267. eprint: astro-ph/0602601.

Carballo-Bello, J. A. et al. (2014). "A search for stellar tidal debris of defunct dwarf galaxies around globular clusters in the inner Galactic halo". Em: *MNRAS* 445, pp. 2971–2993. arXiv: 1409.7390.

Carraro, G. & T. Bensby (2009). "Old open clusters in the Sagittarius dwarf spheroidal galaxy tidal stream - kith or kin?" Em: *MNRAS* 397, pp. L106–L109. arXiv: 0905.4762.

Carraro, G. et al. (2004). "Metal Abundances in Extremely Distant Galactic Old Open Clusters. I. Berkeley 29 and Saurer 1". Em: *AJ* 128, pp. 1676–1683. eprint: astro-ph/0406679.

Correnti, M. et al. (2010). "The Northern Wraps of the Saittarius Stream as Traced by Red Clump Stars: Distances, Intrinsic Widths, and Stellar Densities". Em: *ApJ* 721, pp. 329–356. arXiv: 1007.3510.

Da Costa, G. S. & T. E. Armandroff (1995). "Abundances and Kinematics of the Globular Cluster Systems of the Galaxy and of the Sagittarius Dwarf". Em: *AJ* 109, p. 2533.

Davis, M. et al. (1985). "The evolution of large-scale structure in a universe dominated by cold dark matter". Em: *ApJ* 292, pp. 371–394.

De Boer, T. J. L., V. Belokurov, & S. Koposov (2015). "The star formation history of the Sagittarius stream". Em: *MNRAS* 451, pp. 3489–3503. arXiv: 1505.00787.

D'Ercole, A. et al. (2008). "Formation and dynamical evolution of multiple stellar generations in globular clusters". Em: *MNRAS* 391, pp. 825–843. arXiv: 0809.1438.

Desai, S. et al. (2012). "The Blanco Cosmology Survey: Data Acquisition, Processing, Calibration, Quality Diagnostics, and Data Release". Em: *ApJ* 757, 83, p. 83. arXiv: 1204.1210 [astro-ph.CO].

Dooley, G. A. et al. (2017). "The predicted luminous satellite populations around SMC and LMC-mass galaxies - A missing satellite problem around the LMC?" Em: *ArXiv e-prints*. arXiv: 1703.05321.

Dotter, A., A. Sarajedini, & J. Anderson (2011). "Globular Clusters in the Outer Galactic Halo: New Hubble Space Telescope/Advanced Camera for Surveys Imaging of Six Globular Clusters and the Galactic Globular Cluster Age-metallicity Relation". Em: *ApJ* 738, 74, p. 74. arXiv: 1106.4307.

Dotter, A. et al. (2010). "The ACS Survey of Galactic Globular Clusters. IX. Horizontal Branch Morphology and the Second Parameter Phenomenon". Em: *ApJ* 708, pp. 698–716. arXiv: 0911.2469 [astro-ph.SR].

Downing, J. M. B. & A. Sills (2007). "The Dynamical Implications of Multiple Stellar Formation Events in Galactic Globular Clusters". Em: *ApJ* 662, pp. 341–349. eprint: astro-ph/0702716.

Drlica-Wagner, A. et al. (2015). "Eight Ultra-faint Galaxy Candidates Discovered in Year Two of the Dark Energy Survey". Em: *ApJ* 813, 109, p. 109. arXiv: 1508.03622.

Drlica-Wagner, A. et al. (2016). "An Ultra-faint Galaxy Candidate Discovered in Early Data from the Magellanic Satellites Survey". Em: *ApJL* 833, L5, p. L5. arXiv: 1609.02148.

Elson, R., P. Hut, & S. Inagaki (1987). "Dynamical evolution of globular clusters". Em: *ARA&A* 25, pp. 565–601.

Fadely, R. et al. (2011). "Segue 3: An Old, Extremely Low Luminosity Star Cluster in the Milky Way's Halo". Em: *AJ* 142, 88, p. 88. arXiv: 1107.3151.

Fall, S. M. & C. S. Frenk (1985). "Rotation and flattening of globular clusters". Em: *Dynamics of Star Clusters*. Ed. by J. Goodman & P. Hut. Vol. 113. IAU Symposium, pp. 285–296.

Feng, J. L. (2010). "Dark Matter Candidates from Particle Physics and Methods of Detection". Em: *ARA&A* 48, pp. 495–545. arXiv: 1003.0904 [astro-ph.CO].

Flaugher, B. et al. (2015). "The Dark Energy Camera". Em: *AJ* 150, 150, p. 150. arXiv: 1504.02900 [astro-ph.IM].

Forbes, D. A. & T. Bridges (2010). "Accreted versus in situ Milky Way globular clusters". Em: *MNRAS* 404, pp. 1203–1214. arXiv: 1001.4289.

Friel, E. D. & K. A. Janes (1993). "Metallicities and radial velocities of old open clusters". Em: *A&A* 267, pp. 75–91.

González-Samaniego, A. et al. (2014). "Simulations of Isolated Dwarf Galaxies Formed in Dark Matter Halos with Different Mass Assembly Histories". Em: *ApJ* 785, 58, p. 58. arXiv: 1308.4753.

Gunn, J. E. et al. (1998). "The Sloan Digital Sky Survey Photometric Camera". Em: *AJ* 116, pp. 3040–3081. eprint: astro-ph/9809085.

Hargis, J. R., B. Willman, & A. H. G. Peter (2014). "Too Many, Too Few, or Just Right? The Predicted Number and Distribution of Milky Way Dwarf Galaxies". Em: *ApJL* 795, L13, p. L13. arXiv: 1407.4470.

Harris, W. E. (1996). "A Catalog of Parameters for Globular Clusters in the Milky Way". Em: *AJ* 112, p. 1487.

— (2010). "A New Catalog of Globular Clusters in the Milky Way". Em: *ArXiv e-prints*. arXiv: 1012.3224 [astro-ph.GA].

Helmi, A. (2008). "The stellar halo of the Galaxy". Em: *A&AR* 15, pp. 145–188. arXiv: 0804.0019.

Homma, D. et al. (2016). "A New Milky Way Satellite Discovered in the Subaru/Hyper Suprime-Cam Survey". Em: *ApJ* 832, 21, p. 21. arXiv: 1609.04346.

Homma, D. et al. (2017). "Searches for New Milky Way Satellites from the First Two Years of Data of the Subaru/Hyper Suprime-Cam Survey: Discovery of Cetus˜III". Em: *ArXiv e-prints*. arXiv: 1704.05977.

Hyde, E. A. et al. (2015). "Selecting Sagittarius: Identification and Chemical Characterization of the Sagittarius Stream". Em: *ApJ* 805, 189, p. 189. arXiv: 1505.07926.

Ibata, R. A., G. Gilmore, & M. J. Irwin (1994). "A dwarf satellite galaxy in Sagittarius". Em: *Nat* 370, pp. 194–196.

Jester, S. et al. (2005). "The Sloan Digital Sky Survey View of the Palomar-Green Bright Quasar Survey". Em: *AJ* 130, pp. 873–895. eprint: astro-ph/0506022.

Jethwa, P., D. Erkal, & V. Belokurov (2016). "A Magellanic origin of the DES dwarfs". Em: *MNRAS* 461, pp. 2212–2233. arXiv: 1603.04420.

Johnston, K. V., D. N. Spergel, & L. Hernquist (1995). "The Disruption of the Sagittarius Dwarf Galaxy". Em: *ApJ* 451, p. 598. eprint: astro-ph/9502005.

Jurić, M. et al. (2008). "The Milky Way Tomography with SDSS. I. Stellar Number Density Distribution". Em: *ApJ* 673, pp. 864–914. eprint: astro-ph/0510520.

Kaluzny, J. & A. Udalski (1992). "Photometric study of the old open cluster NGC 6791". Em: *Acta Astron.* 42, pp. 29–47.

Kim, D. & H. Jerjen (2015a). "A Hero's Little Horse: Discovery of a Dissolving Star Cluster in Pegasus". Em: *ApJ* 799, 73, p. 73. arXiv: 1411.3063.

— (2015b). "Horologium II: A Second Ultra-faint Milky Way Satellite in the Horologium Constellation". Em: *ApJL* 808, L39, p. L39. arXiv: 1505.04948.

Kim, D. et al. (2015). "Discovery of a Faint Outer Halo Milky Way Star Cluster in the Southern Sky". Em: *ApJ* 803, 63, p. 63. arXiv: 1502.03952.

Kim, D. et al. (2016a). "KIM 3: An Ultra-faint Star Cluster in the Constellation of Centaurus". Em: *ApJ* 820, 119, p. 119. arXiv: 1512.03530.

Kim, D. et al. (2016b). "Portrait of a Dark Horse: a Photometric and Spectroscopic Study of the Ultra-faint Milky Way Satellite Pegasus III". Em: *ApJ* 833, 16, p. 16. arXiv: 1608.04934.

King, I. (1962). "The structure of star clusters. I. an empirical density law". Em: *AJ* 67, p. 471.

Kleyna, J. T. et al. (1998). "A V and I CCD Mosaic Survey of the Ursa Minor Dwarf Spheroidal Galaxy". Em: *AJ* 115, pp. 2359–2368.

Klypin, A. et al. (1999). "Galaxies in N-Body Simulations: Overcoming the Overmerging Problem". Em: *ApJ* 516, pp. 530–551. eprint: astro-ph/9708191.

Koposov, S. et al. (2007). "The Discovery of Two Extremely Low Luminosity Milky Way Globular Clusters". Em: *ApJ* 669, pp. 337–342. arXiv: 0706.0019.

Koposov, S. E., V. Belokurov, & G. Torrealba (2017). "Gaia 1 and 2. A pair of new Galactic star clusters". Em: *MNRAS* 470, pp. 2702–2709. arXiv: 1702.01122.

Koposov, S. E. et al. (2012). "The Sagittarius Streams in the Southern Galactic Hemisphere". Em: *ApJ* 750, 80, p. 80. arXiv: 1111.7042.

Koposov, S. E. et al. (2015a). "Beasts of the Southern Wild : Discovery of nine Ultra Faint satellites in the vicinity of the Magellanic Clouds." Em: *ApJ* 805, 130, p. 130. arXiv: 1503.02079.

Koposov, S. E. et al. (2015b). "Kinematics and Chemistry of Recently Discovered Reticulum 2 and Horologium 1 Dwarf Galaxies". Em: *ApJ* 811, 62, p. 62. arXiv: 1504.07916.

Kroupa, P. (2001). "On the variation of the initial mass function". Em: *MNRAS* 322, pp. 231–246. eprint: astro-ph/0009005.

Laevens, B. P. M. et al. (2014). "A New Distant Milky Way Globular Cluster in the Pan-STARRS1 3π Survey". Em: *ApJL* 786, L3, p. L3. arXiv: 1403.6593.

Laevens, B. P. M. et al. (2015a). "A New Faint Milky Way Satellite Discovered in the Pan-STARRS1 3π Survey". Em: *ApJL* 802, L18, p. L18. arXiv: 1503.05554.

Laevens, B. P. M. et al. (2015b). "Sagittarius II, Draco II and Laevens 3: Three New Milky Way Satellites Discovered in the Pan-STARRS 1 3π Survey". Em: *ApJ* 813, 44, p. 44. arXiv: 1507.07564.

Law, D. R. & S. R. Majewski (2010a). "Assessing the Milky Way Satellites Associated with the Sagittarius Dwarf Spheroidal Galaxy". Em: *ApJ* 718, pp. 1128–1150. arXiv: 1005.5390.

— (2010b). "Assessing the Milky Way Satellites Associated with the Sagittarius Dwarf Spheroidal Galaxy". Em: *ApJ* 718, pp. 1128–1150. arXiv: 1005.5390.

— (2010c). "The Sagittarius Dwarf Galaxy: A Model for Evolution in a Triaxial Milky Way Halo". Em: *ApJ* 714, pp. 229–254. arXiv: 1003.1132.

Li, T. S. et al. (2016). "Discovery of a Stellar Overdensity in Eridanus–Phoenix in the Dark Energy Survey". Em: *ApJ* 817, 135, p. 135. arXiv: 1509.04296.

Li, T. S. et al. (2017). "Farthest Neighbor: The Distant Milky Way Satellite Eridanus II". Em: *ApJ* 838, 8, p. 8. arXiv: 1611.05052.

Luque, E. et al. (2016). "Digging deeper into the Southern skies: a compact Milky Way companion discovered in first-year Dark Energy Survey data". Em: *MNRAS* 458, pp. 603–612. arXiv: 1508.02381.

Luque, E. et al. (2017a). "Deep SOAR follow-up photometry of two Milky Way outer-halo companions discovered with Dark Energy Survey". Em: *ArXiv e-prints*. arXiv: 1709.05689.

Luque, E. et al. (2017b). "The Dark Energy Survey view of the Sagittarius stream: discovery of two faint stellar system candidates". Em: *MNRAS* 468, pp. 97–108. arXiv: 1608.04033.

Lynden-Bell, D. & R. M. Lynden-Bell (1995). "Ghostly streams from the formation of the Galaxy's halo". Em: *MNRAS* 275, pp. 429–442.

Mackey, A. D. & G. F. Gilmore (2004). "Comparing the properties of local globular cluster systems: implications for the formation of the Galactic halo". Em: *MNRAS* 355, pp. 504–534. eprint: astro-ph/0408404.

Majewski, S. R. et al. (2003). "A Two Micron All Sky Survey View of the Sagittarius Dwarf Galaxy. I. Morphology of the Sagittarius Core and Tidal Arms". Em: *ApJ* 599, pp. 1082–1115. eprint: astro-ph/0304198.

Martin, N. F., J. T. A. de Jong, & H.-W. Rix (2008). "A Comprehensive Maximum Likelihood Analysis of the Structural Properties of Faint Milky Way Satellites". Em: *ApJ* 684, 1075-1092, pp. 1075–1092. arXiv: 0805.2945.

Martin, N. F. et al. (2015). "Hydra II: A Faint and Compact Milky Way Dwarf Galaxy Found in the Survey of the Magellanic Stellar History". Em: *ApJL* 804, L5, p. L5. arXiv: 1503.06216.

Mateo, M. et al. (1996). "Discovery of a Tidal Extension of the Sagittarius Dwarf Spheroidal Galaxy". Em: *ApJL* 458, p. L13.

McConnachie, A. W. (2012). "The Observed Properties of Dwarf Galaxies in and around the Local Group". Em: *AJ* 144, 4, p. 4. arXiv: 1204.1562.

Mohr, J. J. et al. (2012). "The Dark Energy Survey data processing and calibration system". Em: *Society of Photo-Optical Instrumentation Engineers (SPIE) Conference Series*. Vol. 8451. Society of Photo-Optical Instrumentation Engineers (SPIE) Conference Series, p. 0. arXiv: 1207.3189 [astro-ph.IM].

Moore, B. et al. (1999). "Dark Matter Substructure within Galactic Halos". Em: *ApJL* 524, pp. L19–L22. eprint: astro-ph/9907411.

Muñoz, R. R., M. Geha, & B. Willman (2010). "Turning the Tides on the Ultra-faint Dwarf Spheroidal Galaxies: Coma Berenices and Ursa Major II". Em: *AJ* 140, pp. 138–151. arXiv: 0910.3946.

Muñoz, R. R. et al. (2012). "The Discovery of an Ultra-faint Star Cluster in the Constellation of Ursa Minor". Em: *ApJL* 753, L15, p. L15. arXiv: 1204.5750.

Newberg, H. J. et al. (2002). "The Ghost of Sagittarius and Lumps in the Halo of the Milky Way". Em: *ApJ* 569, pp. 245–274. eprint: astro-ph/0111095.

Newberg, H. J. et al. (2003). "Sagittarius Tidal Debris 90 Kiloparsecs from the Galactic Center". Em: *ApJL* 596, pp. L191–L194. eprint: astro-ph/0309162.

Newberg, H. J. et al. (2007). "The Overdensity in Virgo, Sagittarius Debris, and the Asymmetric Spheroid". Em: *ApJ* 668, pp. 221–235. arXiv: 0706.3391.

Odenkirchen, M. et al. (2001). "Detection of Massive Tidal Tails around the Globular Cluster Palomar 5 with Sloan Digital Sky Survey Commissioning Data". Em: *ApJL* 548, pp. L165–L169. eprint: arXiv:astro-ph/0012311.

Odenkirchen, M. et al. (2002). "Tidal Tails of the Globular Cluster Pal 5 Detected With SDSS Commissioning Data". Em: *Modes of Star Formation and the Origin of Field Populations*. Ed. by E. K. Grebel & W. Brandner. Vol. 285. Astronomical Society of the Pacific Conference Series, p. 184.

Pieres, A. et al. (2016). "Physical properties of star clusters in the outer LMC as observed by the DES". Em: *MNRAS* 461, pp. 519–541. arXiv: 1512.01032.

Pieres, A. et al. (2017). "A stellar overdensity associated with the Small Magellanic Cloud". Em: *MNRAS* 468, pp. 1349–1360. arXiv: 1612.03938.

Plummer, H. C. (1911). "On the problem of distribution in globular star clusters". Em: *MNRAS* 71, pp. 460–470.

Renaud, F., O. Agertz, & M. Gieles (2017). "The origin of the Milky Way globular clusters". Em: *MNRAS* 465, pp. 3622–3636. arXiv: 1610.03101.

Rockosi, C. M. et al. (2002). "A Matched-Filter Analysis of the Tidal Tails of the Globular Cluster Palomar 5". Em: *AJ* 124, pp. 349–363.

Sales, L. V. et al. (2017). "Identifying true satellites of the Magellanic Clouds". Em: *MNRAS* 465, pp. 1879–1888. arXiv: 1605.03574.

Salpeter, E. E. (1955). "The Luminosity Function and Stellar Evolution." Em: *ApJ* 121, p. 161.

Sbordone, L. et al. (2015). "Chemical abundances of giant stars in <ASTROBJ>NGC 5053</ASTROBJ> and <ASTROBJ>NGC 5634</ASTROBJ>, two globular clusters associated with the Sagittarius dwarf spheroidal galaxy?" Em: *A&A* 579, A104, A104. arXiv: 1505.01487.

Schlegel, D. J., D. P. Finkbeiner, & M. Davis (1998). "Maps of Dust Infrared Emission for Use in Estimation of Reddening and Cosmic Microwave Background Radiation Foregrounds". Em: *ApJ* 500, pp. 525–553. eprint: astro-ph/9710327.

Searle, L. & R. Zinn (1978). "Compositions of halo clusters and the formation of the galactic halo". Em: *ApJ* 225, pp. 357–379.

Sevilla, I. et al. (2011). "The Dark Energy Survey Data Management System". Em: *ArXiv e-prints*. arXiv: 1109.6741 [astro-ph.IM].

Simon, J. D. & M. Geha (2007). "The Kinematics of the Ultra-faint Milky Way Satellites: Solving the Missing Satellite Problem". Em: *ApJ* 670, pp. 313–331. arXiv: 0706.0516.

Simon, J. D. et al. (2015). "Stellar Kinematics and Metallicities in the Ultra-faint Dwarf Galaxy Reticulum II". Em: *ApJ* 808, 95, p. 95. arXiv: 1504.02889.

Simon, J. D. et al. (2017). "Nearest Neighbor: The Low-mass Milky Way Satellite Tucana III". Em: *ApJ* 838, 11, p. 11. arXiv: 1610.05301.

Slater, C. T. et al. (2013). "A Pan-STARRS1 View of the Bifurcated Sagittarius Stream". Em: *ApJ* 762, 6, p. 6. arXiv: 1211.2817.

Stewart, K. R. et al. (2008). "Merger Histories of Galaxy Halos and Implications for Disk Survival". Em: *ApJ* 683, pp. 597–610. arXiv: 0711.5027.

Suntzeff, N. B. et al. (1993). "Spectroscopy of Giants in the Sextans Dwarf Spheroidal Galaxy". Em: *ApJ* 418, p. 208.

Szabo, T. et al. (2011). "An Optical Catalog of Galaxy Clusters Obtained from an Adaptive Matched Filter Finder Applied to Sloan Digital Sky Survey Data Release 6". Em: *ApJ* 736, 21, p. 21. arXiv: 1011.0249 [astro-ph.CO].

The Dark Energy Survey Collaboration (2005). "The Dark Energy Survey". Em: *ArXiv e-prints*. arXiv: astro-ph/0510346.

Tollerud, E. J. et al. (2008). "Hundreds of Milky Way Satellites? Luminosity Bias in the Satellite Luminosity Function". Em: *ApJ* 688, 277-289, pp. 277–289. arXiv: 0806.4381.

Torrealba, G. et al. (2016a). "At the survey limits: discovery of the Aquarius 2 dwarf galaxy in the VST ATLAS and the SDSS data". Em: *MNRAS*. arXiv: 1605.05338.

Torrealba, G. et al. (2016b). "The feeble giant. Discovery of a large and diffuse Milky Way dwarf galaxy in the constellation of Crater". Em: *MNRAS* 459, pp. 2370–2378. arXiv: 1601.07178.

Walker, M. G. et al. (2007). "Velocity Dispersion Profiles of Seven Dwarf Spheroidal Galaxies". Em: *ApJL* 667, pp. L53–L56. arXiv: 0708.0010.

Walker, M. G. et al. (2015). "Magellan/M2FS Spectroscopy of the Reticulum 2 Dwarf Spheroidal Galaxy". Em: *ApJ* 808, 108, p. 108. arXiv: 1504.03060.

Walker, M. G. et al. (2016). "Magellan/M2FS Spectroscopy of Tucana 2 and Grus 1". Em: *ApJ* 819, 53, p. 53. arXiv: 1511.06296.

Westfall, K. B. et al. (2006). "Exploring Halo Substructure with Giant Stars. VIII. The Extended Structure of the Sculptor Dwarf Spheroidal Galaxy". Em: *AJ* 131, pp. 375–406. eprint: astro-ph/0508091.

White, S. D. M. & M. J. Rees (1978). "Core condensation in heavy halos - A two-stage theory for galaxy formation and clustering". Em: *MNRAS* 183, pp. 341–358.

Willman, B. & J. Strader (2012). ""Galaxy," Defined". Em: *AJ* 144, 76, p. 76. arXiv: 1203.2608.

Yanny, B. et al. (2009). "Tracing Sagittarius Structure with SDSS and SEGUE Imaging and Spectroscopy". Em: *ApJ* 700, pp. 1282–1298. arXiv: 0905.4502 [astro-ph.GA].

York, D. G. et al. (2000). "The Sloan Digital Sky Survey: Technical Summary". Em: *AJ* 120, pp. 1579–1587. eprint: astro-ph/0006396.

Zinn, R. (1993). "The Galactic Halo Cluster Systems: Evidence for Accretion". Em: *The Globular Cluster-Galaxy Connection*. Ed. by G. H. Smith & J. P. Brodie. Vol. 48. Astronomical Society of the Pacific Conference Series, p. 38.